NASA CR-156662

14897-6011-RU-00

APPLICATION STUDIES

INSTRUMENT POINTING SYSTEM APPLICABILITY AND ORBITER STABILIZATION FOR EVAL MISSIONS

(NASA-CR-156662) INSTRUMENT POINTING SYSTEM APPLICABILITY AND ORBITER STABILIZATION FOR EVAL MISSIONS. APPLICATION STUDIES (TRW Defense and Space Systems Group) 327 p HC A15/MF A01 CSCL 22B G3/18
N78-15164
Unclas
58019

MARCH 1977

CONTRACT NO. NAS5-21188

Prepared for

NATIONAL AERONAUTICS AND SPACE ADMINISTRATION
Goddard Space Flight Center
Greenbelt, Maryland 20771

TRW
DEFENSE AND SPACE SYSTEMS GROUP

ONE SPACE PARK • REDONDO BEACH, CALIFORNIA 90278

14897-6011-RU-00

INSTRUMENT POINTING SYSTEM APPLICABILITY AND ORBITER STABILIZATION FOR EVAL MISSIONS

Prepared by
V. A. Spector

March 1977

Contract No. NAS5-21188

Approved by: AMFrew
A. M. Frew, Manager
Control Systems Engineering Dept.

Approved by: Will A. Finley.
W. A. Finley, Manager
Control & Sensor Systems
Laboratory

Prepared for
National Aeronautics and Space Administration
Goddard Space Flight Center
Greenbelt, Maryland 20771

TRW
Defense and Space Systems Group

One Space Park Redondo Beach, California 90278

TABLE OF CONTENTS

Page

1.0 INTRODUCTION 1-1

2.0 SUMMARY AND CONCLUSIONS 2-1
  2.1 IPS Capability Assessment 2-1
  2.2 Orbiter Stabilization 2-9
  2.3 System Definition 2-15

3.0 FUNCTIONAL REQUIREMENTS 3-1
  3.1 IPS Requirements 3-1
  3.2 Orbiter Stabilization Requirements 3-1

4.0 IPS GIMBAL/PAYLOAD MASS PROPERTIES 4-1
  4.1 Derivation of Inertia About CR 4-1
  4.2 Numerical Results 4-9

5.0 IPS SLEWING ANALYSIS 5-1
  5.1 Time/Angle Relations for Accelerate/Decelerate Phases . 5-3
  5.2 Time/Angle Relations for Slewing 5-5

6.0 IPS EARTH POINTING ANALYSIS 6-1
  6.1 Aim Point in Orbit Plane 6-1
  6.2 General Aim Point 6-4
  6.3 Earth Pointing/Payload Capability Relations 6-11

7.0 IPS CONTROL SYSTEM DEFINITION 7-1
  7.1 Attitude Reference System 7-1
  7.2 Command and Error Processing 7-8
  7.3 IPS Servo Control Law/Shaping 7-13

TABLE OF CONTENTS
(continued)

Page

8.0 EVALUATION OF ORBITER EARTH VIEWING ORIENTATIONS 8-1
    8.1 Definition of Potential Earth Viewing Orientations . . 8-2
        8.1.1 Coordinate Systems and Transformations 8-2
        8.1.2 Potential Earth Viewing Orientations 8-6
    8.2 Disturbance Torques 8-14
    8.3 Null Torque Attitudes and Sensitivities 8-15
        8.3.1 Orientation 1 8-21
        8.3.2 Orientation 2 8-21
        8.3.3 Orientation 3 8-22
        8.3.4 Orientation 4 8-26
        8.3.5 Orientation 5 8-26
        8.3.6 Orientation 6 8-30
        8.3.7 Conclusions 8-30
    8.4 Effect of Atmospheric Density Variations on Null Torque Attitudes 8-31
        8.4.1 Long Term Variations 8-34
        8.4.2 Short Term Variations 8-38

9.0 ORBITER CONTROL REQUIREMENT ANALYSIS 9-1
    9.1 Stability Analysis 9-1
        9.1.1 Open Loop Stability 9-5
        9.1.2 Closed Loop Stability 9-6
    9.2 Actuator Requirement Estimate 9-9
        9.2.1 Capture From RCS Limit Cycle 9-9
        9.2.2 Normal Operation 9-13

TABLE OF CONTENTS
(continued)

Page

10.0 MAGNETIC CONTROL OF ORBITER 10-1
  10.1 Control Design 10-4
  10.2 Implications of Magnetic Control 10-7
    10.2.1 Interaxis Coupling 10-7
    10.2.2 Magnet Sizing 10-14
  10.3 Conclusions 10-19

11.0 MOMENTUM EXCHANGE CONTROL OF ORBITER 11-1
  11.1 System Equations 11-1
  11.2 Control Design 11-5
  11.3 Initial Capture From RCS Limit Cycle 11-8
    11.3.1 Momentum Estimate 11-9
    11.3.2 Torque Estimate 11-11
    11.3.3 Simulation 11-13
  11.4 Normal Operation 11-15
    11.4.1 Selection of Control Law 11-20
    11.4.2 Nose Forward Orientation 11-22
    11.4.3 Nose Down Orientation 11-26
  11.5 Momentum Exchange Device Selection 11-29

12.0 ORBITER NULL TORQUE ATTITUDE STABILIZATION SYSTEM DEFINITION . 12-1
  12.1 Command and Error Processing 12-1
  12.2 Control Law 12-4
  12.3 CMG Control and Momentum Management 12-7

REFERENCES R-1

Appendix A. Space Shuttle Orbiter Data A-1
Appendix B. IPS Data B-1
Appendix C. Derivation of Earth Pointing Relations C-1
Appendix D. Orbiter Disturbance Model D-1
Appendix E. Tilted Dipole Magnetic Field Model E-1
Appendix F. Momentum Exchange Device Tradeoff F-1

1.0 INTRODUCTION

TRW Systems has performed a series of Application Studies for NASA Goddard Space Flight Center under contract NAS5-21188. These studies have focused on three-axis stabilized control system designs employing momentum/reaction wheel and magnetic or thruster torquing. Tasks included in these studies have been conceptual design, system tradeoffs, control law development, performance analysis and simulation. The current study investigates two distinct but related aspects of the Earth Viewing Applications Laboratory (EVAL) shuttle missions. The first is evaluating the applicability of the gimballed Instrument Pointing System (IPS) to EVAL missions by comparing the IPS capabilities with the EVAL requirements. The other area of study is assessment of means of stabilizing the shuttle orbiter attitude in earth viewing orientations for prolonged periods without use of the orbiter gas reaction control system (RCS).

The IPS, currently under development by the European Space Agency for Spacelab, has primarily been considered as a gimballed platform for stellar or solar viewing experiments which require pointing to an inertially fixed target. One objective of this study is to conduct analyses of an earth oriented, shuttle-borne IPS and determine which modifications, if any, should be made to the current IPS design to make it suitable to earth viewing applications. Shuttle orbits from as low as 150 km up to 1000 km are to be considered with small and large (maximum permissible size/weight) IPS mounted payloads. Specific tasks included in this phase of the study are:

- Generation and graphic presentation of parametric data relating payload weight and dimensions to the slewed inertia about the IPS center of rotation.
- Analysis of slewing requirements and comparison with existing IPS rate and torque capabilities to establish an EVAL payload envelope for slewing.

- Analysis of dynamic requirements for pointing at earth fixed targets and generation of an EVAL payload capability envelope for earth pointing.
- Definition of an IPS control system suitable for the EVAL mission, including the attitude reference system and data flow.

EVAL shuttle missions impose specialized, and somewhat unusual, pointing and control requirements on the shuttle orbiter. To minimize translational and rotational accelerations on the orbiter, as well as to reduce contamination of certain experiment payloads, the orbiter reaction control system (RCS) should not be used for orbiter attitude control during some phases of EVAL missions. The second main objective of this study is to analyze the control requirements for maintaining the orbiter in an earth viewing orientation for prolonged periods without use of the RCS, and to define an auxiliary orbiter control system capable of meeting these requirements. Specific tasks included in this phase of the study are:

- Evaluation of potential earth viewing orientations for the orbiter with respect to field of view, dynamic stability, and sensitivity to system and environmental variations. To minimize the control actuator requirements the desirable orientations are null torque attitudes, meaning attitudes at which the total external disturbance torque on the orbiter is zero.
- Selection of one or more orbiter null torque orientations, so that both earth surface and earth limb viewing can be performed. Analysis of the orbiter auxiliary control system requirements for the selected orientations based on the initial conditions imposed by the orbiter RCS and the external disturbance environment.
- Analysis and definition of a suitable set of control actuators to stabilize the orbiter near the null torque attitude. Candidate actuators to be evaluated include electro-magnets and momentum exchange devices (reaction wheels or control moment gyros).

- Definition of an orbiter null torque attitude stabilization system employing the selected set of control actuators.

Each of the above defined tasks is addressed in one or more sections of the main body of this report. First, however, is a section devoted to summarizing the main results and conclusions of the study, and another section summarizing the functional requirements and assumptions that underlie the study. The data base and supporting details for the study are contained in the appendices.

2.0 SUMMARY AND CONCLUSIONS

2.1 IPS CAPABILITY ASSESSMENT

Three aspects of the current IPS design limit its earth pointing and slew capabilities

- The gimbal rate limit of P = 2.5 deg/sec imposed by the rate gyros.
- The maximum gimbal drive motor torque of T_m = 20 N-m.
- The increased value of effective inertia about the gimbal center of rotation (CR), due to the payload CG/gimbal CR offset (minimum offset is 1.19 m, of which 0.69 m results from inside-out gimbal arrangement and 0.50 m results from payload support clamp requirements).

Of the above factors the gimbal rate limit has the smallest impact on performance, mainly by setting the lower altitude limit for earth-fixed target tracking at h_{min} = 175 Km. The primary restraining factor on both tracking and slewing performance is the peak acceleration available from the nominal 20 N-m drive motor. As the elevation axis has an inertia at least as great as the cross-elevation axis and significantly greater rate and acceleration requirements, only the elevation axis need be considered in determining the current IPS capability envelopes.

To realistically evaluate the time required to reposition the IPS between tracking targets, while including the effect of the gimbal angle hard limits and the angle/rate/acceleration boundary conditions at the start and end of tracking, the total maneuver between tracking targets has been divided into three submaneuvers. For the accelerate/decelerate phases, the worst case condition results when the boundary condition on rate, at the start or end of tracking, is the maximum track rate for the particular altitude in question. Table 2-1 summarizes the IPS accelerate/decelerate capability with the nominal motor torque $T_m = 20$ N-m, under the conditions of allowing a maximum time of 10 seconds and a maximum gimbal travel of 10 degrees to go from rest to the maximum track rate listed (or vice versa). Figure 2-1 compares this capability with the required payload envelope, in terms of payload length and mass (dashed rectangle). To yield a two-dimensional plot, the payload radius has been assumed as $r_p = 1.0$ m. Varying r_p within the range $0.25 \leq r_p \leq 1.5$ m has little effect on the plotted curves, however. For each indicated altitude, the region below the solid curve represents the payload range that can be accelerated or decelerated between rest and the maximum track rate for the altitude in less than 10 seconds with less than 10 degrees gimbal travel. Even at the lowest altitude (175 Km), a large range of payloads can be accommodated, while at 1000 Km virtually all payloads meet the requirements.

The nominal IPS slew capability, where the slew angle is measured betwee zero gimbal rate points, is summarized in Table 2-2. The requirement here is to achieve an average slew rate $R_S = \Delta\gamma/t_f \geq 1.0$ deg/sec, with the rate limit P = 2.5 deg/sec. Figure 2-2 compares this capability with the required payload envelope. For the larger slew angles, where the slew time is most important, the nominal IPS is capable of meeting the average rate requirement with most payloads.

With most combinations of slew angle and payload mass properties, the gimbal rate limit of P = 2.5 deg/sec is not reached. Increasing the value of P therefore will not result in any significant reduction in slew time. The only way of decreasing slew time while retaining the basic IPS structure is to increase the maximum motor torque T_m on the elevation drive. Slew performance is relatively satisfactory

Table 2-1. Nominal IPS Accelerate/Decelerate to/from Maximum Track Rate Capability for $t_{max} = 10$ sec, $\Delta\gamma_{max} = 10$ deg

Altitude h (Km)	Maximum Track Rate $\dot{\gamma}_{max}$ (deg/sec)	Maximum Inertia about CR with $T_m = 20$ N-m ($Kg\text{-}m^2$)
175	2.49	3600
200	2.16	4340
300	1.41	8128
500	0.869	13182
700	0.554	20695
1000	0.364	31466

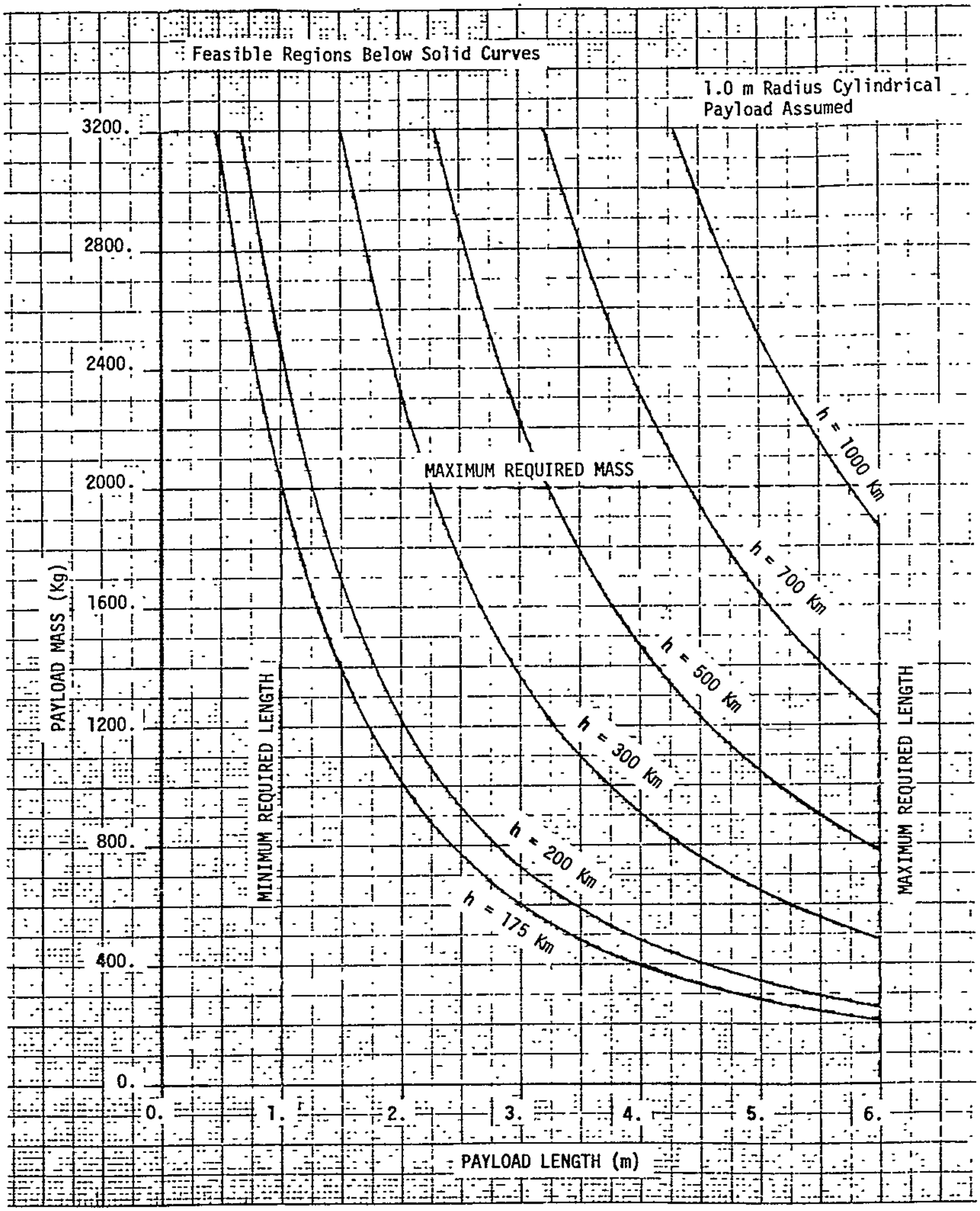

Figure 2-1. Nominal IPS Accelerate/Decelerate Capability vs Requirements With t_{max} = 10 sec and $\Delta\gamma_{max}$ = 10 deg Allowed for Reaching Maximum Track Rate

Table 2-2. Nominal IPS Slew (Zero Rate to Zero Rate) Capability for Average Slew Rate $R_S \geq 1$ deg/sec with Rate Limit P = 2.5 deg/sec

Slew Angle $\Delta\gamma$ (deg)	Maximum Inertia about CR with T_m = 20 N-m ($Kg-m^2$)
20	5740
40	11460
60	17200
80	22920
100	28640
120	34380

Table 2-3. Nominal IPS Tracking Capability

Altitude h (Km)	Maximum Inertia about CR with T_m = 20 N-m ($Kg-m^2$)
150	11600
175	15911
200	20940
250	33218
300	48556
500	143043
700	296796
1000	657625

ORIGINAL PAGE IS
OF POOR QUALITY

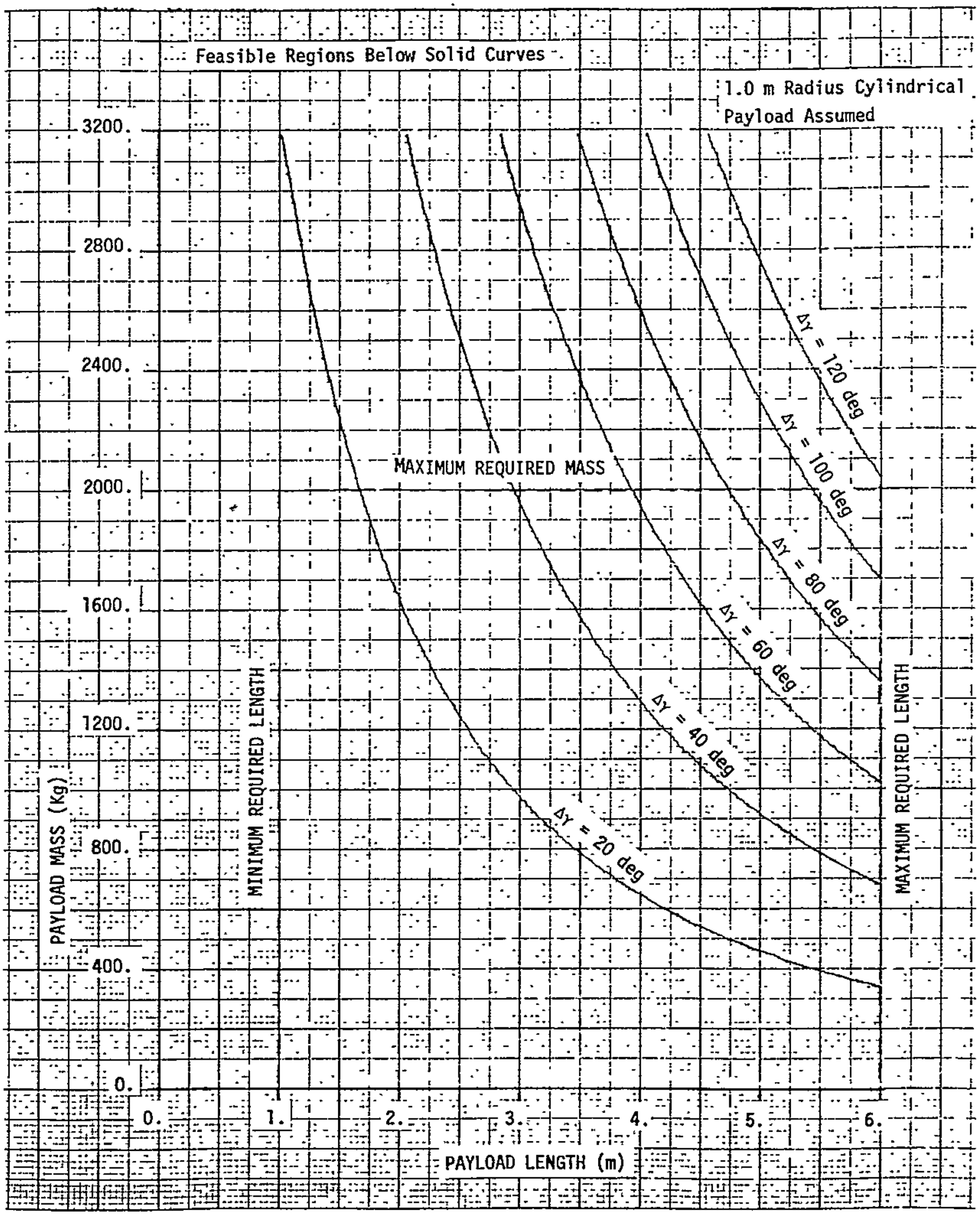

Figure 2-2. Nominal IPS Slew Capability vs Requirements for Average Slew Rate R_S > 1 Deg/Sec and Rate Limit P = 2.5 Deg/Sec

with the nominal motor, and in any case slewing is a secondary consideration in the IPS design. Increasing the motor torque solely to improve slew performance cannot therefore be justified.

The primary IPS performance capability required for EVAL is tracking earth-fixed targets within acceptable error limits. This is obviously contingent on being able to meet the required tracking rates and accelerations. The tracking rate requirement can be met with the nominal rate limit P = 2.5 deg/sec for all altitudes above 175 Km. This covers all anticipated EVAL missions. The available motor torque and required acceleration sets the upper limit on the inertia about the CR that can follow the track profile. As tracking will be done with a closed loop control system, some portion of the motor torque capability must be reserved for fine control perturbations and disturbance torques. The amount of torque that must be reserved for these purposes depends on the control bandwidth, disturbance environment, etc., but it is in general small. Determination of these factors is beyond the scope of the present study. Lacking this data, it will be assumed here that the full 20 N-m torque is available for accelerating the payload. Table 2-3 summarizes the IPS tracking capability, in terms of maximum inertia about the CR. The data at h = 150 km is for reference only; the gyro rate limit restricts operation to altitudes above 175 km. Figure 2-3 translates the data in Table 2-3 into payload length/mass terms. The figure clearly shows that earth pointing is feasible for all except the largest payloads in the lowest orbits.

The main attitude determination problem for controlling the IPS is that the star tracker view of the celestial sphere is highly restricted for the EVAL mission by the combined geometry of the orbiter payload bay doors and radiators, the orbiter wing surfaces, the orbiter tail, the cockpit (crew cabin), the Spacelab pressurized module, and the earth. There is a solution to the problem, however, and an

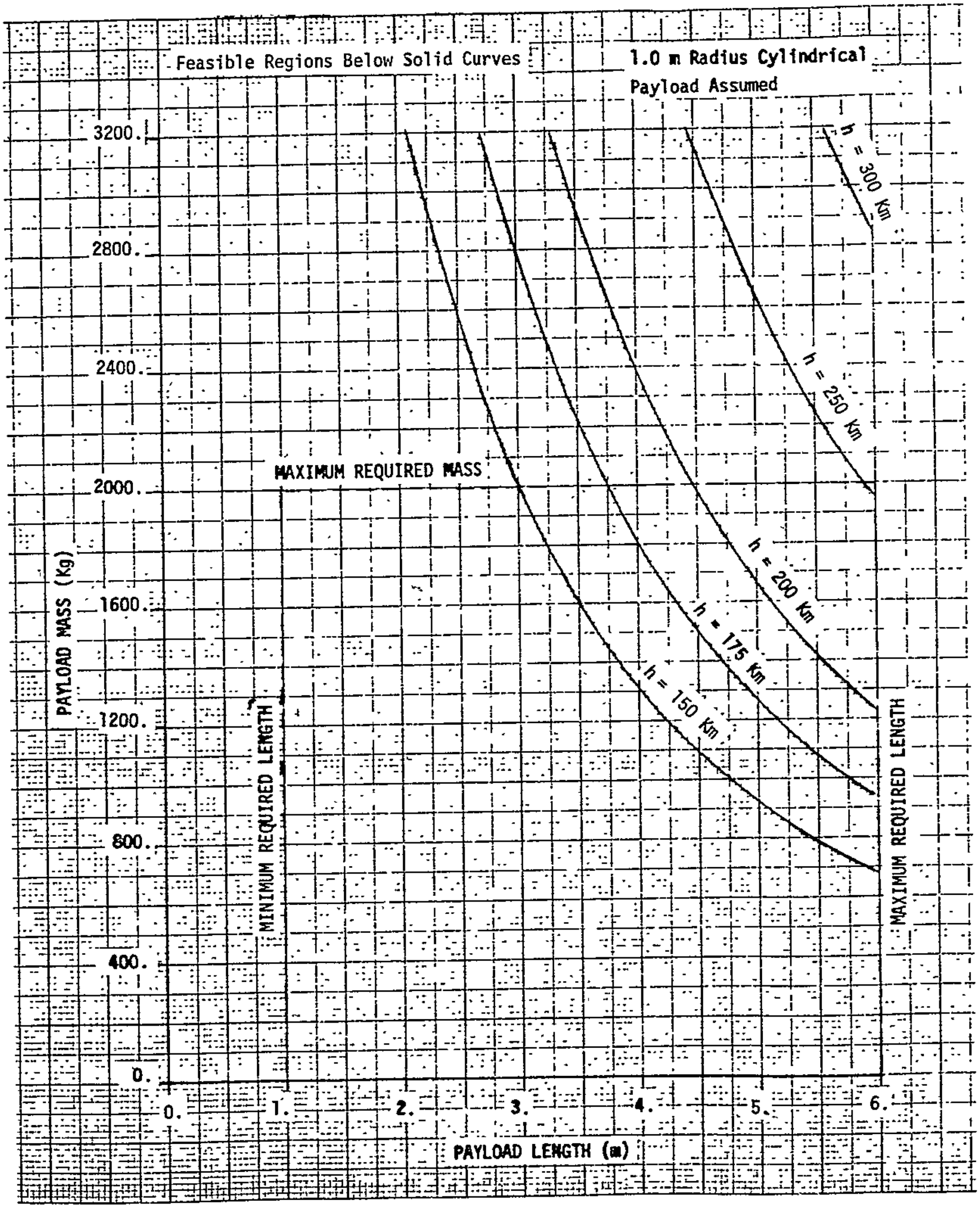

Figure 2-3. Nominal IPS Tracking Capability vs Requirements Assuming 20 N-m Available to Accelerate Payload

8° x 40° window of the celestial sphere is available if it is permissible for the tracker field of view (FOV) to come within 20 degrees of the earth's limb and 15 degrees of the orbiter surfaces. Depending somewhat on the star tracker aperture, a reasonably sized shade in the 15 - 25 inch range can be successfully utilized to permit the tracker to operate within 20 degrees of the earth's limb. The available 8° x 40° window always contains at least one guide star of +6 M_V or brighter (based on Yale catalog) and with 95% confidence contains at least one star of +4 M_V or brighter. The baseline IPS star tracker (Honeywell HEAO-B) for solar and stellar missions has insufficient track rate capability to permit "on the fly" star tracker readings during EVAL payload pointing. Either a tracker with a higher track rate is required (up to 0.068 deg/sec for limb viewing, up to 2.5 deg/sec to track a point on the earth surface) or payload pointing must be interrupted to get a star reading.

2.2 ORBITER STABILIZATION

When the combined effects of the external disturbance torques and coupled rigid body dynamics are considered, all low altitude ($h < 400$ km) and almost all high altitude null torque attitudes of the shuttle suitable for EVAL are unstable equilibriums. An active attitude stabilization system must therefore be provided, that can satisfy the following requirements:

- stabilizes orbiter motion
- able to capture from RCS limit cycle
- able to tolerate variation and uncertainty in location of torque null.

The two most generally applicable null torque orientations are illustrated in Figures 2-4 and 2-5, in both the nominal and maximum offset positions. The nose forward orientation is highly unstable in pitch, due to gravity gradient torques but provides the best

NOMINAL ORIENTATION: h > 400 km

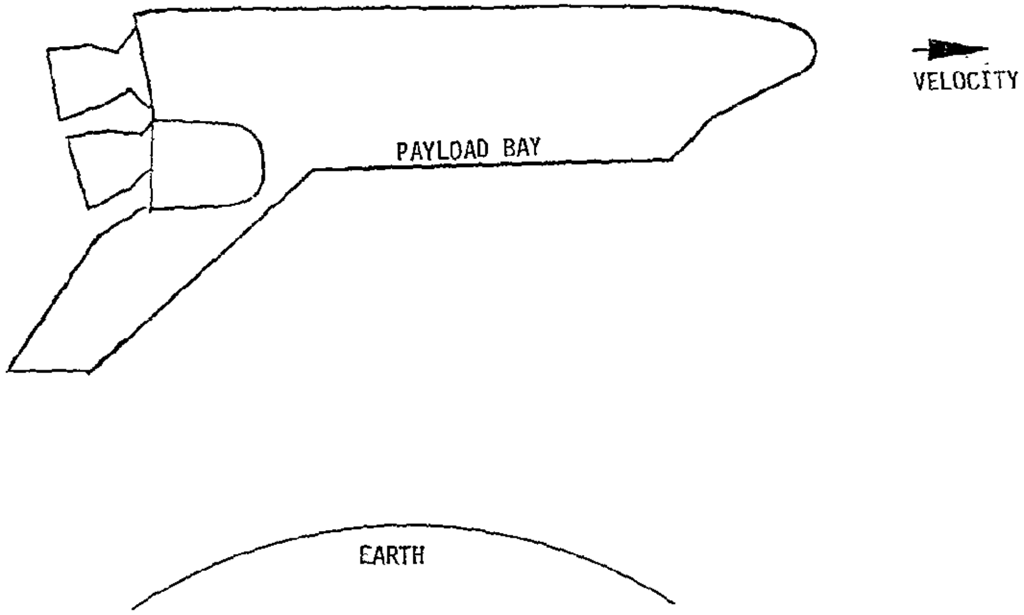

MAXIMUM OFFSET: h = 180 km

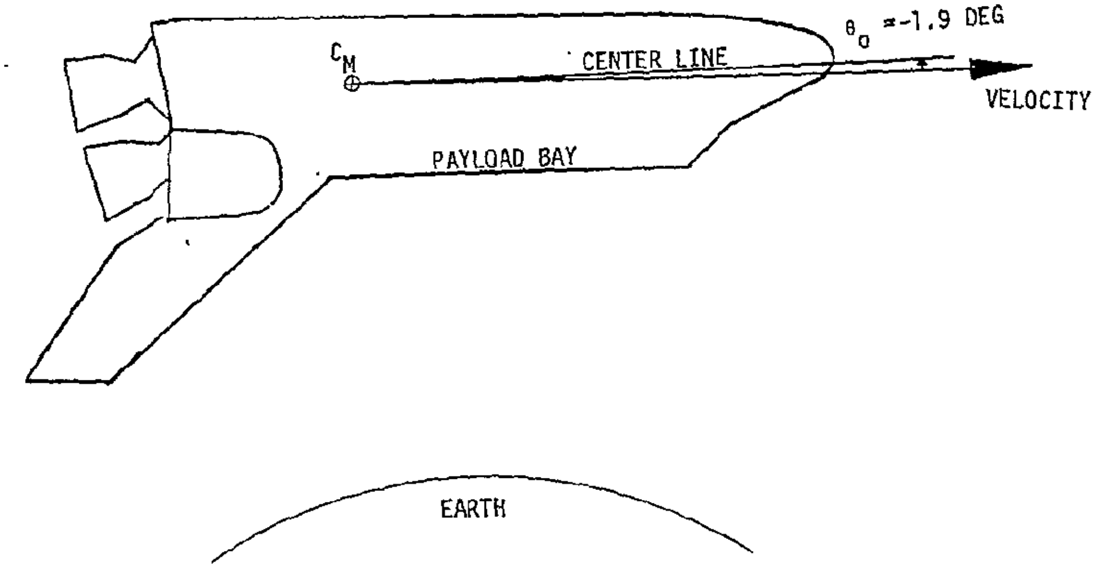

Figure 2-4. Nose Forward Orientation

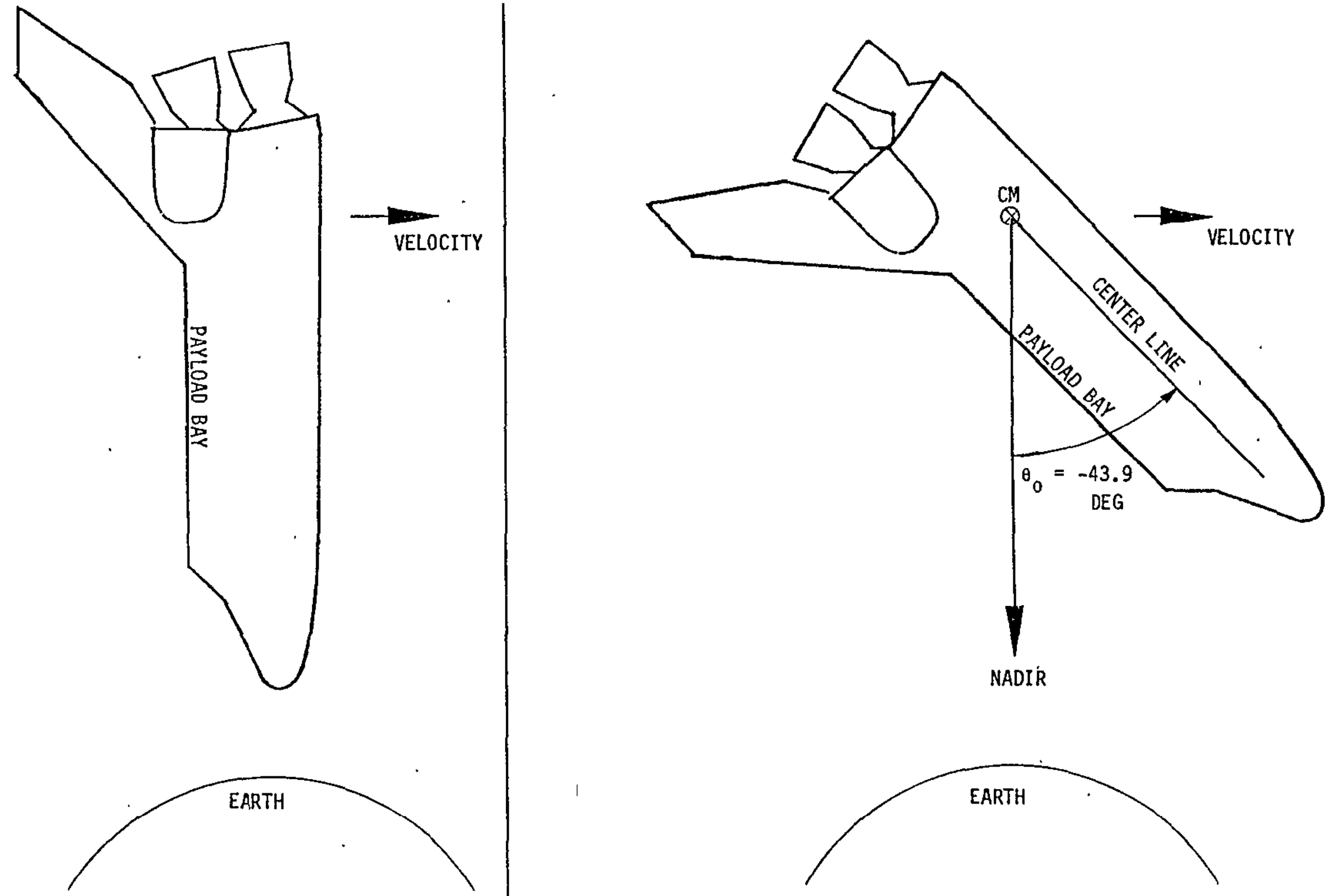

NOMINAL ORIENTATION: h > 400 km

MAXIMUM OFFSET: h ≈ 180 km

Figure 2-5. Nose Down Orientation

view of the earth and has a relatively predictable null torque attitude. The nose down orientation permits earth limb viewing and is only slightly unstable in roll, but the null torque attitude is highly sensitive to atmospheric density variations. This is due not only to the large cross section of the orbiter in this orientation, but also to a near resonance between the orbiter gravity gradient libration frequency for the pitch axis and the predominant orbit frequency variation in the atmospheric density.

With the current nominal orbiter parameters, the largest torque requirement in most cases is for capture from the orbiter RCS limit cycle, rather than during normal steady state operation. The steady state torque requirement is sized largely by the variation and uncertainty in the location of the null torque attitude, as determined by the atmospheric density (the primary influence at low altitudes) and the orbiter mass properties. The dominant influence on the transient torque requirement for attitude capture from the RCS limit cycle is the nominal limit cycle rate of 0.01 deg/sec rather than the nominal limit cycle deadzone of 0.1 deg. The size of the actuators required for the null torque attitude stabilization system can be reduced significantly if an additional "low rate" RCS mode is made available. It is recommended that such a mode be provided, with the limit cycle rates reduced by at least a factor of 10 from the current nominal. A proportional increase in the RCS deadzone, if required to achieve the reduced rates, would be acceptable.

Even if several optimistic assumptions are made, magnets are incapable of providing prolonged three axis stabilization for the orbiter. Among the points weighing against magnets are the following:

- Physical limitations of magnetic control due to the relative orbiter/magnetic field geometry introduce undesirable interaxis coupling, with adverse effects on stability.

- Very large magnets (10^7 pole-cm per axis) required for even marginal performance.
- RCS limit cycle rates must be reduced from current nominal values by a factor of 25 to 40 to permit attitude capture. The feasibility of doing this is highly doubtful.
- Lack of reserve torque capability can result in loss of control due to variations in atmospheric density or orbiter mass properties.
- Possible adverse effects of large magnetic field on nearby payloads.

Momentum exchange control, on the other hand, is capable of stabilizing the orbiter in either of the selected null torque orientations over almost the entire EVAL altitude range. The relatively large control torque available allows a more sophisticated control system, including adaptive features, than is practical with magnets. The adaptive loops can reduce the steady state momentum storage requirement by constantly tracking the location of the uncertain and variable null torque attitude, and by using the external disturbance torques for momentum unloading. In order to obtain full advantage of this potential reduction in the steady state momentum requirement, the transient momentum requirement for capture from the RCS limit cycle must be reduced. At least two methods of achieving a reduction in the transient momentum storage requirement are possible:

- Providing a "low rate" RCS limit cycle mode as a transition between the normal RCS limit cycle and EVAL operation.
- Using short (~50 msec) vernier thruster firings to unload excess momentum during the capture transient.

If neither of these options is provided, simulation shows that the capture transient requires per axis capabilities on the order of 12 N-m torque and 2700 N-m-sec momentum.

Two idealized control strategies have been examined for orbiter control after the capture transient:

1. Follow the null torque attitude exactly
2. Hold the null torque attitude corresponding to the mean density.

Analysis shows that the first strategy requires less torque and momentum for disturbance variations with frequencies less than the pitch gravity gradient libration frequency, while the second strategy should be chosen on this basis for higher frequency disturbance variations. That is, the control system should attempt to follow low frequency null torque attitude variations, and resist being perturbed by high frequency variations. For all altitudes in the EVAL range for which aerodynamic torques are significant, the predominant orbit frequency variation in the atmospheric density falls into the range where following the null torque attitude is more efficient. In the nose forward orbiter orientation, this implies a peak-to-peak pitch motion of less than one degree over an orbit with a ±20% density variation. This motion is at a frequency far below the IPS bandwidth and is unlikely to adversely affect IPS pointing.

In the "nose down" orbiter orientation a ±20% density variation results in peak-to-peak null-torque attitude variations of over 30 degrees at 180 km and 10 degrees at 200 km. If the orbiter attempts to follow the null torque attitude, the peak pitch rate relative to the orbit reference frame is 0.017 deg/sec at 180 km and 0.005 deg/sec at 200 km. If the orbiter attempts to maintain a fixed attitude relative to the orbit reference frame instead, the peak-to-peak momentum excursion would be over 6000 N-m-sec at 180 km and 3600 N-m sec at 200 km. These values exceed the momentum storage capability required to capture from a 0.001 deg/sec RCS limit cycle, and could thus size the CMG's. Expected atmospheric density variations in the "nose down" orientation result in either excessive attitude excursions or extreme momentum storage requirements, and therefore may make operation in this orientation unfeasible below about 250 km.

Control compensation has been designed to use the available measurements to approximate the selected control strategy. The momentum required to accommodate the orbit period atmospheric density variations with the practical control law is about twice that required with ideal control.

A tradeoff study has indicated that double gimbal control moment gyros (DG CMG) are the most suitable momentum exchange devices for the orbiter null torque attitude stabilization system. Three orthogonally mounted DG CMG's, each capable of producing 2710 N-m-sec (2000 ft-lb-sec) momentum and 13.6 N-m (10 ft-lb) torque, will allow capture from the nominal 0.01 deg/sec RCS limit cycle and provide orbiter attitude stabilization in the nose forward orientation above 180 km and in the nose down orientation above 200 km. Smaller CMG's could be used if the recommended reduction in RCS limit cycle rates is provided and if operation in the nose down orientation is restricted to altitudes above 250 km.

2.3 SYSTEM DEFINITION

Figure 2-6 shows the interfaces between the major subsystems and components comprising the EVAL pointing and control system. Four subsystems participate in the pointing and control task

- the orbiter flight control system (FCS)
- Spacelab
- Orbiter null torque attitude stabilization system
- IPS control system

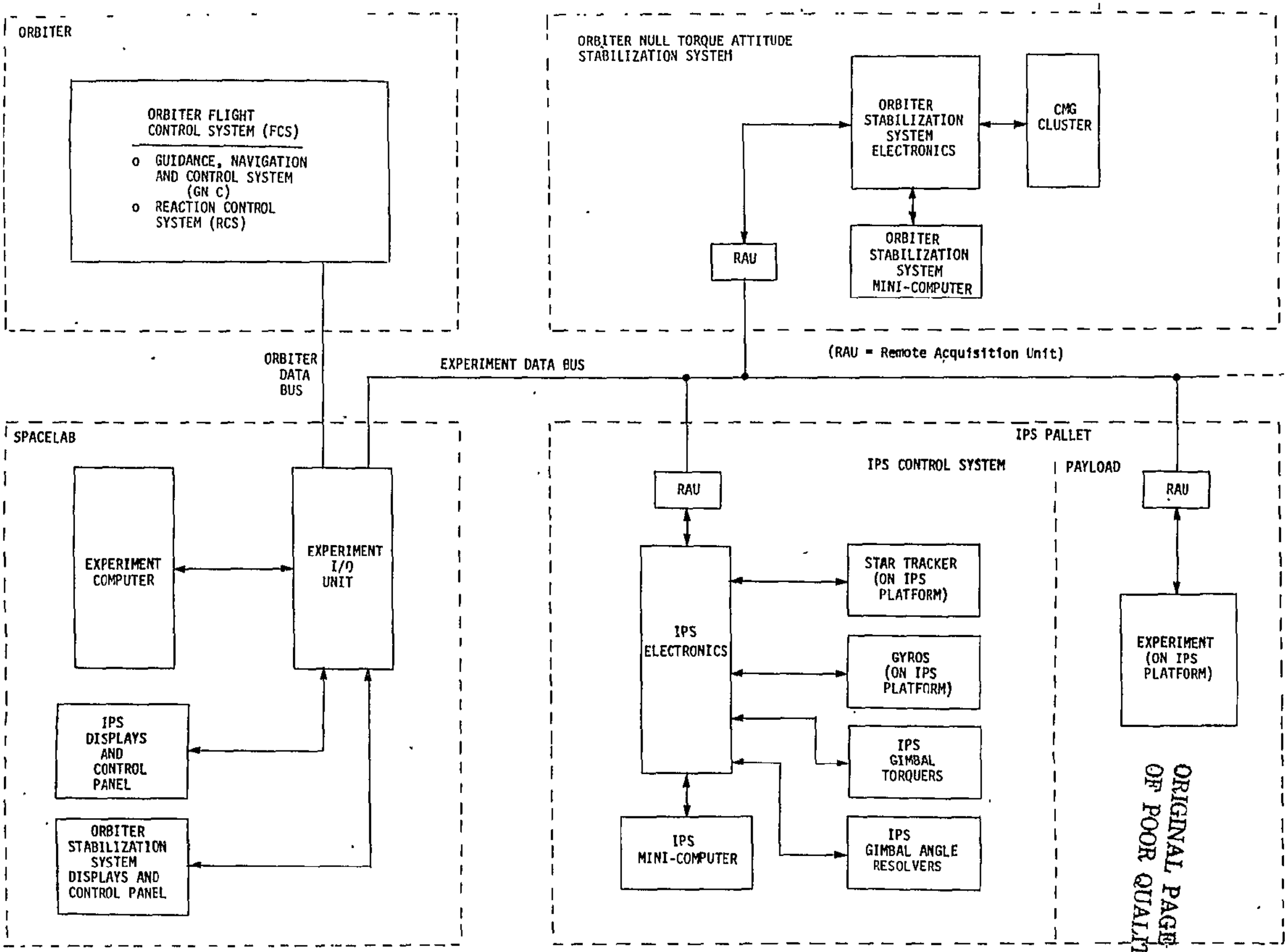

Figure 2-6. IPS/EVAL Pointing and Control System Interfaces

The first two of these subsystems fall, for the most part, outside the scope of the present study and will be discussed only in terms of functional requirements implied by the study results. The latter two subsystems are peculiar to EVAL, and detailed data flow diagrams for each are presented and discussed in Sections 7 and 12 respectively.

Several steps have been taken to simplify the interfaces, minimize the amount of data that must be interchanged, and minimize the computational burden on the spacelab experiment computer. For uniformity in the interfaces, all pointing and control data transfer is performed digitally over data buses. Remote acquisition units (RAU's), described in Reference 1, are used to perform the necessary addressing and data formatting functions. The pointing and control data flow through the experiment data bus and the computational burden on the spacelab experiment computer has been minimized by performing all high rate data processing locally within the subsystems, using programmable digital electronics (PDE). For definiteness, Figure 2-6 indicates the PDE as mini-computers, but a future trade study is required to choose between mini-computers, general purpose microprocessors, dedicated special purpose microprocessors, or some combination of the above. In any case, the experiment data bus is only required to handle the following low rate data

- pointing commands (i.e., target coordinates)
- orbiter attitude data
- orbiter ephemeris data
- mode control commands
- housekeeping data

The guidance, navigation, and control (GN&C) and reaction control system (RCS) elements of the orbiter flight control system are utilized by the EVAL pointing and control system. The required operating modes and GN&C system outputs are for the most part included in the baseline system described in Reference 1. The attitude and ephemeris data listed in Table 2-4 (or its equivalent) is required for EVAL and is assumed available from the GN&C computer on an external data bus. The transformation from the earth centered inertial (ECI) to orbit reference frame (R), A_{RI}, can be derived from the ephemeris data if not computed in the GN&C computer. The orbiter null torque attitude stabilization system requires A_{RI} plus the orbiter attitude reference data $\bar{\omega}_B$ and A_{BI}. The IPS control system includes its own inertial attitude reference system and requires attitude data from the orbiter only for initialization. Ephemeris data is required for IPS pointing at and tracking of earth fixed targets. The orbiter null torque attitude stabilization system supercedes the orbiter reaction control system in controlling the orbiter attitude during EVAL operation requiring either low accelerations or low contamination levels. The RCS is, however, needed to support the null torque attitude stabilization system by providing suitable initial conditions on the orbiter state vector and by producing torques to unload excess CMG momentum. The modes of RCS operation required are:

- The existing rotational maneuver mode is needed to initialize the orbiter in the estimated null torque attitude.
- The existing attitude hold mode should be modified to provide a 0.001 deg/sec limit cycle about the estimated null torque attitude.
- A new momentum unloading mode is required for minimum on-time ($\sim$ 40 msec) vernier thruster firings to desaturate the CMG cluster. This mode is used during initial capture from the RCS attitude hold limit cycle and for occasional unloading of secular torque build-up.

Table 2-4. Attitude and Ephemeris Data Required from Orbiter GN&C Computer

Symbol	Description
$\bar{\omega}_B$	Orbiter body components of orbiter inertial rate
A_{BI}	Direction cosine matrix indicating the attitude of the orbiter body (GN&C base) relative to the ECI frame
A_{RI}	Direction cosine matrix indicating the attitude of the orbit reference frame relative to the ECI frame
$\bar{r}_I$	Orbiter position in ECI coordinate
$\bar{v}_I$	Orbiter velocity in ECI coordinate
$\bar{a}_I$	Orbiter acceleration in ECI coordinates
GMT	Greenwich mean time

Overall operation of the EVAL pointing and control system is controlled and coordinated by equipment in the Spacelab module. This equipment consists of display and control panels for the IPS and for the orbiter null torque attitude stabilization system, the experiment computer, and the experiment I/O unit. To minimize the burden on the experiment computer, processing in the spacelab is limited to generation of target commands and transfer of attitude and ephemeris data. All high rate loops should be closed locally in the IPS control and orbiter null torque attitude stabilization system computers.

3.0 FUNCTIONAL REQUIREMENTS

This section briefly summarizes the EVAL functional requirements relevant to this study. Requirements relating to control of the IPS are presented first, followed by orbiter stabilization requirements.

3.1 IPS REQUIREMENTS

Table 3-1 summarizes the IPS/payload constraints and requirements for EVAL that have been identified. The values given in the table for the performance/capability constraining parameters are the nominal values for the baseline IPS design; modifications may be necessary or desirable to adapt IPS to EVAL.

The requirement side of the picture is less clear. Data on specific payload/orbit/viewing requirement combinations for potential EVAL missions is sparse or lacking. For this reason, and also to provide results with wider applicability, the assumption is made that tracking of earth-fixed targets is required over the entire 60 degree half angle view cone, over the indicated orbit range, for all combinations of payload mass properties satisfying the baseline IPS payload constraints. No data has been available on specific slew time/angle requirements; Table 3-1 therefore gives assumed values.

3.2 ORBITER STABILIZATION REQUIREMENTS

The orbiter attitude is normally stabilized using the vernier reaction control system (RCS) thrusters described in Appendix A. To reduce contamination and translational accelerations to the level required by some EVAL missions, the RCS must be disabled and the orbiter stabilized by auxiliary means. Table 3-2 summarizes the functional requirements for orbiter stabilization with the RCS disabled.

Table 3-1. IPS Constraints and Requirements for EVAL

Parameter	Constraint/ Requirement	Symbol	Value or Range	Comments
Drive motor torque	C	T_m	20 N-m	Both motors in drive used simultaneously
Maximum slew rate	C	P	2.5 deg/sec	Limited by maximum input rate permitted by rate gyros
Payload CG/Gimbal CR* Offset	C	-	1.19→3.69 m	Payload constraints dictated by payload support clamp requirements
Payload length	C/R	ℓ_p	1 → 6 m	
Payload Mass	C	m_p	$\leq$ 3000 kg	
	R		$\leq$ 2000 kg	
Payload radius	C/R	r_p	0.25→1.5 m	
Minimum inertia about CR (no payload)	C	I_M^{CR}	56 kg-m^2	Estimated from outer gimbal and payload integration ring mass properties
Gimbal motion limits	C	$\|\beta\|_{max}$, $\|\gamma\|_{max}$	70 deg	Limited mechanically in gimbal assembly and electronically in drive electronics
View cone half-angle	R	-	60 deg	Target tracking required in view cone, centered on local vertical
Target tracking error	R	-	N/A	Largely determined by gyro, star tracker and ephemeris errors

* CR = center of rotation

Table 3-1. IPS Constraints and Requirements for EVAL (cont'd)

Parameter	Constraint/ Requirement	Symbol	Value or Range	Comments
Shuttle orbiter altitude	R	h	150→1000 Km	Missions below 200 Km unlikely
Orbit inclination	R	i	30 → 60 deg	Some polar orbits probable, equatorial orbits unlikely
Average "Slew" Rate	R	R_s	1.0 deg/sec*	Minimum value of average slew rate (slew angle/slew time) starting and ending with zero
Maximum Accelerate/ Decelerate Time	R	t_{max}	10^* sec	Time/angle allowed to go from track rate at end of track maneuver to rest (or from rest at end of slew to initial track rate of next target)
Maximum Accelerate/ Decelerate Angle	R	$\Delta\gamma_{max}$	10^* deg	

* Assumed values

Table 3-2. Orbiter Stabilization Requirements for EVAL With RCS Disabled

Requirement	Value or Range	Comments
Shuttle orbiter altitude	150 to 1000 Km	Missions below 200 Km unlikely
Orbit inclination	30 to 60 deg	Some polar orbits probable, equatorial orbits unlikely
Two orbiter orientations to provide following fields of view from payload bay:		
• Earth surface viewing	nadir to horizon	Subject to limitations imposed by orbiter structural obstructions
• Earth limb viewing	$\geq$120 deg sector	
Candidate actuators to stabilize orbiter when reaction control system (RCS) cannot be used		
• Electro-magnets		Preferred if feasible due to lower cost
• Momentum exchange devices*		Acceptable if electro-magnet control is not feasible
Initial conditions on magnet or momentum exchange device control system		
• Maximum offset from null torque attitude	0.1 deg	Worst case vernier RCS limit cycle conditions
• Maximum angular rate	0.01 deg/sec	

* Reaction wheels or control moment gyros

4.0 IPS GIMBAL/PAYLOAD MASS PROPERTIES

This section contains a derivation and numerical results on the possible range of inertias, about the gimbal center of rotation (CR), that can be expected for IPS payloads. The IPS gimbal arrangement and allowable payload envelope, based on Appendix B, is presented in Figure 4-1 and Table 4-1. Figure 4-2 shows the nominal payload orientation relative to the shuttle orbiter payload bay. The following assumptions about the payload have been made to allow the results to be presented parametrically:

- The payload is a uniform right circular cylinder of mass m_p, length ℓ_p, and radius r_p.
- The payload CG is offset from the CR only along the $\hat{z}_E$ axis.

A complete mass model of structures composing the outer gimbal, payload integration ring, gyro package, and data electronics is not available. This structure is therefore conservatively modeled as a thin circular ring of radius r_M, containing the total estimated mass, located at the front surface of the payload integration ring. Since most of the inertia about the CR is due to the payload mass and CG/CR offset (in most cases), the final results are relatively insensitive to the above assumptions.

4.1 DERIVATION OF INERTIA ABOUT CR

The total inertia about the CR can be expressed in dyadic form (Reference 2) as

$$\bar{\bar{I}}_T^{CR} = \bar{\bar{I}}_P^{CR} + \bar{\bar{I}}_M^{CR}$$

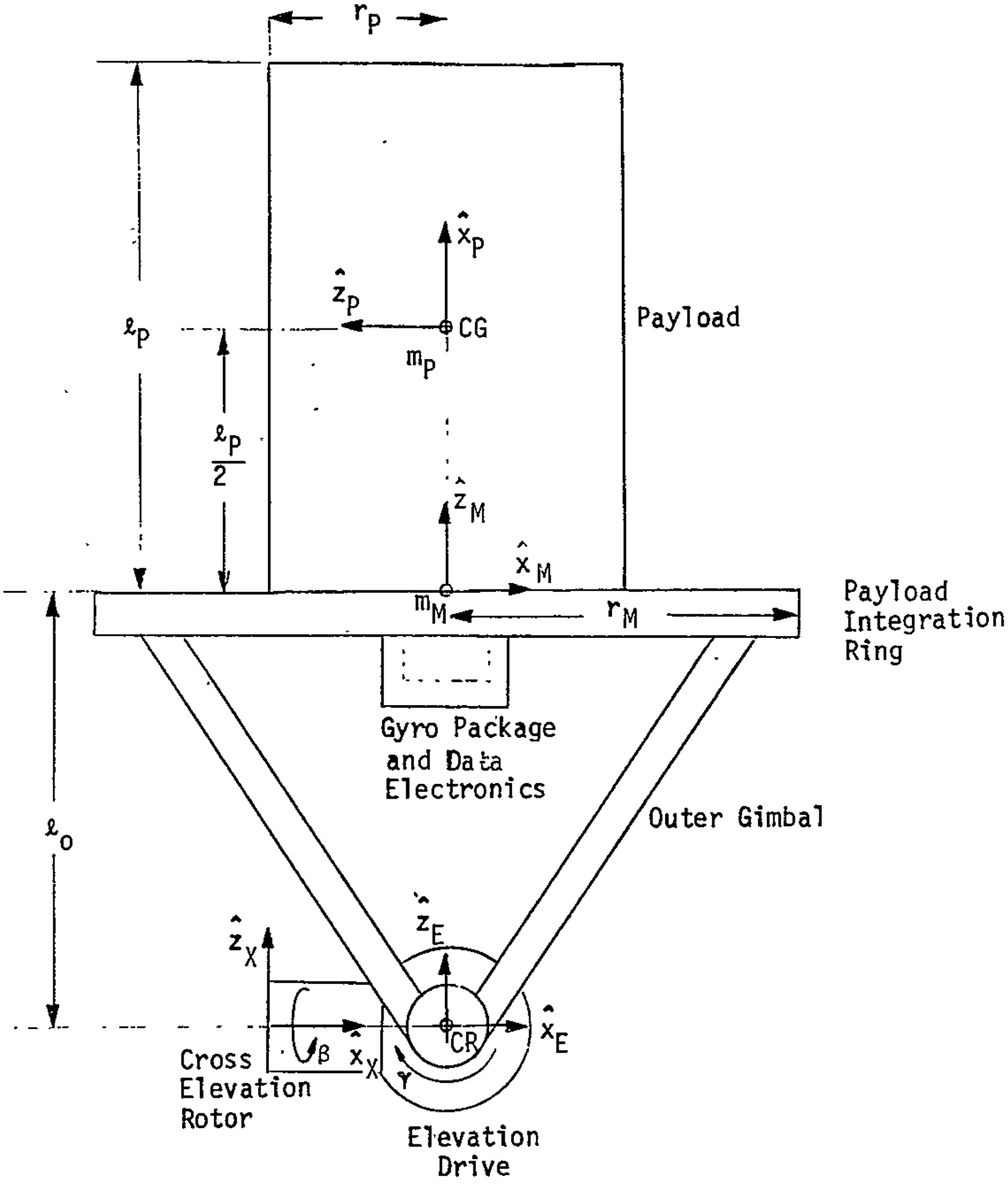

Figure 4-1. Definition of Payload Envelope and Gimbal Axes

Table 4-1. Summary of Gimbal/Payload Envelope

Symbol	Definition	Range or Value
CG	Payload CG	-
CR	Gimbal Center of Rotation	-
β	Cross-Elevation Angle	$-70 \leq \beta \leq 70$ deg
γ	Elevation Angle	$-70 \leq \gamma \leq 90$ deg
ℓ_o	CR/Payload Integration Ring Offset	0.69 m
ℓ_p	Payload Length	1 → 6 m
r_p	Payload Radius	0.25 → 1.5 m
m_p	Payload Mass	0 → 2000 kg
r_M	Payload Integration Ring Radius	0.6 m
m_M	Total Mass of Payload Integration Ring, Outer Gimbal, Gyro Package and Data Electronics	~ 85 kg

IPS LOCATION IN PAYLOAD BAY MAY VARY

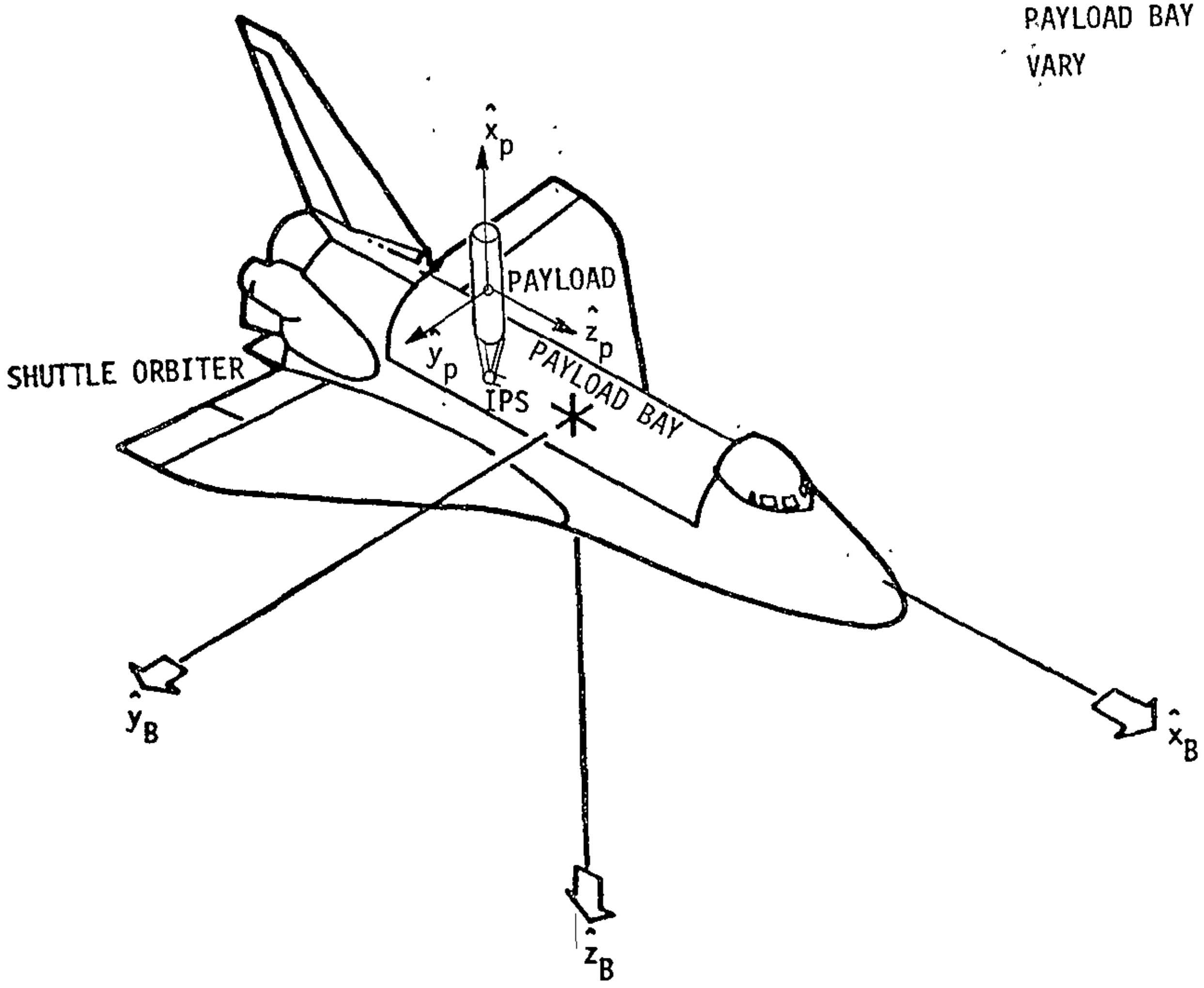

Figure 4-2. Nominal Payload Orientation

where

$$\overline{\overline{I}}_P^{CR} = \overline{\overline{I}}_P^{CG} + m_p \left[(\overline{r}_{CG} \cdot \overline{r}_{CG}) \,\overline{\overline{1}} - \overline{r}_{CG} \,\overline{r}_{CG} \right]$$

$$\overline{\overline{I}}_M^{CR} = \overline{\overline{I}}_M^{M} + m_M \left[(\overline{r}_M \cdot \overline{r}_M) \,\overline{\overline{1}} - \overline{r}_M \,\overline{r}_M \right]$$

$$\overline{\overline{1}} = \text{Unit dyadic}$$

Expressed in the p-frame, the payload inertia dyadic about its CG is

$$\overline{\overline{I}}_P^{CG} = I_{xx}^{CG} \,\hat{x}_p \,\hat{x}_p + I_{yy}^{CG} \,\hat{y}_p \,\hat{y}_p + I_{zz}^{CG} \,\hat{z}_p \,\hat{z}_p$$

where for a right circular cylinder

$$I_{xx}^{CG} = \frac{1}{2} m_p \, r_p^2$$

$$I_{yy}^{CG} = \frac{m_p}{12} \left(3 \, r_p^2 + \ell_p^2 \right)$$

$$I_{zz}^{CG} = \frac{m_p}{12} \left(3 \, r_p^2 + \ell_p^2 \right)$$

The CG/CR offset vector is

$$\overline{r}_{CG} = - (\ell_o + \ell_p/2) \, \hat{x}_p$$

and therefore

$$\bar{\bar{I}}_P^{CR} = (\frac{1}{2} m_P\ r_P^2)\ \hat{x}_P\ \hat{x}_P + \left[\frac{m_P}{12} (3r_P^2 + \ell_P^2) + m_P\ (\ell_o + \ell_P/2)^2\right] \hat{y}_P\ \hat{y}_P$$

$$+ \left[\frac{m_P}{12} (3r_P^2 + \ell_P^2) + m_P\ (\ell_o + \ell_P/2)^2\right] \hat{z}_P\ \hat{z}_P$$

$$= \left[m_P\ (\frac{r_P^2}{4} + \frac{\ell_P^2}{3} + \ell_o^2 + \ell_o\ \ell_P)\right]\ \hat{x}_E\ \hat{x}_E + \left[m_P (\frac{r_P^2}{4} + \frac{\ell_P^2}{3} + \ell_o^2 + \ell_o\ \ell_P)\right]$$

$$\hat{y}_E\ \hat{y}_E + (\frac{1}{2} m_P\ r_P^2)\ \hat{z}_E\ \hat{z}_E$$

The "payload integration ring" inertia about its CG is

$$\bar{\bar{I}}_M^M = I_{xx}^M\ \hat{x}_M\ \hat{x}_M + I_{yy}^M\ \hat{y}_M\ \hat{y}_M + I_{zz}^M\ \hat{z}_M\ \hat{z}_M$$

where for a thin circular ring

$$I_{xx}^M = \frac{m_M}{2}\ r_M^2$$

$$I_{yy}^M = \frac{m_M}{2}\ r_M^2$$

$$I_{zz}^M = m_M\ r_M^2$$

The CG/CR offset is

$$\bar{r}_M = - \ell_o \hat{z}_M$$

and therefore

$$\bar{\bar{I}}_M^{CR} = (\frac{m_M}{2} r_M^2 + m_M \ell_o^2) \hat{x}_M \hat{x}_M + (\frac{m_M}{2} r_M^2 + m_M \ell_o^2) \hat{y}_M \hat{y}_M + (m_M r_M^2) \hat{z}_M \hat{z}_M$$

$$= \left[m_M (\frac{r_M^2}{2} + \ell_o^2)\right] \hat{x}_E \hat{x}_E + \left[m_M (\frac{r_M^2}{2} + \ell_o^2)\right] \hat{y}_E \hat{y}_E + (m_M r_M^2) \hat{z}_E \hat{z}_E$$

The total inertia about the CR is finally

$$\bar{\bar{I}}_T^{CR} = I_1 \hat{x}_E \hat{x}_E + I_1 \hat{y}_E \hat{y}_E + I_2 \hat{z}_E \hat{z}_E$$

where

$$I_1 = m_P (\frac{r_P}{4} + \frac{\ell_P}{3} + \ell_o^2 + \ell_o \ell_P) + m_M (\frac{r_M^2}{2} + \ell_o^2)$$

$$I_2 = \frac{1}{2} m_P r_P^2 + m_M r_M^2$$

The elevation motor axis is along $\hat{y}_E$ and therefore the inertia that must be slewed by the elevation torquer is

$$I_{YY} = I_1$$

The cross elevation axis is along $\hat{x}_X$. Using the unit vector relations (Appendix B)

$$\hat{x}_E = \cos\gamma\ \hat{x}_X - \sin\gamma\ \hat{z}_X$$

$$\hat{y}_E = \hat{y}_X$$

$$\hat{z}_E = \sin\gamma\ \hat{x}_X + \cos\gamma\ \hat{z}_X$$

the total inertia can be expressed in the X-frame as

$$\overline{\overline{I}}{}_T^{CR} = (I_1 \cos^2\gamma + I_2 \sin^2\gamma)\ \hat{x}_X\ \hat{x}_X + I_1\ \hat{y}_X\ \hat{y}_X$$

$$(I_2 - I_1) \sin\gamma \cos\gamma\ \hat{x}_X\ \hat{z}_X + (I_2 - I_1) \sin\gamma \cos\gamma\ \hat{z}_X\ \hat{x}_X$$

$$+ (I_2 \cos^2\gamma + I_1 \sin^2\gamma)\ \hat{z}_X\ \hat{z}_X$$

The inertia seen by the cross elevation torquer (neglecting the insignificant inertia of the cross-elevation rotor) is thus

$$I_{\beta\beta} = I_1 \cos^2 \gamma + I_2 \sin^2 \gamma$$

4.2 NUMERICAL RESULTS

All payloads in the allowable range result in $I_1 > I_2$. The maximum value of $I_{\beta\beta}$ as a function of γ is therefore I_1. Since $I_{\gamma\gamma}$ is also equal to I_1, only I_1 need be considered further.

Using the values in Table 4-1, the constant non-payload contribution to I_1 is

$$m_R \left(\frac{r_M^2}{2} + \ell_o^2\right) = 55.7685 \text{ kg-m}^2$$

while the payload contributes

$$m_P \left[\frac{r_P^2}{4} + \frac{\ell_P^2}{3} + \ell_o \ell_P + \ell_o^2 \right] = m_P \left[\frac{r_P^2}{4} + \frac{\ell_P^2}{3} + 0.69 \ell_P + 0.4761 \right]$$

Therefore I_1 is, as a function of the payload properties m_P, ℓ_P, and r_P

$$I_1 = 55.7685 + m_P \left[\frac{r_P^2}{4} + \frac{\ell_P^2}{3} + 0.69 \ell_P + 0.4761 \right]$$

The minimum value of I_1 occurs for $m_p = 0$

$$(I_1)_{min} \simeq 56 \text{ kg-m}^2$$

while the maximum value for the specified payload envelope occurs for $m_p = 2000$ kg, $r_p = 1.5$m, $\ell_p = 6$m

$$(I_1)_{max} \simeq 34413 \text{ kg-m}^2$$

Figures 4-3 to 4-5 contain plots of I_1 vs ℓ_p with the limiting values of r_p (.25 and 1.5 m) for three values of m_p (10, 200, 3000 kg). It is clear from these figures that I_1 is relatively insensitive to r_p within the allowed range. This shows that the exact radial mass distribution of the payload has little effect on the final inertia value and therefore the assumption of a uniform cylindrical payload does not unduly restrict the applicability of the results. All following plots assume $r_p = 1$ m.

Figure 4-6 to 4-8 contain plots of I_1 vs ℓ_p for selected values of payload mass m_p ranging from 10 to 3000 kg. Curves of constant I_1 in the range 60 to 30000 kg-m^2 are plotted versus payload length ℓ_p and mass m_p in Figures 4-9 to 4-14. These curves are useful in establishing the bounds on payload length and mass for a given inertia about the CR.

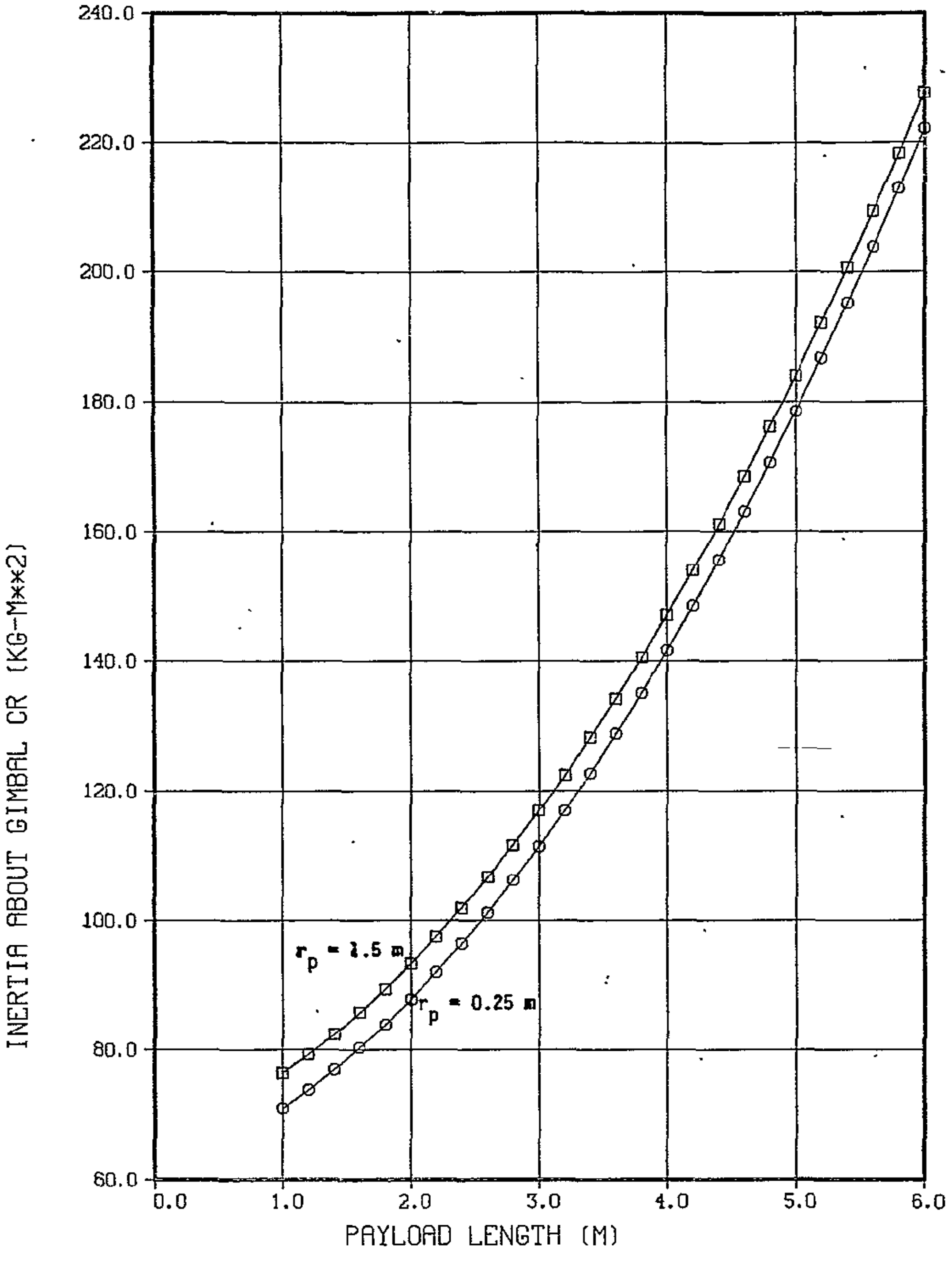

Figure 4-3. Inertia About Gimbal CR, m_p = 10 Kg

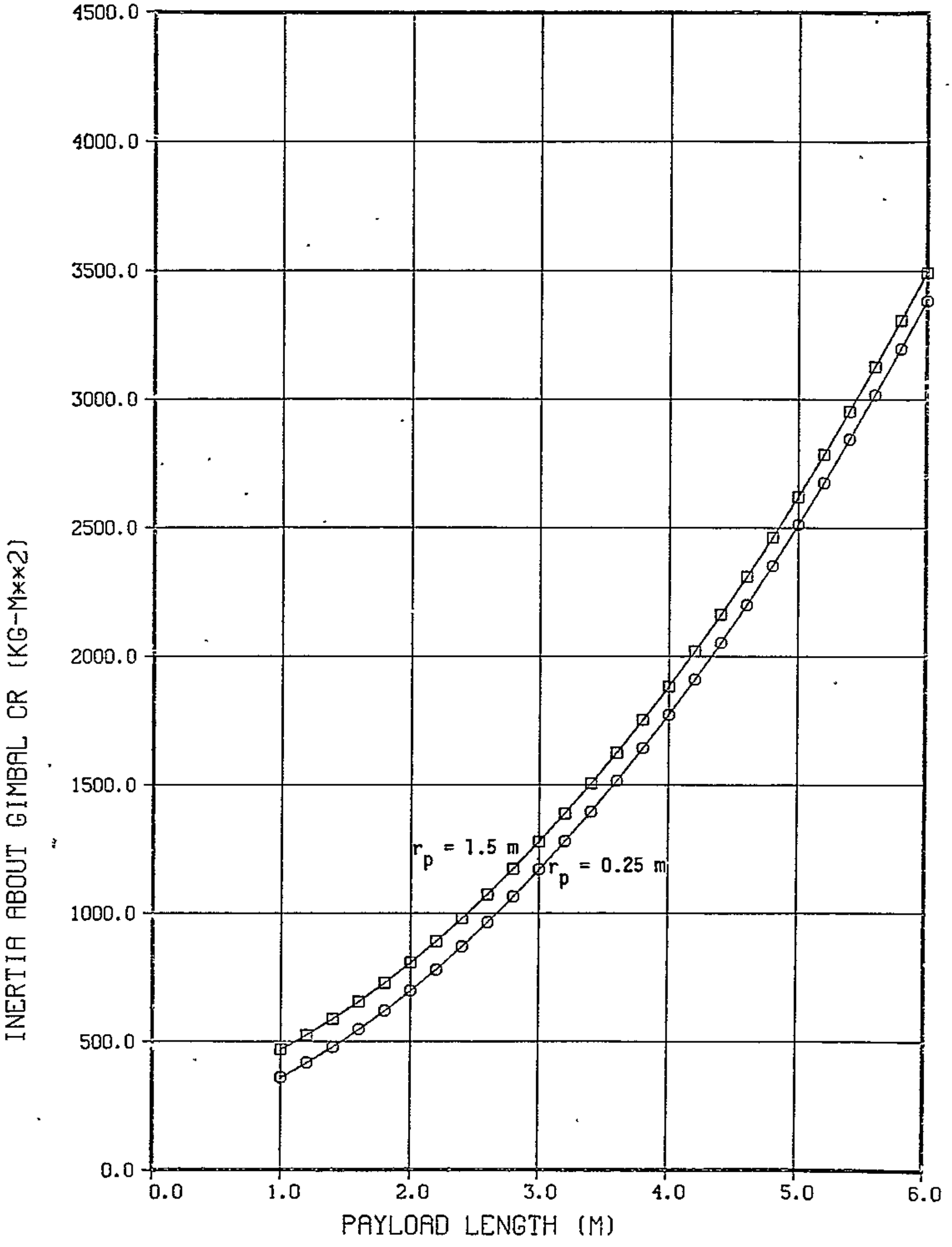

Figure 4-4. Inertia About Gimbal CR, m_p = 200 Kg

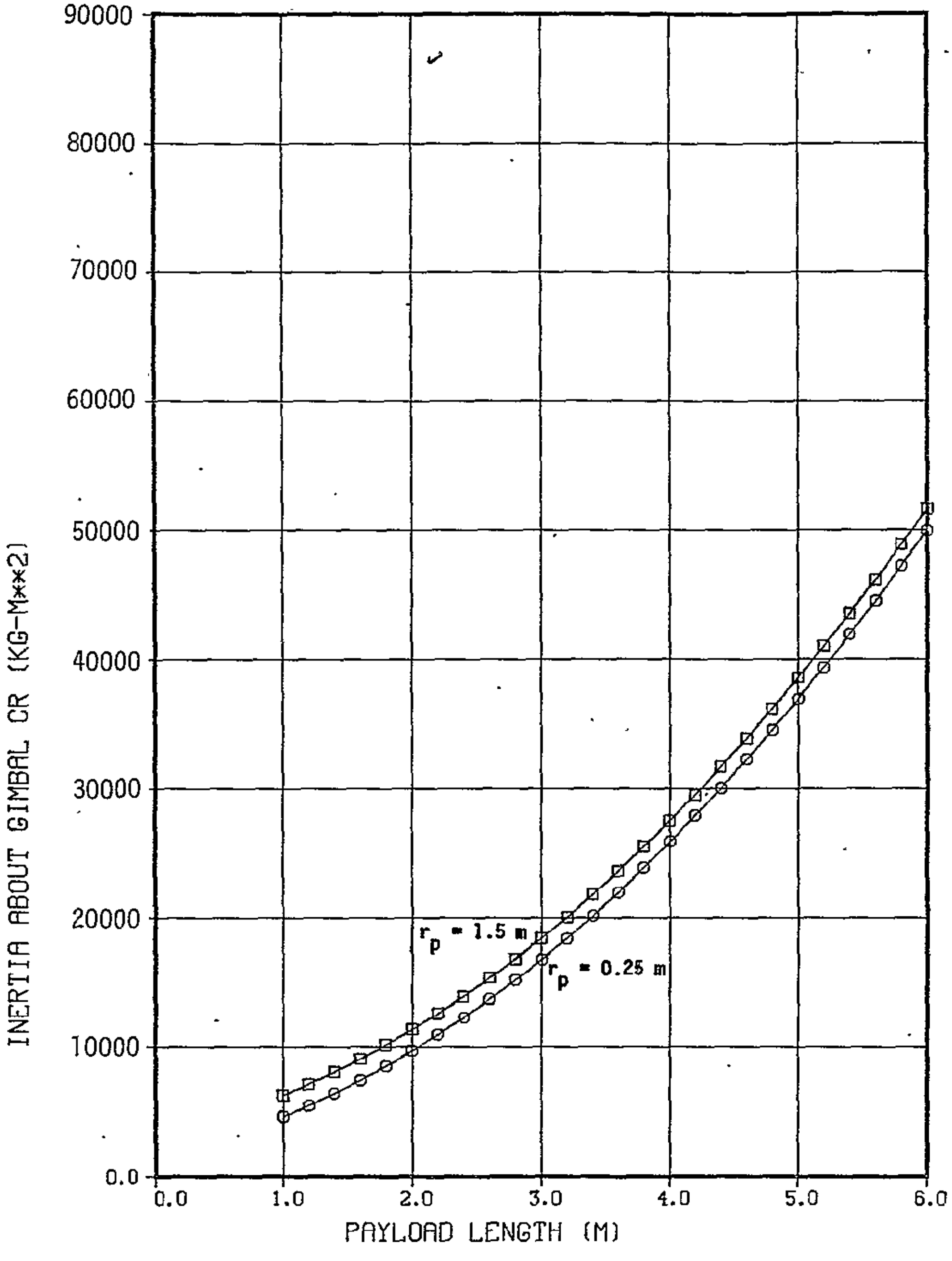

Figure 4-5. Inertia About Gimbal CR, m_p = 3000 Kg

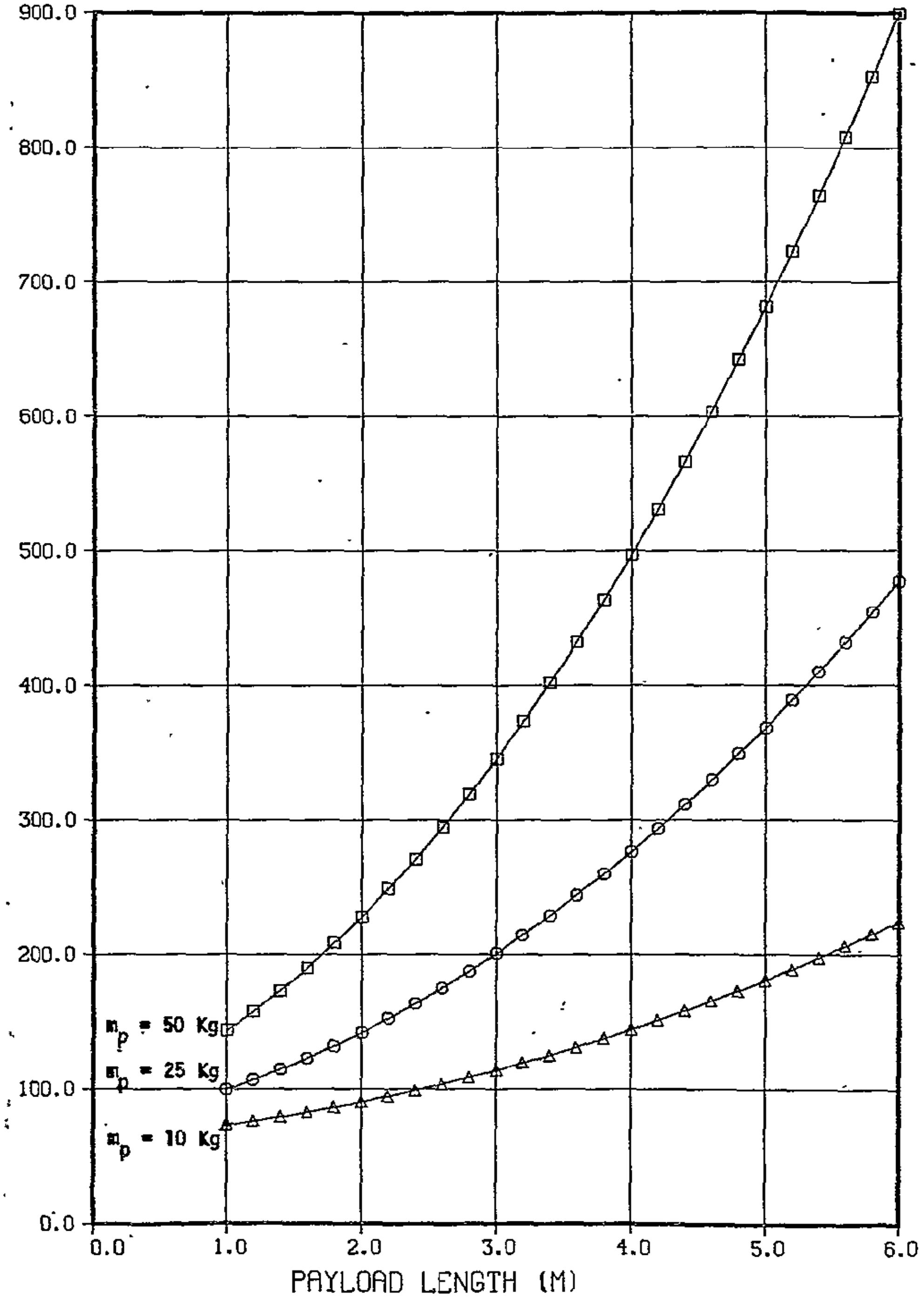

Figure 4-6. Inertia About Gimbal CR, m_p = 10, 25, 50 Kg

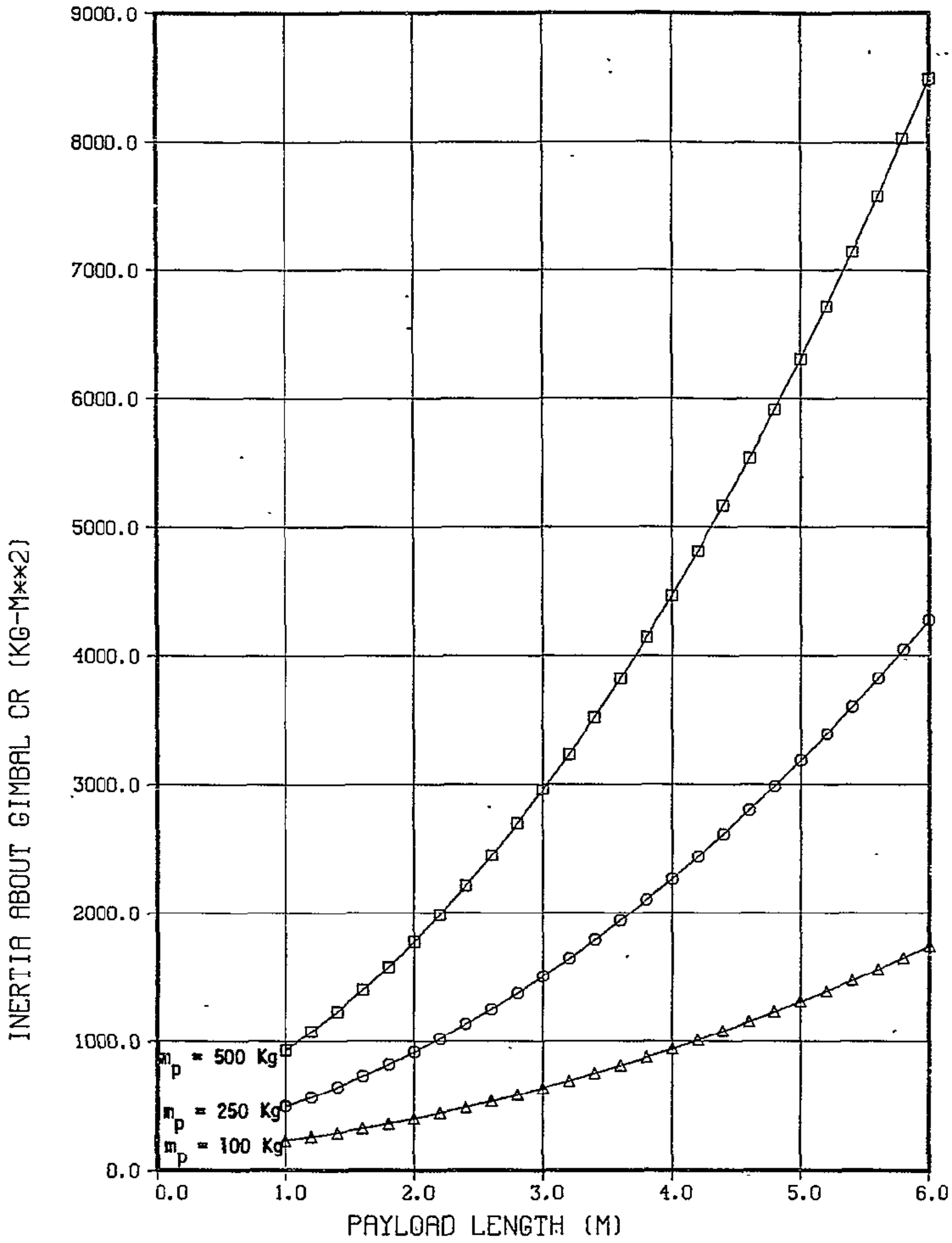

Figure 4-7. Inertia About Gimbal CR, m_p = 100, 250, 500 Kg

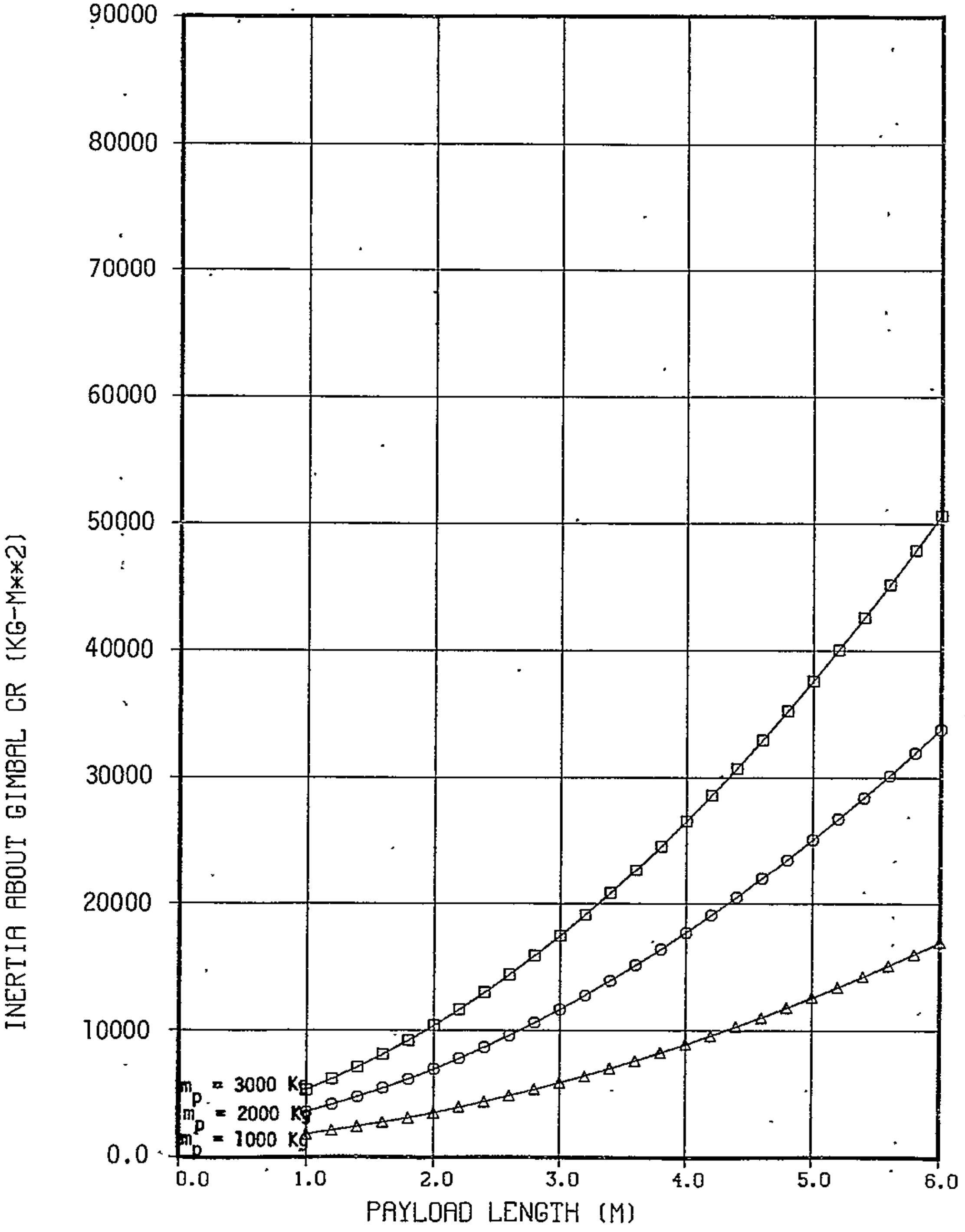

Figure 4-8. Inertia About CR, m_p = 1000, 2000, 3000 Kg

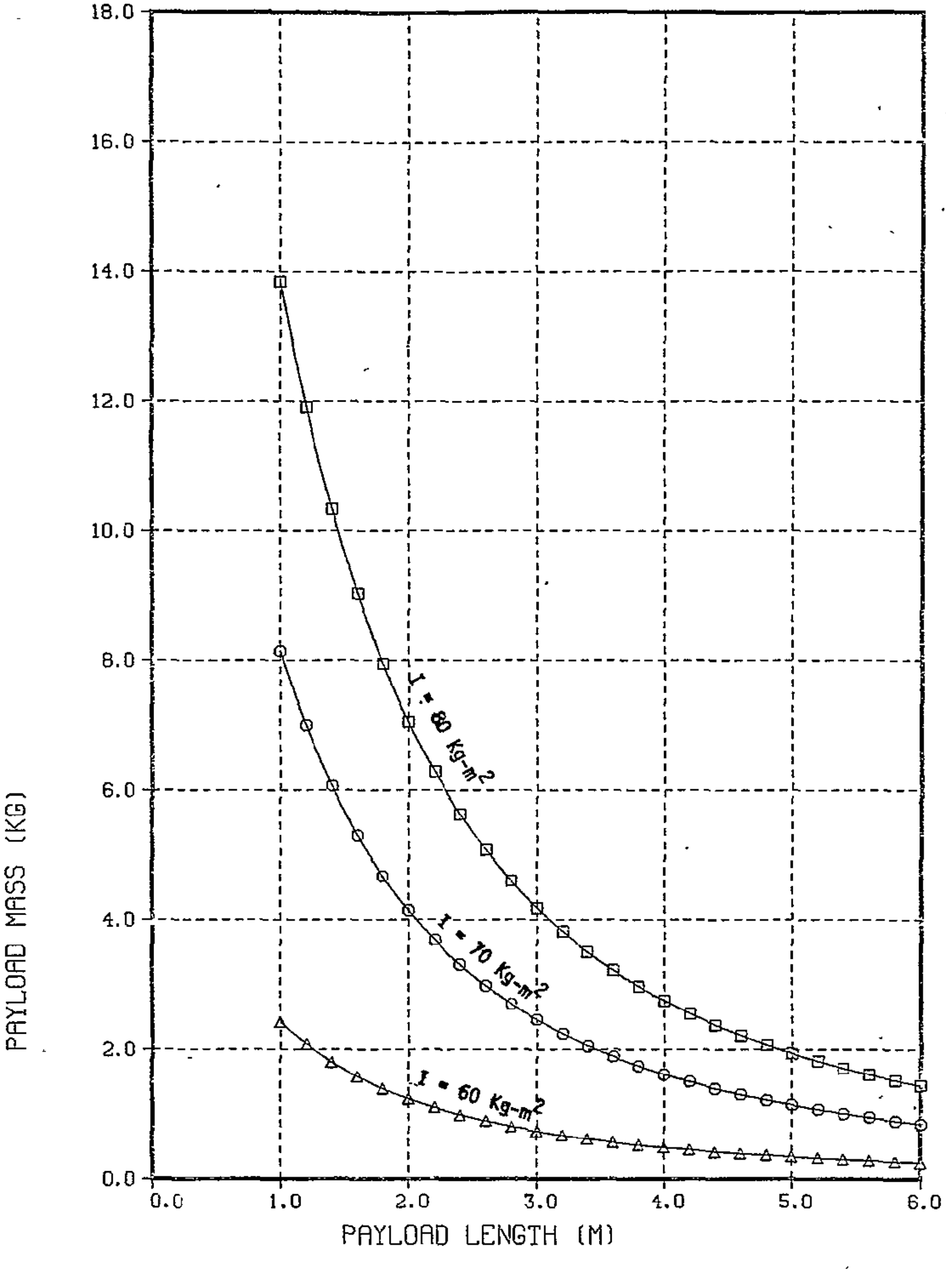

Figure 4-9. Payload Length and Mass for Inertia About CR of 60, 70, 80, Kg-m^2

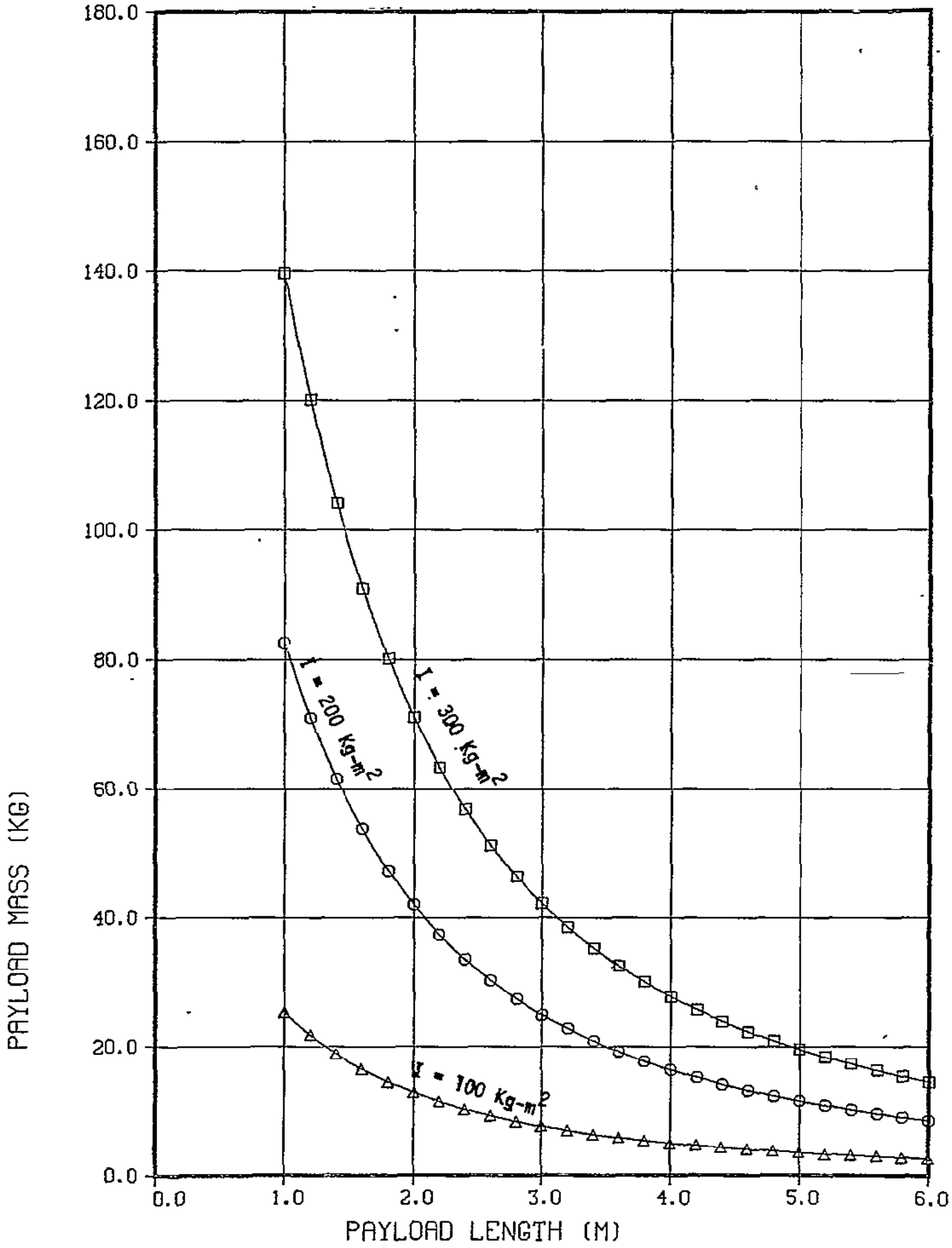

Figure 4-10. Payload Length and Mass for Inertia About CR of 100, 200, 300 Kg-m^2

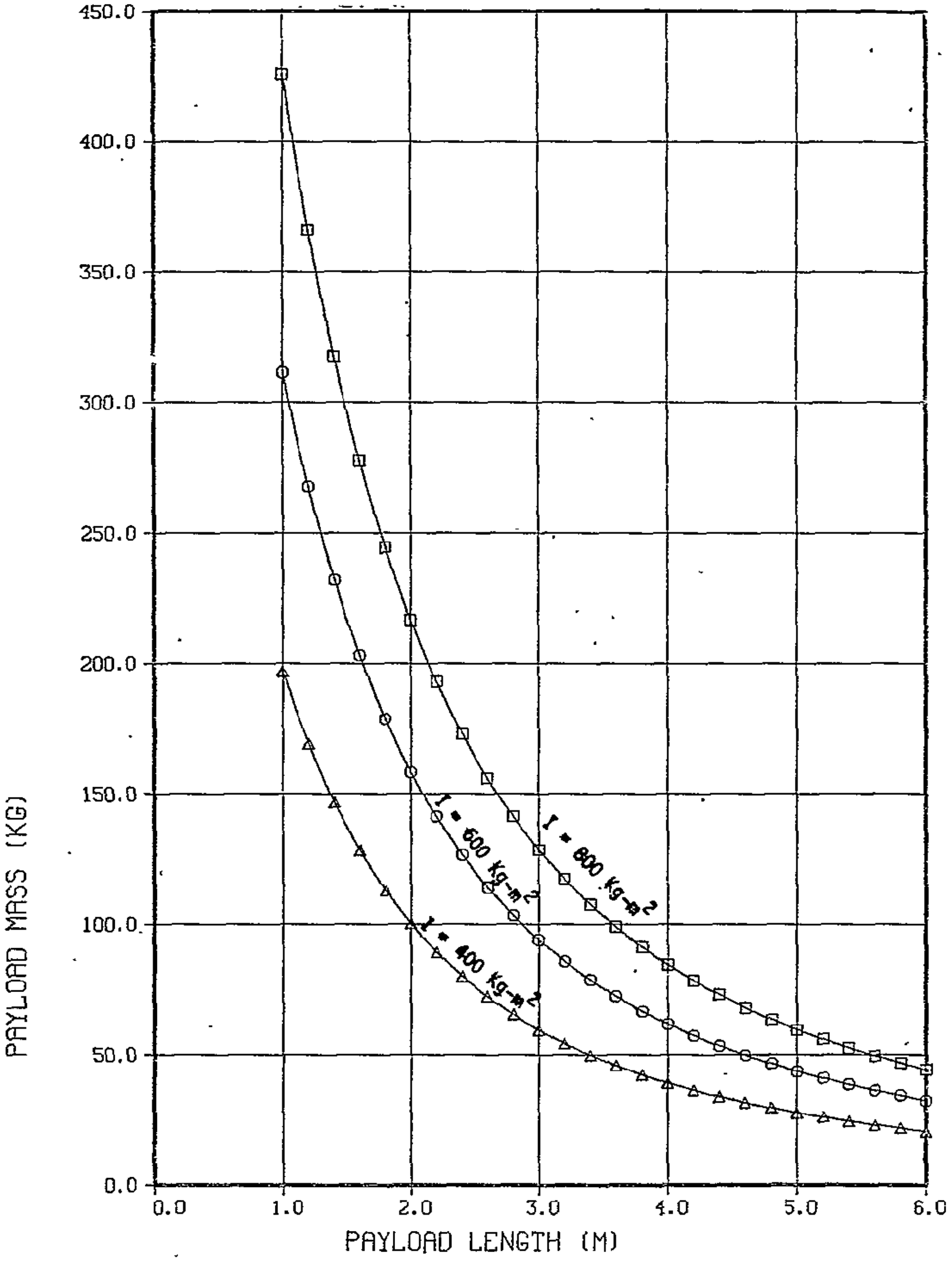

Figure 4-11. Payload Length and Mass for Inertia About CR of 400, 600, 800 Kg-m^2

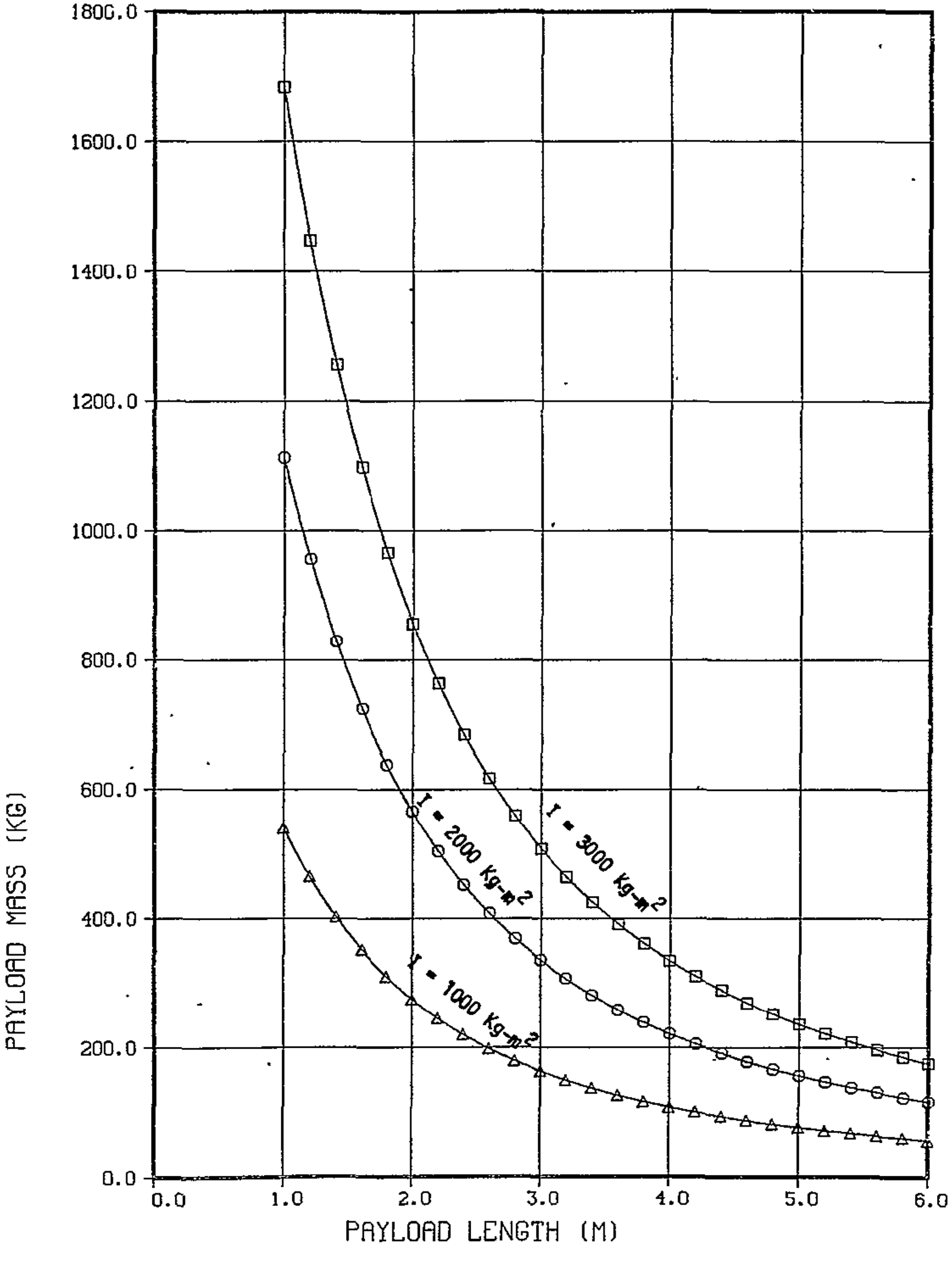

igure 4-12. Payload Length and Mass for Inertia About CR of 1000, 2000, 3000 Kg-m^2

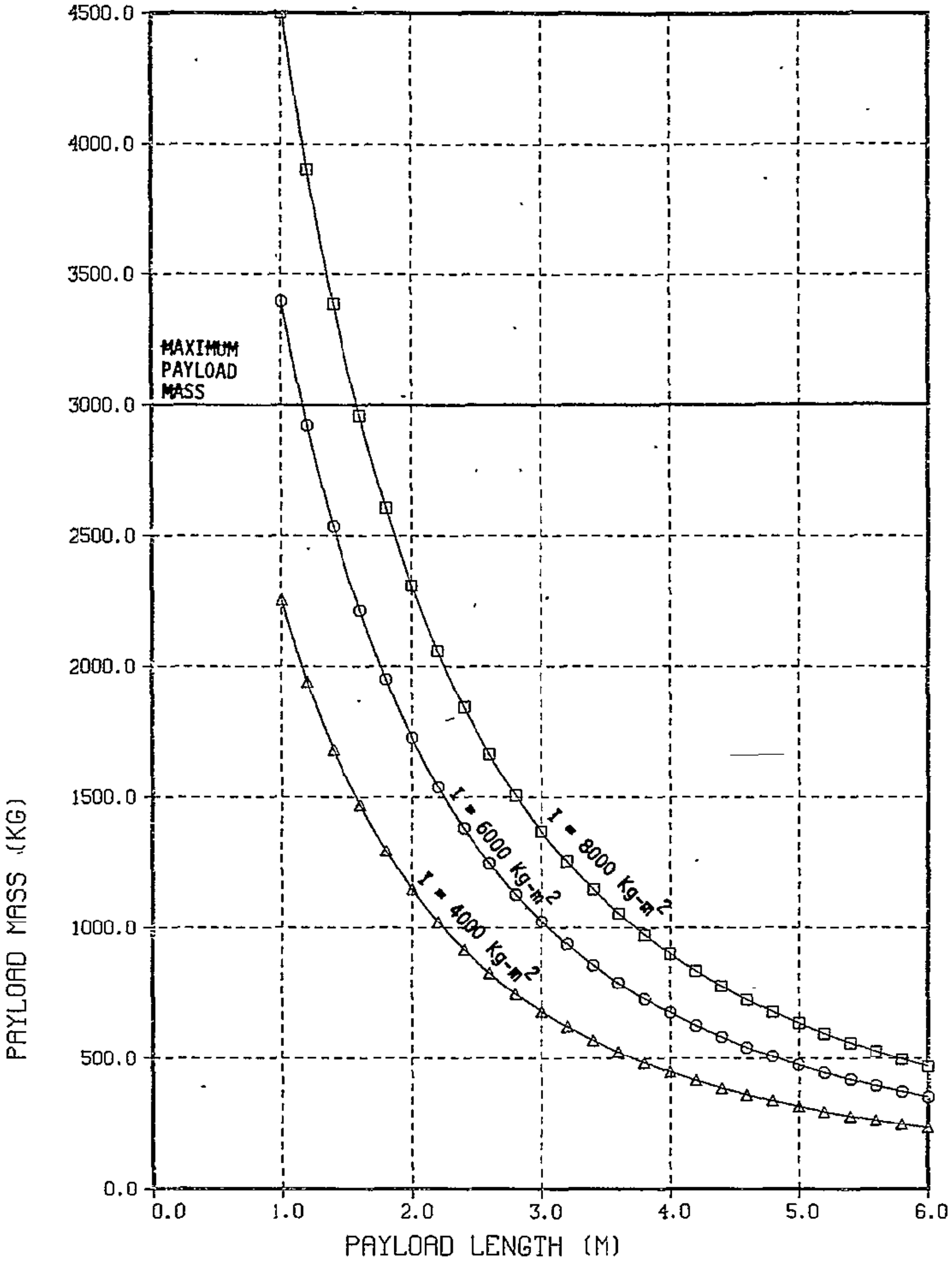

Figure 4-13. Payload Length and Mass for Inertia About CR of 4000, 6000, 8000 Kg-m^2

ORIGINAL PAGE IS
OF POOR QUALITY

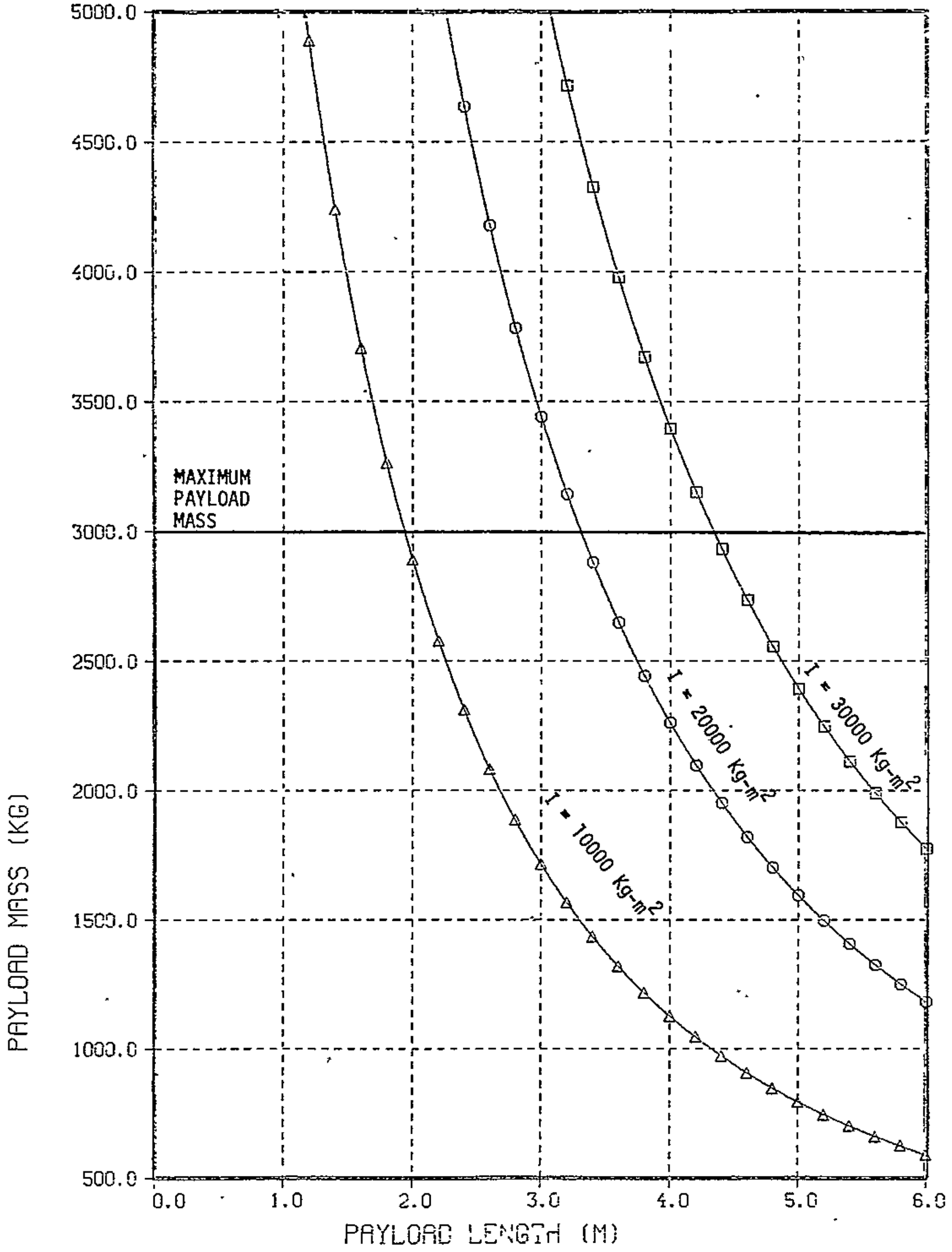

Figure 4-14. Payload Length and Mass for Inertia About CR of 10000, 20000, 30000 Kg-m^2

5.0 IPS SLEWING ANALYSIS

The ± 60 degree half-angle visibility cone about nadir of the IPS restricts the viewing time of a given earth-fixed target to a relatively small fraction of the time the target is above the horizon. For example, at 150 Km altitude, a target on the ground track is above the horizon for 179 seconds on each side of nadir, but is within the ± 60 degree half-angle view cone for only 35 seconds on each side of nadir (see Figure 6-6). Therefore, efficient experiment utilization requires that the slew time between target locks be minimized. In general, the gimbals must already be moving when the target enters the field of view, and are still moving when the target leaves the field of view. The direction of gimbal motion may therefore have to reverse <u>twice</u> between loosing one target and acquiring the next. This situation is illustrated schematically in Figure 5-1. The elevation and cross-elevation axes are independent and do not necessarily reverse direction at the same time.

Although the entire sequence of events between loosing track with one target and starting to track the next is essentially one maneuver, it is convenient for the present purposes to divide the maneuver into three phases: decelerate, slew, and accelerate. This not only simplifies the analysis, but also provides a means for including the gimbal angle hard limits. For IPS, the "buffer zone" between the gimbal angle hard limits and the gimbal angle limits for target tracking extends from 60 deg $\leq |\gamma| \leq$ 70 deg and 60 deg $\leq |\beta| \leq$ 70 deg.

In addition to the above, three other factors also limit the slew response for IPS

- The rate gyro limit of 2.5 deg/sec.
- The acceleration limit imposed by the available motor torque and slewed inertia.
- The softmount dynamic response.

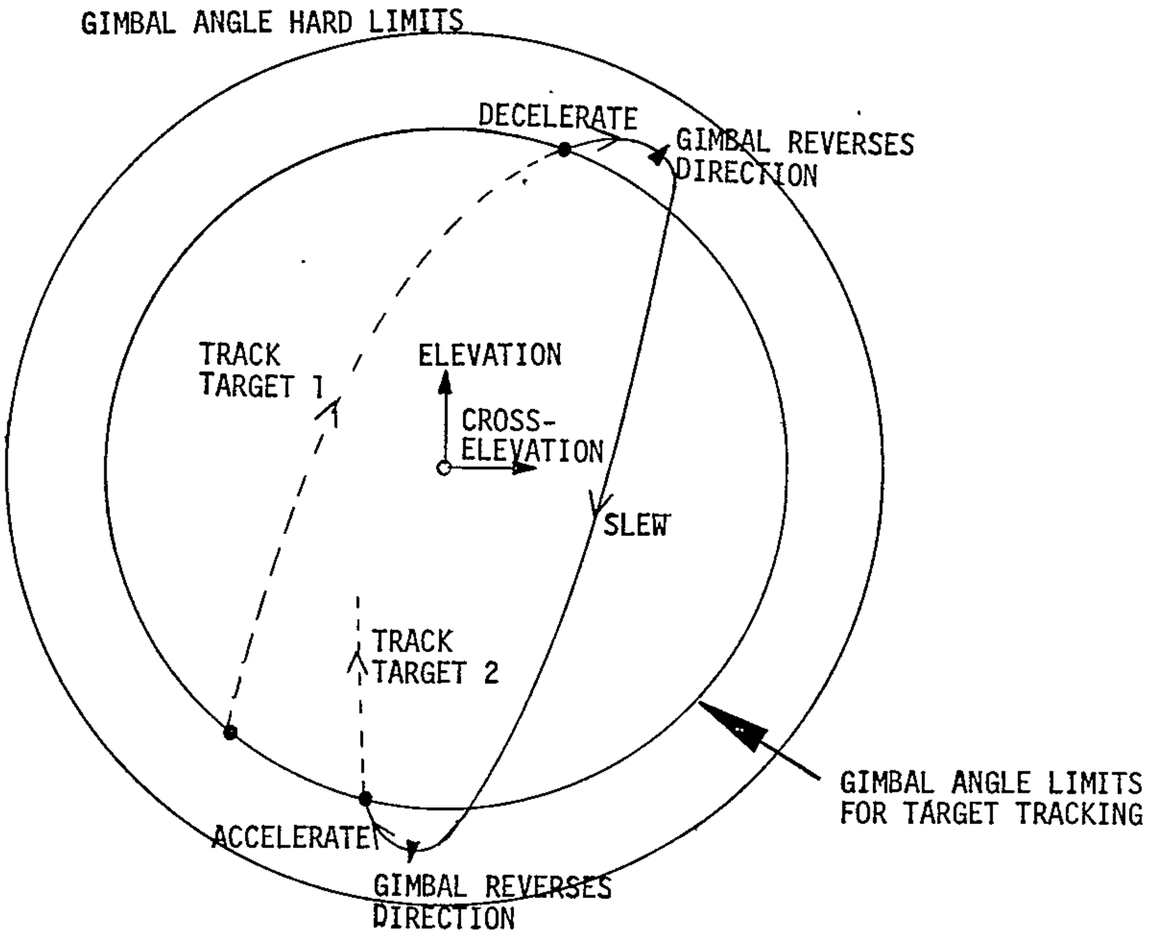

Figure 5-1. Typical Track/Slew/Track Sequence

The softmount dynamic response is beyond the scope of the present phase of the study. The remaining factors are analyzed in the following sections, with the results presented as parametric plots.

5.1 TIME/ANGLE RELATIONS FOR ACCELERATE/DECELERATE PHASES

During the accelerate/decelerate phase it is required to bring the gimbal axes from/to rest to/from the required track rate at the start/end of a track maneuver. The motions of the two gimbal axes are essentially independent, but must be coordinated to reach the correct vector rates. The means of achieving the required coordination are beyond the current scope. The coordination requirement does, however, limit the response capability to the weaker of the two axes. For IPS, this is the elevation axis. Compared to the cross-elevation axis, the elevation axis has greater or equal slewed inertia for all payloads and gimbal angles, and maximum tracking rate requirements an order of magnitude higher. Therefore only the elevation axis need be considered.

Lack of detailed information about the IPS gimbal drives requires that the following reasonable assumptions be made:

- The maximum drive motor torque T_m is independent of motor speed over the range of interest.
- The time required to change the drive motor torque is small compared to times of interest.

Under these assumptions, the minimum time required to accelerate from rest to the required track rate results from application of full torque until the rate is reached. The resulting acceleration is

$$\ddot{\gamma} = T_m/I_1$$

while the rate is governed by

$$\dot{\gamma} = T_m\, t/I_1$$

and the change in angle is

$$\Delta\gamma = T_m\, t^2/2I_1$$

The deceleration equations are similar, with obvious minor changes.

The maximum rate that can be reached in time t within an angular change $\Delta\gamma$ is

$$(\dot{\gamma})_{max} = 2\ \Delta\gamma/t$$

More useful for evaluating capabilities are the relations involving the slewed inertia and motor torque

$$(\dot{\gamma})_{max} = \frac{t}{(I_1/T_m)}$$

$$(\dot{\gamma})_{max} = \left(\frac{2\ \Delta\gamma}{(I_1/T_m)}\right)^{1/2}$$

The above two families of curves have been plotted as functions of the ratio (I_l/T_m) in Figure 5-2. To illustrate some uses of these curves, Figure 5-3 is presented as an example. The spotted region of this plot indicates the range of rates that can be reached in less than 10 seconds with a change of gimbal angle of less than 10 degrees. If the motor torque T_m is 20 N-m and it is required to reach a rate of 2.5 deg/sec within the given constraints, the maximum slewed inertia is found to be 20 x 180 = 3600 kg-m^2. Interpolating between the upper curve of Figure 4-12 and the lower curve of Figure 4-13 shows this to represent a moderate size payload. As another example, suppose again that T_m = 20 N-m but now there is a larger payload with I_l = 8000 kg-m^2. The plot shows that the maximum rate achievable within the given constraints is 1.45 deg/sec. As will be shown in Figure 6-3, this represents the peak tracking rate requirement at a 240 km altitude.

5.2 TIME/ANGLE RELATIONS FOR SLEWING

During the slew phase, it is required to bring the gimbal angle from rest at $\gamma = \gamma_0$ to rest at $\gamma = \gamma_f$ in minimum time subject to limitations on the gimbal acceleration and rate. The gimbal acceleration is limited physically by the torque/inertia ratio T_m/I_l. The gimbal rate for IPS is limited by the drive electronics to P = 2.5 deg/sec so as not to exceed the allowable gyro input rates. The rate limit is considered a parameter in the following analysis, however, to permit evaluation of the impact of the rate limit on overall performance.

For a minimum-time reposition with rate and acceleration limits, either the rate or acceleration must be at a limiting value at all times (Reference 3). Two cases exist here, depending on whether the rate limit is reached, as shown in Figure 5-4. In case 1, maximum

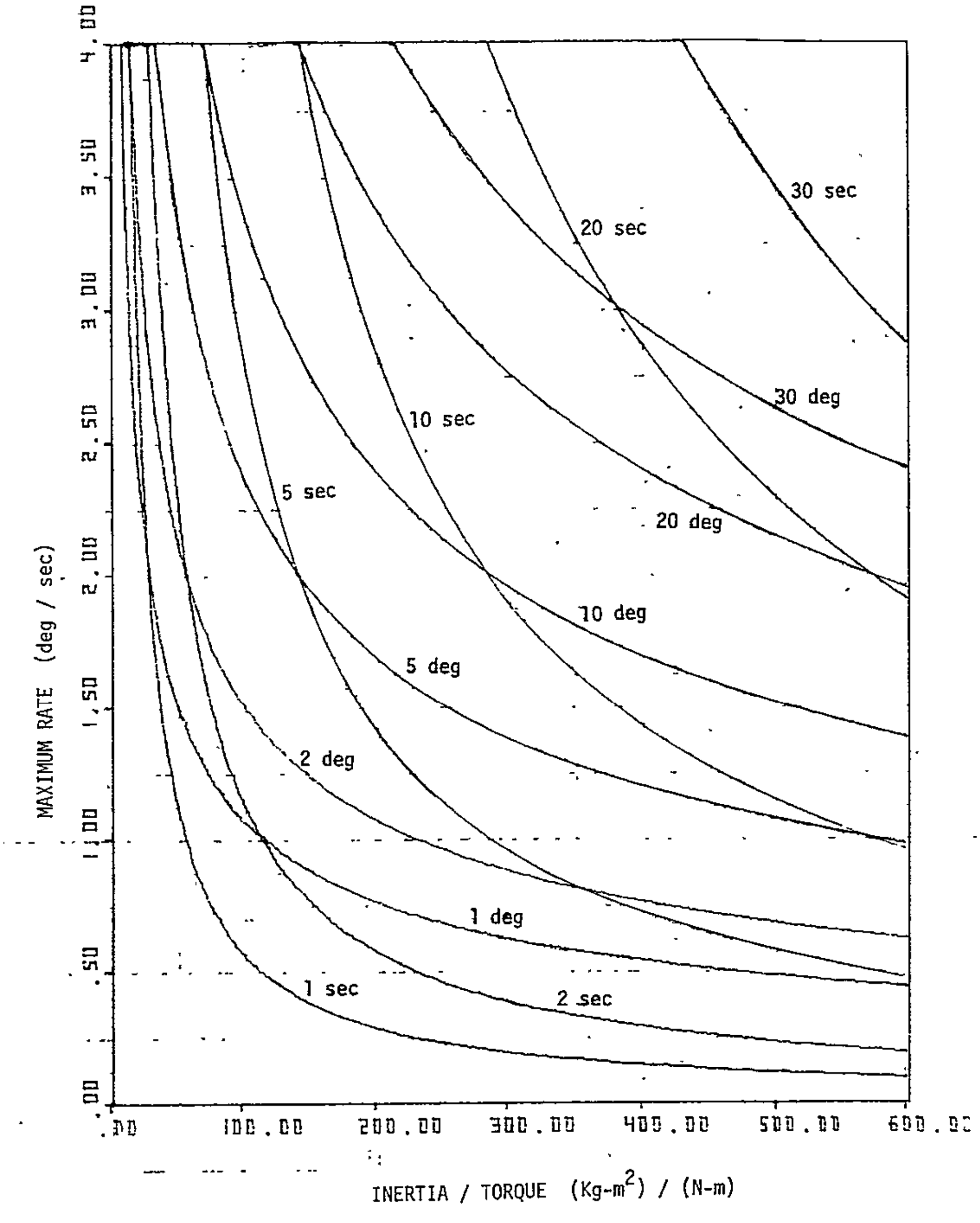

Figure 5-2. Time/Angle/Rate Curves for Acceleration/Deceleration Phases

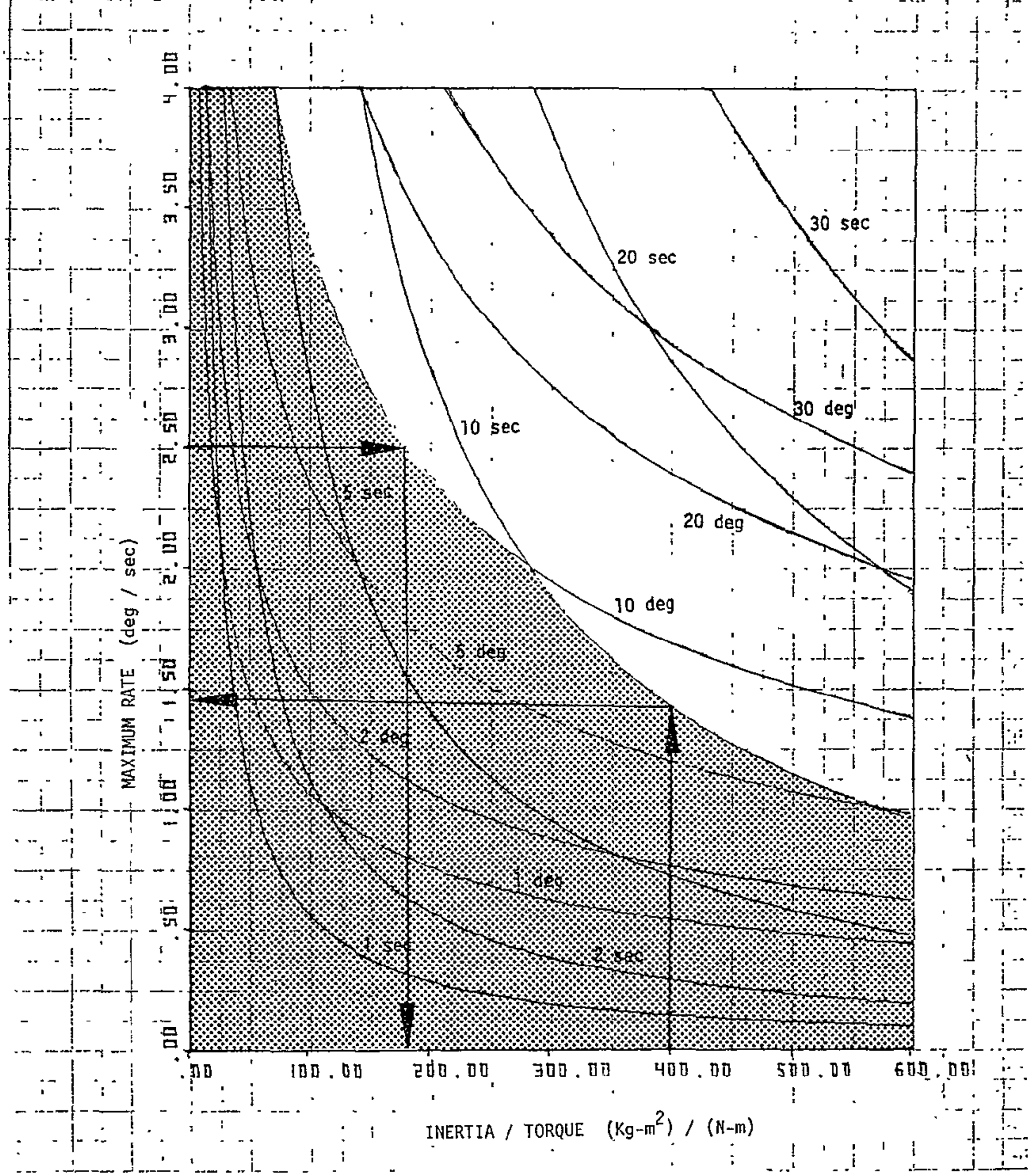

Figure 5-3. Examples With t_{max} = 10 sec, $\Delta\gamma_{max}$ = 10 deg

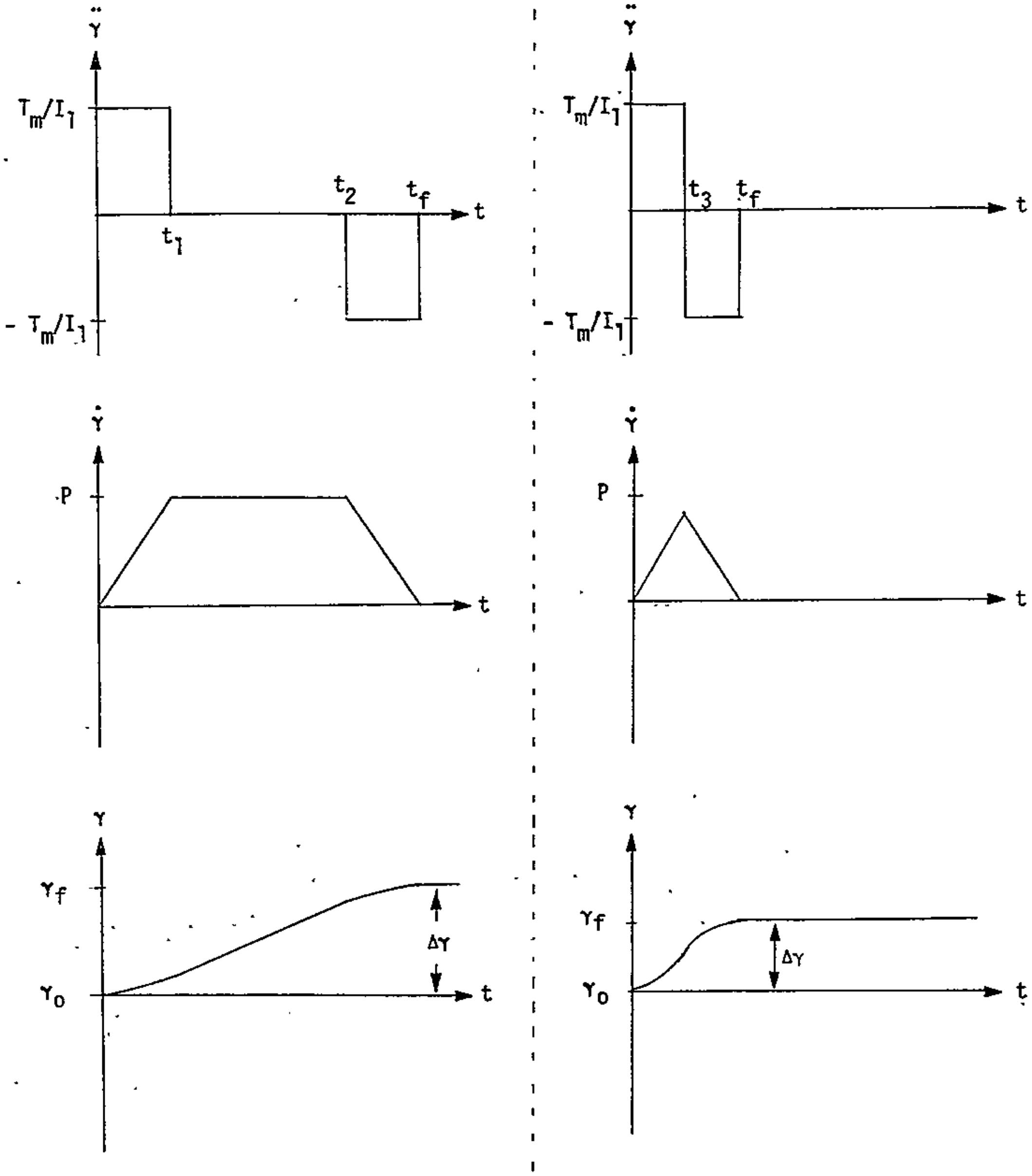

Case 1: $\Delta\gamma \geq I_1 P^2 / T_m$

Case 2: $\Delta\gamma < I_1 P^2 / T_m$

Figure 5-4. Slew Profiles

torque is applied until the rate limit is reached at

$$t = t_1 = PI_1/T_m$$

The motor is then turned off (neglecting friction), resulting in constant rate P until

$$t = t_2 = t_f - t_1$$

when the maximum torque is applied in the opposite direction. The change in angle

$$\Delta\gamma = \gamma_f - \gamma_o$$

from t = 0 to t = t_f is equal to the area under the rate curve

$$\Delta\gamma = Pt_2 = P(t_f - t_1) = P(t_f - PI_1/T_m)$$

Solving the above for the slew time gives

$$t_f = \frac{\Delta\gamma}{P} + \frac{PI_1}{T_m}$$

Case 1 applies when

$$t_f \geq 2\ t_1$$

or

$$\Delta\gamma \geq \frac{I_1}{T_m} P^2$$

Otherwise, the rate limit is not reached and case 2 applies. Here, the torque switches from maximum one direction to maximum the opposite direction at

$$t = t_3 = t_f/2$$

The maximum rate reached is

$$\dot{\gamma}_{max} = T_m\ t_3/I_1$$

The area under the rate curve is then

$$\Delta\gamma = \int_0^{t_f} \dot{\gamma}\ dt = \dot{\gamma}_{max}\ t_3 = T_m\ t_3^2/I_1 = T_m\ t_f^2/4T_1$$

so the slew time is

$$t_f = 2 \left(I_1 \Delta\gamma / T_m\right)^{1/2}$$

Slew time, as a function of inertia/torque ratio, is plotted in Figures 5-5 to 5-10 for selected values of $\Delta\gamma$ in the range of 20 to 120 degrees, with the rate limit P as a parameter. It is apparent from these plots that the slew time is relatively insensitive to the rate limit for all but the smallest payloads. The IPS rate limit of 2.5 deg/sec does not unduly restrict the slew time and any increase would produce only a marginal improvement.

Figures 5-11 to 5-15 contain the same data, plotted for fixed values of the rate limit with the slew angle as the parameter.

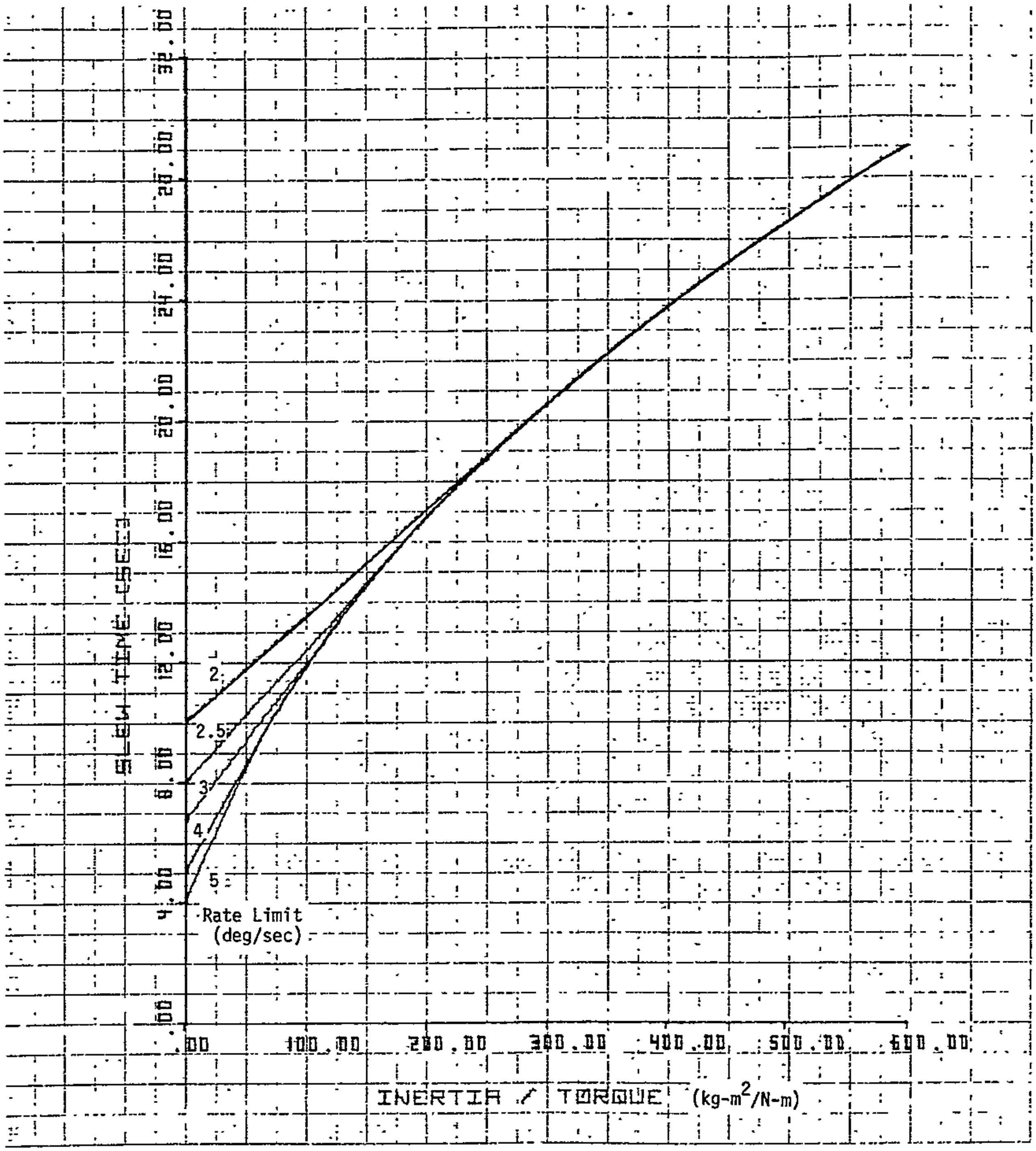

Figure 5-5. Slew Time for 20 Degree Slew Angle

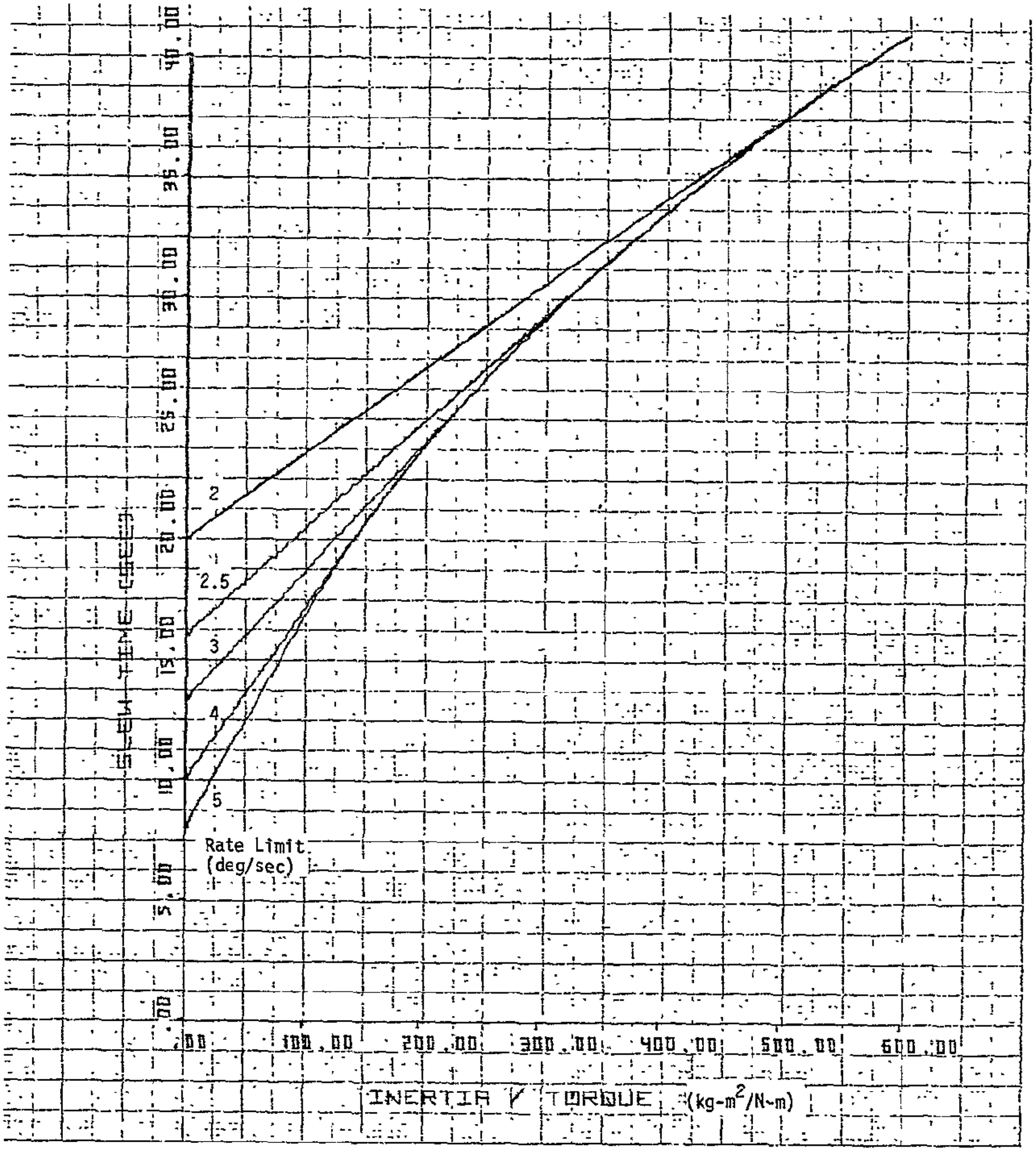

Figure 5-6. Slew Time for 40 Degree Slew Angle

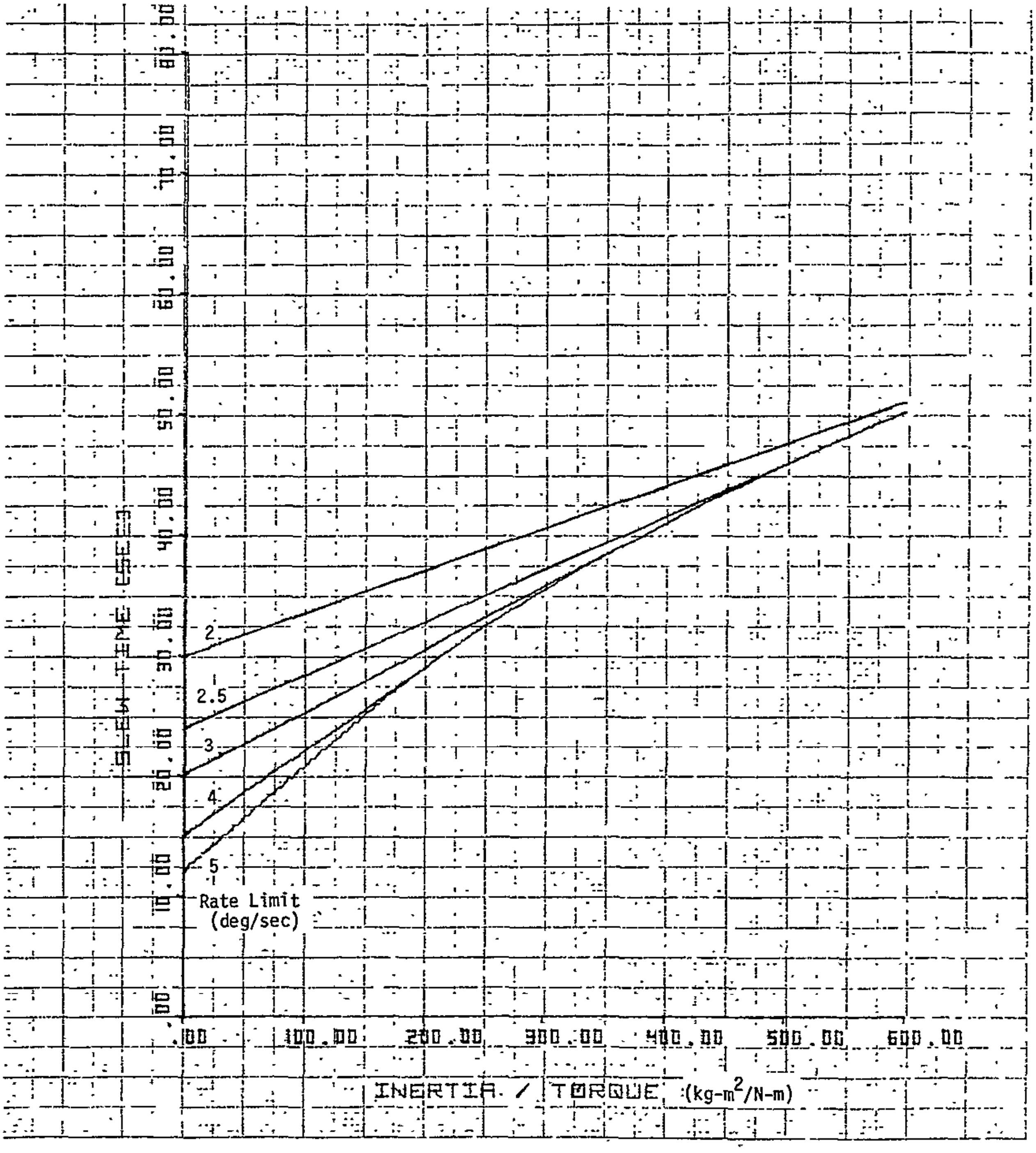

Figure 5-7. Slew Time for 60 Degree Slew Angle

ORIGINAL PAGE IS
OF POOR QUALITY

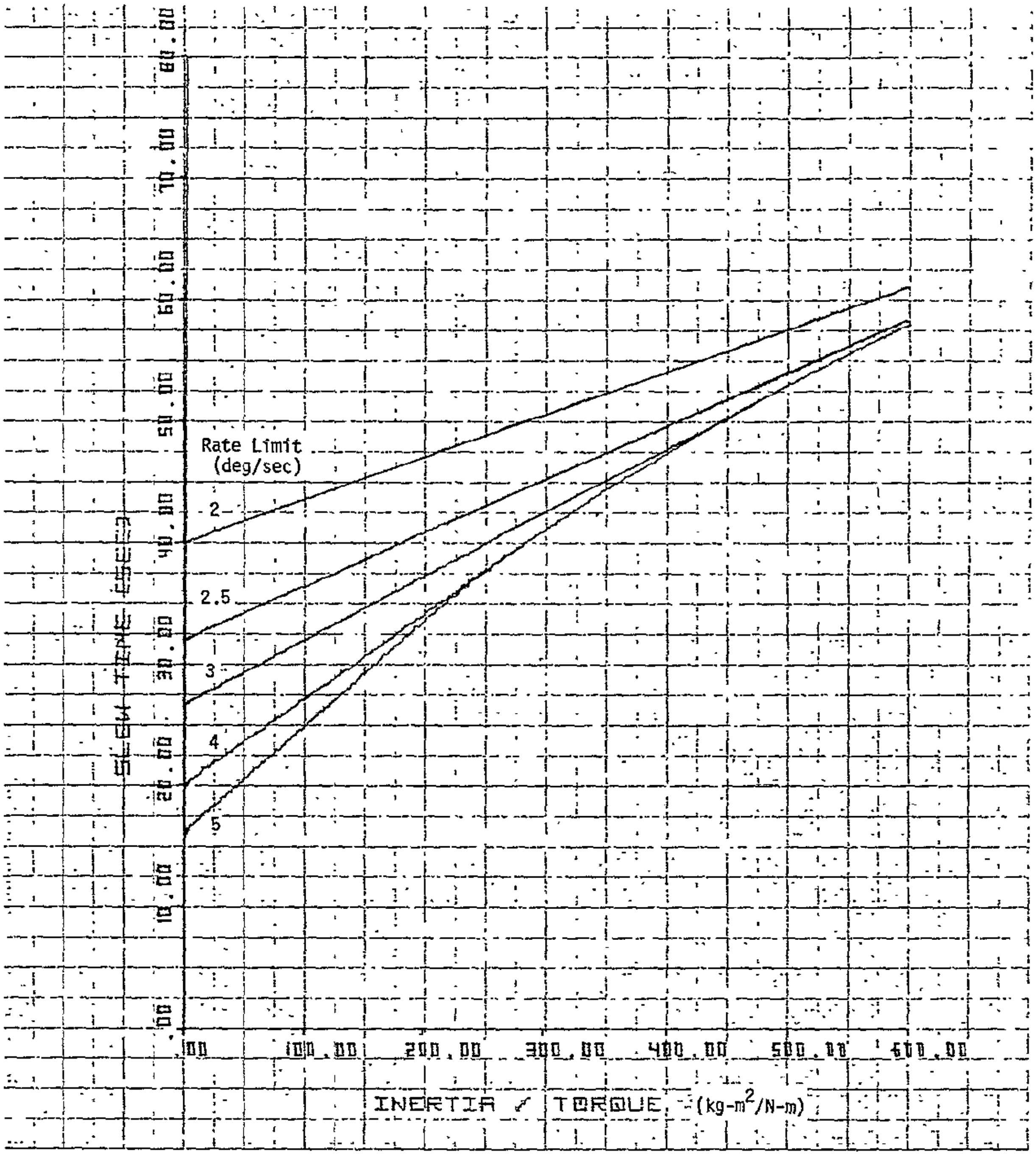

Figure 5-8. Slew Time for 80 Degree Slew Angle

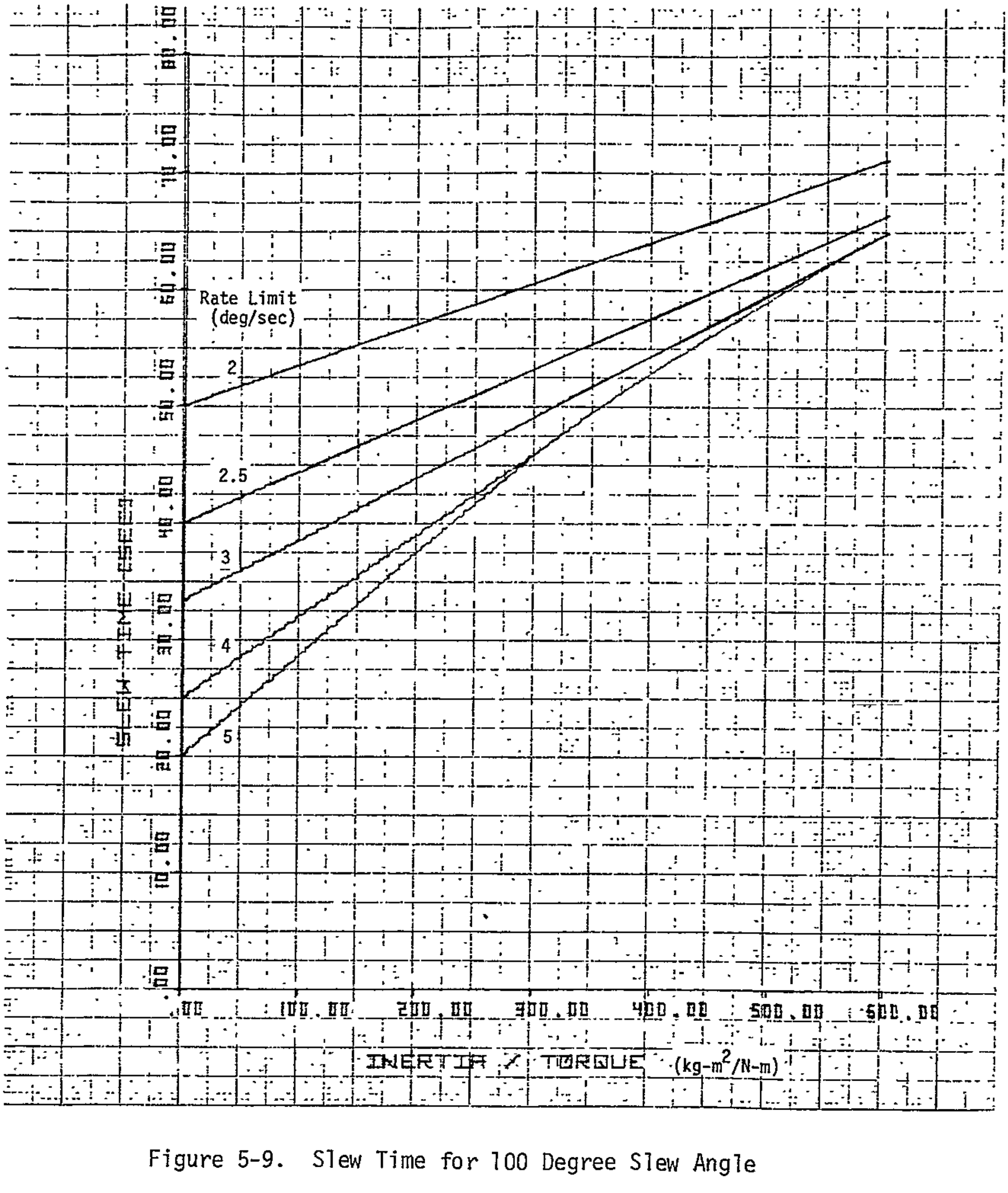

Figure 5-9. Slew Time for 100 Degree Slew Angle

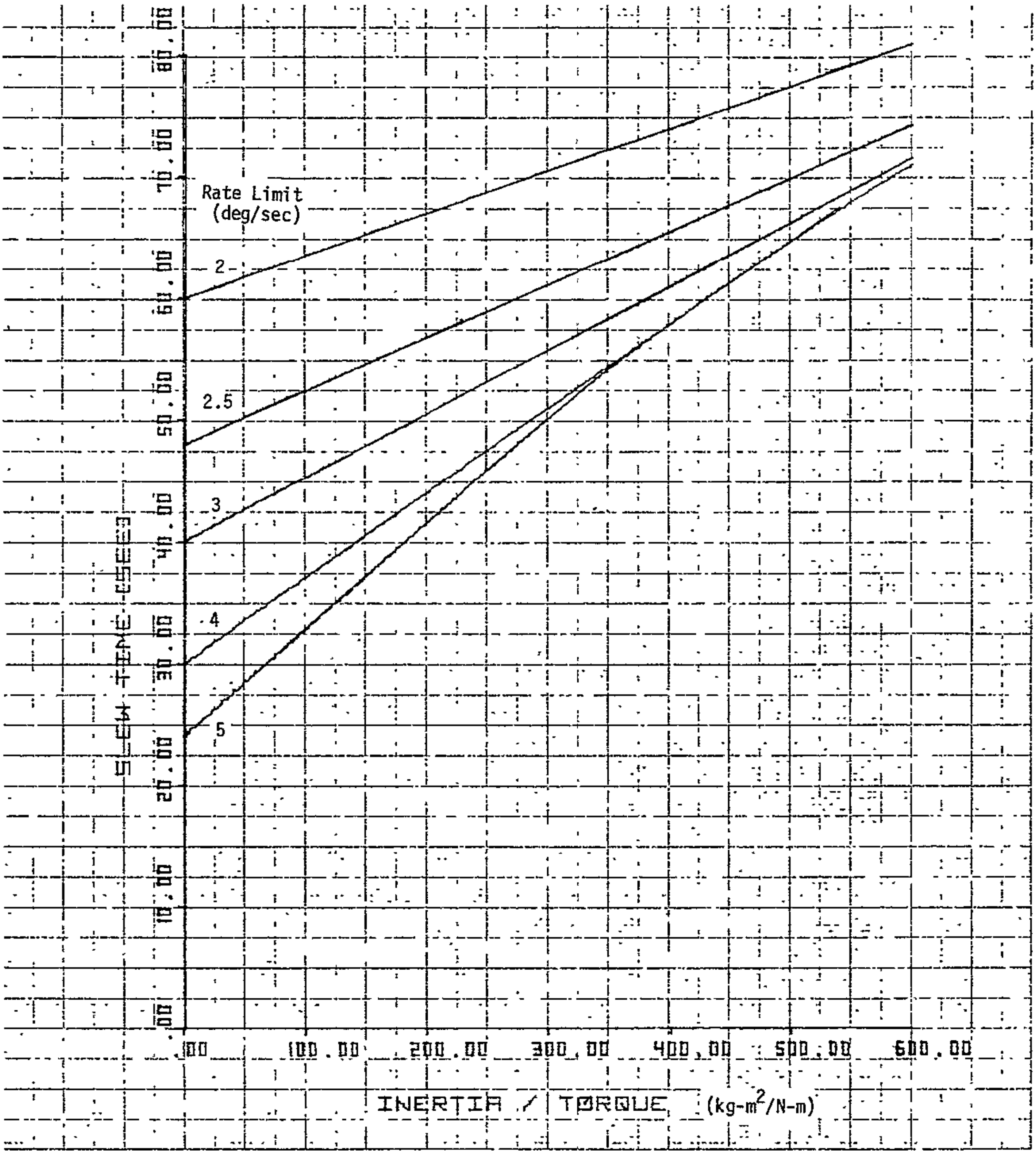

Figure 5-10. Slew Time for 120 Degree Slew Angle

ORIGINAL PAGE IS
OF POOR QUALITY

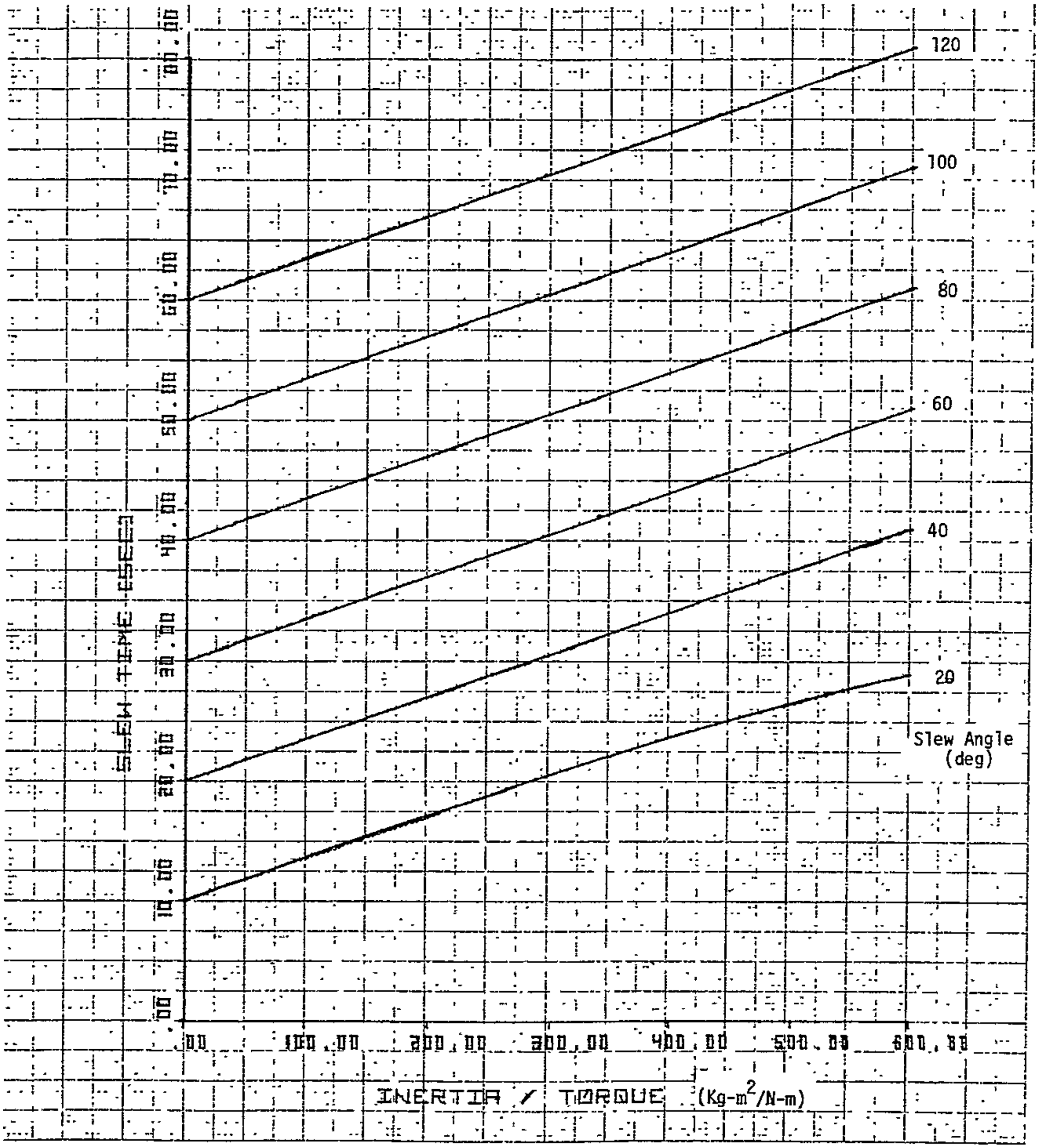

Figure 5-11. Slew Time for Rate Limit P = 2.0 Deg/Sec

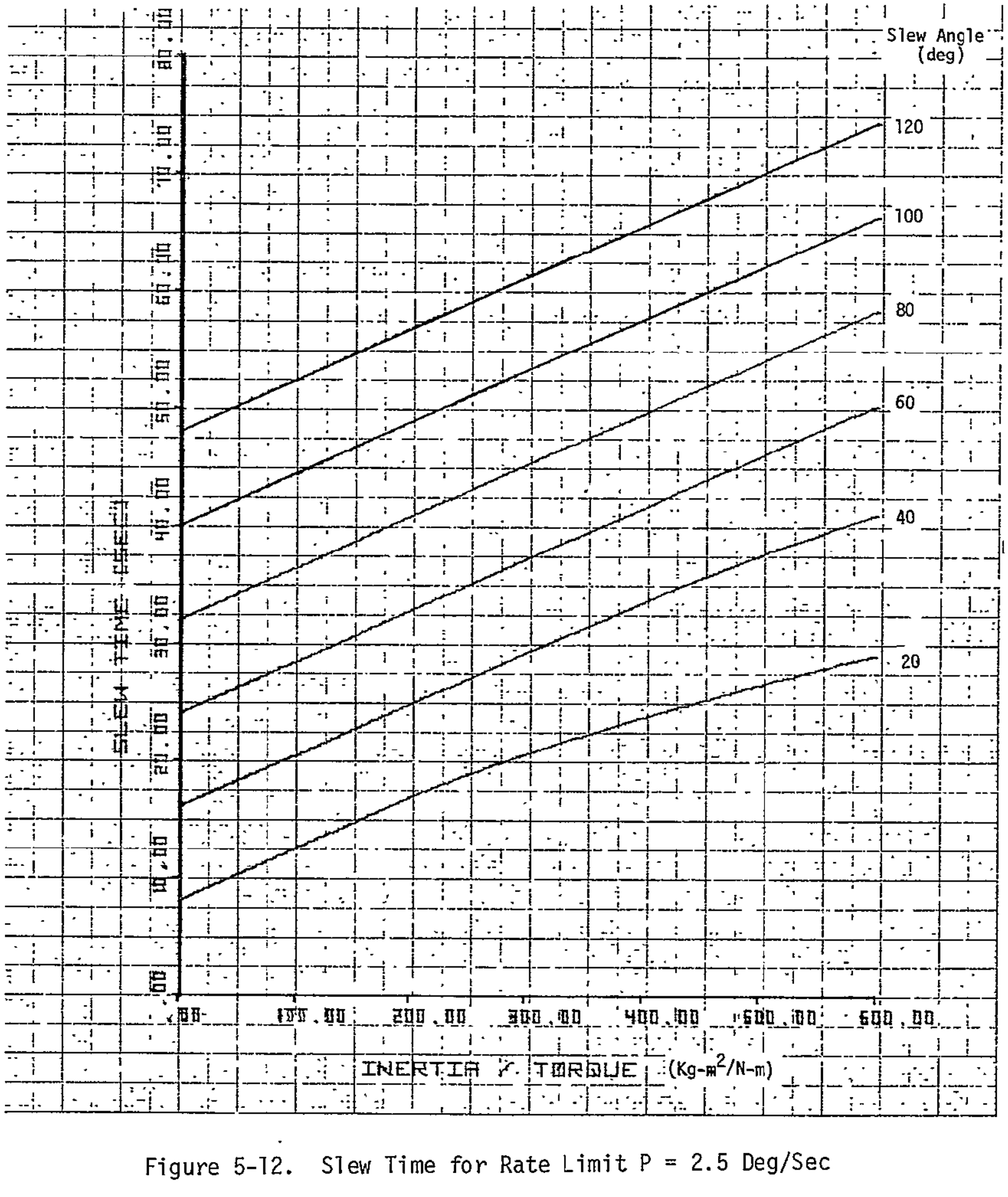

Figure 5-12. Slew Time for Rate Limit P = 2.5 Deg/Sec

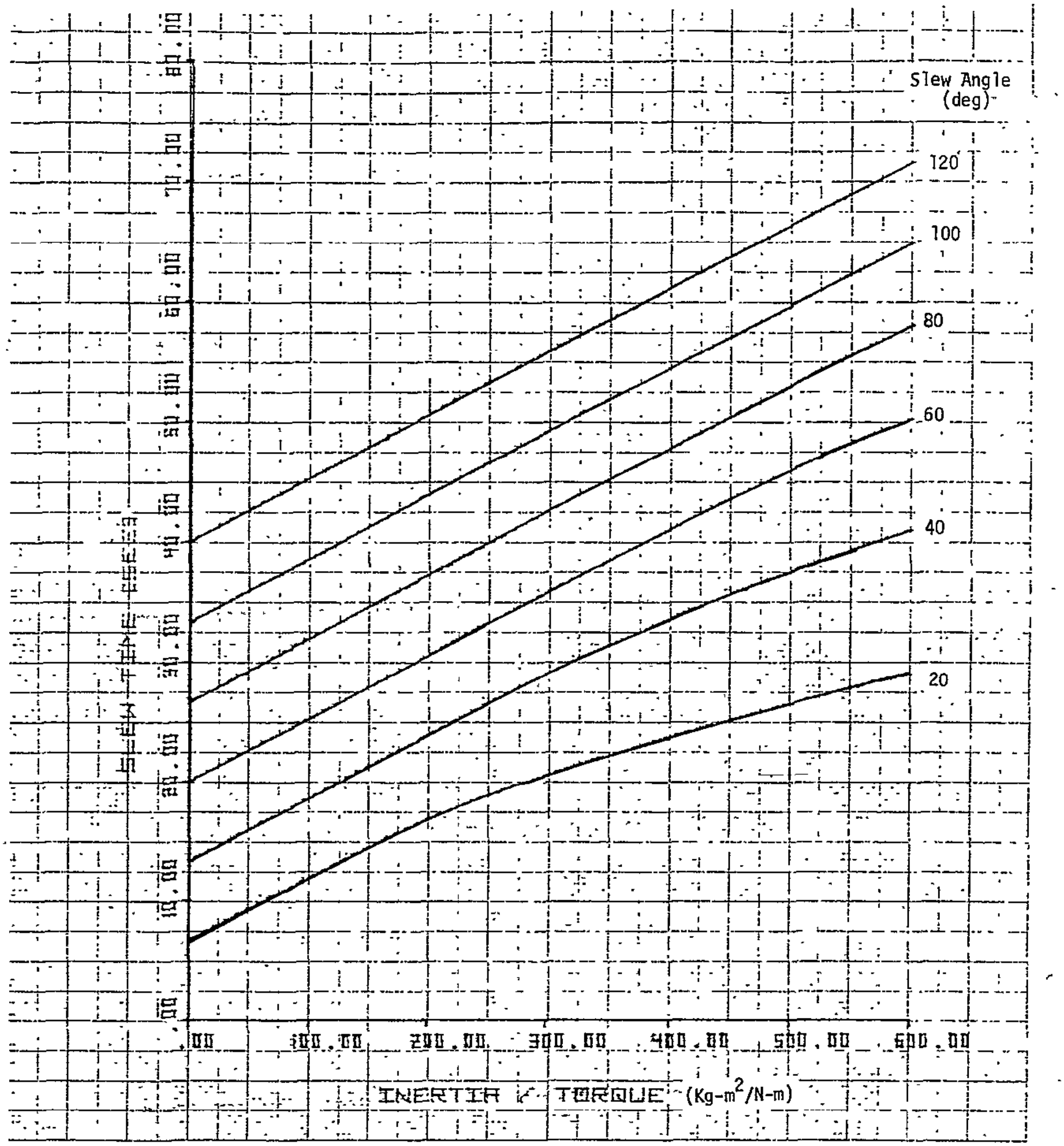

Figure 5-13. Slew Time for Rate Limit P = 3.0 Deg/Sec

ORIGINAL PAGE IS
OF POOR QUALITY

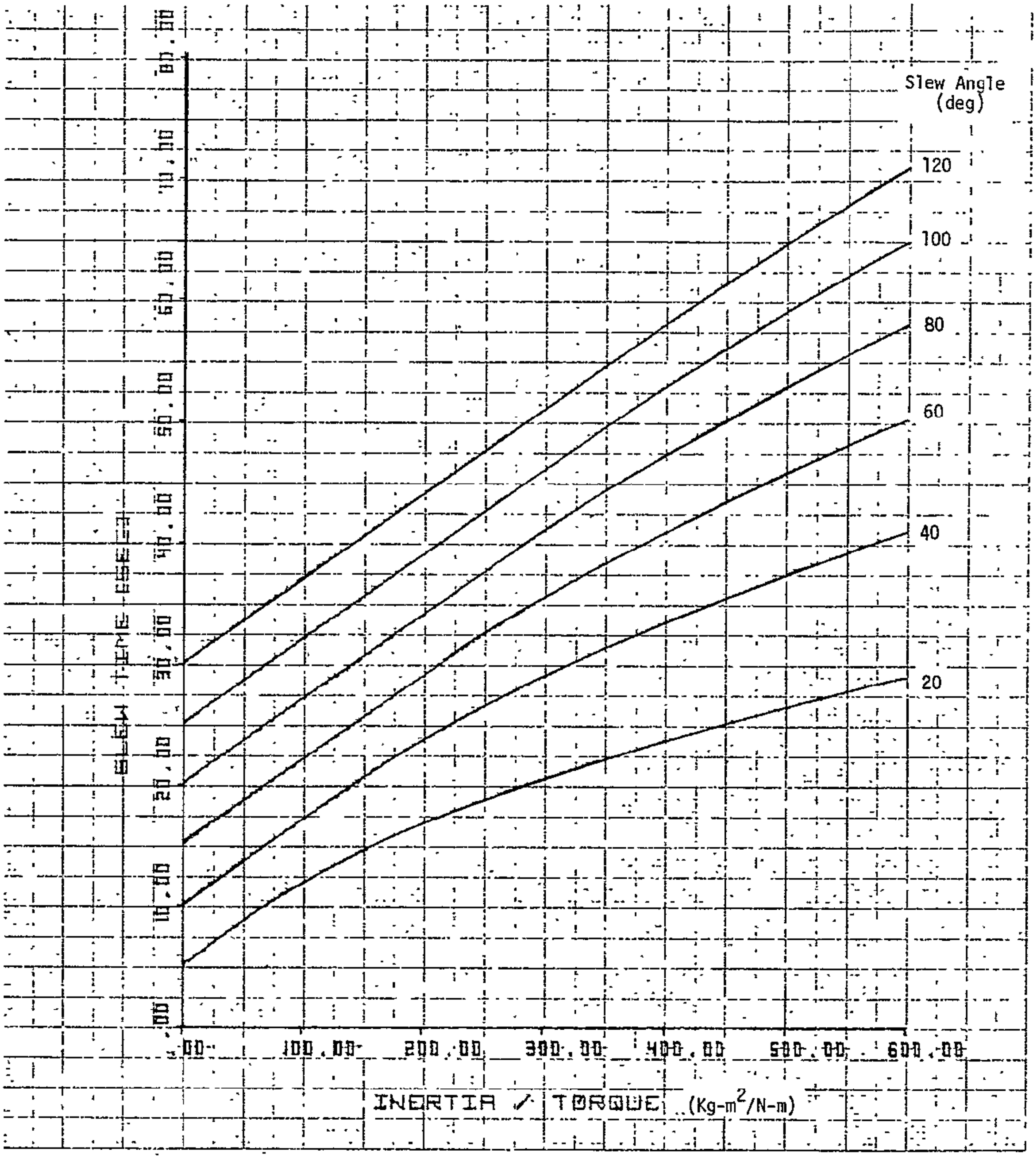

Figure 5-14. Slew Time for Rate Limit P = 4.0 Deg/Sec

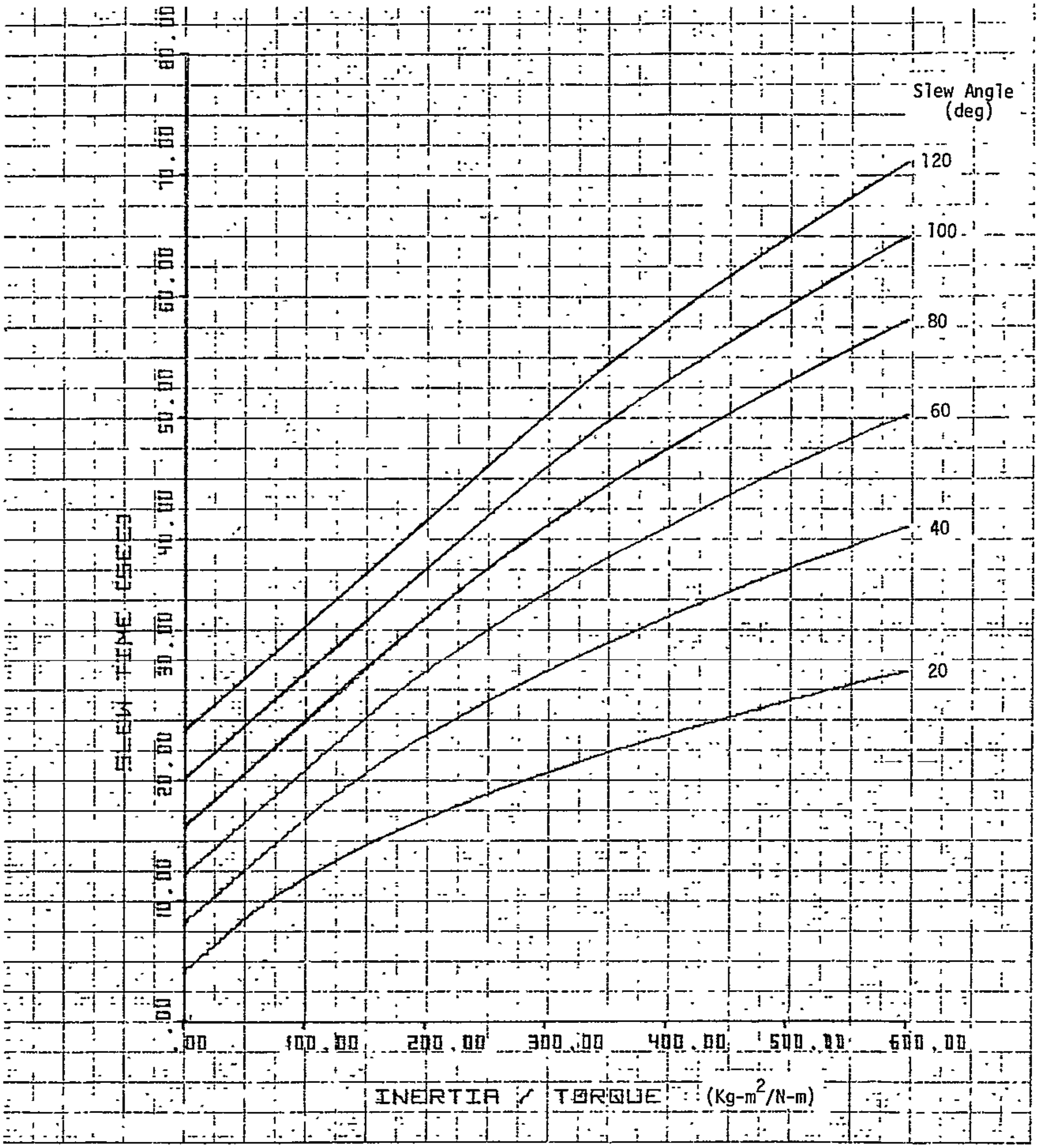

Figure 5-15. Slew Time for Rate Limit P = 5.0 Deg/Sec

6.0 IPS EARTH POINTING ANALYSIS

This section contains the general relationships for the gimbal angles, rates, and accelerations required to maintain the LOS aimed at a fixed point on earth. The special case of the aim point in the orbit plane is considered first. This case represents the worst case condition for the elevation axis and yields closed form expressions for the maximum elevation gimbal rates and accelerations as a function of altitude. The case of the general aim point is considered next, to determine requirements on the cross-elevation axis. The complexity of the resulting relationships precludes an analytical determination of the maximum cross-elevation rates and accelerations. A computer program was therefore written to evaluate the gimbal angle time histories for the general aim point case. A number of sample runs indicates the peak cross-elevation rate and acceleration requirements are about an order of magnitude less than the elevation requirements. Finally, the relationship between earth pointing and payload capability is presented.

6.1 AIM POINT IN ORBIT PLANE

A simple but enlightening case results when the aim point is on the intersection of the earth surface and the orbit plane and earth rotation is neglected. This case is illustrated in Figure 6-1. The shuttle orbiter is assumed to be flying in an inverted orientation, with the payload bay "down" ($\hat{x}_B$ along the velocity vector and $\hat{z}_B$ pointing "up" along the local vertical). In this configuration, the IPS elevation gimbal angle γ, to point the LOS at the aim point, is as shown in the figure. The elevation angle relationship is easily derived by considering the two right triangles indicated by the dashed line.

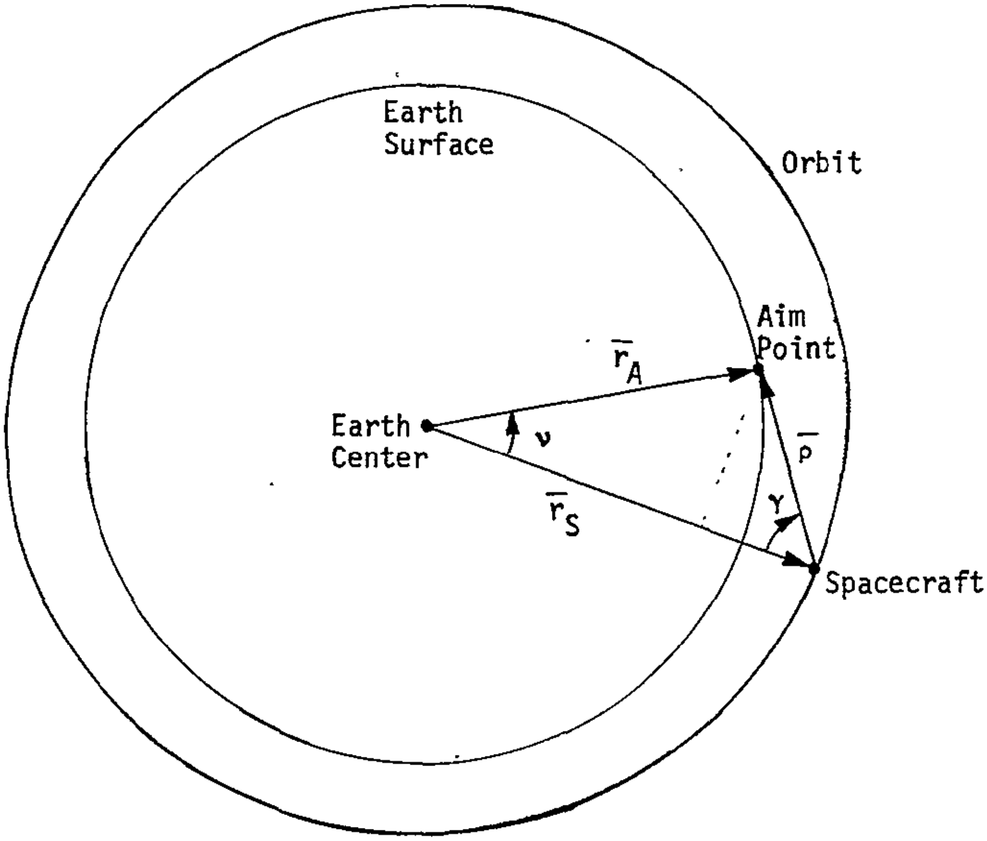

$$\gamma = \tan^{-1}\left[\frac{r_o \sin \nu}{r_S - r_o \cos \nu}\right]$$

$$\dot{\gamma} = \frac{\omega_o \, r_o \, [r_S \cos \nu - r_o]}{\rho^2}$$

$$\ddot{\gamma} = \frac{-\,\omega_o^2 \, (r_S^2 - r_o^2) \, r_o \, r_S \sin \nu}{\rho^4}$$

$$\dddot{\gamma} = \frac{-\,\omega_o^3 \, (r_S^2 - r_o^2) \, r_o \, r_S}{\rho^6}\left[(r_S^2 + r_o^2) \cos \nu - 2 \, r_S \, r_o \, (2 - \cos^2 \nu)\right]$$

where

$r_S = |\bar{r}_S|$ = orbit radius

$r_o = |\bar{r}_A|$ = earth radius

$\rho = |\bar{\rho}| = (r_S^2 + r_o^2 - 2 \, r_S \, r_o \cos \nu)^{1/2}$ = S/C-Aim Point Distance

$\nu = \nu_o + \omega_o t$

Figure 6-1. Aim Point in Orbit Plane

The odd derivatives of γ are even functions of t (with $\nu_o = 0$) and reach their maximum values at $t = 0$, i.e., when pointing at nadir. These maximum values are

$$\dot{\gamma}_{max} = \dot{\gamma}(0) = \frac{\omega_o \, r_o}{h}$$

$$\dddot{\gamma}_{max} = \dddot{\gamma}(0) = \frac{\omega_o^3 \, r_o \, r_s \, (r_s + r_o)}{h^3}$$

where

$$h = r_s - r_o = \text{S/C altitude}$$

The maximum values of γ and $\ddot{\gamma}$ occur at non-zero times determined by setting the next higher derivative to zero. These maximum values are

$$\gamma_{max} = \gamma \left[t = \frac{1}{\omega_o} \cos^{-1}\left(\frac{r_o}{r_s}\right) \right] = \sin^{-1} \left[\frac{r_o}{r_o + h} \right]$$

$$\ddot{\gamma}_{max} = \ddot{\gamma}(t = t_m) = \frac{-\,\omega_o^2 \, r_o \, r_s \, (r_s^2 - r_o^2) \sin \omega_o \, t_m}{(r_s^2 + r_o^2 - 2\, r_o \, r_s \cos \omega_o \, t_m)^2}$$

where

$$t_m = \frac{1}{\omega_o} \cos^{-1} \left\{ \left[2 + \left(\frac{r_s^2 + r_o^2}{4 r_o \, r_s} \right)^{\frac{1}{2}} \right]^2 - \frac{r_s^2 + r_o^2}{4 \, r_o \, r_s} \right\}$$

When $\gamma = \gamma_{max}$, the LOS is tangent to the earth at the aim point. For most payloads, the target is effectively lost before this angle is reached.

Figures 6-2 to 6-5 contain plots of these maximum values as a function of altitude. Figures 6-6 and 6-7 show time plots of the elevation angle and its derivatives for a low (150 km) and high (700 km) altitude orbit. Note that for the 150 km case, the rate and acceleration are still significant when the elevation angle reaches 60 degrees. Also note that the maximum value of jerk ($\dddot{\gamma}$) required for tracking an earth fixed-target is relatively low, about 0.016 deg/sec^3. The IPS gimbal rate limit of 2.5 deg/sec is only exceeded for altitudes below 175 km. No earth pointing missions below 175 km are anticipated however.

6.2 GENERAL AIM POINT

When earth rotation and aim points displaced from the orbit plane are considered, the complexity of the gimbal angle relationships for target tracking is vastly increased. These relationships are presented in Appendix C. A computer program for generating the gimbal angle time historics and peak values, for a general aim point on a rotating earth, is also described in Appendix C. A large number of cases were run with this program, one of which is contained in Appendix C. The results of this series of runs can be summarized as follows:

- The relations in Section 6.1 accurately describe the elevation axis requirements.
- The cross-elevation axis rate and acceleration requirements for target tracking are no more than 10% of those for the elevation axis (azimuth axis not used).

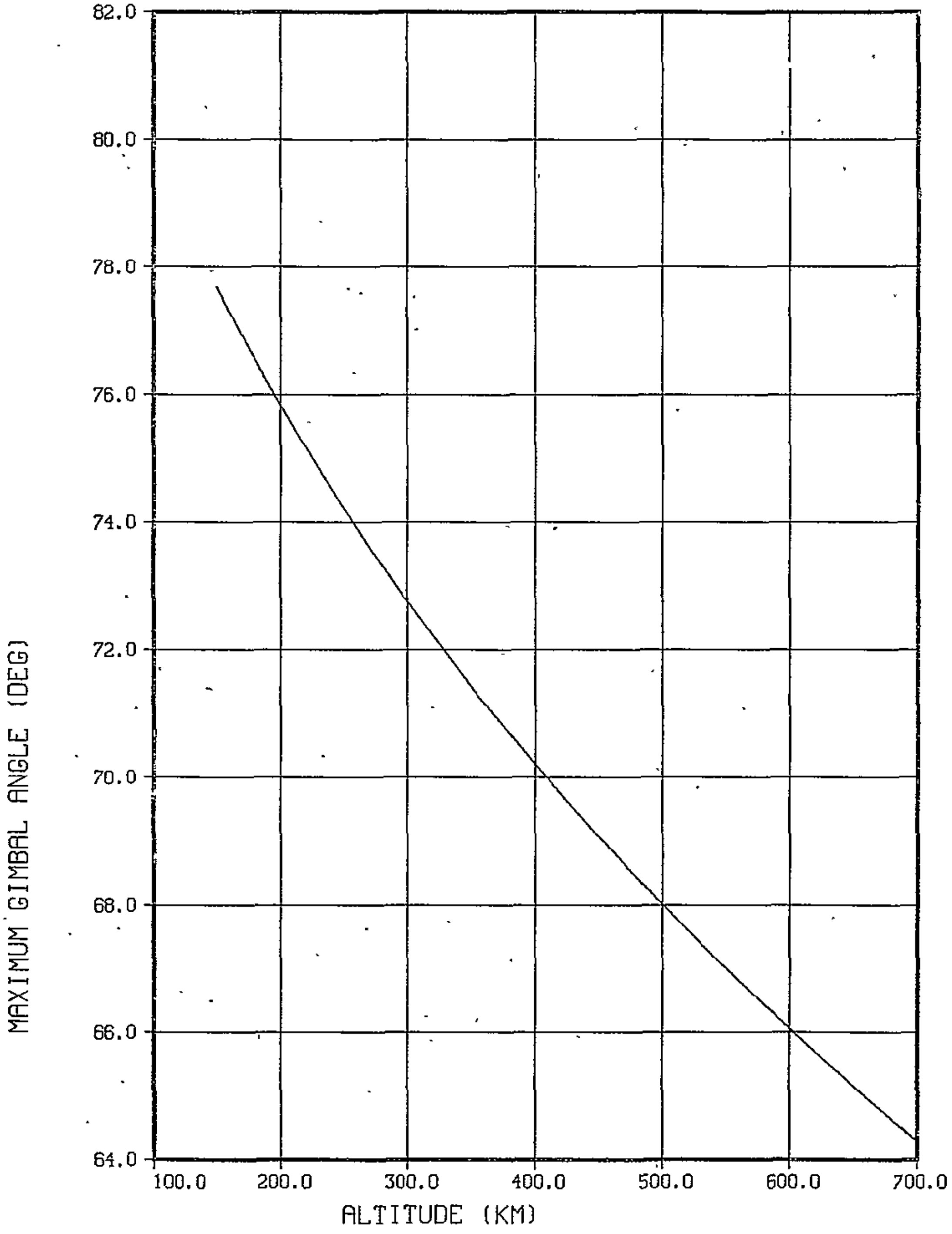

Figure 6-2. Maximum Angle VS Altitude

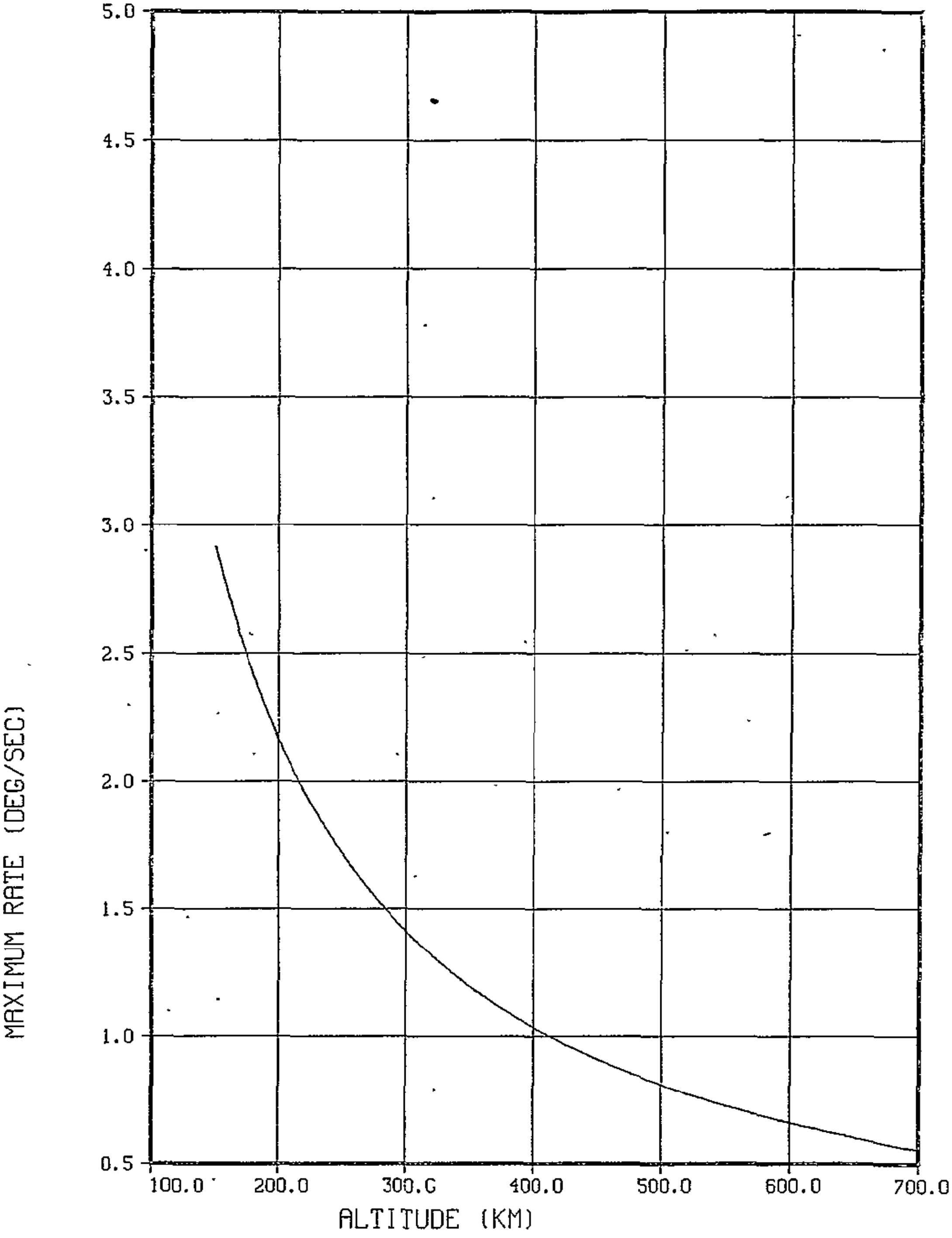

Figure 6-3. Maximum Rate VS Altitude

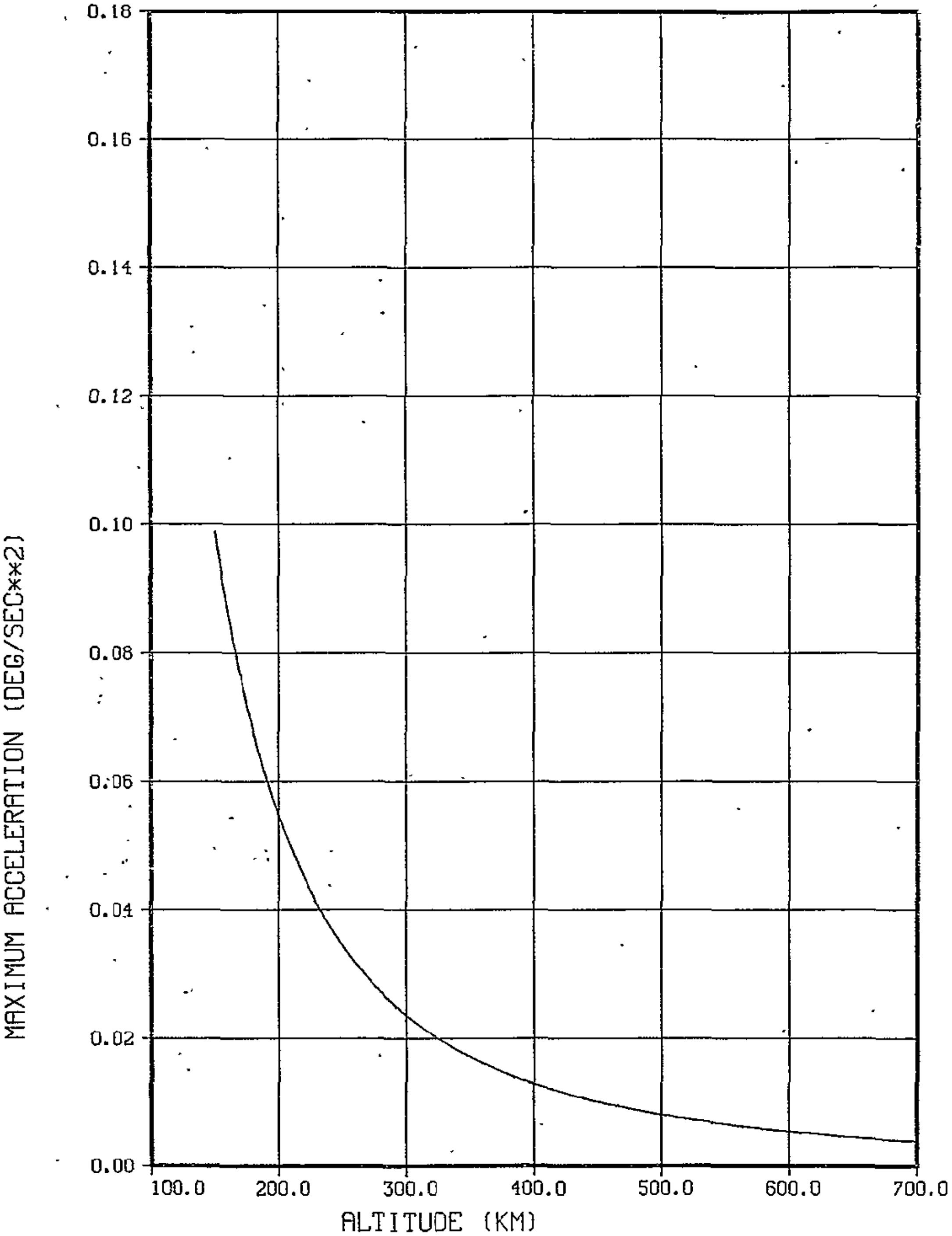

Figure 6-4. Maximum Acceleration VS Altitude

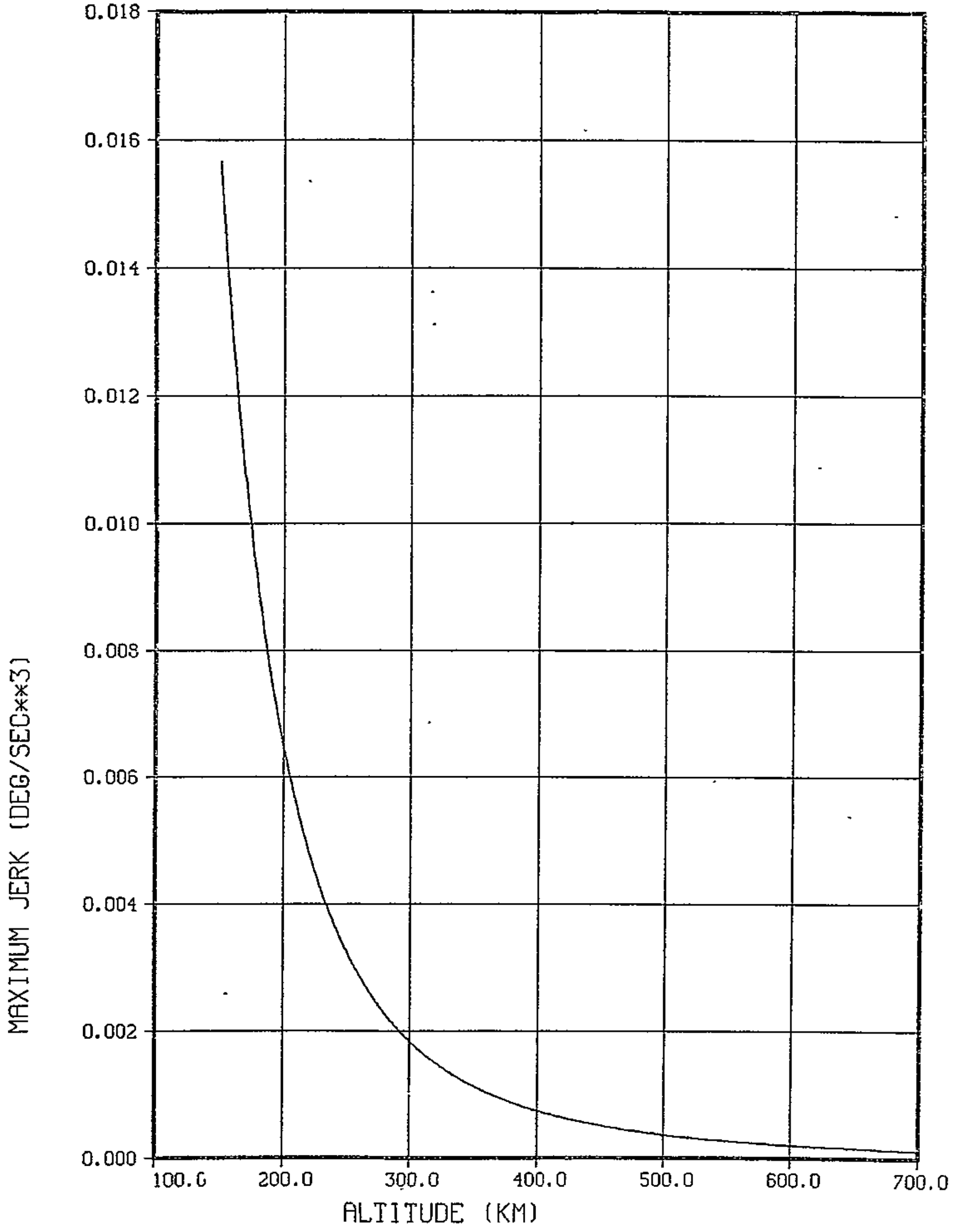

Figure 6-5. Maximum Jerk VS Altitude

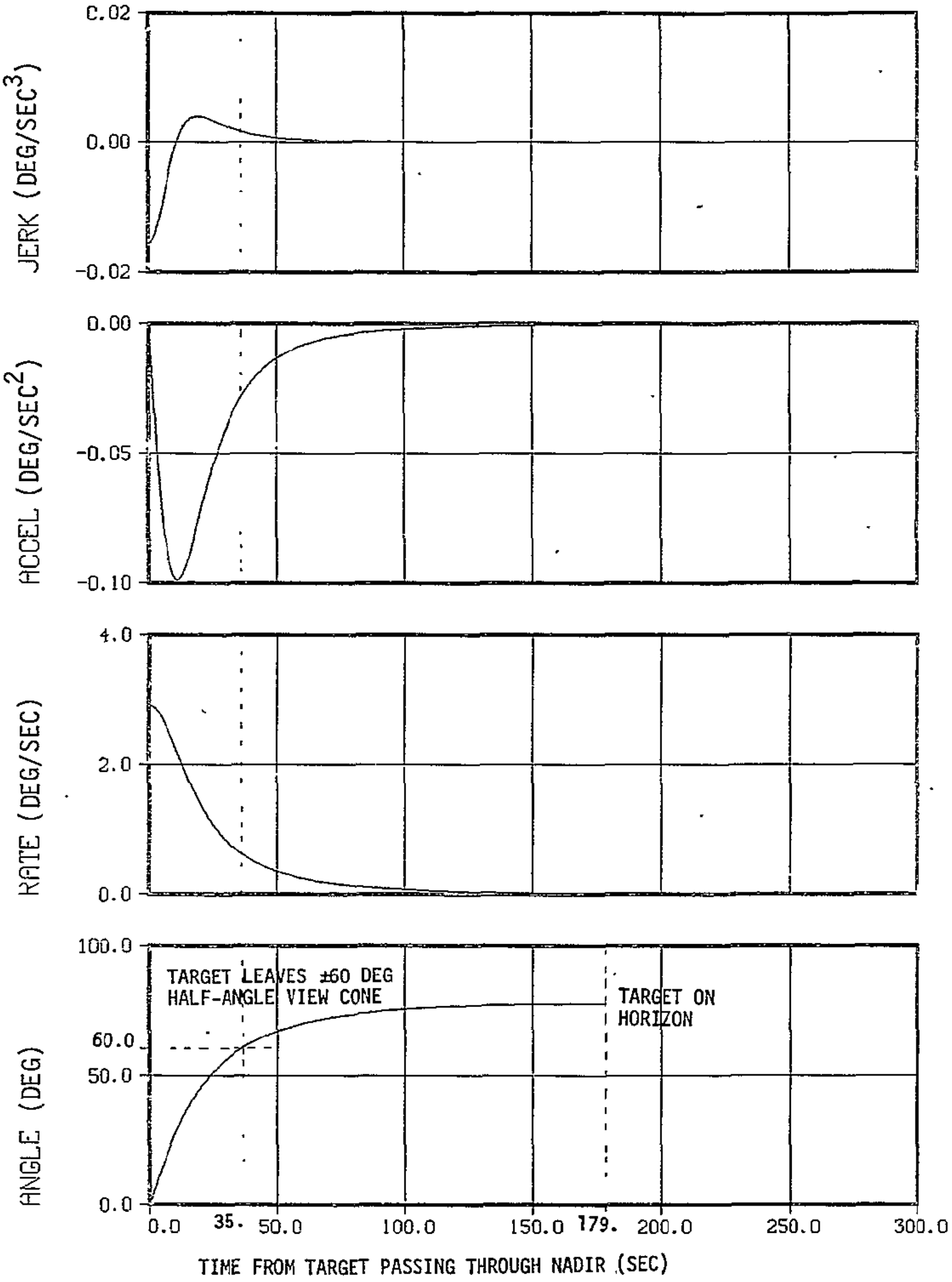

Figure 6-6. Altitude = 150 KM

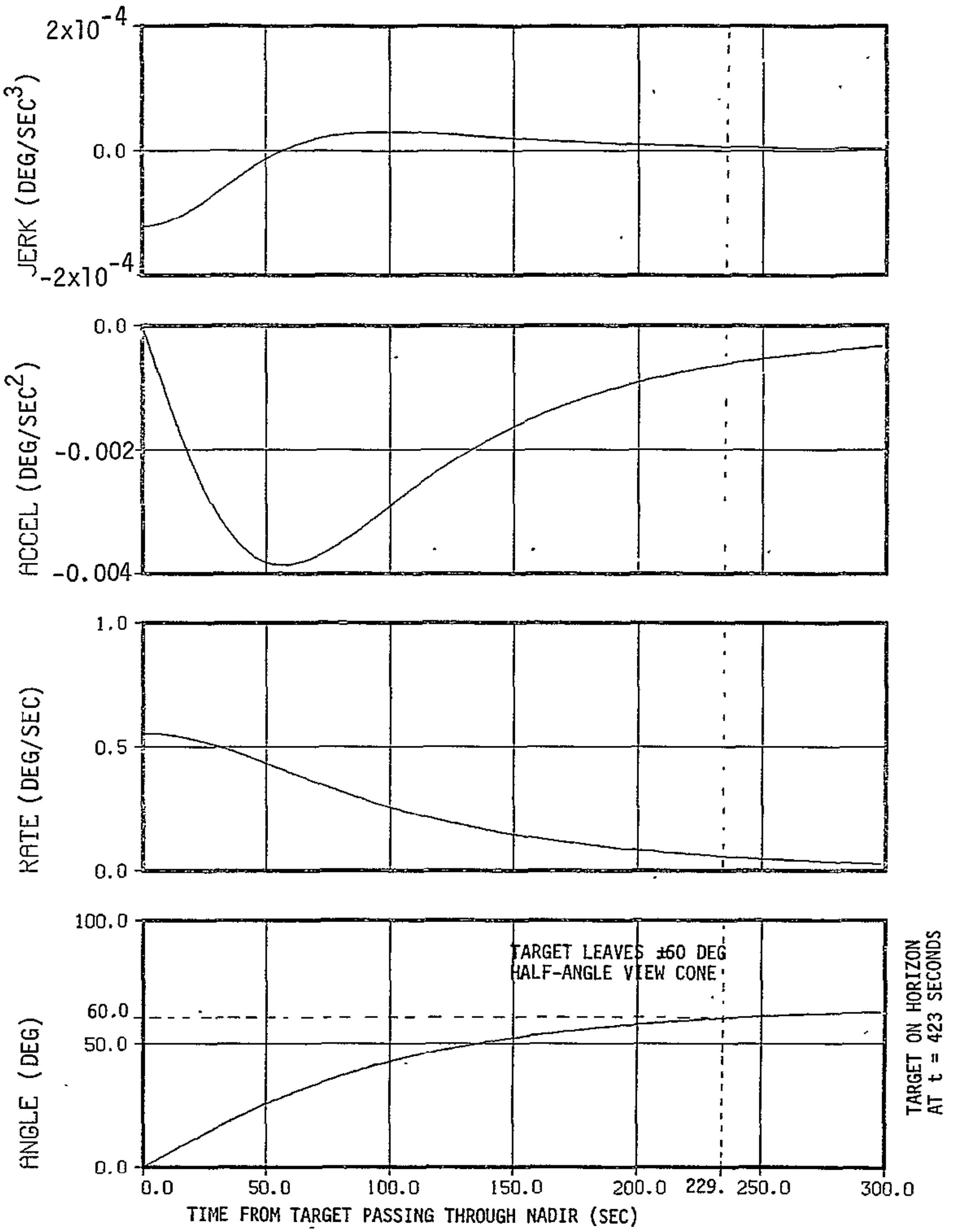

Figure 6-7. Altitude = 700 KM

The second point leads to the conclusion that the cross-elevation axis capability is not the limiting factor in earth pointing for IPS and need not be further considered in this regard.

6.3 EARTH POINTING/PAYLOAD CAPABILITY RELATIONS

The maximum inertia about the gimbal CR that the IPS is capable of maintaining pointed at an earth-fixed aim point at S/C altitude h is

$$(I_1)_{max} = T_m/\ddot{\gamma}_{max}(h)$$

where the expression for $\ddot{\gamma}_{max}$ as a function of h was presented in Section 6.1. The maximum gimbal rate required for tracking has also been expressed and plotted as a function of altitude. Both of the above relations are combined in Figure 6-8 to yield the overall relationship among altitude, gimbal rate limit, motor torque, and maximum inertia about the gimbal CR.

Figure 6-9 illustrates the use of these curves by indicating the range of allowable inertias about the CR (shaded area) using the nominal IPS parameter values T_m = 20 N-m and P = 2.5 deg/sec. The rate limit sets the lower limit on altitude (175 Km) while the motor torque sets the upper limit on inertia. For any given altitude the maximum inertia about the CR can be read off. The inertia about the CR can then be translated into ranges of payload mass and length using Figures 4-9 to 4-14.

Feasible Regions Below Curves

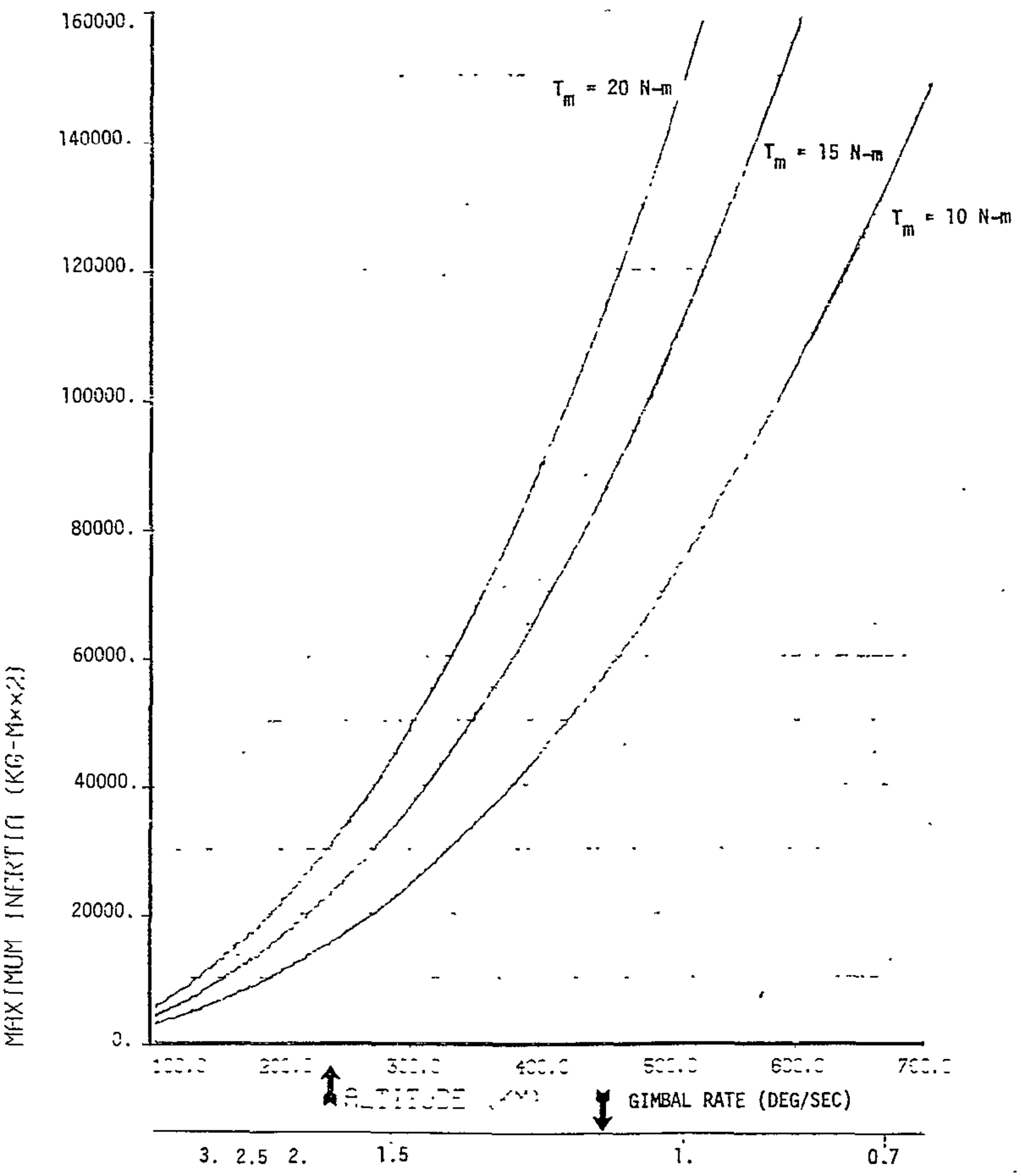

Figure 6-8. Maximum Inertia About CR for Earth Tracking VS Altitude
T_m = 10, 15, 20 N-m

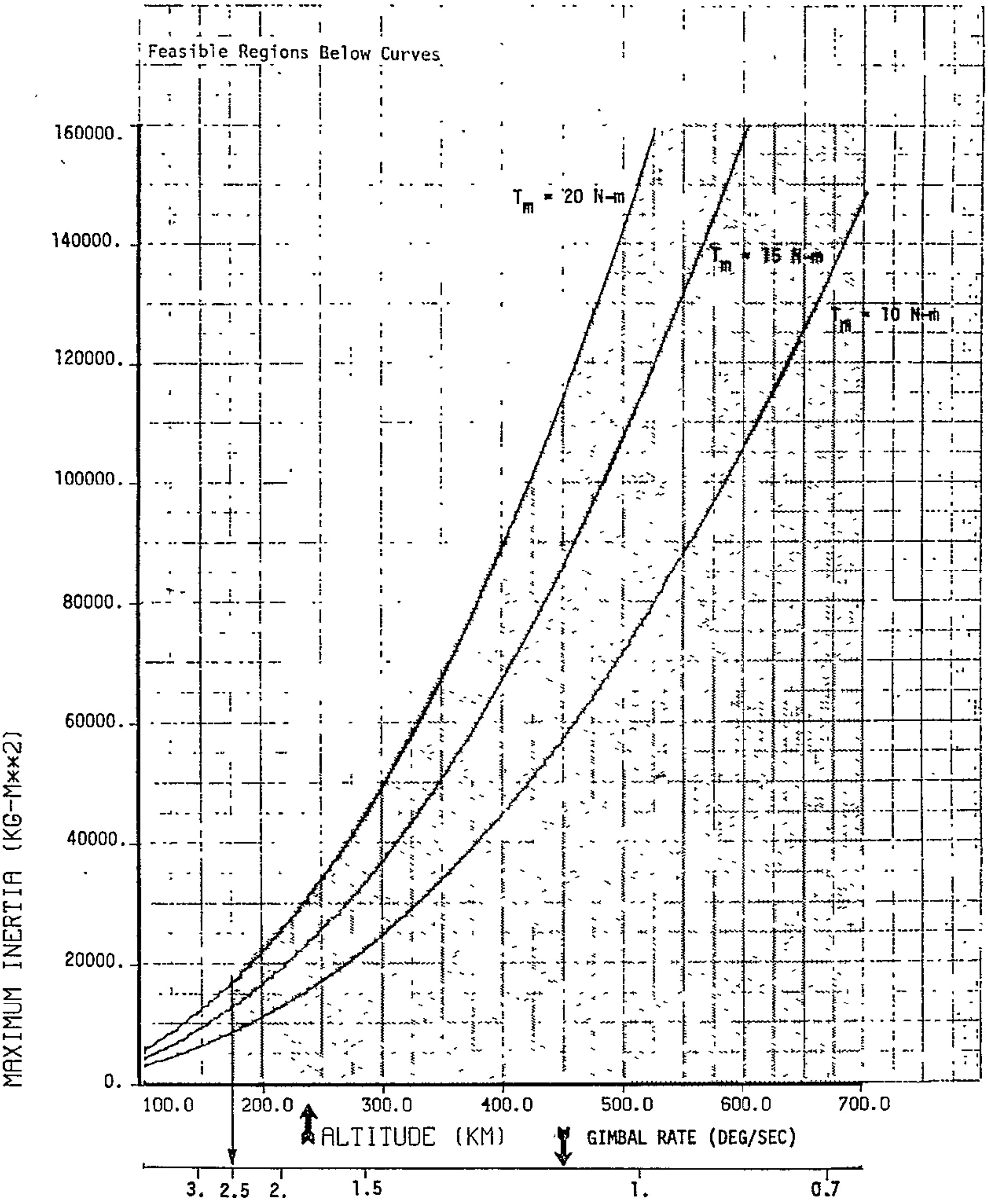

Figure 6-9. Altitude/Maximum Inertia About CR Envelope for T_m = 20 N-m, P = 2.5 Deg/Sec

7.0 IPS CONTROL SYSTEM DEFINITION

This section defines an IPS control system configuration suitable for the EVAL mission. The IPS control system, shown in block form in Figure 7-1, is configured to be as nearly autonomous as possible. Inputs required from the spacelab experiment computer include only target commands and orbiter ephemeris data, and all control loops are closed locally on the pallet with programmable digital electronics (PDE). The computational burden on the spacelab experiment computer and the transfer of control related data through the experiment data bus are thereby minimized.

The major blocks of the IPS control system are described in the following subsections. Figure 7-2, illustrates the IPS gimbal structure and coordinate frames.

7.1 ATTITUDE REFERENCE SYSTEM

A functional block diagram of the IPS ARS is shown in Figure 7-3. The ARS inertial sensors, gyros and a star tracker, are mounted along with the payload on the IPS platform. Processing of the sensor data is performed on the pallet with PDE. A high bandwidth, stabilized attitude reference is obtained by integrating processed gyro rates with a closed form quaternion algorithm (Reference 4). The gyro processing consists of correcting for gyro biases, misalignments and scale factor errors.

The star tracker data is processed to correct for known errors, compared to data in the star catalog for identification, and combined with estimated platform attitude to yield the attitude residual. The attitude residual is processed by an extended Kalman filtering algorithm to compute optimal attitude and gyro bias updates for long term attitude reference stability. The frequency of the required update depends on the quality of the system components and the required attitude determination accuracy.

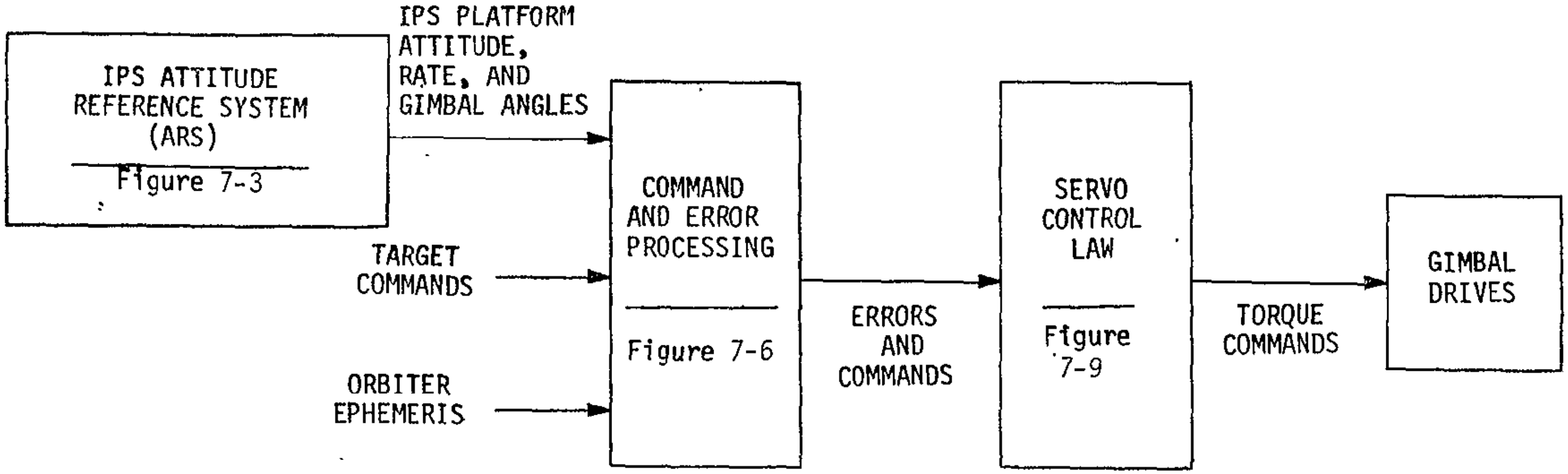

Figure 7-1. IPS Control System Functional Block Diagram

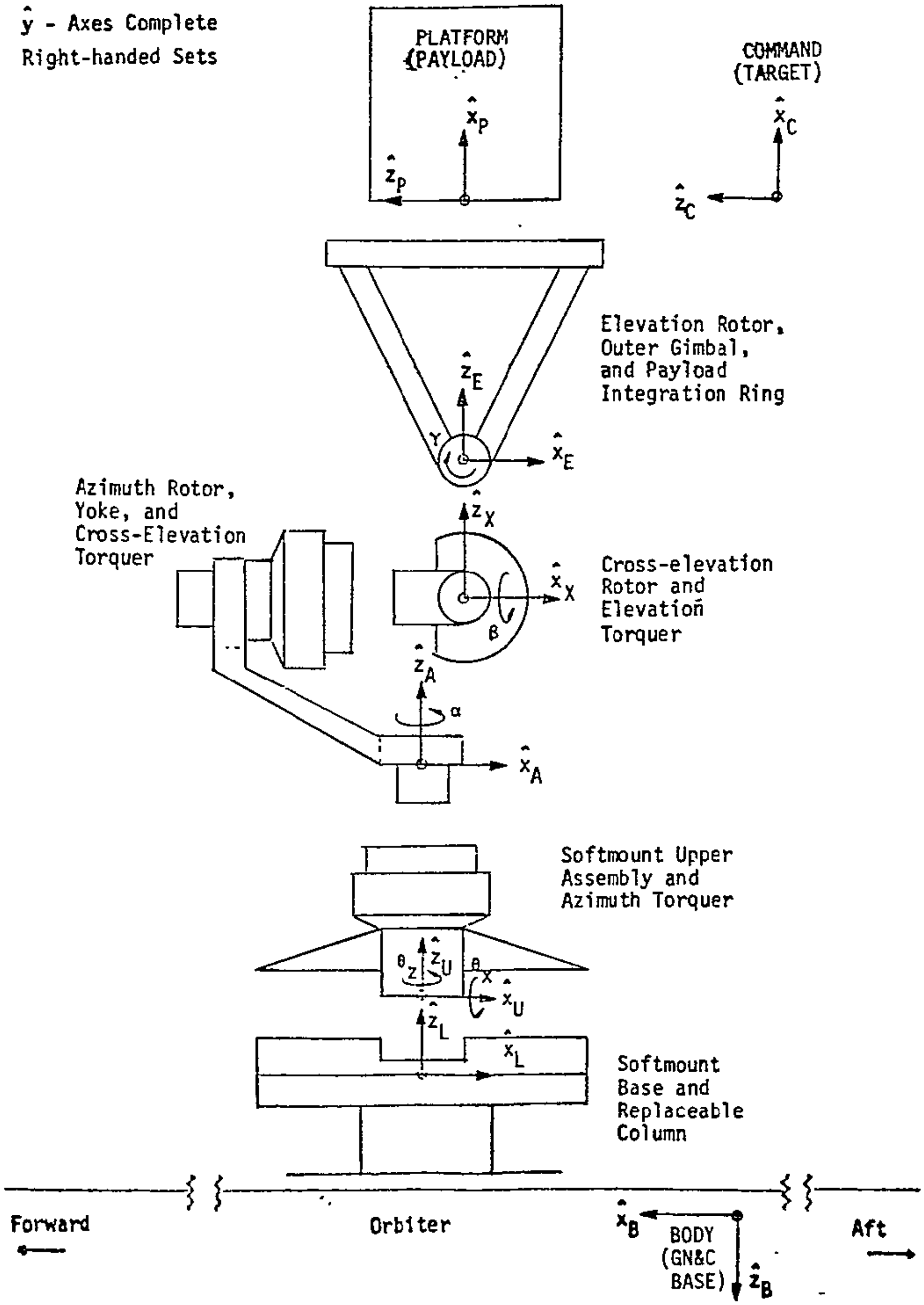

Figure 7-2. IPS Coordinate Frames

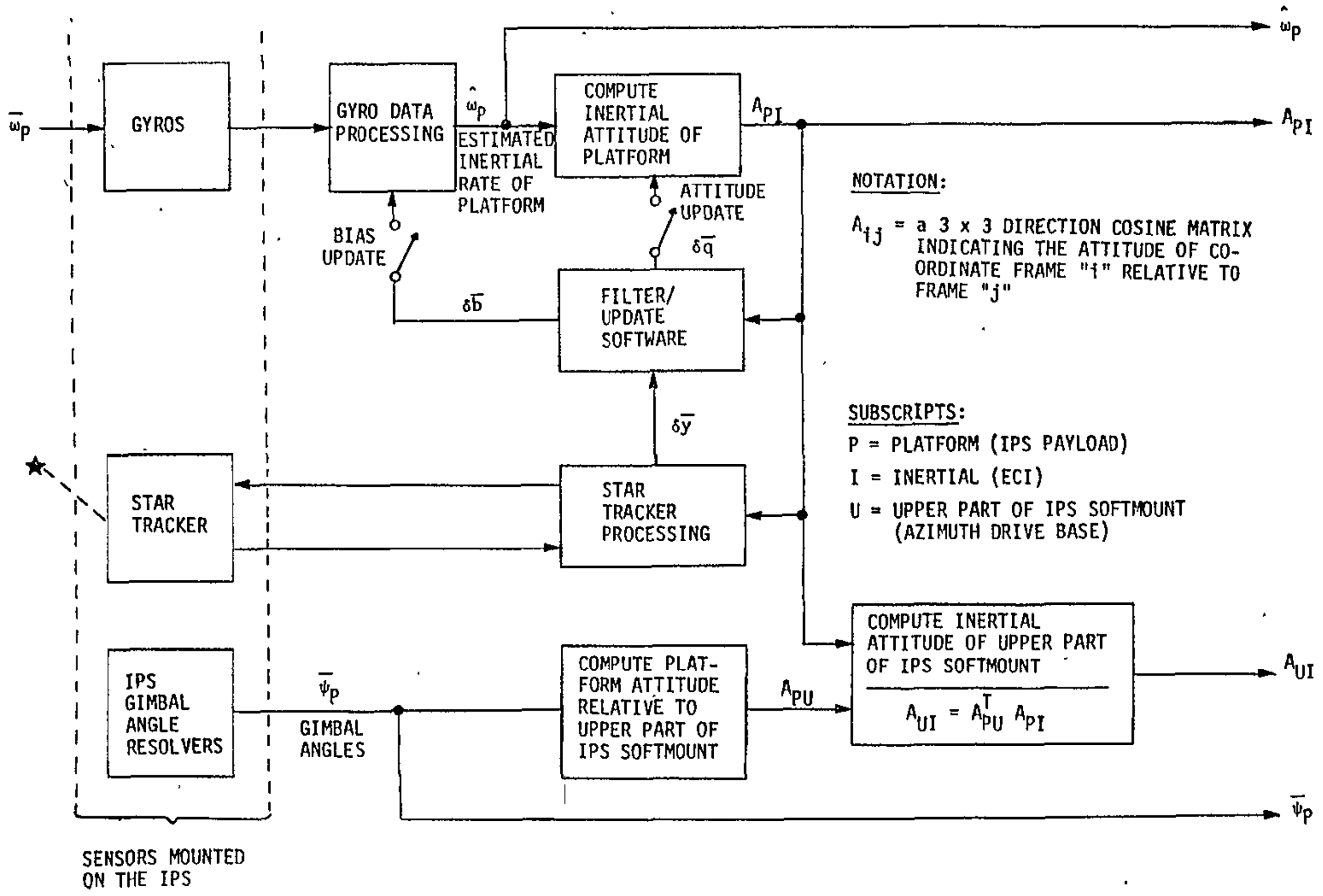

Figure 7-3. IPS Inertial Attitude Reference System Functional Block Diagram

The main attitude determination problem is that the star tracker view of the celestial sphere is highly restricted for the EVAL mission by the combined geometry of the orbiter payload bay doors and radiators, the orbiter wing surfaces, the orbiter tail, the cockpit (crew cabin), the Spacelab pressurized module, and the earth. Figure 7-4 illustrates this restrictive geometry. The figure also indicates that there is a solution to the problem, and that an 8° x 40° window of the celestial sphere is available if it is permissible for the tracker field of view (FOV) to come within 20 degrees of the earth's limb and 15 degrees of the orbiter surfaces. Depending somewhat on the star tracker aperture, a reasonably sized shade in the 15-25 inch range can be successfully utilized to permit the tracker to operate within 20 degrees of the earth's limb.

Since the window on the celestial sphere available to the star tracker is limited to a region comprising only 8° x 40° = 320 square degrees, star availability must be examined. Figure 7-5 plots the width of one side of the square field of view required on the celestial sphere versus star visual magnitude to assure with 95% confidence the presence of at least one star of the indicated brightness, or brighter. For example, if one can detect stars up to $M_V = +6$, then with 95% confidence one can find a usable star within any 5x5 = 25 square degrees of the celestial sphere. The actual worst case is also plotted using Yale star catalog data. For $M_V = +6$ the plot indicates that one can find no 10° x 10° area on the entire celestial sphere where there is not at least one 6th order magnitude star or brighter. Guide star availability within the 320 square degree window is, therefore, assured. In fact, with 95% confidence the guide star will be a 4th order magnitude star or brighter.

The baseline IPS star tracker, described in Appendix B, has a maximum tracking rate of only 0.05 deg/sec. Since, as derived in Section 6, earth pointing will often require higher rates, payload pointing will usually have to be interrupted to obtain a star reading. At update time, the IPS will therefore interrupt payload pointing and move, if required, to acquire a star with the 2°x2° FOV tracker within the available 8°x40° area of the celestial sphere.

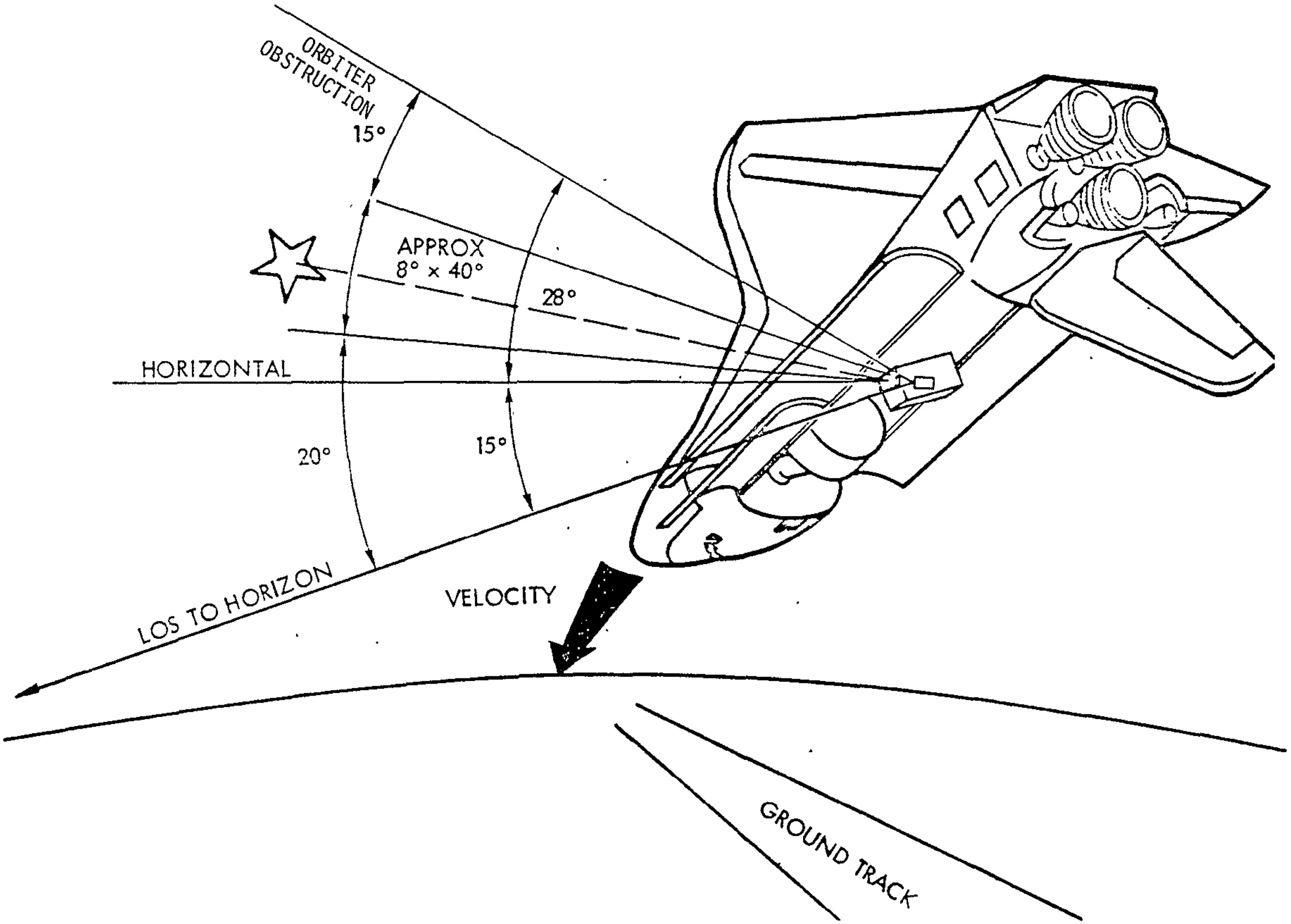

Figure 7-4. IPS Star Tracker Field of View of Celestial Sphere

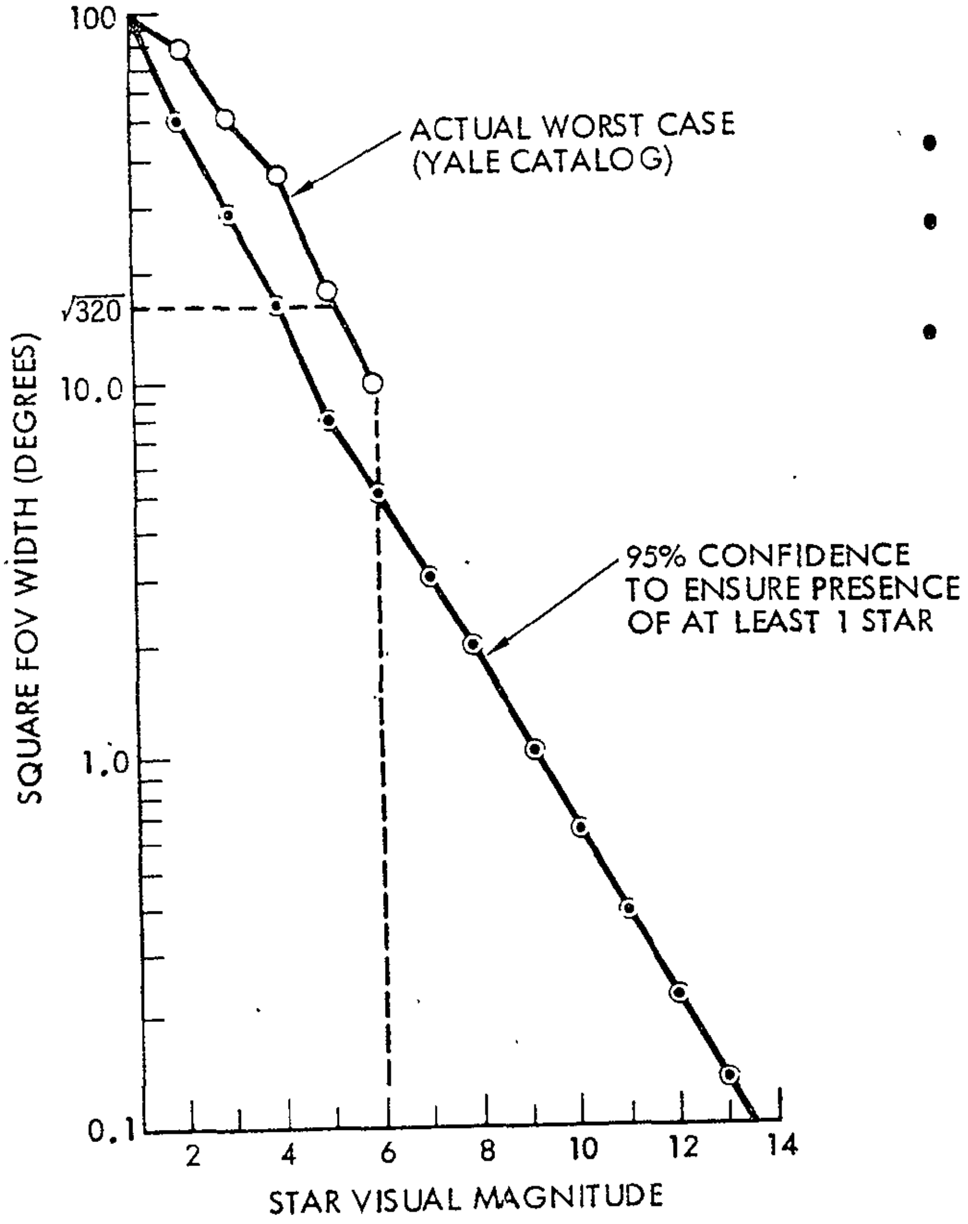

- VERY HIGH PROBABILITY OF CONTINUOUS GUIDE STAR PRESENCE
- SHADE DESIGN REQUIRES EXTENSION TO ABOUT 0.41 METERS (16 INCHES LONG BY 5.6 INCHES SQUARE)
- AT UPDATE TIME IPS INTERRUPTS PAYLOAD POINTING AND MOVES TO ACQUIRE A STAR AS REQUIRED

Figure 7-5. Guide Star Availability

In normal IPS pointing/tracking operation, the attitude control loops are closed through the gyros and the IPS gimbal angle resolvers play no part in generating attitude errors. The gimbal angle resolvers are used, however, in acquisition mode for attitude control, and the gimbal angles and direction cosine matrix A_{UI} are ARS outputs. Initializing the IPS ARS requires an attitude transfer from the orbiter GN&C base to the IPS platform. Potentially large errors from orbiter/pallet flexibility, softmount rotation, and gimbal angle resolver inaccuracy enter into the transfer through the relation

$$A_{PI} = A_{PU} A_{UL} A_{LB} A_{BI}$$

where A_{PU} involves unknown gimbal angle resolver errors, A_{UL} involves unknown softmount rotation angles, A_{LB} involves unknown orbiter/pallet flexibility, and A_{BI} is the orbiter inertial attitude (relayed through the spacelab computer). The initial errors in the attitude transfer are eventually reduced by using the IPS star tracker for attitude updates. A visual star tracker, such as described in Reference 5, would improve the attitude transfer and speed convergence to the required pointing accuracy by providing a direct visual indication of the IPS platform attitude.

7.2 COMMAND AND ERROR PROCESSING

The IPS command and error processing data flow is shown in Figure 7-6. The target command and orbiter ephemeris are the only inputs required from the spacelab computer. The target command is given in a user convenient coordinate frame that is identified as part of the command.

C-2

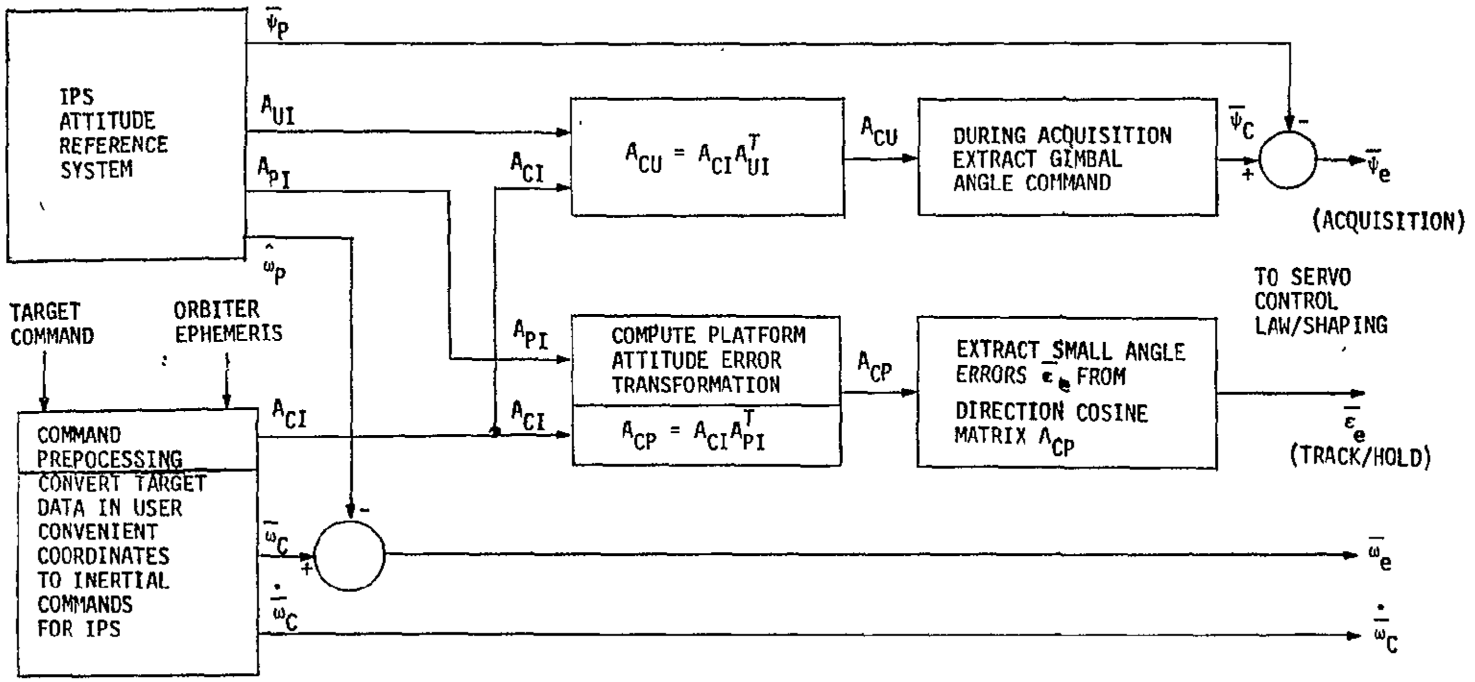

SUBSCRIPTS:

U = IPS UPPER SOFTMOUNT
C = COMMAND (TARGET)
I = INERTIAL (ECI)
P = PLATFORM (PAYLOAD)
e = ERROR

NOTATION:

A_{ij} = DIRECTION COSINE MATRIX, "i" RELATIVE TO "j"
$\bar{\psi}_P$ = IPS GIMBAL ANGLES
$\bar{\psi}_e$ = IPS GIMBAL ANGLE ERRORS (ACQUISITION)
$\bar{\epsilon}_e$ = SMALL ANGLE PLATFORM ATTITUDE ERRORS (TRACK/HOLD)
$\dot{\bar{\omega}}_C$ = COMMANDED INERTIAL ACCELERATION OF PLATFORM
$\bar{\omega}_C$ = COMMANDED INERTIAL RATE OF PLATFORM
$\bar{\omega}_e$ = PLATFORM INERTIAL RATE ERROR

Figure 7-6. IPS Command and Error Processing

Using the orbiter ephemeris, the target command is converted to inertial coordinates in the command preprocessing block. This allows simple and uniform command processing, whether the target is the earth limb, a point fixed to the earth surface, or an inertially fixed target, because the ARS provides an inertial reference. The command preprocessing also computes the commanded inertial rates $\bar{\omega}_c$ and angular accelerations $\dot{\bar{\omega}}_c$ required to maintain the platform pointed at the target. The commanded rate is compared to the processed gyro rates to yield an inertial rate error $\bar{\omega}_e$ for the servo control law. The commanded angular acceleration is used as a feedforward input to the servo control law for improved performance in tracking earth-fixed targets.

There are two modes of operation, one for acquiring targets and one for tracking and holding. When a new target is acquired the IPS gimbal angles are commanded and controlled relative to the gimbal base (upper part of softmount) and the resolvers are used as position sensors. When the IPS is pointing at or tracking a target, the attitude error is computed directly from the inertial attitude reference and resolver inaccuracies do not influence fine pointing.

The ultimate IPS pointing accuracy for EVAL depends not only on the accuracy of the ARS and IPS gimbal servos but also on the quality of available ephemeris data. It is interesting to note that ephemeris errors influence the pointing accuracy differently, depending upon the type of pointing being considered. For example, space pointing of experiments to targets defined on the celestial sphere is independent of ephemeris. Furthermore, the accuracy of pointing relative to local vertical is much less sensitive to ephemeris errors (by the ratio of altitude to orbital radius) than pointing at landmark targets (i.e., latitude, longitude, radius). This latter point becomes apparent from the geometry shown in Figure 7-7, where this somewhat simplified case considers only in-track ephemeris errors, Δx. To demonstrate the effects which ephemeris errors contribute, relative to ARS errors, it is most meaningful to consider angular resolution. This is summarized for a 200 Km orbit in Figure 7-8.

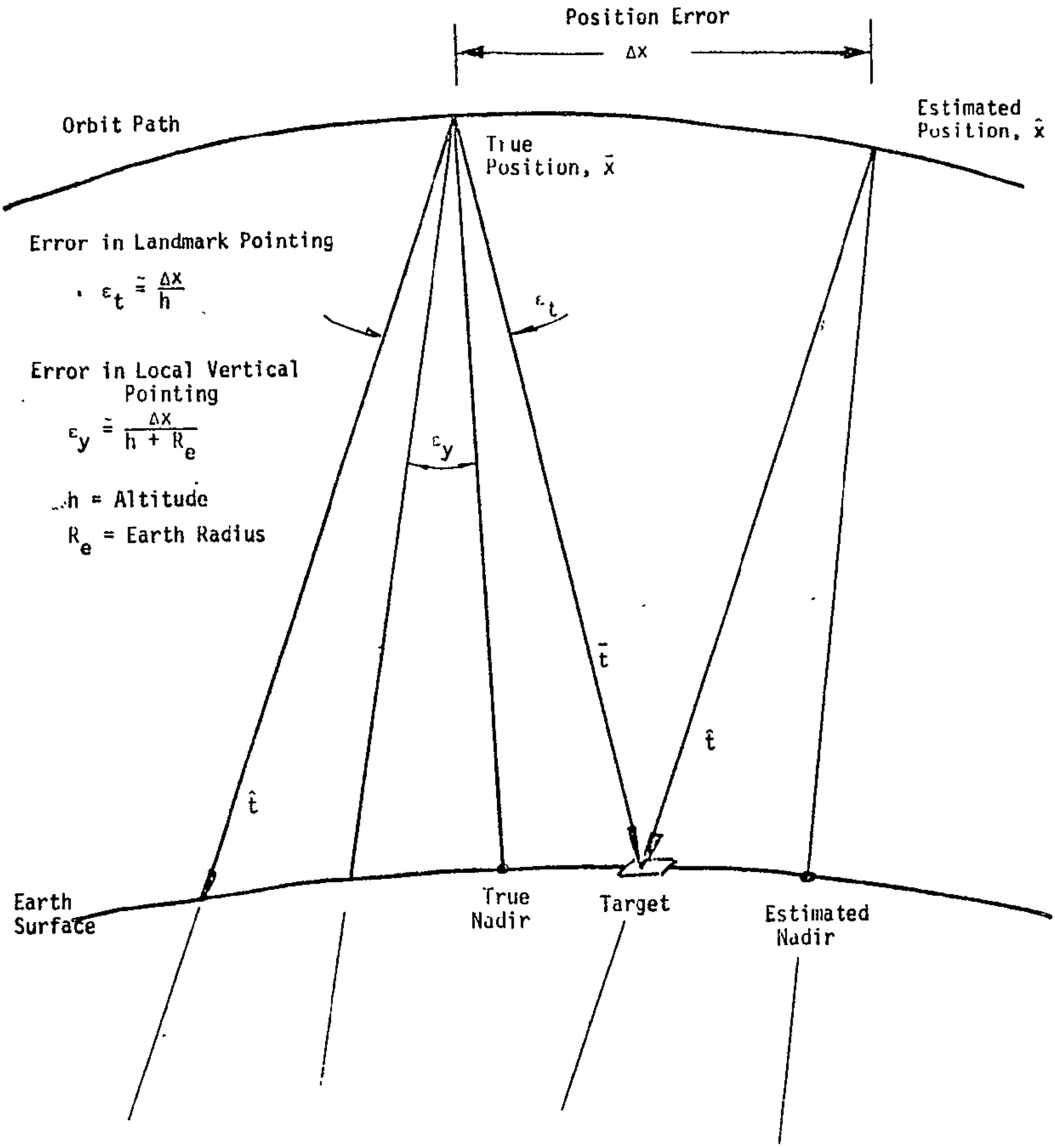

Figure 7-7. Ephemeris Error Geometry

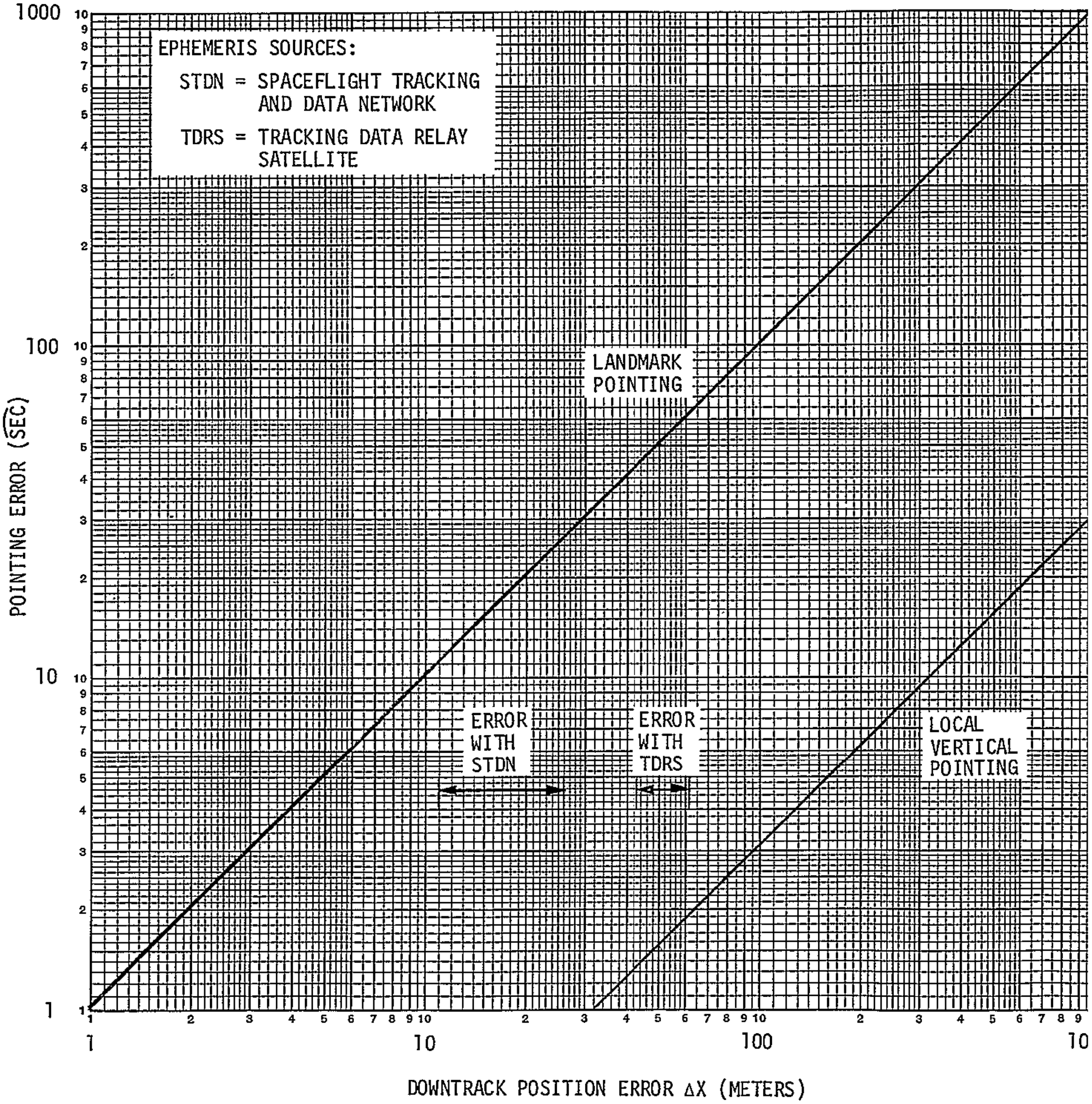

Figure 7-8. EFFECT OF EPHEMERIS ERROR ON POINTING ACCURACY AT 200 KM ALTITUDE

Note that for pointing relative to the local vertical frame the down track ephemeris errors given in Reference 1 add less than 2 arc sec to the pointing error. For landmark pointing, however, the ephemeris error contribute from 10 to 65 arc sec to the pointing error, depending on the ephemeris source used and the time since the last tracking pass.

7.3 IPS SERVO CONTROL LAW/SHAPING

The IPS servo control law/shaping block diagram is shown is Figure 7-9. As with the command and error processing, there are two modes of operation. In the acquisition mode, the IPS gimbal angle errors are applied to a proportional plus integral plus rate shaping function (implemented with PDE) to yield commanded gimbal drive torques.

In track/hold mode, the attitude error $\bar{\varepsilon}_e$ is processed (again digitally) with a proportional plus integral compensation function and rate feedback is provided with the computed rate error $\bar{\omega}_e$. An important feature of the track/hold control law is the feedforward of commanded angular acceleration to improve pointing performance without excessive bandwidth in the feedback path. The reduced feedback bandwith minimizes the effect of sensor noise on attitude stability. Feedforward control is particularly important for raster scanning and tracking earth fixed targets. The commanded torque in track/hold mode is in platform fixed coordinates and is converted to gimbal axis coordinates through a gimbal angle dependent transformation matrix.

Selection of control law gains, especially feedforward gains and compensation for gimbal compliance poles, is strongly dependent on payload mass properties and mission requirements. This is a direct result of the IPS design, in particular the softmount and large center of mass/center of rotation offset.

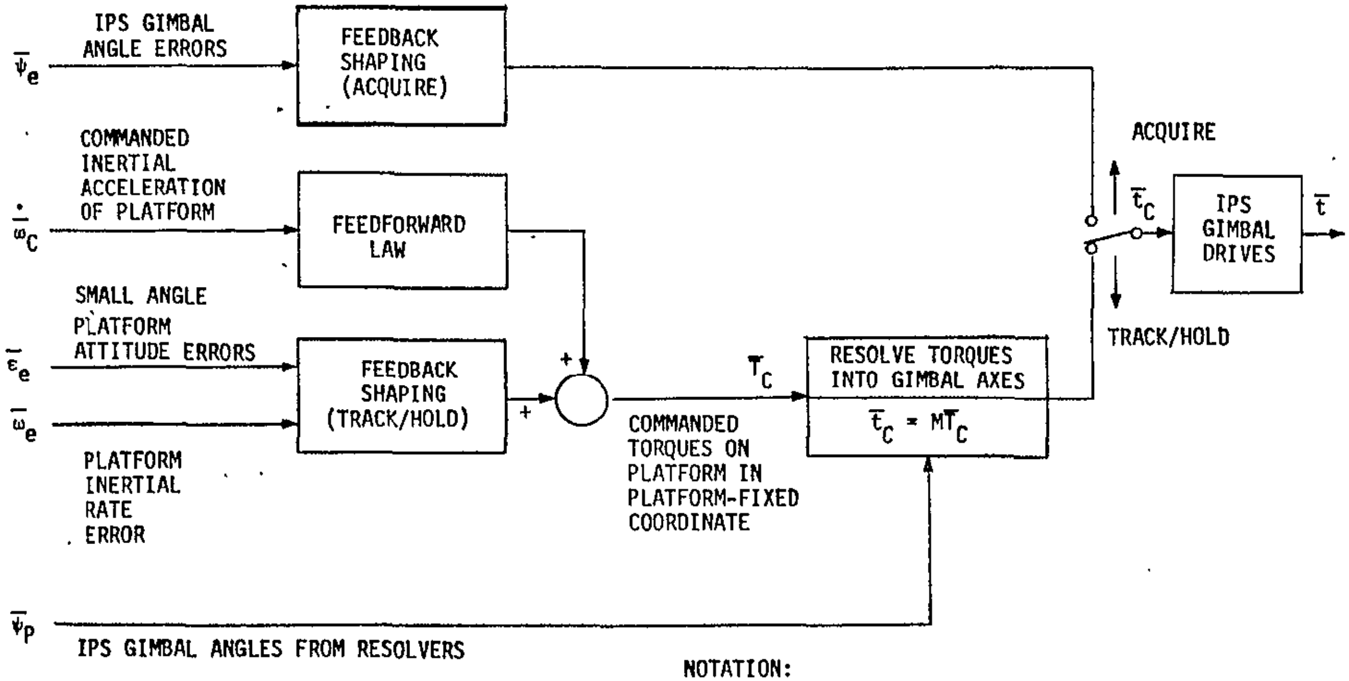

NOTATION:

$\overline{t}_C$ = COMMANDED GIMBAL DRIVE TORQUES

$\overline{t}$ = ACTUAL GIMBAL DRIVE TORQUES

M = TRANSFORMATION MATRIX FOR RESOLVING PLATFORM TORQUES INTO GIMBAL AXES (FUNCTION OF $\overline{\psi}_P$)

Figure 7-9. IPS Servo Control Law Block Diagram

8.0 EVALUATION OF ORBITER EARTH VIEWING ORIENTATIONS

Some EVAL missions may require that the shuttle orbiter RCS be disabled to eliminate either the high frequency disturbances or contamination caused by firing the RCS thrusters. An earth pointing orientation can be maintained without the RCS by flying the orbiter at a null torque attitude, that is an attitude for which the total external torque on the orbiter vanishes. For the EVAL altitude range, 150 to 1000 km, the predominant external torques are gravity gradient and aerodynamics. As the gravity gradient nulls are in general unstable equilibriums, the sensitivity of the torque to small perturbations in attitude from the null are equal in interest to the location of the null itself.

The following topics relating to the existance and characterization of null torque attitudes and their suitability for EVAL are covered in this section:

- definition of coordinate systems and transformations.
- definition of potential earth viewing orientations.
- aerodynamic and gravity gradient disturbance torque models for the shuttle orbiter.
- discussion of method of determining null torque attitudes and incremental sensitivity matrices.
- discussion of each potential orientation, including existence and location of torque nulls, stability and sensitivity, and relative merits for EVAL.
- selection of two baseline earth viewing orientations, one for viewing the earth surface and the other for viewing the earth limb.
- discussion of the effect of atmospheric density variations on the null torque attitude.

All of the null torque attitudes found are either unstable or highly sensitive to atmospheric density variations at low altitude, and most are unstable at all altitudes. Some form of active fine control will therefore be required to stabilize the orbiter near the null torque attitude. The design of such an orbiter null torque attitude stabilization system is discussed in following sections of this report.

8.1 DEFINITION OF POTENTIAL EARTH VIEWING ORIENTATIONS

In this section potential orbiter orientations for earth viewing are defined. The necessary coordinate systems and transformations for describing and analyzing these orientations are presented first.

8.1.1 Coordinate Systems and Transformations

The orientation of the orbiter body axes relative to the orbit reference frame is described by the 3 x 3 transformation matrix

$$A_{BR} = A_{BO} \, A_{ON} \, A_{NR} \tag{8-1}$$

The orbit reference axes are defined in Figure 8-1 and the orbiter body axes are defined in Figure 8-2.

Each nominal orbiter orientation relative to the orbit reference frame is defined by an A_{NR} matrix. As the nominal orientations involve rotations in multiples of 90 degrees about one or more principal axes, the A_{NR} matrix contains a single + 1 or - 1 in each row and column and zeros elsewhere.

The A_{ON} matrix defines the rotation from the nominal orientation (N-frame) to the offset attitude required to achieve a torque null (O-frame). In general, the required offset angles will be large and vary with altitude. In terms of the offset angles ϕ_0, θ_0, ψ_0 the A_{ON} matrix is

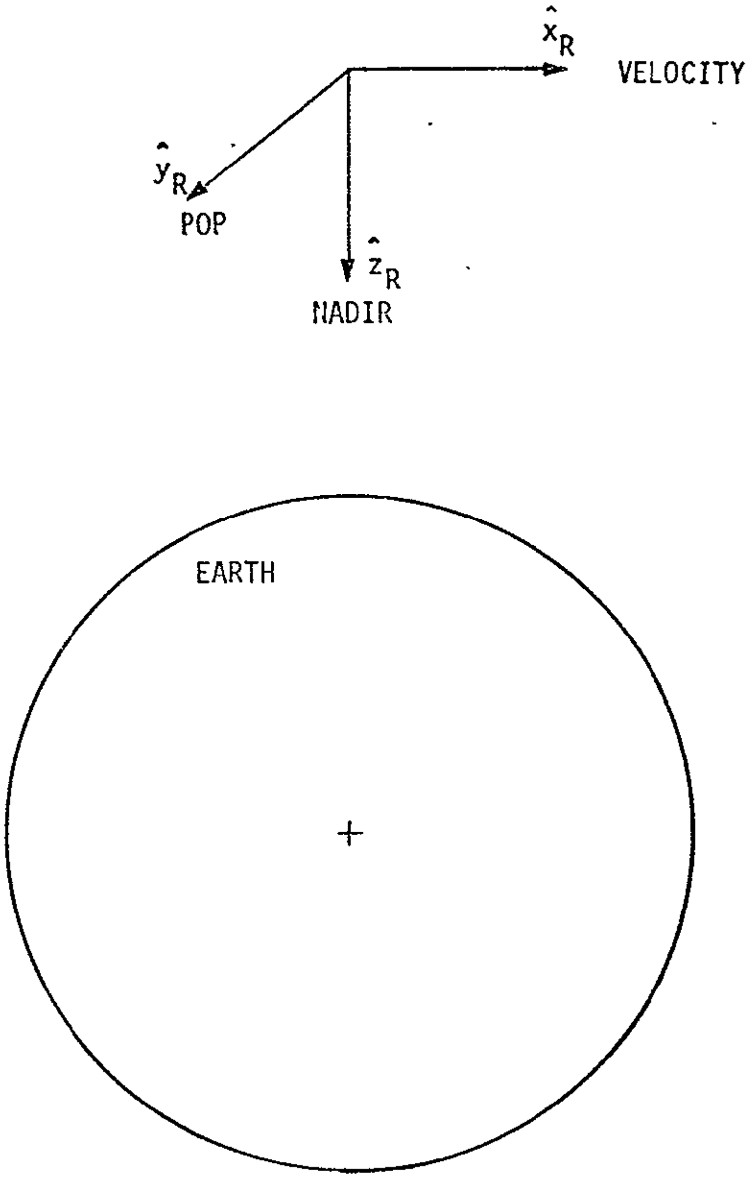

Figure 8-1. Definition of Orbit Reference Axes

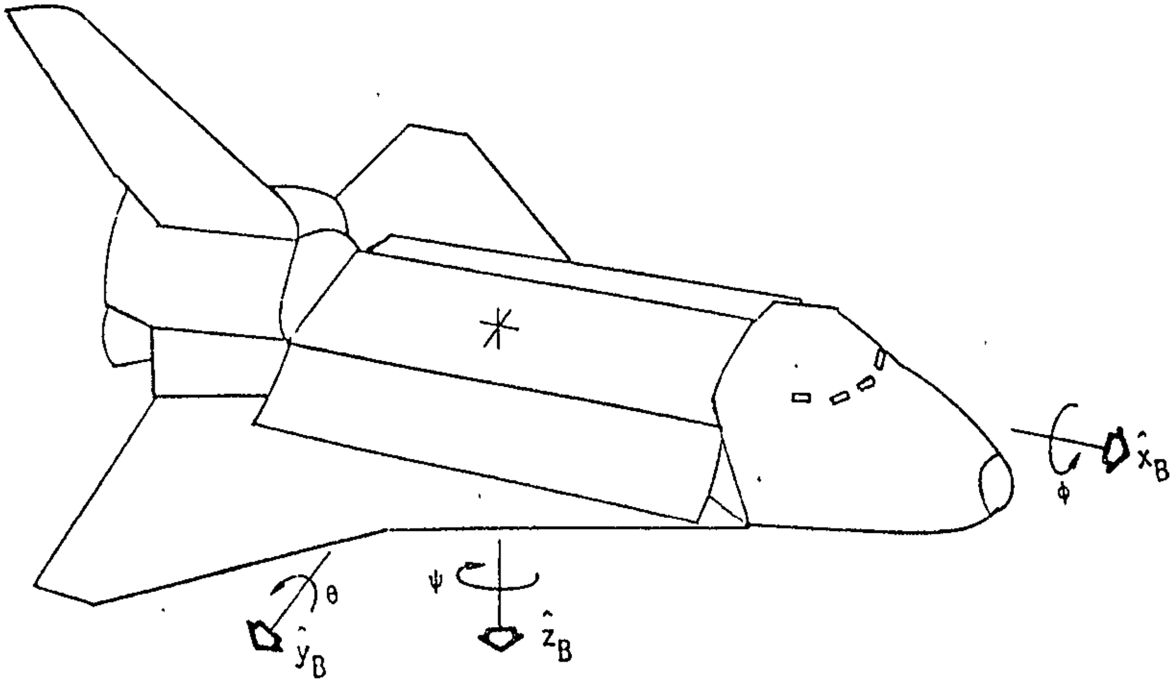

Figure 8-2. Definition of Orbiter Body Axes and Small Angle Rotations

$$A_{ON} = \begin{bmatrix} \cos\psi_0 & \sin\psi_0 & 0 \\ -\sin\psi_0 & \cos\psi_0 & 0 \\ 0 & 0 & 1 \end{bmatrix} \begin{bmatrix} \cos\theta_0 & 0 & -\sin\theta_0 \\ 0 & 1 & 0 \\ \sin\theta_0 & 0 & \cos\theta_0 \end{bmatrix} \begin{bmatrix} 1 & 0 & 0 \\ 0 & \cos\phi_0 & \sin\phi_0 \\ 0 & -\sin\phi_0 & \cos\phi_0 \end{bmatrix} \quad (8\text{-}2)$$

Since the nominal orientations are 90 degrees apart, the maximum total (eigenaxis) offset rotation allowed for A_{ON} is 45 degrees. This condition can be expressed as

$$\mathrm{Tr}\left[A_{ON}\right] \geq 1 + \sqrt{2} \quad (8\text{-}3)$$

where Tr [·] is the sum of the diagonal elements of the matrix. If the disturbance torque $\overline{T}_D$ cannot be made to equal $\overline{0}$ without violating relation (8-3) then a null torque attitude does not exist for the given nominal orientation.

The A_{BO} matrix describes the <u>small angle</u> perturbations of the orbiter body from the null torque attitude, as illustrated in Figure 8-2

$$A_{BO} = \begin{bmatrix} 1 & \psi & -\theta \\ -\psi & 1 & \phi \\ \theta & -\phi & 1 \end{bmatrix}$$

This matrix is used for stability analysis.

8.1.2 Potential Earth Viewing Orientations

The potential earth viewing orientations considered in this study are listed in Table 8-1 and illustrated in Figures 8-3 to 8-8. The orientations consist of all combinations of orbiter rotations, in multiples of 90 degrees, that satisfy both of the following conditions

- some part of the earth's surface is visible from the payload bay.
- the orbiter "tail" is not between the payload bay and the earth.

Each orientation is categorized by an alphanumeric "orientation number". The six possible combinations of axes perpendicular to the orbit plane (POP) and to nadir are denoted by the numerical part, as indicated in Table 8-1. The axis to nadir determines the gravity gradient properties. The letter suffix distinguishes the two possible orientations the orbiter may have with respect to its orbit velocity, with given axes POP and to nadir, as follows

- A = payload bay "forward"
- B = payload bay "back"
- C = orbiter nose "forward"
- D = orbiter tail "forward"

The axis along the velocity influences the orbiter aerodynamic properties. The orbiter $\hat{x}_B - \hat{z}_B$ plane is a plane of symmetry, and therefore no distinction need be made between the $\pm \hat{y}_B$ axes in defining the orientations.

Table 8-1. Definition of Potential Earth Viewing Orientations

Orientation Number	Axis POP*	Axis to Nadir	Axis Along Velocity
1A	$\hat{x}_B$	$\pm \hat{y}_B$ (wing "down")	$- \hat{z}_B$ (bay "forward")
1B			$\hat{z}_B$ (bay "back")
2		$- \hat{z}_B$ (bay "down")	$\pm \hat{y}_B$ (wing "forward")
3C	$\hat{y}_B$	$- \hat{z}_B$ (bay "down")	$\hat{x}_B$ (nose "forward")
3D			$- \hat{x}_B$ (tail "forward")
4A		$\hat{x}_B$ (nose "down")	$- \hat{z}_B$ (bay "forward")
4B			$\hat{z}_B$ (bay "back")
5	$\hat{z}_B$	$\hat{x}_B$ (nose "down")	$\pm \hat{y}_B$ (wing "forward")
6C		$\pm \hat{y}_B$ (wing "down")	$\hat{x}_B$ (nose "forward")
6D			$- \hat{x}_B$ (tail "forward")

* POP = Perpendicular to orbit plane.

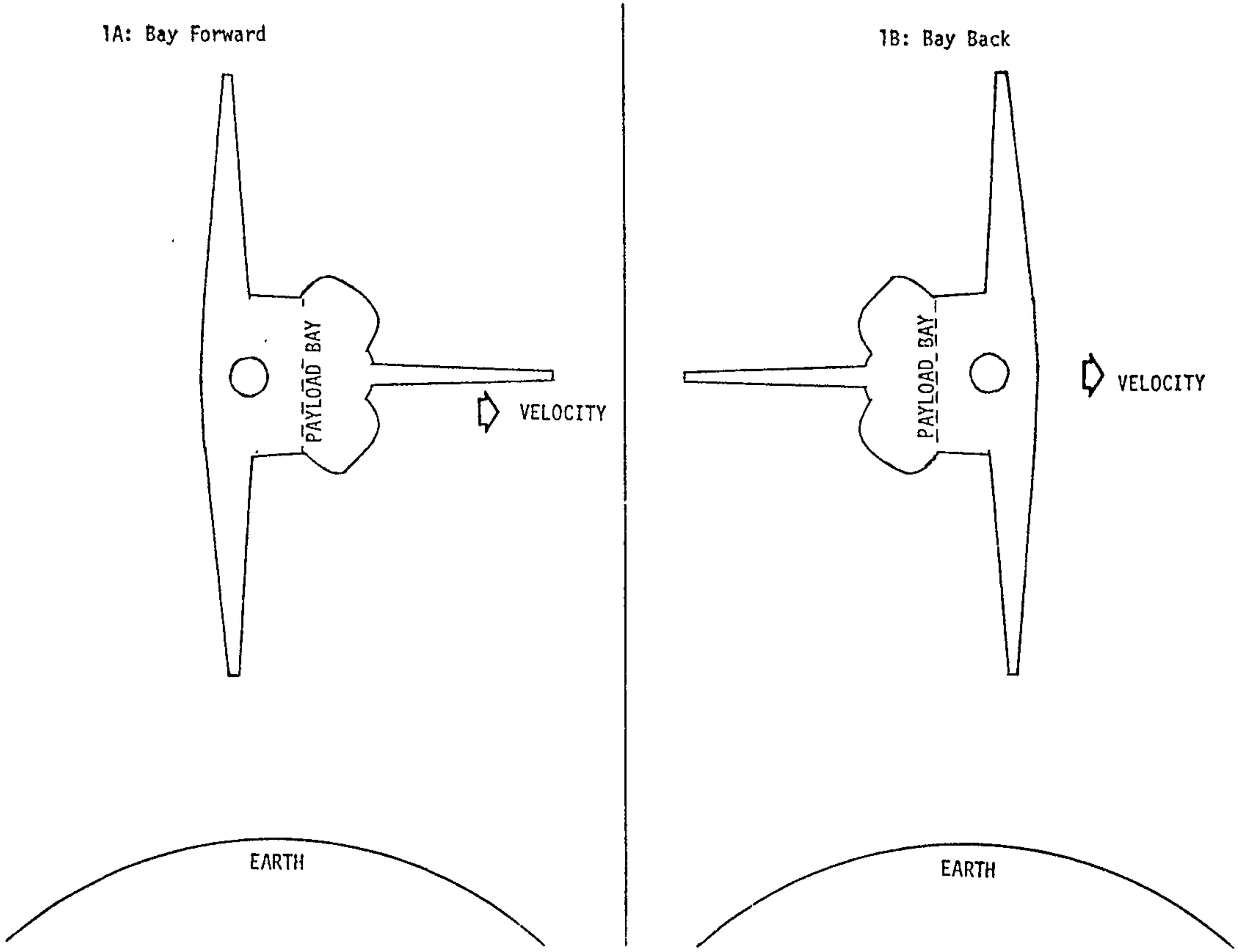

Figure 8-3. Orientation 1 - XPOP, Wing Down

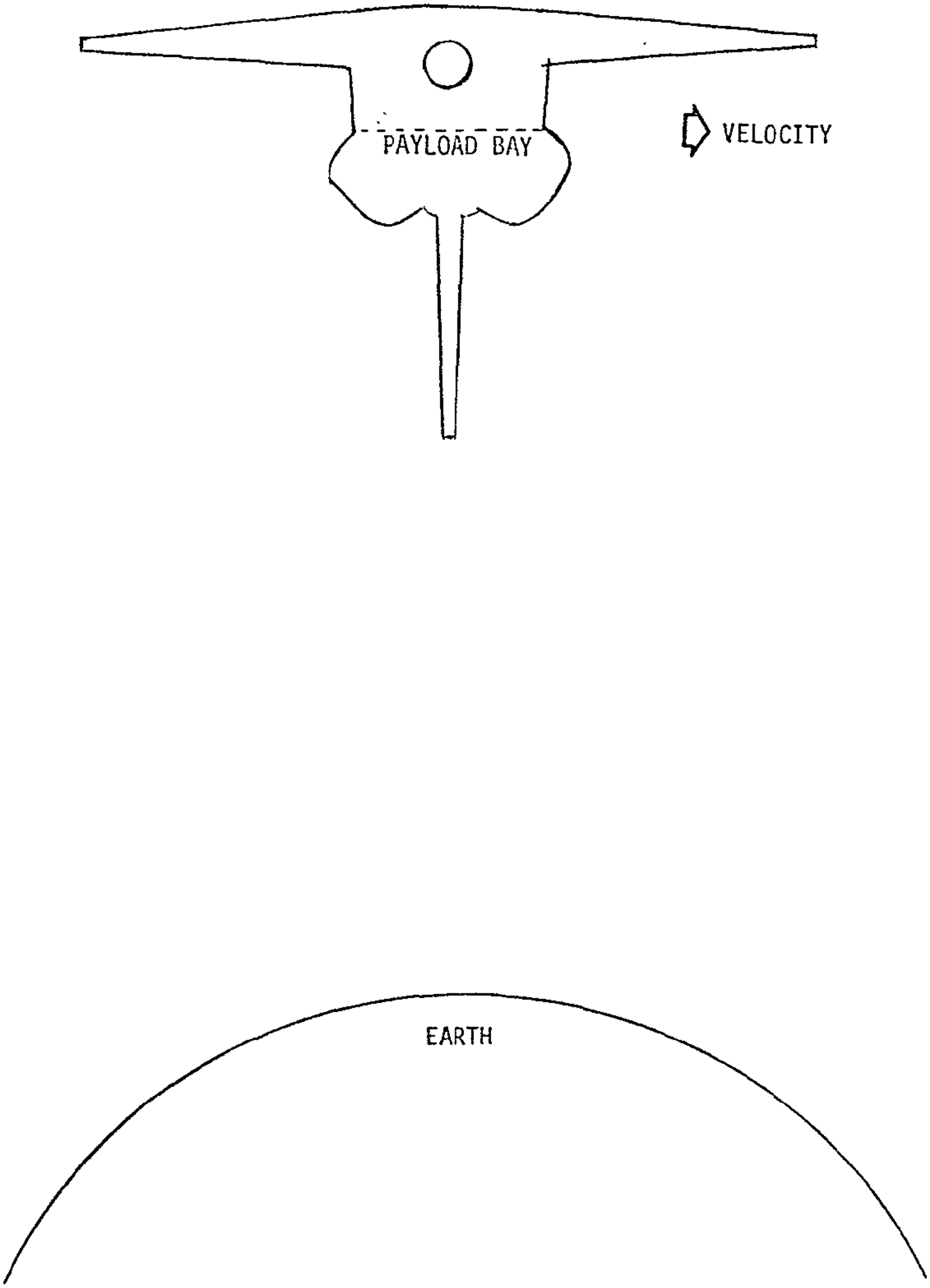

Figure 8-4. Orientation 2 - XPOP, Bay Down

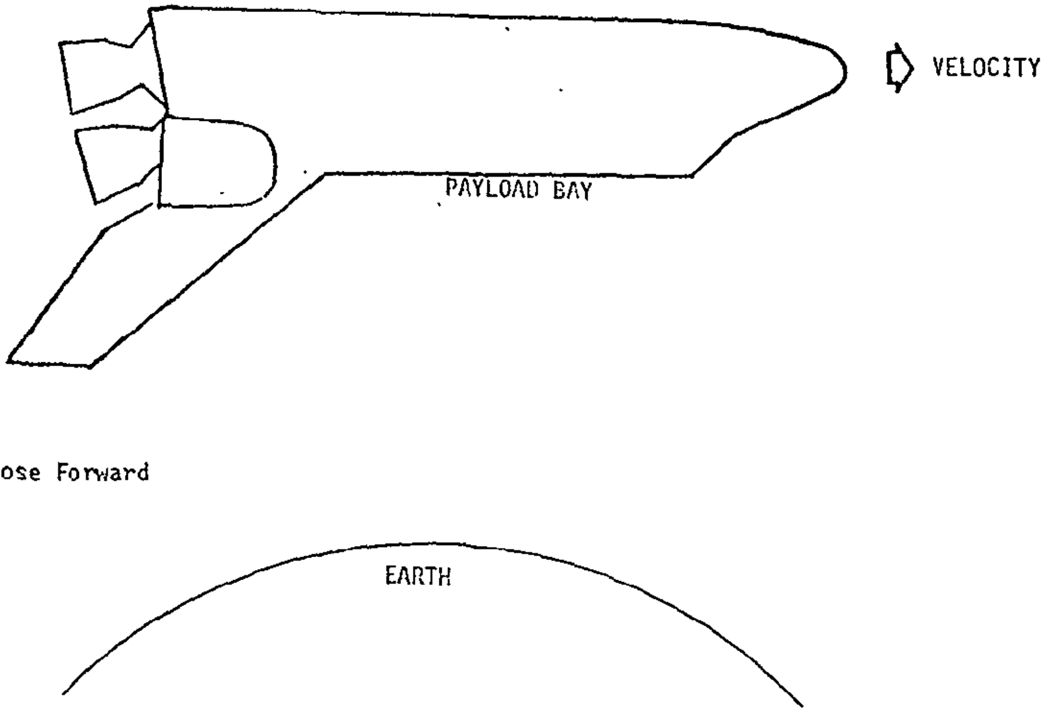

3C: Nose Forward

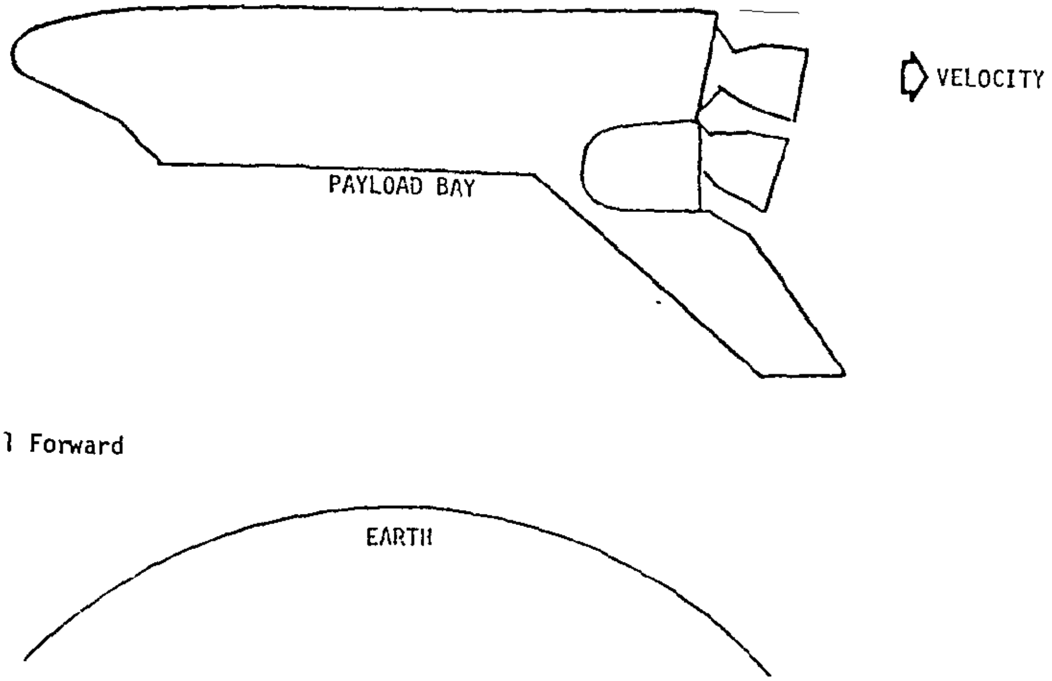

3D: Tail Forward

Figure 8-5. Orientation 3 - YPOP, Bay Down

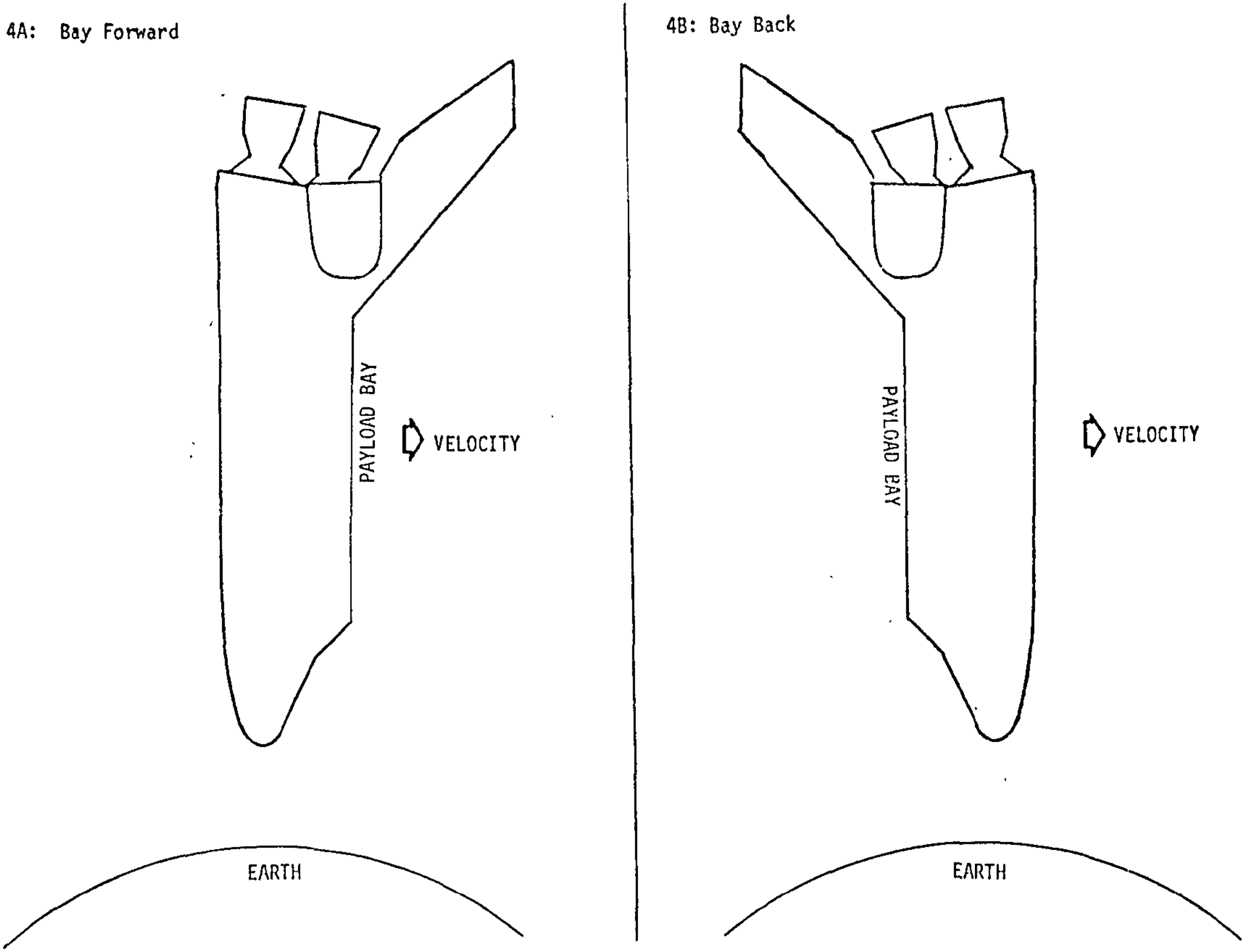
4A: Bay Forward

4B: Bay Back

Figure 8-6. Orientation 4 - YPOP, Nose Down

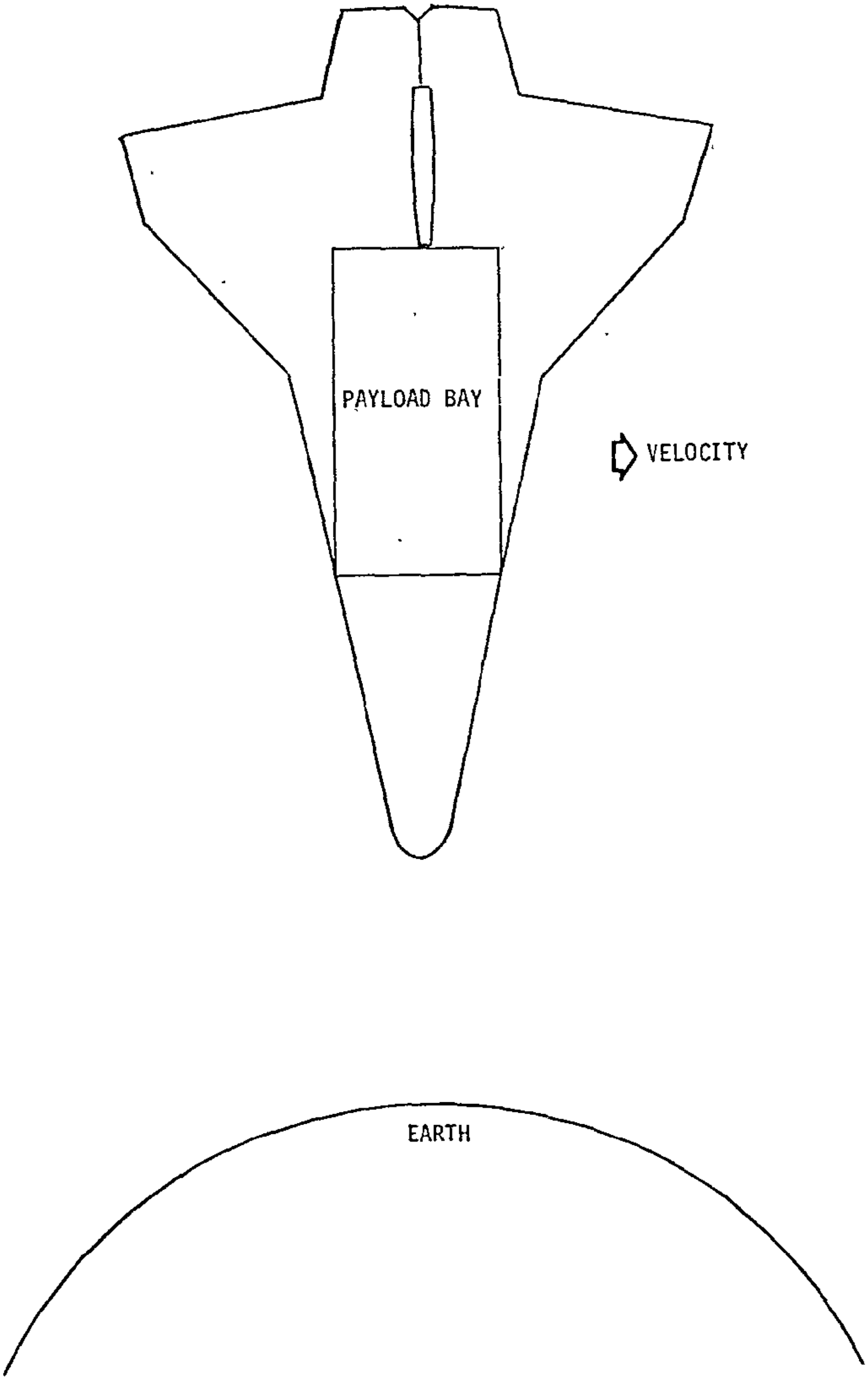

Figure 8-7. Orientation 5 - ZPOP, Nose Down

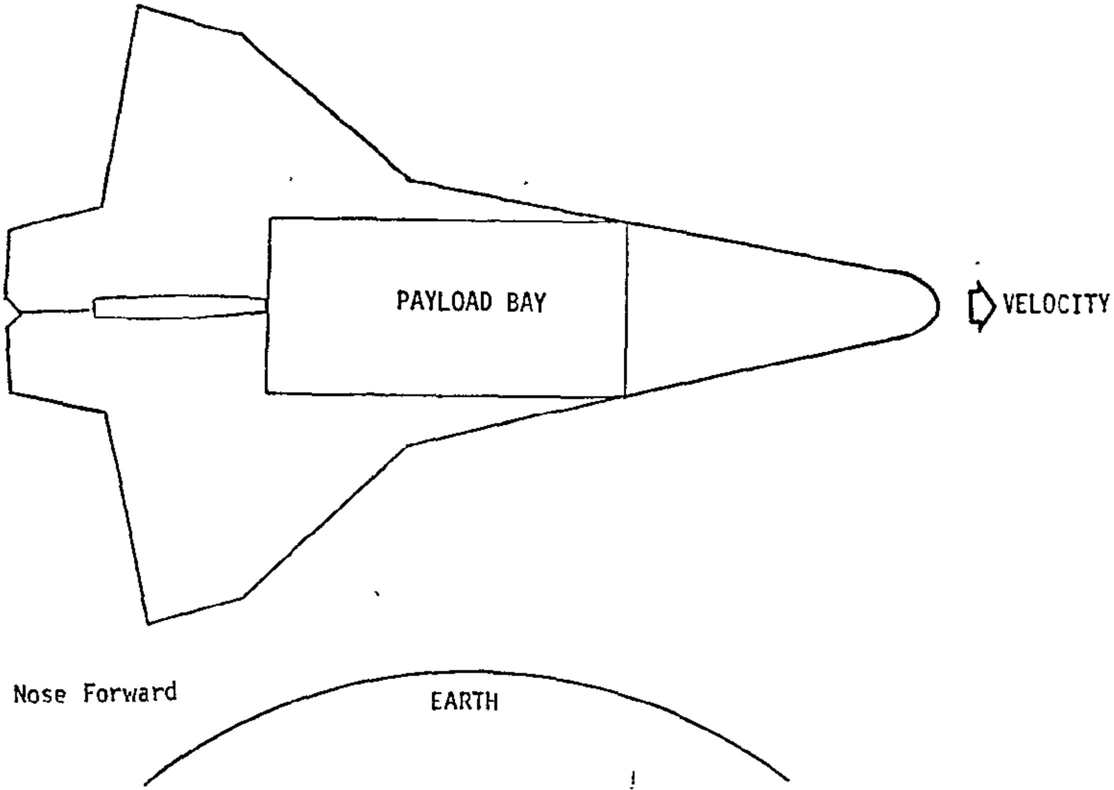

6C: Nose Forward

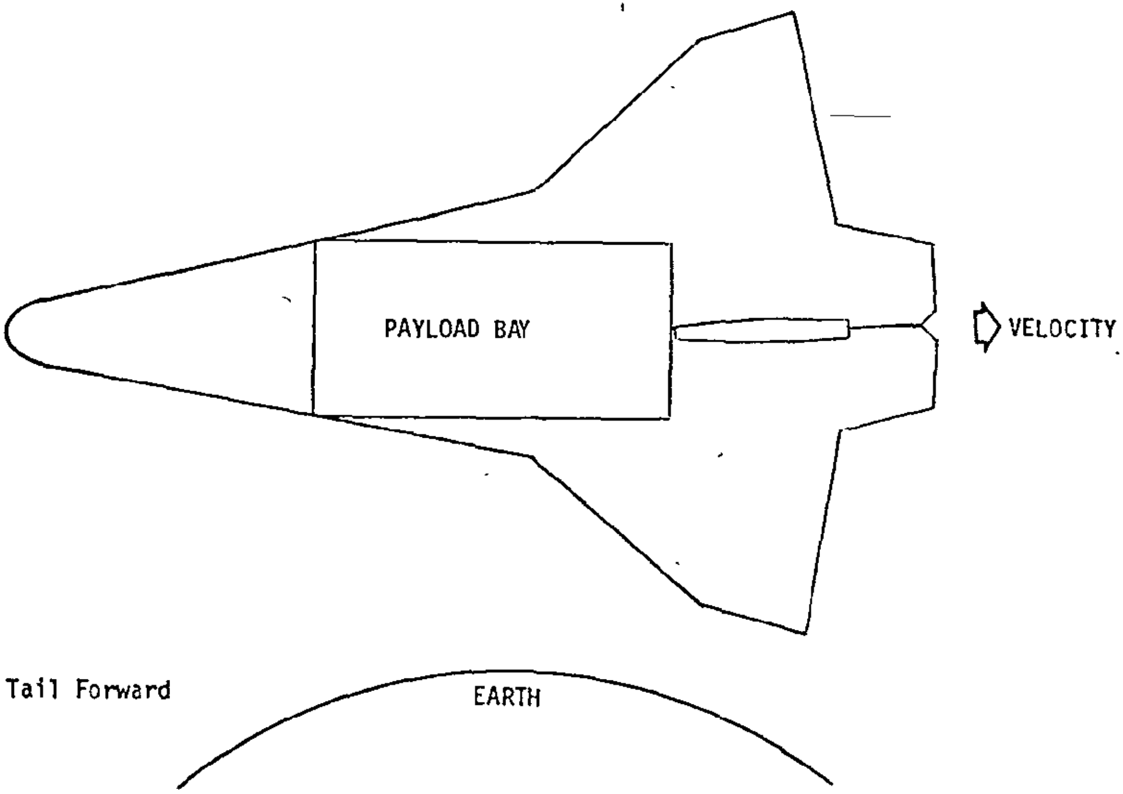

6D: Tail Forward

Figure 8-8. Orientation 6 - ZPOP, Wing Down

8.2 DISTURBANCE TORQUES

A null torque attitude is, by definition, one at which the total external disturbance torque is zero

$$\bar{T} = \bar{T}_A + \bar{T}_G + \bar{T}_S + \bar{T}_M = \bar{0} \tag{8-4}$$

where the four external disturbance torques acting on the shuttle orbiter are

- aerodynamics ($\bar{T}_A$)
- gravity gradient ($\bar{T}_G$)
- solar ($\bar{T}_S$)
- residual magnetism ($\bar{T}_M$)

The disturbance torque models adopted for this study are discussed in detail in Appendix D, and only the major results will be summarized here.

Over the shuttle orbiter altitude range expected for EVAL missions, 150 to 1000 km, the disturbance torques have the following relative importance

- gravity gradient - significant at all altitudes
- aerodynamic - largest disturbance below 200 km, negligible above 400 km
- residual magnetism - somewhat uncertain, but estimated to be at least an order of magnitude less than gravity gradient and aerodynamic torques
- solar pressure - negligible at all altitudes

The residual magnetism and solar pressure torques can be safely neflected in this preliminary study on the ground that the mission-to-mission variation in the gravity gradient and aerodynamic torques exceed the neglected terms. Orbiter fuel and payload variations result in changes in the orbiter inertias and CG location. The inertia variations, in particular the products of inertia, influence the gravity gradient torques while CG shifts affect the aerodynamic moment coefficients. An even greater uncertainty in the aerodynamic torques is produced by the large (i.e., factor of 5 or more) variation in dynamic pressure at a given altitude due to envirionmental factors. The nominal parameter values used in this study are the best estimates currently available and are believed to be sufficiently representative to allow a valid comparison of the candidate null torque orientations.

8.3 NULL TORQUE ATTITUDES AND SENSITIVITIES

At altitudes above 400 km, gravity gradient torque is the only significant external disturbance, and with the assumed zero products of inertia, all of the proposed nominal orientations are gravity gradient null attitudes with zero offset angles. Table 8-2, based on Table D-2, summarizes the gravity gradient stability properties of the candidate orientations. All except orientations 4 and 5 (orbiter nose "down") are unstable for small perturbations from the null attitude, however, unless a control system is used. In particular, the orientations with the most favorable fields of view towards the earth, orientations 2 and 3, are unstable in both roll and pitch, with sensitivities of 1.32 N-m/rad = 0.023 N-m/deg in roll and 33.9 N-m/rad = 0.59 N-m/deg in pitch. Even orientations 4 and 5 may possess long term instabilities when the complete nonlinear coupled dynamics/kinematics are considered along with the residual aerodynamic, solar and magnetic disturbance torques (Reference 6). As an example, the destabilizing effect of periodic atmospheric density variations on orientation 4 is discussed in Section 8.4.

Table 8-2. Gravity Gradient Stability Summary

Orientation Number	Attitude		Gravity Gradient Stability*		
	Axis POP	Axis to Nadir	In Orbit Plane	Out of Orbit Plane	Both
1	$\hat{x}_B$	$\hat{y}_B$	S	U	U
2		$\hat{z}_B$	U	U	U
3	$\hat{y}_B$	$\hat{z}_B$	U	U	U
4		$\hat{x}_B$	S	S	S
5	$\hat{z}_B$	$\hat{x}_B$	S	S	S
6		$\hat{y}_B$	U	S	U

* S = STABLE
U = UNSTABLE

As the orbiter altitude is decreased, the aerodynamic torque increases rapidly, and the null torque attitudes become offset from the nominal orientations. Indeed, in many cases no null torque attitude exists "near" (i.e., within a 45 degree eigenaxis rotation) the nominal orientation. By definition, a null torque attitude is one for which

$$\bar{T}(A_{OR}) = \bar{T}(A_{ON}\ A_{NR}) = \bar{0} \qquad (8\text{-}5)$$

where

$\bar{T}$ = $\bar{T}_A + \bar{T}_G$ = total disturbance torque

$\bar{T}_A$ = aerodynamic disturbance torque

$\bar{T}_G$ = gravity gradient disturbance torque

A_{NR} = nominal orientation direction cosine matrix

A_{ON} = A_{ON} $(\phi_o, \theta_o, \psi_o)$ = null offset direction cosine matrix

ϕ_o, θ_o, ψ_o = offset angles

Equation (8-5), when expanded with equations (8-2), (D-4), (D-10), (D-11), and (D-17), is a nonlinear function of the unknowns ϕ_o, θ_o, and ψ_o and involves the tabulated aerodynamic moment coefficients C_ℓ, C_m, and C_n. In general, numerical search techniques must be used to find the null attitude, if it exists, as a function of altitude.

The sensitivity of the disturbance torque to incremental attitude perturbations from the null torque attitude can be expressed by the matrix of partial derivatives.

$$\frac{\partial \overline{T}}{\partial \overline{\delta}} = \left. \begin{bmatrix} \partial T_x/\partial \phi & \partial T_x/\partial \theta & \partial T_x/\partial \psi \\ \partial T_y/\partial \phi & \partial T_y/\partial \theta & \partial T_y/\partial \psi \\ \partial T_z/\partial \phi & \partial T_z/\partial \theta & \partial T_z/\partial \psi \end{bmatrix} \right|_{A_{BR} = A_{OR}} \qquad (8\text{-}6)$$

The partials are evaluated at the null torque attitude. The negative of the above matrix has the form of a compliance or spring matrix, with the usual convention that a positive spring constant K indicates a restoring torque

$$-\frac{\partial \overline{T}}{\partial \overline{\delta}} = K = \begin{bmatrix} K_{x\phi} & K_{x\theta} & K_{x\psi} \\ K_{y\phi} & K_{y\theta} & K_{y\psi} \\ K_{z\phi} & K_{z\theta} & K_{z\psi} \end{bmatrix} \qquad (8\text{-}7)$$

The K matrix can be used in deriving the incremental equations of motion about the null torque attitude. This will be deferred until the next phase of the study. Instead, attention will be focused here on the diagonal elements of K to obtain estimates of the comparative sensitivity of the proposed orientations.

Since the gravity gradient torques are analytical functions, the required sensitivity partials are straightforward. For example

$$T_{Gx} = 3\omega_0^2 \, (I_{zz} - I_{yy}) \, a_{23} \, a_{33}$$

and therefore

$$\frac{\partial T_{Gx}}{\partial \phi} = 3\omega_0^2 \, (I_{zz} - I_{yy})(a_{23}\frac{\partial a_{33}}{\partial \phi} + \frac{\partial a_{23}}{\partial \phi} a_{33})\Bigg|_{A_{BR} = A_{OR}}$$

The aerodynamic torques, on the other hand, are functions of the tabulated moment coefficients C_ℓ, C_m and C_n. For example

$$T_{Ax} = q \, S \, b \, C_\ell(\alpha, \beta)$$

and therefore

$$\frac{\partial T_{Ax}}{\partial \phi} = q \, S \, b \left(\frac{\partial \, C_\ell(\alpha,\beta)}{\partial \alpha} \cdot \frac{d\alpha}{d\phi} + \frac{\partial C_\ell(\alpha, \beta)}{\partial \beta} \frac{d\beta}{d\phi} \right)\Bigg|_{A_{BR} = A_{OR}}$$

The required partials of the moment coefficients are obtained by fitting the tabulated data over a rectangular region with corners (α_0, β_0), (α_0, β_1), (α_1, β_0), (α_1, β_1) with the interpolation function

$$C(\alpha, \beta) \approx c_0 + c_\alpha \, (\alpha - \alpha_0) + c_\beta \, (\beta - \beta_0) + c_{\alpha\beta}(\alpha - \alpha_0) \cdot (\beta - \beta_0) \qquad (8\text{-}8)$$

where

$$c_0 = C(\alpha_0, \beta_0) \tag{8-9}$$

$$c_\alpha = \frac{C(\alpha_1, \beta_0) - C(\alpha_0, \beta_0)}{(\alpha_1 - \alpha_0)} \tag{8-10}$$

$$c_\beta = \frac{C(\alpha_0, \beta_1) - C(\alpha_0, \beta_0)}{(\beta_1 - \beta_0)} \tag{8-11}$$

$$c_{\alpha\beta} = \frac{C(\alpha_1, \beta_1) + C(\alpha_0, \beta_0) - C(\alpha_0, \beta_1) - C(\alpha_1, \beta_0)}{(\alpha_1 - \alpha_0)(\beta_1 - \beta_0)} \tag{8-12}$$

and $C(\alpha_0, \beta_0)$, $C(\alpha_0, \beta_1)$, $C(\alpha_1, \beta_0)$, $C(\alpha_1, \beta_1)$ are tabulated data points. This interpolation function is also used in computing the null torque attitudes. The partials of the moment coefficients are then simply

$$\frac{\partial C(\alpha, \beta)}{\partial \alpha} = c_\alpha + c_{\alpha\beta}\,(\beta - \beta_0) \tag{8-13}$$

$$\frac{\partial C(\alpha, \beta)}{\partial \beta} = c_\beta + c_{\alpha\beta}(\alpha - \alpha_0) \tag{8-14}$$

In the following subsections each potential orientation is discussed in turn. Only the more promising and generally applicable orientations are analyzed in depth. Conclusions are contained in Section 8.3.7.

8.3.1 Orientation 1

Orientation 1 (Figure 8-3) has one of the orbiter wings "down" and the payload bay either along (1A) or opposite (1B) the velocity vector. In general, no null torque attitude exists near this orientation, due to the imbalance between the aerodynamic and gravity gradient torques about the $\hat{y}_B$ axis. For small offsets from the nominal orientation

$$T_y = 33.92\, \phi_o\, \psi_o + q\, S\, \bar{c}\, C_m\, (\theta_o \mp \frac{\pi}{2}, \mp \phi_o)$$

where the top set of signs applies to 1A and the lower to 1B. At an altitude of 200 km, for example, $q\, S\, \bar{c} \simeq 30$ N-m. For the range of offsets $|\theta_o| \leq 10$ degrees, $|\phi_o| \leq 15$ degrees the moment coefficient C_m is in the range for orientation 1A

$$-0.31 \leq C_m \leq -0.18$$

and for orientation 1B

$$0.22 \leq C_m \leq 0.34$$

The magnitude of aerodynamic torque about $\hat{y}_B$ is thus at least 5.4 N-m, while there is no first order gravity gradient torque for cancellation.

8.3.2 Orientation 2

Orientation 2 has one of the wings along the velocity vector and the payload bay pointing towards nadir. Again, no null torque attitude exists in general because of torque imbalances about the $\hat{x}_B$ and $\hat{z}_B$ axes. The asymmetry of the orbiter with respect to the airflow in this orientation (mainly due to the vertical stabilizer) results in large aerodynamic torques around the axes ($\hat{x}_B$ and $\hat{z}_B$) that have the smallest gravity gradient torques in this orientation.

8.3.3 Orientation 3

Orientation 3 has the payload bay pointing "down" and either the orbiter nose (3C) or tail (3D) along the velocity. Since the orbiter is aerodynamically symmetric about the airflow in this orientation, $C_\ell = C_n = 0$ and the only offset required for a torque null is about y_B. The required offset angle θ_o is plotted in Figure 8-9 for orientation 3C and in Figure 8-10 for orientation 3D. The primary abcissa scale is the aerodynamic constant $q\ S\ \bar{c}$, because this is the actual parameter that influences the offset angle. The nominal altitude corresponding to the aerodynamic constant is also indicated, but it should be recalled that wide variations in q at a given altitude occur in practice.

Also shown on Figure 8-9 and 8-10 are the torque "compliance"

$$K_{y\theta} = -\frac{\partial T_y}{\partial \theta}$$

In both cases, $K_{y\theta} < 0$, and the orbiter is unstable in pitch. Orientation 3C is less unstable than orientation 3D, however, at low altitudes because the slope of the aerodynamic torque tends to oppose rather than add to the slope of the destabilizing gravity gradient torque. Orientation 3C is therefore preferable to orientation 3D. Table 8-3 summarizes the torque compliances for small perturbation from the null torque attitude of orientation 3C. Only the yaw axis has a restoring torque. Roll and pitch are unstable at all altitudes and a control system is therefore essential to remain near the null torque attitude.

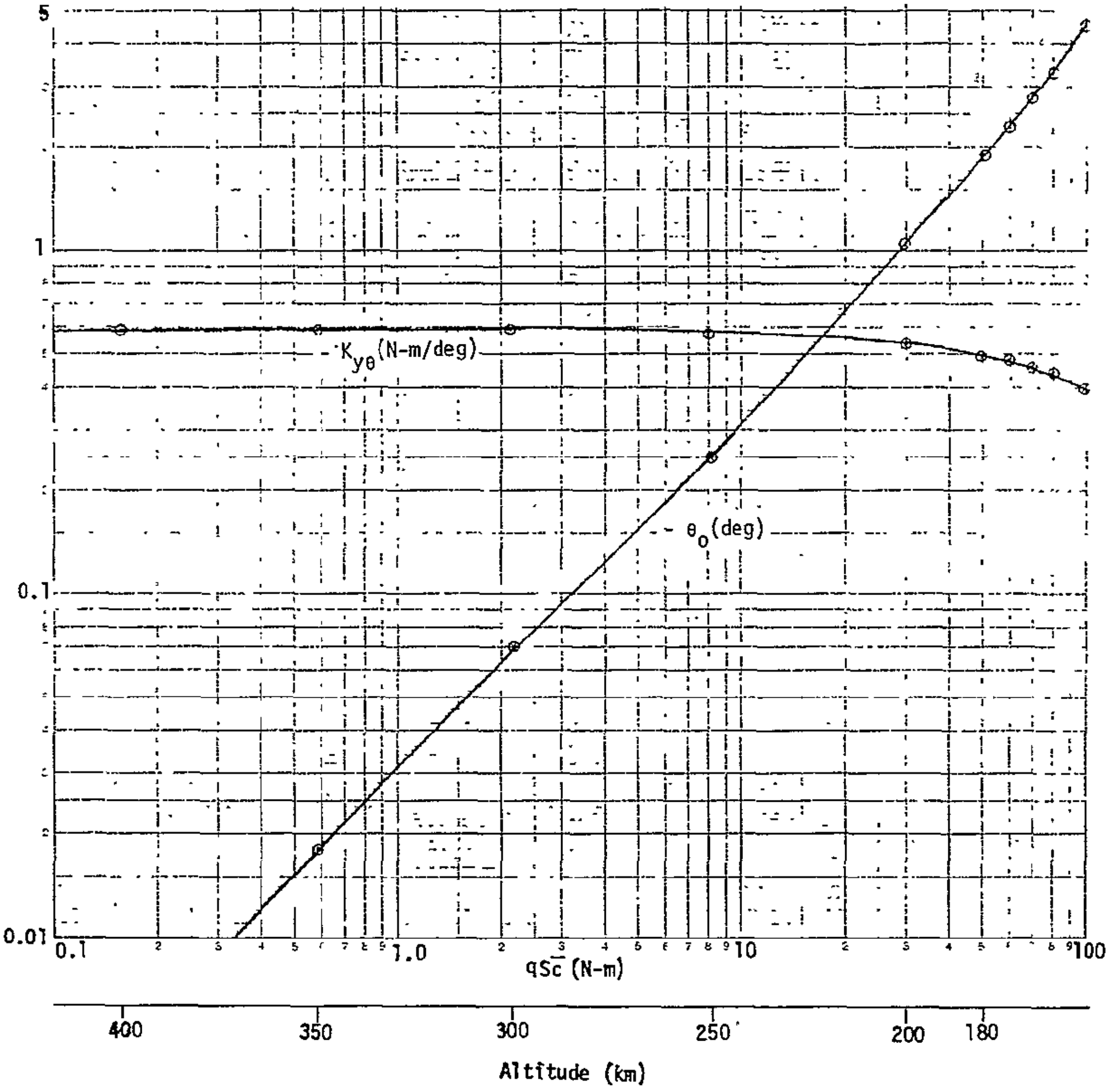

Figure 8-9. Pitch Offset and Sensitivity for Orientation 3C

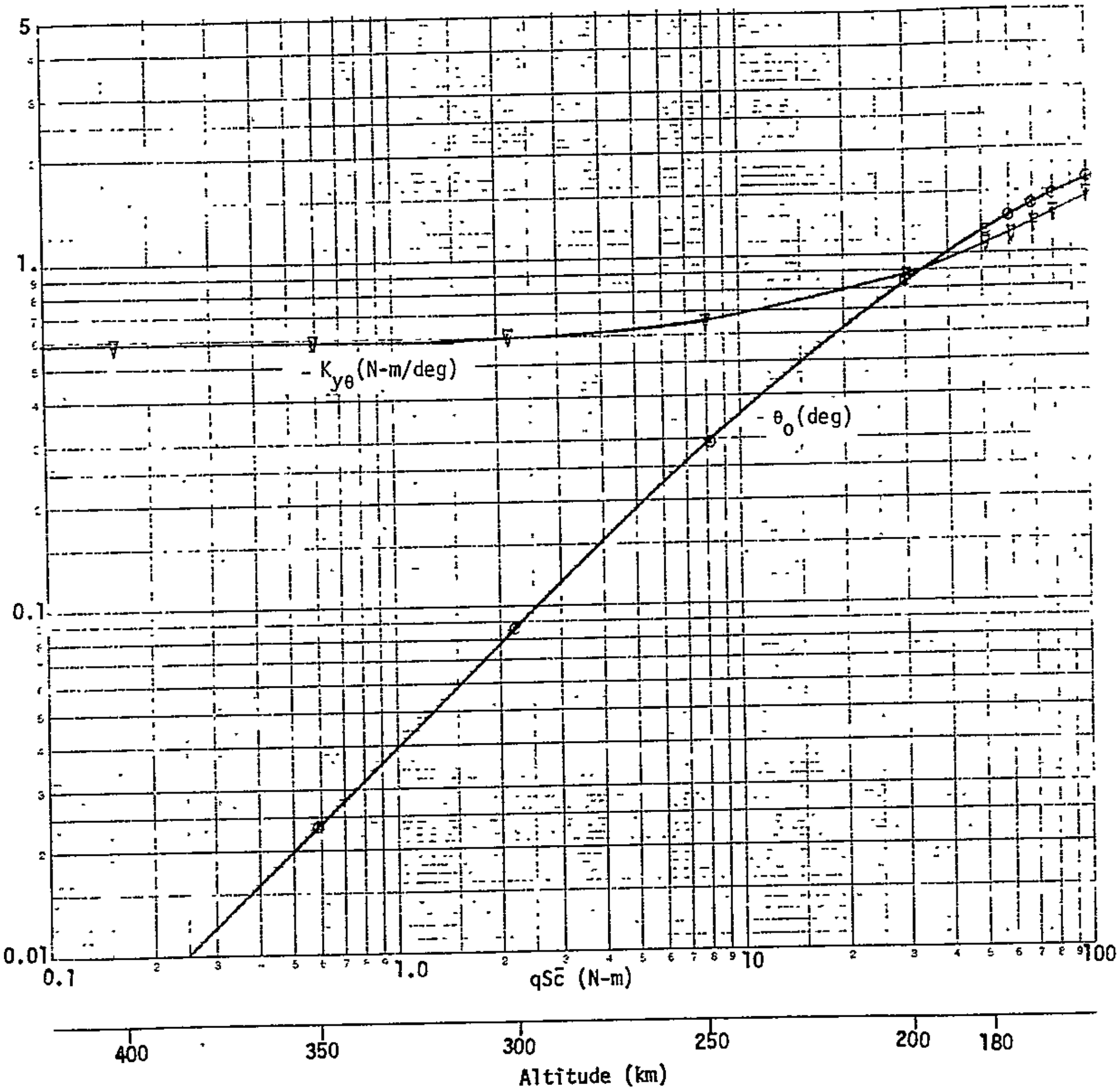

Figure 8-10. Pitch Offset and Sensitivity for Orientation 3D

Table 8-3. Torque Compliances for Orientation 3C

Attitude (km)	Torque Compliances (N-m/deg)								
	$K_{x\phi}$	$K_{x\theta}$	$K_{x\psi}$	$K_{y\phi}$	$K_{y\theta}$	$K_{y\psi}$	$K_{z\phi}$	$K_{z\theta}$	$K_{z\psi}$
180	-0.023	0	-0.047	0	-0.50	0	-0.019	0	0.22
200	-0.023	0	-0.029	0	-0.54	0	-0.0099	0	0.13
250	-0.023	0	-0.0082	0	-0.58	0	-0.0025	0	0.036
300	-0.023	0	-0.0022	0	-0.59	0	-0.0007	0	0.0097

8.3.4 Orientation 4

Orientation 4 has the orbiter nose "down" and the payload bay either along (4A) or opposed (4B) to the velocity vector. As with orientation 3, only a pitch offset is required to achieve a null torque attitude. The required offsets are plotted in Figures 8-11 and 8-12. It is obvious that much larger offsets are required as compared to orientation 3. In fact, the offset angle for orientation 4B exceeds 45 degrees for altitudes below 180 km. This is not necessarily a disadvantage, however, because the offset tilts the payload bay towards the earth, increasing its usable field of view for EVAL. The low altitude null attitudes of orientation 4A, on the other hand, tilt the payload bay away from the earth and are generally unusable for EVAL.

Figure 8-12 also shows that the pitch torque compliance $K_{y\theta}$ is positive and therefore pitch is incrementally stable around the null. The compliance decreases rapidly at low altitude, changing sign for an offset angle of approximately $\theta_0 \simeq 60$ degrees. Because of the variability of q with environmental factors, it would be risky to assume stability at altitudes below 200 km.

Table 8-4 summarizes the torque compliances for orientation 4B. It is clear from the table that the large offsets caused by the aerodynamic torques at low altitudes has a destabilizing effect on the system and that active control is required to stay near the torque null.

8.3.5 Orientation 5

Orientation 5 has the orbiter nose "down" and one of the wings in the direction of the velocity vector. There is, in general, no

ORIGINAL PAGE IS
OF POOR QUALITY

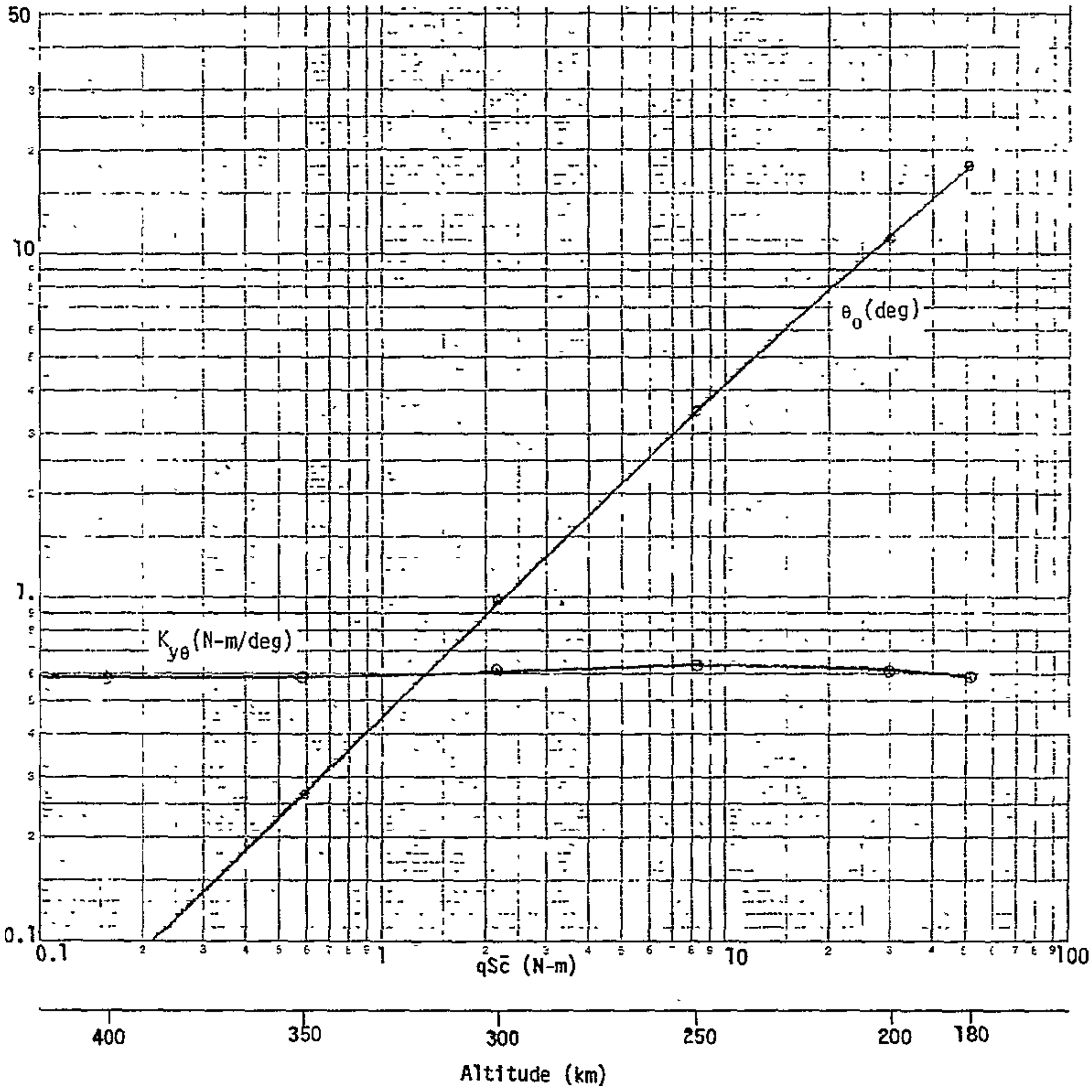

Figure 8-11. Pitch Offset and Sensitivity for Orientation 4A

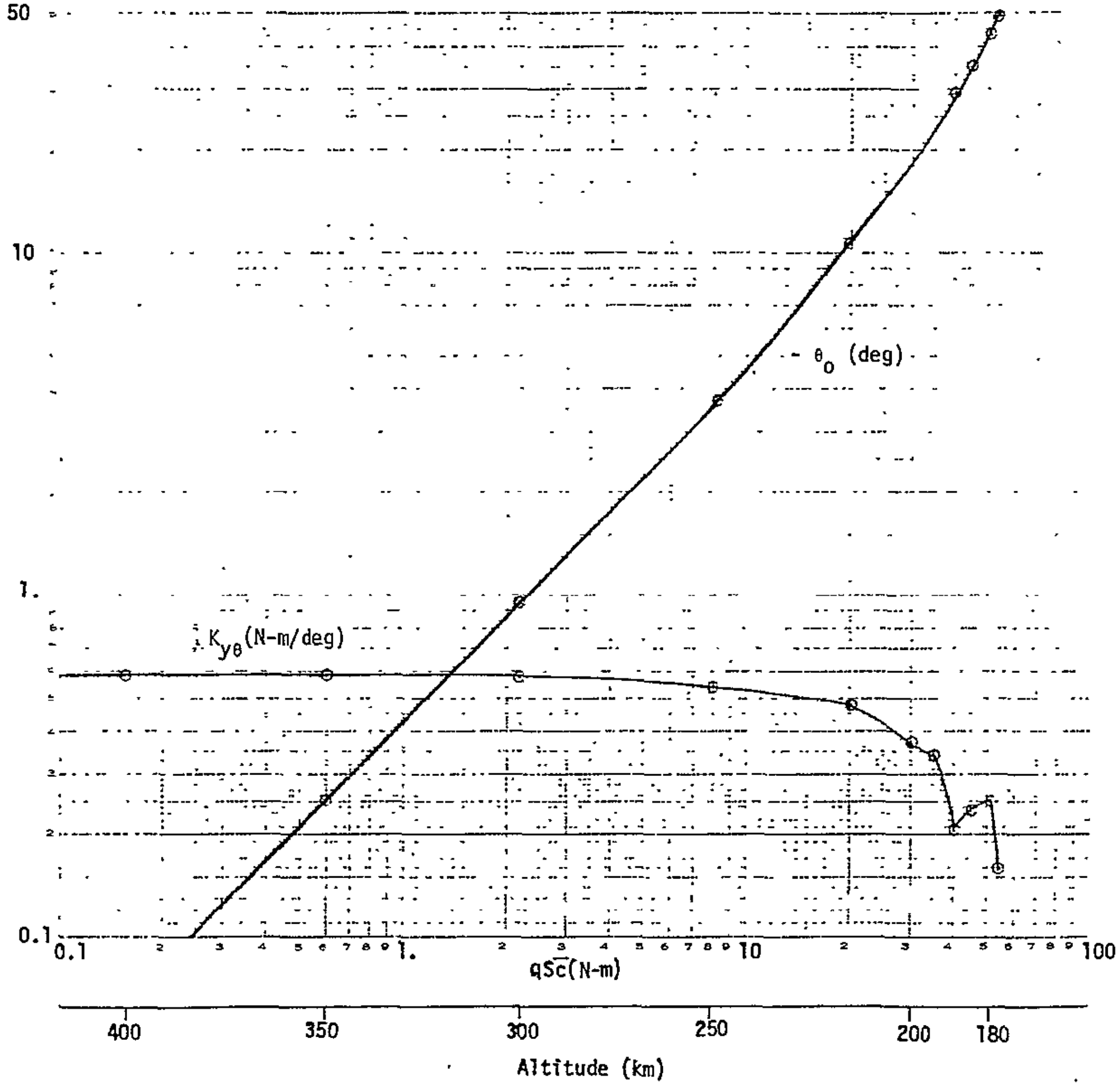

Figure 8-12. Pitch Offset and Sensitivity for Orientation 4B

Table 8-4. Torque Compliances for Orientation 4B

Altitude (Km)	Torque Compliances (N-m/deg)								
	$K_{x\phi}$	$K_{x\theta}$	$K_{x\psi}$	$K_{y\phi}$	$K_{y\theta}$	$K_{y\psi}$	$K_{z\phi}$	$K_{z\theta}$	$K_{z\psi}$
180	-0.079	0	0.054	0	0.25	0	0.083	0	0.49
200	-0.095	0	0.024	0	0.37	0	0.037	0	0.56
250	-0.028	0	0.0003	0	0.55	0	0.0011	0	0.57
300	-0.0076	0	-0.0003	0	0.58	0	-0.0002	0	0.57

null torque attitude near this orientation because there is no first order gravity gradient torque about $\hat{x}_B$ to oppose the large aerodynamic torque about this axis caused by the vertical stabilizer.

8.3.6 Orientation 6

This orientation has a wing pointing towards nadir and either the nose (6C) or tail (6D) directed along the velocity. For this orientation there is no first order gravity gradient torque to cancel the aerodynamic torque about $\hat{y}_B$. The aerodynamic torque about $\hat{y}_B$ is relatively small however and a torque null about $\hat{y}_B$ may exist for some combination of offset angles. It is extremely unlikely, however, that nulls will exist about the three axes simultaneously. Besides, the null, if it exists, is certain to be unstable and this orientation has no particular field of view advantage for EVAL. Further analysis of this orientation cannot therefore be justified.

8.3.7 Conclusions

In general, null torque attitudes exist at the lower altitude range only for those orientations having the orbiter plane of symmetry in the orbit plane. These are the YPOP orientations, namely orientations 3 and 4. Of the two variations of orientation 3, the more favorable is orientation 3C with the orbiter nose "forward" and payload bay "down". This orientation is unstable with a negative pitch "spring constant" $K_{y\theta} \approx -0.6$ N-m/deg, but provides the best view of the earth and has a small and relatively insensitive offset angle. For convenience, orientation 3C will be referred to as the "nose forward" orientation in the sequel.

Of the two variations of orientation 4, only orientation 4B with the orbiter nose nominally "down" and the payload bay nominally "back", allows viewing of the earth limb and a significant portion of the earth's surface at low altitudes. The pitch offset angle for orientation 4B increases rapidly with decreasing altitude, reaching 50 degrees at h = 180 km. However, pitch is incrementally stable and the offset increases the area of the earth visible from the payload bay. The roll axis is unstable with a maximum spring constant $K_{x\phi} \approx 0.1$ N-m/deg and again a fine pointing control system is required to maintain the orbiter near the null attitude. Orientation 4B will be referred to as the "nose down" orientation.

8.4 EFFECT OF ATMOSPHERIC DENSITY VARIATIONS ON ALL TORQUE ATTITUDES

Variations in atmospheric density, at a given altitude, produce variations in the null torque attitude through changes in the aerodynamic disturbance torque. The effect of these density variations on the orbiter motion depends strongly on the frequency content, as can be seen with a linear analysis.

Linearizing the orbiter pitch equation of motion about the nominal null torque offset angle $\bar{\theta}_0$, corresponding to the nominal atmospheric density ρ_0, yields the perturbation equation

$$I_y \, \delta\ddot{\theta} + K_{y\theta} \, \delta\theta = \delta T_{A\rho} \tag{8-15}$$

where

I_y = orbiter pitch inertia

$\delta\theta$ = attitude perturbation from nominal null torque offset angle $\bar{\theta}_0$

$K_{y\theta} = - \left. \frac{\partial T_y}{\partial \theta} \right|_{\theta_0 = \bar{\theta}_0, \, \rho = \rho_0}$ = nominal disturbance torque compliance

$\delta T_{A\rho} = \left. \frac{\partial T_{Ay}}{\partial \rho} \right|_{\theta_0 = \bar{\theta}_0, \, \rho = \rho_0} (\rho - \rho_0)$ = aerodynamic disturbance torque perturbation due to atmospheric density variation

For a sinusoidal atmospheric density variation of magnitude $\Delta\rho$ at frequency ω_ρ,

$$\rho - \rho_0 = \Delta\rho \sin \omega_\rho t \tag{8-16}$$

the magnitude of the orbiter response is for $K_{y\theta} > 0$

$$\left| \frac{\delta\theta}{\delta T_{A\rho}} \right| = \frac{1}{K_{y\theta}} \left[\frac{1}{1 - (\omega_\rho/\omega_\theta)^2} \right] \tag{8-17}$$

and for $K_{y\theta} < 0$

$$\left| \frac{\delta\theta}{\delta T_{A\rho}} \right| = \left| \frac{1}{K_{y\theta}} \right| \left[\frac{1}{1 + (\omega_\rho/\omega_\theta)^2} \right] \tag{8-18}$$

where the orbiter incremental pitch motion natural frequency is

$$\omega_\theta = (|K_{y\theta}|/I_y)^{1/2} \tag{8-19}$$

The normalized responses, $|K_{y\theta}\ \delta\theta/\delta T_{A\rho}|$, are plotted in Figure 8-13 versus the normalized frequency ratio $\omega_\rho/\omega_\theta$ for the two cases.

For frequency ratios far removed from unity, the response is independent of the sign of $K_{y\theta}$. When the atmospheric density variation is at a low frequency compared to ω_θ, the orbiter tends to follow the resulting motion of the null torque attitude. In contrast, the orbiter shows little response to density variations with frequencies that are high compared to ω_θ. For density variations with frequencies near ω_θ, the response depends drastically on the sign of $K_{y\theta}$. If $K_{y\theta} > 0$, as in the nose down orientation, the response shows a sharp resonant peak around $\omega_\rho = \omega_\theta$. Thus, although the nose down orientation is stable in

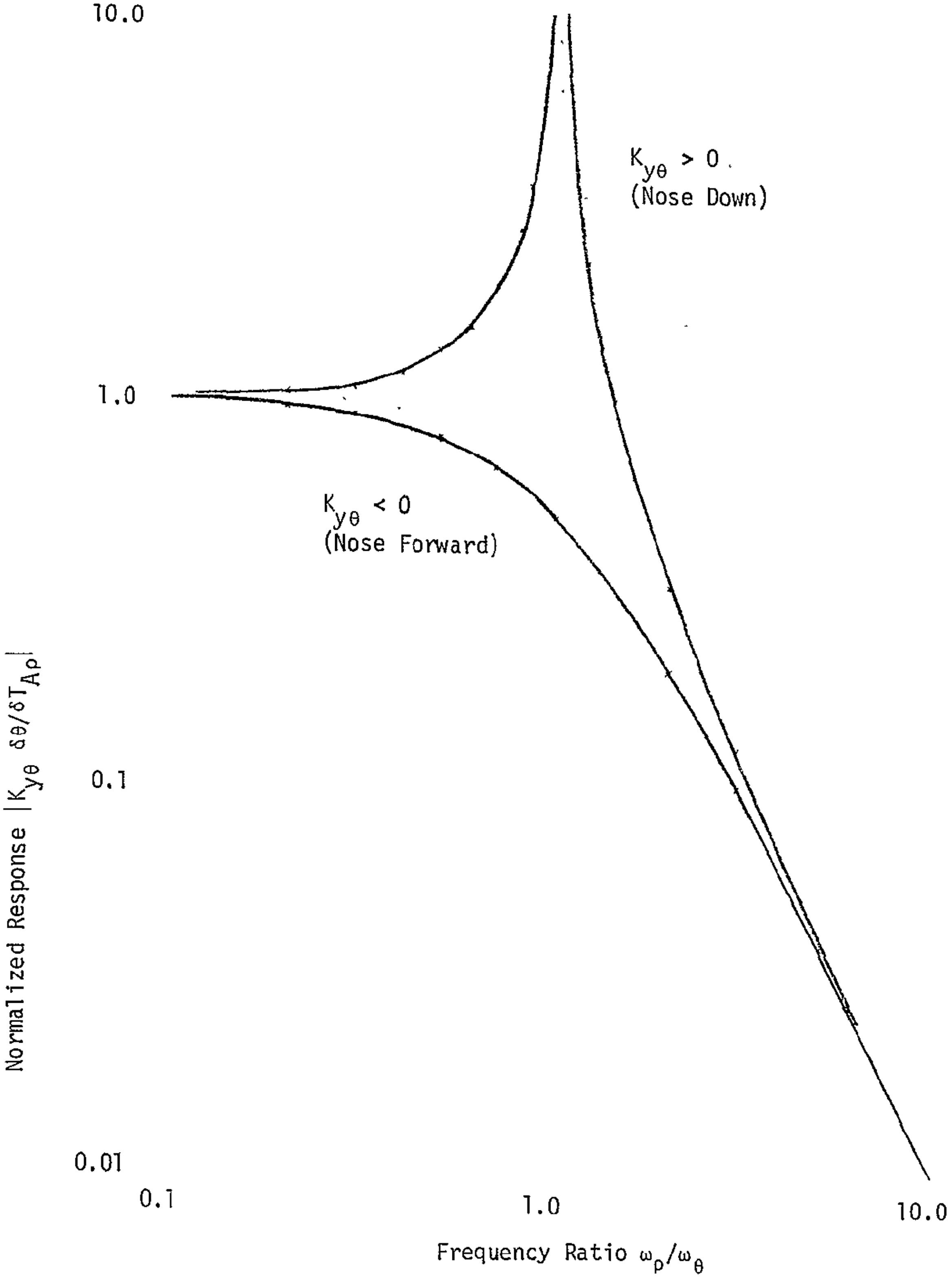

Figure 8-13. Pitch Response of Orbiter to Aerodynamic Disturbance Variation VS Frequency Ratio

pitch in a constant atmospheric density environment, atmospheric density variations at $\omega_\rho = \omega_\theta$ can have a strong destabilizing effect by producing orbiter attitude motions far larger than the change in null torque attitude. On the other hand, if $K_{y\theta} < 0$, as in the nose forward orientation, pitch is unstable regardless of the density variations and density variations at frequencies near ω_θ have no particular additional effect on the system stability properties.

The effect of atmospheric density variations on the orbiter null torque attitude is discussed in quantitative terms in the following subsections.

8.4.1 Long Term Variations

Long term atmospheric density variations are those with frequency components $\omega_\rho << \omega_\theta$. Over the altitude range $180 \leq h \leq 300$ km, Tables 8-3 and 8-4 show a range of $0.25 \leq |K_{y\theta}| \leq 0.59$ N-m/deg or $14 \leq |K_{y\theta}| \leq 34$ N-m/rad. With the nominal value $I_y = 9.39 \times 10^6$ Kg - m^2, Equation (8-19) yields the range of orbiter incremental pitch motion natural frequencies $1.2 \times 10^{-3} \leq \omega_\theta \leq 1.9 \times 10^{-3}$ rad/sec. The corresponding periods for one cycle of pitch motion are $3300 \leq T_\theta \leq 5150$ sec, or on the order of one half to one orbit period. Therefore any density variation with a period greater than roughly four orbits or about six hours can be considered long term.

The pitch null torque offset angle is plotted as a function of altitude and percent deviation from nominal atmospheric density in Figure 8-14 for the nose forward orientation and in Figure 8-15 for the nose down orientation. These results apply directly in a constant atmospheric density environment or when the density varies with a period of greater than about six hours. It is apparent from these figures that both the nominal offset angles and the variations, at a given altitude, are more than an order of magnitude larger in the "nose down" orientation than in the "nose forward" orientation. This is due to the larger aerodynamic torque in the "nose down" orientation resulting from the larger surface area intercepting the air stream. Figure 8-16 compares the nominal aerodynamic torques in the two orientations.

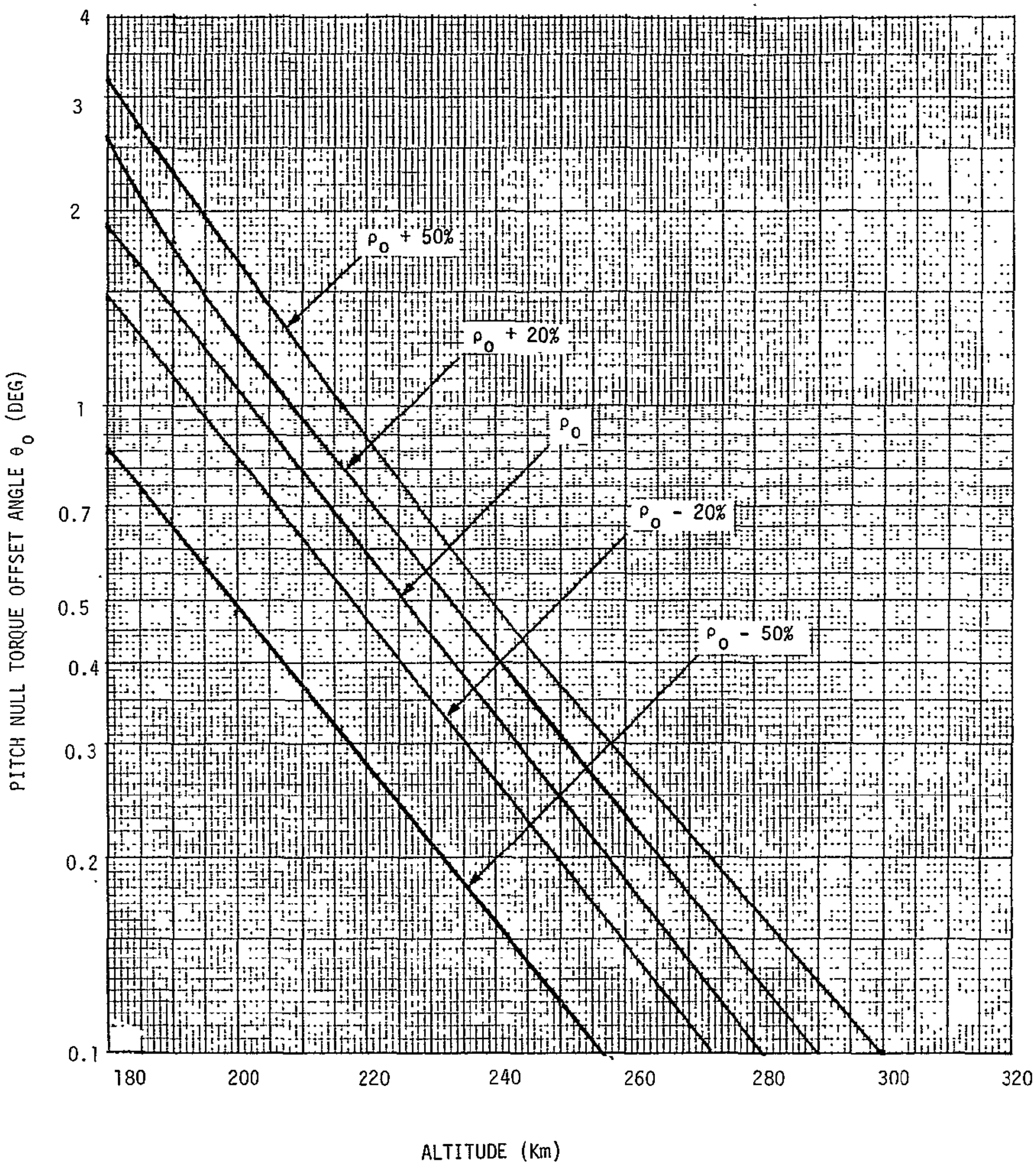

Figure 8-14. Variation of Pitch Null Torque Offset Angle With Atmospheric Density In "Nose Forward" Orientation

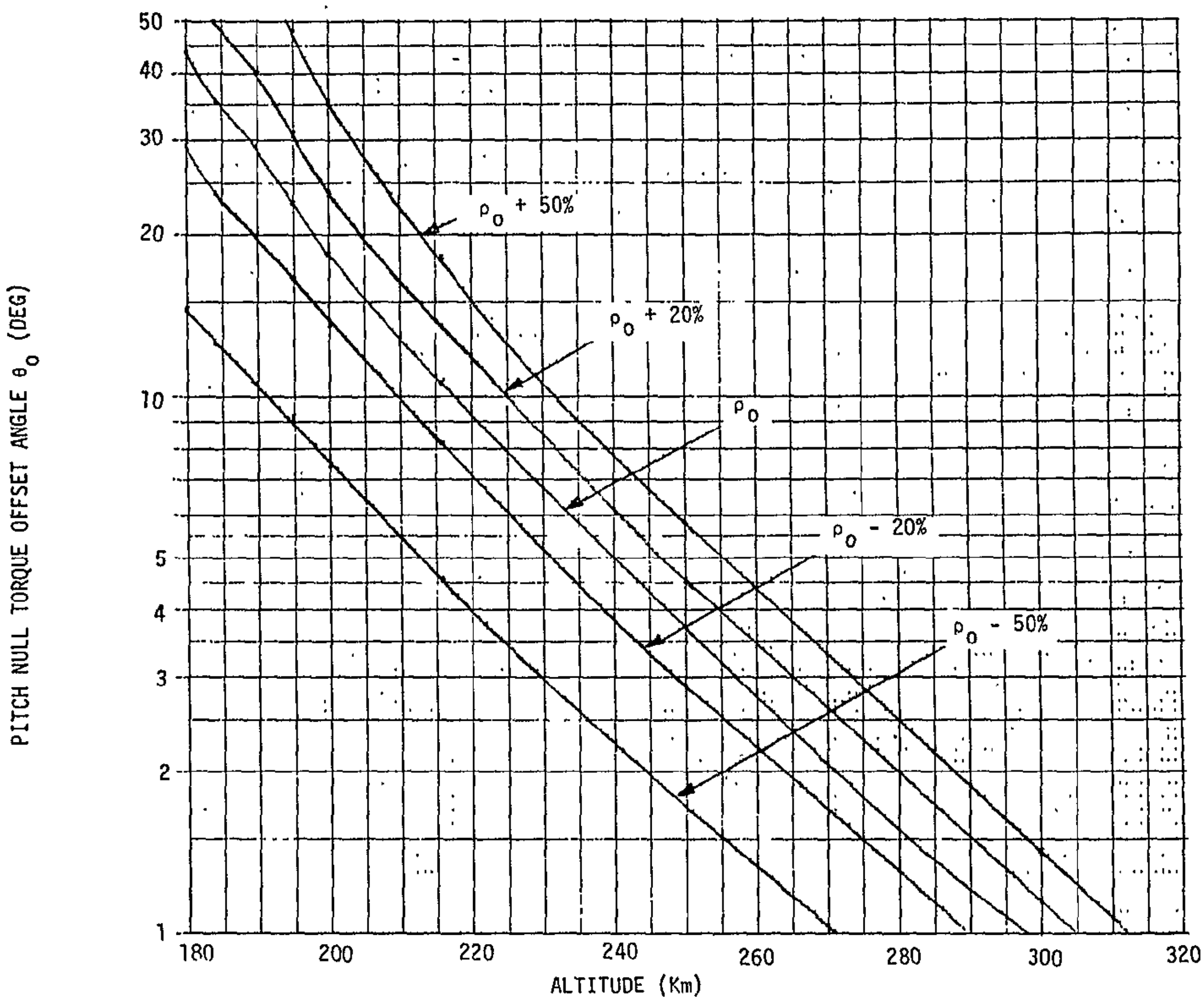

Figure 8-15. Variation of Pitch Null Torque Offset Angle With Atmospheric Density In "Nose Down" Orientation

ORIGINAL PAGE IS OF POOR QUALITY

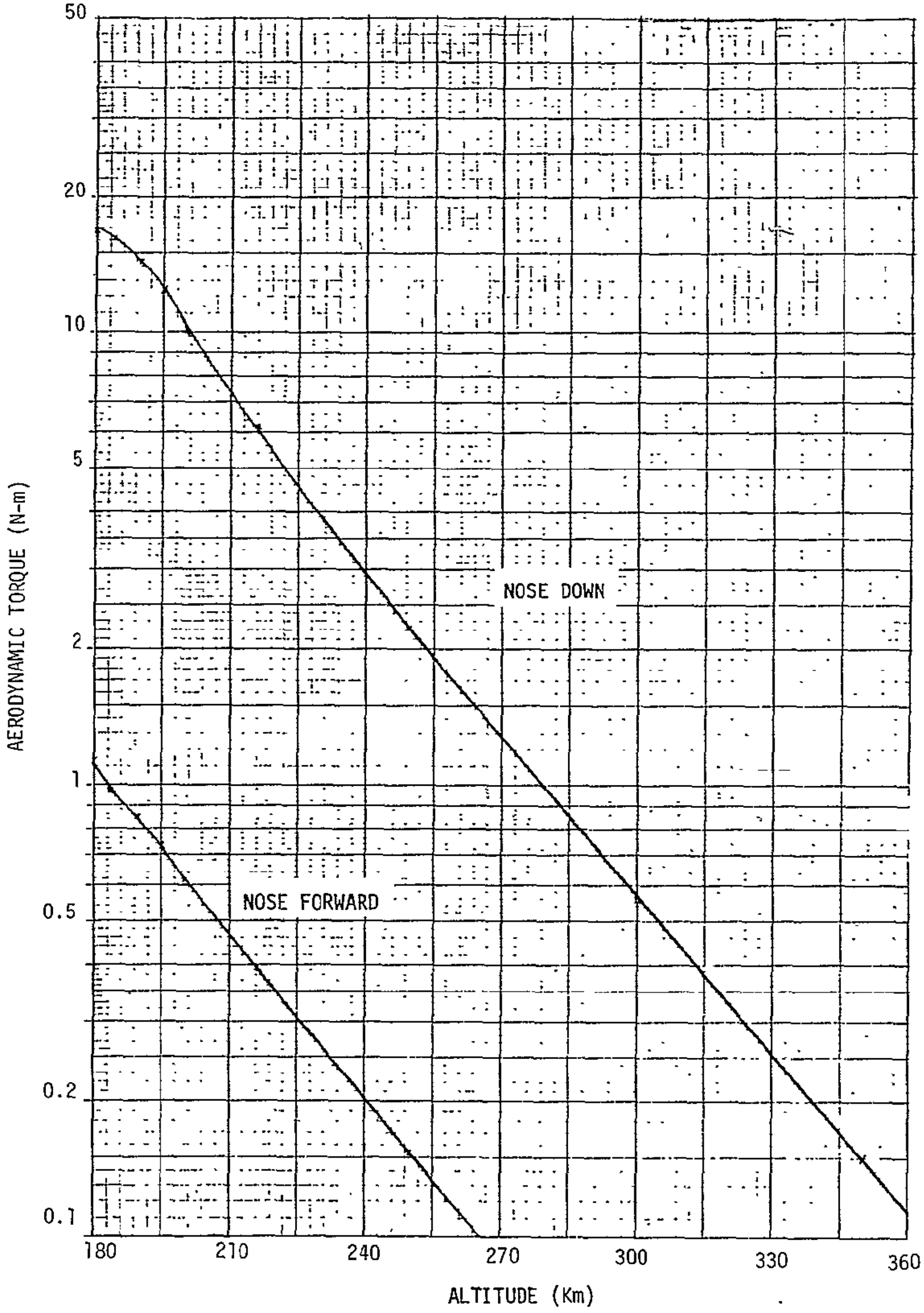

Figure 8-16. Pitch Aerodynamic Torque at Nominal Null Torque Offset Angle

8.4.2 Short Term Variations

The orbiter dynamics attenuates the orbiter attitude response to null torque attitude variations due to atmospheric density variations occurring at frequecies $\omega_\rho >> \omega_\theta$. In practical terms, this means that the orbiter will not respond significantly to disturbance variations with $\omega_\rho > 3\ \omega_\theta$, that is, with periods of less than about twenty minutes.

In the nose down orientation, the linear analysis indicated a resonant type of response for $\omega_\rho \approx \omega_\theta$. As explained in Appendix D, a significant atmospheric density variation can occur at orbit frequency due to differences in density on the day/night sides of the earth. As mentioned previously, ω_θ is also nearly equal to the orbit frequency for altitudes below 300 km. This unfortunate coincidence leads to the conclusion that atmospheric density variations may be highly disruptive to the otherwise stable nose down orientation at low altitudes.

As the linear analysis is strictly valid only for small perturbations, simulation is required to obtain meaningful results in the near resonant case. A digital simulation was therefore written to simulate the orbiter rigid body pitch dynamics along with the complete disturbance torque model described in Appendix D. The case run simulates the orbiter in the nose down orientation at 200 km altitude with a ±20% sinusoidal variation in atmospheric density at orbit frequency. Time plots of the results, spanning slightly more than two orbits, are presented in Figures 8-17 and 8-18. The variable $\theta_B = \theta_o + \theta$ in Figure 8-17 represents the total pitch angle from the nominal nose down attitude. For this case, θ_B is initially equal to the nominal offset angle for the nominal atmospheric density at this altitude. In other words, the orbiter starts at the nominal null torque attitude with the nominal atmospheric density. The atmospheric density variation induces a divergent pitch motion, reaching a peak-to-peak amplitude of over 57 degrees. In comparison, Figure 8-15 shows that the null torque attitude has a peak-to-peak variation of only 10 degrees under the stated conditions. Figure 8-17 also shows that the pitch rate and total disturbance torque are also divergent.

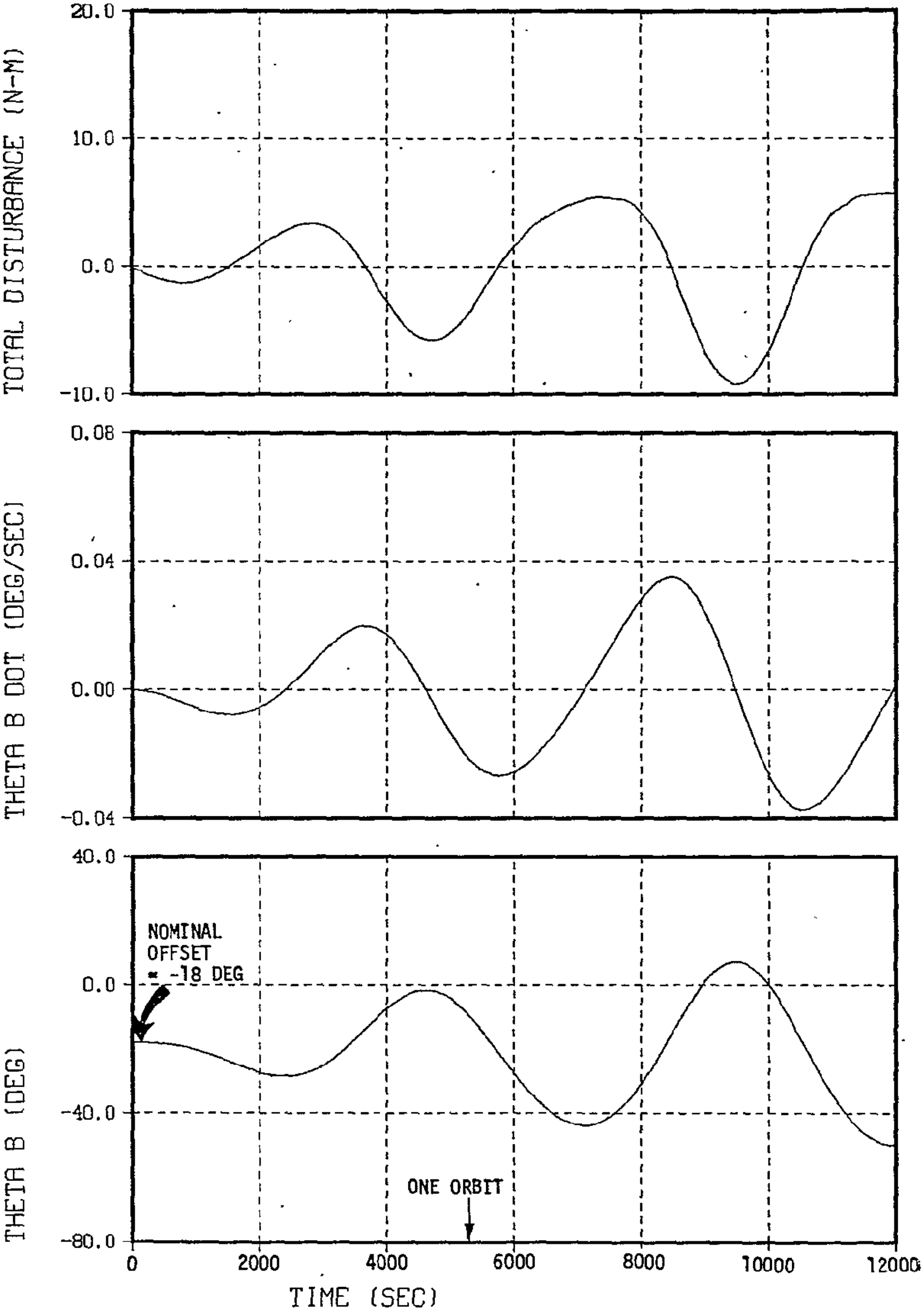

Figure 8-17. Orbiter Response to ±20% Atmospheric Density Variation at 200 Km in Nose Down Orientation

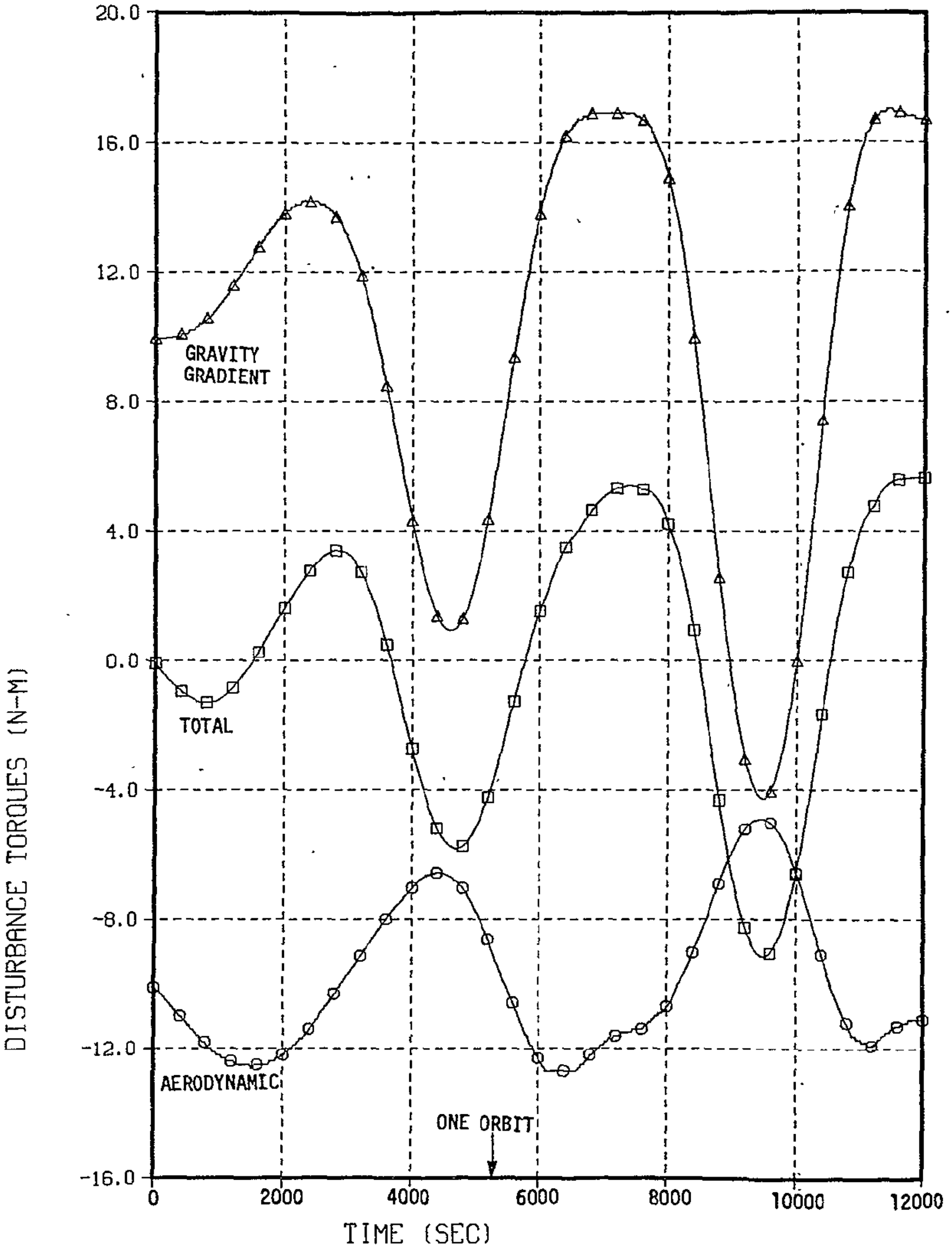

Figure 8-18. Disturbance Torques on Orbiter With ±20% Atmospheric Density Variation at 200 Km in Nose Down Orientation

Figure 8-18 expands the total disturbance torque into its gravity gradient and aerodynamic components. The gravity gradient and aerodynamic torques are initially equal in magnitude and opposite in sign, signifying that the orbiter is initially at the null torque attitude. The aerodynamic torque variation is nearly sinusoidal at orbit frequency, at least initially, reflecting the fact that the aerodynamic torque is proportional to atmospheric density but only weakly dependent on attitude. The gravity gradient torque is a nonlinear function of attitude only, and shows a complicated variation with large amplitude.

9.0 ORBITER CONTROL REQUIREMENT ANALYSIS

The analysis in the preceding section has demonstrated that the external disturbance torques cause all potential low altitude ($h < 400$ Km), and most of the high altitude, orbiter null torque attitudes suitable for earth surface or limb viewing to be unstable. An active attitude stabilization system is therefore required to keep the orbiter near the null torque attitude.

At a minimum, the orbiter null torque attitude control system should meet the following requirements:

- incremental stability - orbiter stays near torque null if started nearby.
- ability to capture from orbiter vernier RCS limit cycle rates and attitudes in a reasonable time.
- relative insensitivity to such uncertain quantities as the location of the torque null and the slopes of the torques about the null (K matrix)
- capable of controlling the orbiter in either the nose forward (3C) or nose down (4B) orientation, with at most a change of gains.

These requirements are examined in general terms in this section, without regard to the type of control actuator used. The particular implications of using either magnets or momentum exchange devices for control are discussed in detail in following sections.

9.1 STABILITY ANALYSIS

The incremental stability of the orbiter about the null torque attitude can be determined from the eigenvalues of the matrix A in the state equation

$$\dot{\bar{x}} = A\,\bar{x} \qquad (9\text{-}1)$$

The state vector is

$$\overline{x} = \begin{bmatrix} \phi \\ \theta \\ \psi \\ \omega_x \\ \omega_y - \omega_o \\ \omega_z \end{bmatrix} \tag{9-2}$$

where ϕ, θ, ψ are the small angle attitude perturbations from the torque null, ω_x, ω_y, ω_z are the body components of the inertial rates, and ω_o is the orbit rate. It is important to realize that the location of the torque null is uncertain and variable; the stability analysis is, however, conducted about the true null. The 6 x 6 matrix A can be expressed as the sum of three matrices

$$A = A_{DYNAMICS} + A_{DISTURBANCE} + A_{CONTROL} \tag{9-3}$$

For either the nose forward or nose down orientation, the dynamics/kinematics are described by

$$A_{DYNAMICS} = \begin{bmatrix} 0 & 0 & -\omega_o & 1 & 0 & 0 \\ 0 & 0 & 0 & 0 & 1 & 0 \\ \omega_o & 0 & 0 & 0 & 0 & 1 \\ 0 & 0 & 0 & 0 & 0 & -\omega_o \frac{(I_{zz} - I_{yy})}{I_{xx}} \\ 0 & 0 & 0 & 0 & 0 & 0 \\ 0 & 0 & 0 & -\omega_o \frac{(I_{yy} - I_{xx})}{I_{zz}} & 0 & 0 \end{bmatrix} \qquad (9\text{-}4)$$

The slopes of the disturbance torques about the null enter in the partitioned matrix

$$A_{DISTURBANCE} = \left[\begin{array}{c:c} \underline{0} & \underline{0} \\ \hdashline -I^{-1} K & \underline{0} \end{array}\right] \qquad (9\text{-}5)$$

where $\underline{0}$ is the 3 x 3 zero matrix, I is the diagonal inertia matrix for the orbiter

$$I = \begin{bmatrix} I_{xx} & 0 & 0 \\ 0 & I_{yy} & 0 \\ 0 & 0 & I_{zz} \end{bmatrix} \qquad (9\text{-}6)$$

and K is the disturbance compliance matrix defined in Section 8.3

$$K = \begin{bmatrix} K_{x\phi} & K_{x\theta} & K_{x\psi} \\ K_{y\phi} & K_{y\theta} & K_{y\psi} \\ K_{z\phi} & K_{z\theta} & K_{z\psi} \end{bmatrix} \tag{9-7}$$

The nominal values of K for orientations 3C and 4B are given in Section 8.3 for several altitudes; the units must be converted to N-m/rad for use here.

The control law is assumed for now to be state variable feedback, leading to

$$A_{CONTROL} = \left[\begin{array}{c:c} \underline{0} & \underline{0} \\ \hdashline \multicolumn{2}{c}{I^{-1}\ G} \end{array}\right] \tag{9-8}$$

where G is the 3 x 6 feedback control gain matrix

$$G = \begin{bmatrix} G_{1x} & G_{2x} & G_{3x} & G_{4x} & G_{5x} & G_{6x} \\ G_{1y} & G_{2y} & G_{3y} & G_{4y} & G_{5y} & G_{6y} \\ G_{1z} & G_{2z} & G_{3z} & G_{4z} & G_{5z} & G_{6z} \end{bmatrix} \tag{9-9}$$

The control torque vector $\overline{T}_c$ is

$$\overline{T}_C = \begin{bmatrix} T_{Cx} \\ T_{Cy} \\ T_{Cz} \end{bmatrix} = G\,\overline{x} \tag{9-10}$$

9.1.1 Open Loop Stability

With the control loops open, stability is determined by the eigenvalues of

$$A_{DYNAMICS} + A_{DISTURBANCE}$$

Evaluating these eigenvalues for the nose forward and noise down orientations over the altitude range 180 to 300 km reveals the following:

- roll - unstable in both orientations at all altitudes
- pitch - unstable in the nose forward orientation at all altitudes, pure imaginary eigenvalues (oscillatory with no damping) in the nose down orientation at all altitudes.
- yaw - marginally stable (oscillatory with damping ratio $\zeta \simeq 0.02$) in both orientations at all altitudes

Both orientations at all altitudes thus have at least one unstable axis, and long term earth viewing with the RCS disabled will require active control.

9.1.2 Closed Loop Stability

In general, Equation (9-1) represents a coupled sixth order system. In the orientations under consideration, however, near the null torque attitude

$$K_{x\theta} = K_{y\phi} = K_{y\psi} = K_{z\theta} = 0$$

Therefore pitch is uncoupled from roll/yaw and there is no reason not to choose

$$G_{2x} = G_{5x} = G_{1y} = G_{3y} = G_{4y} = G_{6y} = G_{2z} = G_{5z} = 0$$

The remaining ten gains are available for achieving the following desired dynamic characteristics

- stability - all eigenvalues in left half plane.
- decoupling - each axis to behave as an (approximately) uncoupled second order system.
- insensitivity - both of the above conditions to be met in both orientations at all altitudes.

Greater insight into achieving these goals can be gained by using the relations

$$\dot{\phi} = \omega_x - \omega_o \psi \tag{9-11}$$

$$\dot{\theta} = \omega_y - \omega_o \tag{9-12}$$

$$\dot{\psi} = \omega_z + \omega_o \phi \tag{9-13}$$

to change variables. The dynamic equations become

$$I_{xx} \ddot{\phi} + B_{Rx} \dot{\phi} + B_{Px} \phi = C_{Rx} \dot{\psi} + C_{Px} \psi \tag{9-14}$$

$$I_{yy} \ddot{\theta} + B_{Ry} \dot{\theta} + B_{Py} \theta = 0 \tag{9-15}$$

$$I_{zz} \ddot{\psi} + B_{Rz} \dot{\psi} + B_{Pz} \psi = C_{Rz} \dot{\phi} + C_{Pz} \phi \tag{9-16}$$

where the effective rate and position gains are

$$B_{Rx} = - G_{4x} \tag{9-17}$$

$$B_{Px} = - G_{1x} + \omega_o G_{6x} - \omega_o^2 (I_{zz} - I_{yy}) + K_{x\phi} \tag{9-18}$$

$$B_{Ry} = - G_{5y} \tag{9-19}$$

$$B_{Py} = - G_{2y} + K_{y\theta} \tag{9-20}$$

$$B_{Rz} = - G_{6z} \tag{9-21}$$

$$B_{Pz} = - G_{3z} - \omega_o G_{4z} + \omega_o^2 (I_{yy} - I_{xx}) + K_{z\psi} \tag{9-22}$$

and the interaxis coupling gains are

$$C_{Rx} = G_{6x} - \omega_o (I_{zz} + I_{xx} - I_{yy}) \tag{9-23}$$

$$C_{Px} = G_{3x} + \omega_o G_{4x} - K_{x\psi} \tag{9-24}$$

$$C_{Rz} = G_{4z} + \omega_o (I_{zz} + I_{xx} - I_{yy}) \tag{9-25}$$

$$C_{Pz} = G_{1z} - \omega_o G_{6z} - K_{z\phi} \tag{9-26}$$

The design goals can be met, by applying classical control theory, in the following ways:

- stability: select the control gains, G, to yield positive "rate gains" B_{Ri} and "position gains", B_{Pi}, $i = x, y, z$.
- decoupling: select the control gains, G, to yield (nearly) zero "rate coupling gains" C_{Ri} and "position coupling gains" C_{Pi}, $i = x,z$.
- insensitivity to disturbance variations: select the control gains, G, to insure the previous two conditions are met over the expected range of disturbances, K.

_If_ adequate control torque is available and the state variables can be measured, the control gains can be selected to yield a closed loop system with virtually any desired response. With the limited control torque available from momentum exchange devices, and more particularly magnets, tight control of the orbiter around the null torque attitude is not feasible. A more realistic goal is to merely stabilize the orbiter, with relatively low gain loops, yielding low bandwidth, low damping responses. For example, the orbiter can be stabilized about the null torque attitude in a constant atmospheric density environment, in either the nose forward or nose down orientation, at all altitudes above 180 km with the gain matrix

$$G = \left[\begin{array}{ccc:ccc} -31.8 & 0. & 3.90 & -3100. & 0. & 1850. \\ 0. & -52.6 & 0. & 0. & -7510. & 0. \\ -6.80 & 0. & -30.5 & -1850. & 0. & -7290. \end{array}\right]$$

$$\begin{array}{c:c} \text{[N-m/rad]} & \text{[N-m/(rad/sec]} \end{array}$$

The variation of the closed loop roots over the altitude range 180 to 300 km, using the associated nominal disturbance compliances from Section 8.3 is shown in Figure 9-1. The relatively large difference in pitch roots between the two orientation can be reduced by using a different value of G_{2y} for each orientation.

9.2 ACTUATOR REQUIREMENT ESTIMATE

In this section, estimates of the control actuator requirements are obtained. Torque requirements can be better defined without extensive analysis than can momentum requirements, and apply to both magnets and momentum exchange devices. Therefore emphasis is placed on torque requirements although momentum storage requirements are addressed where appropriate. Initial capture from the orbiter RCS limit cycle is considered first, followed by an analysis of normal operations, and finally conclusions.

9.2.1 Capture From RCS Limit Cycle

An approximate analysis of actuator torque requirements for initial capture from the orbiter vernier RCS limit cycle is presented here. Momentum requirements for momentum exchange actuators are considered in Sections 11.3 and 11.4.

ORIGINAL PAGE IS
OF POOR QUALITY

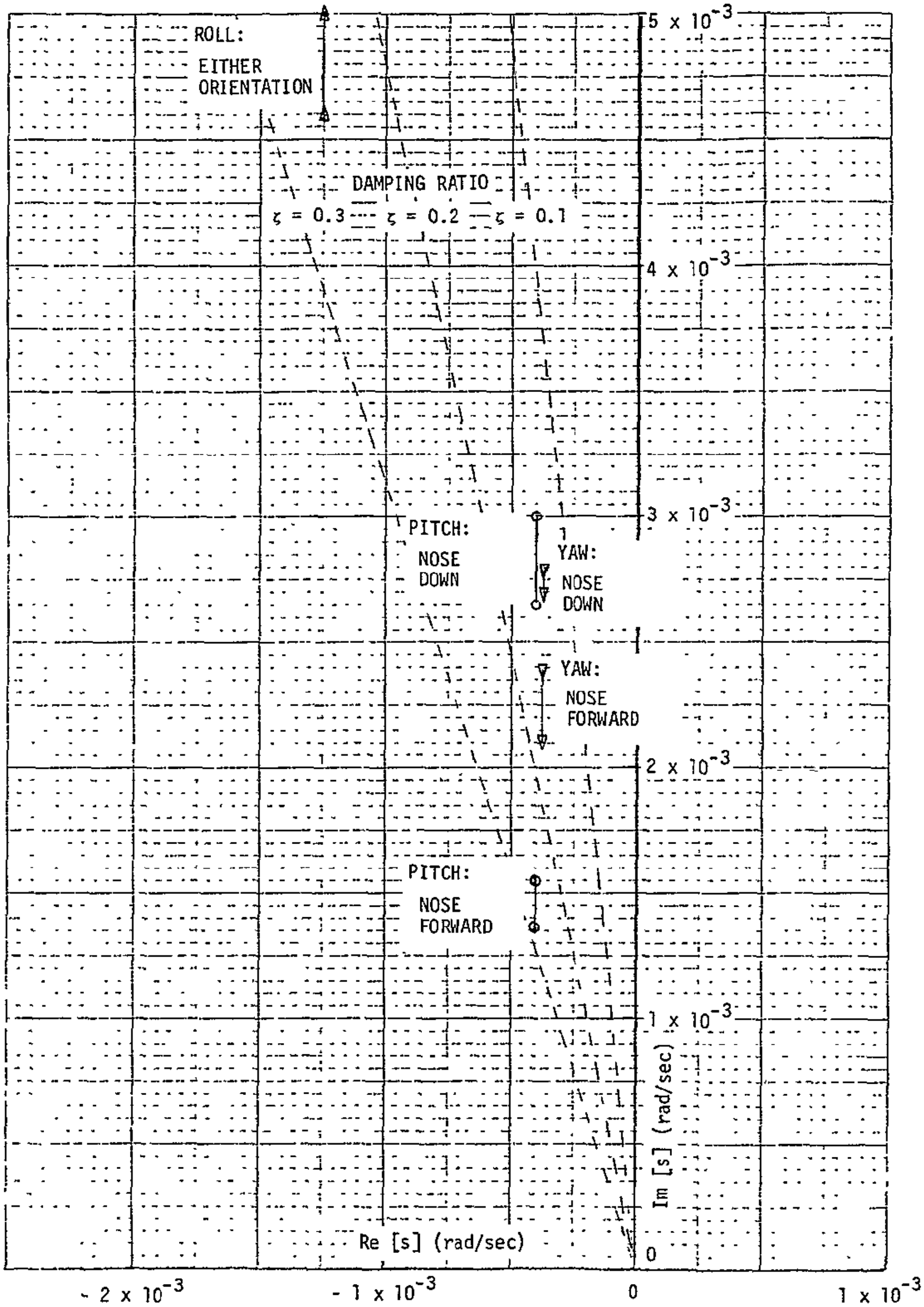

Figure 9-1. Range of Closed Loop Eigenvalues for Altitude Range 180 to 300 Km

For the second order system

$$I\ddot{\eta} + K\eta = T_\eta \tag{9-27}$$

with feedback control law

$$T_\eta = G_{R\eta}\,\dot{\eta} + G_{P\eta}\,\eta \tag{9-28}$$

and initial conditions

$$\eta(0) = \eta_0 \tag{9-29}$$

$$\dot{\eta}(0) = \dot{\eta}_0 \tag{9-30}$$

the peak torque required for control is approximately, for small values of the damping ratio ζ,

$$|T_\eta|_{peak} \simeq \frac{[\omega^2\ I\ (1 + 2\ \zeta) - K]}{(1 - \zeta^2)^{1/2}} \left[\eta_0^2 + \left(\frac{\dot{\eta}_0}{\omega}\right)^2\right]^{1/2} \tag{9-31}$$

where the feedback gains are related to the bandwidth ω and damping ratio ζ by

$$G_R = -\ 2\ \omega\ \zeta\ \ I \tag{9-32}$$

$$G_P = -\ (\omega^2\ I - K) \tag{9-33}$$

The estimate in equation (9-31) assumes the worst case combination of the signs of the initial conditions and is exact in the limit as $\zeta \to 0$.

For the orbiter, the largest torque requirement is likely to be along pitch in the nose forward orientation. For this case

$$K = K_{y\theta} = - 33.8 \text{ N-m/rad}$$

$$I = I_{yy} = 9.39 \times 10^{6} \text{ kg-m}^{2}$$

and the worst case initial conditions are the estimated attitude error and rate at the time the RCS thrusters are disabled

$$\eta_{0} = \theta(0) = 0.1 \text{ deg} = 1.745 \times 10^{-3} \text{ rad}$$

$$\dot{\eta}_{0} = \dot{\theta}(0) = 0.01 \text{ deg/sec} = 1.745 \times 10^{-4} \text{ rad/sec}$$

With these parameters, the peak torque in equation (9-31) is minimized for $\zeta = 0$, $\omega \simeq 2 \times 10^{-3}$ rad/sec, resulting in

$$|T_{Cy}|_{Peak} \simeq 6.23 \text{ N-m}$$

Minimizing $|T_{Cy}|_{Peak}$ leads to completely unsatisfactory performance, however, with a continuous pitch oscillation with amplitude

$$|\theta|_{max} \simeq \frac{\dot{\theta}(0)}{\omega} = 8.73 \times 10^{-2} \text{ rad} = 5.00 \text{ deg}$$

It can therefore be concluded that a control torque greater than 6.23 N-m will be required for satisfactory attitude capture from the RCS limit cycle with the assumed error and rate at the transition time.

An order of magnitude reduction in orbiter RCS limit cycle rate may be possible through modification of the RCS. This would reduce the rate initial condition to

$$\dot{\eta}_0 = \dot{\theta}(0) = 0.001 \text{ deg/sec} = 1.745\text{x}10^{-5} \text{ rad/sec}$$

The peak torque in Equation (9-31) is minimized for $\zeta = 0$, $\omega \approx 0.0018$ $\text{x}10^{-3}$ rad/sec, resulting in

$$|T_{Cy}|_{peak} \approx 0.633 \text{ N-m}$$

For future reference, $|T_{Cy}|_{peak}$ is plotted against $\dot{\theta}(0)$ in Figure 9-2.

9.2.2 Normal Operation

Following the initial capture transient, the period of normal operation is entered. If the null torque attitude was constant and known exactly, essentially no control torque would be required to remain at the torque null once the initial transient was damped out. Realistically, however, the null torque attitude is neither constant over the period the orbiter is to be stabilized nor readily determinable in real time.

The largest source of variation and uncertainty in the location of the null torque attitude at low altitudes is temporal variations in atmospheric density. In the two selected YPOP orbiter orientations, the gravity gradient and aerodynamic components of the total disturbance torque individually vanish at the null torque attitude, for both the orbiter roll and yaw axes. Therefore atmospheric density variations have no significant effect on the roll and yaw axes, and actuator sizing is based on the initial capture transient. Along pitch, however, both the gravity

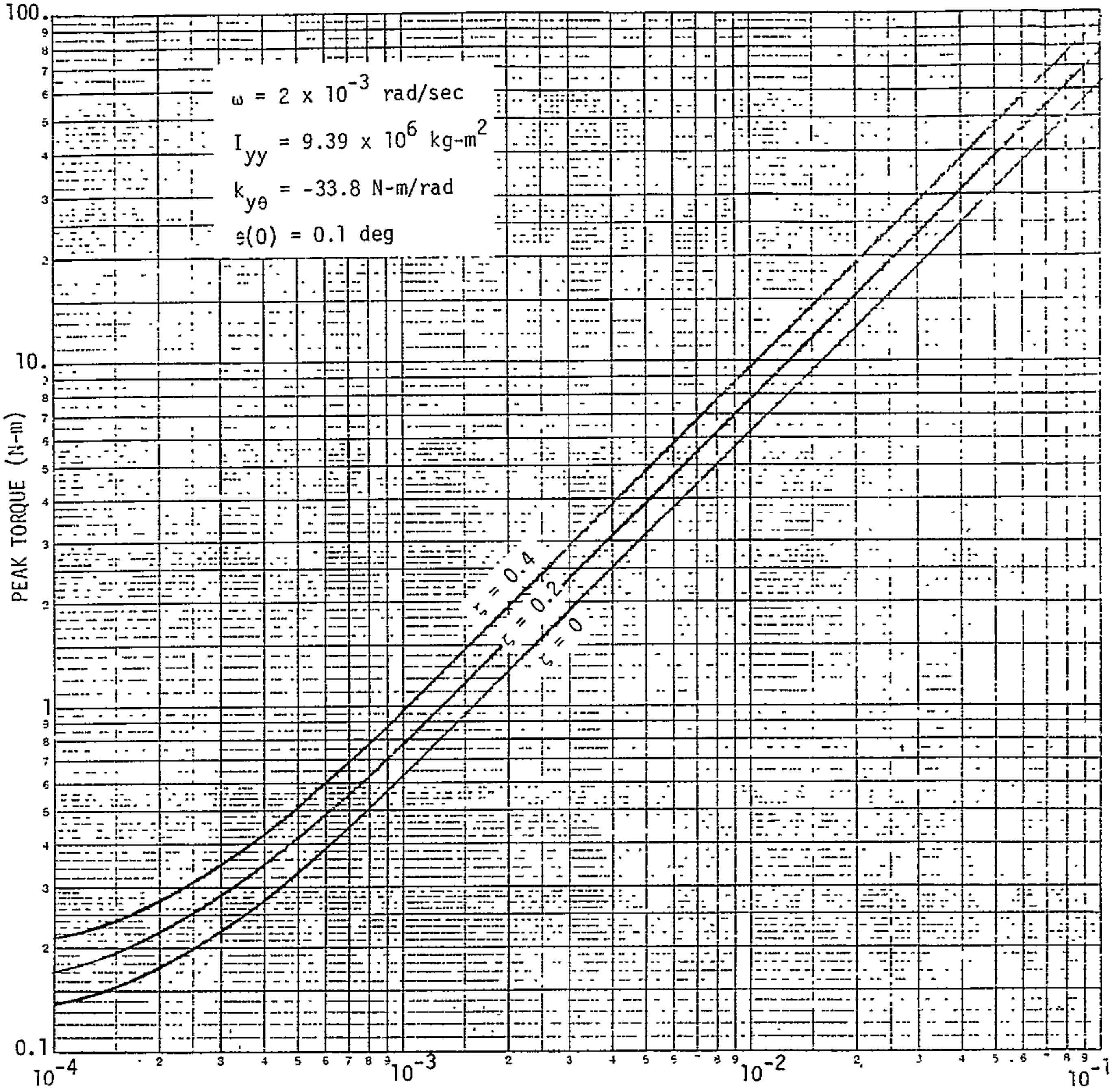

Figure 9-2. Minimum Peak Torque Required for Pitch Capture From RCS Limit Cycle

gradient and aerodynamic components of the total disturbance torque may have large magnitudes (Figure 8-16) at the null torque attitude, with cancellation resulting from opposite signs. Sensitivity to atmospheric density variations can therefore be of sufficient magnitude to influence actuator sizing.

A linearized incremental model of the pitch control system is illustrated in Figure 9-3. The model is linearized about the null torque offset angle corresponding to the nominal aerodynamic disturbance torque. The dynamics are described in general by the pair of equations

$$I_y \, \delta\ddot{\theta} = \delta T_c + \delta T_\theta + \delta T_{A\rho} \tag{9-34}$$

$$\delta\dot{h} = -\delta T_c \tag{9-35}$$

where

$$\delta T_\theta = -K_{y\theta} \, \delta\theta \tag{9-36}$$

δh = change in momentum exchange device stored momentum

δT_c = incremental control torque

and the remaining quantities are as defined in Section 8.4. Equation (9-35) applies only when a momentum exchange device is used as the control actuator.

Assume that the aerodynamic torque variation is at frequency ω with amplitude $\delta T_{A\rho}$ (ω), that is

$$\delta T_{A\rho} = \delta T_{A\rho} \, (\omega) \sin \omega t \tag{9-37}$$

Two idealized control strategies will be considered:

(1) Follow the null torque attitude exactly at all times

(2) Hold the nominal null torque attitude exactly at all times

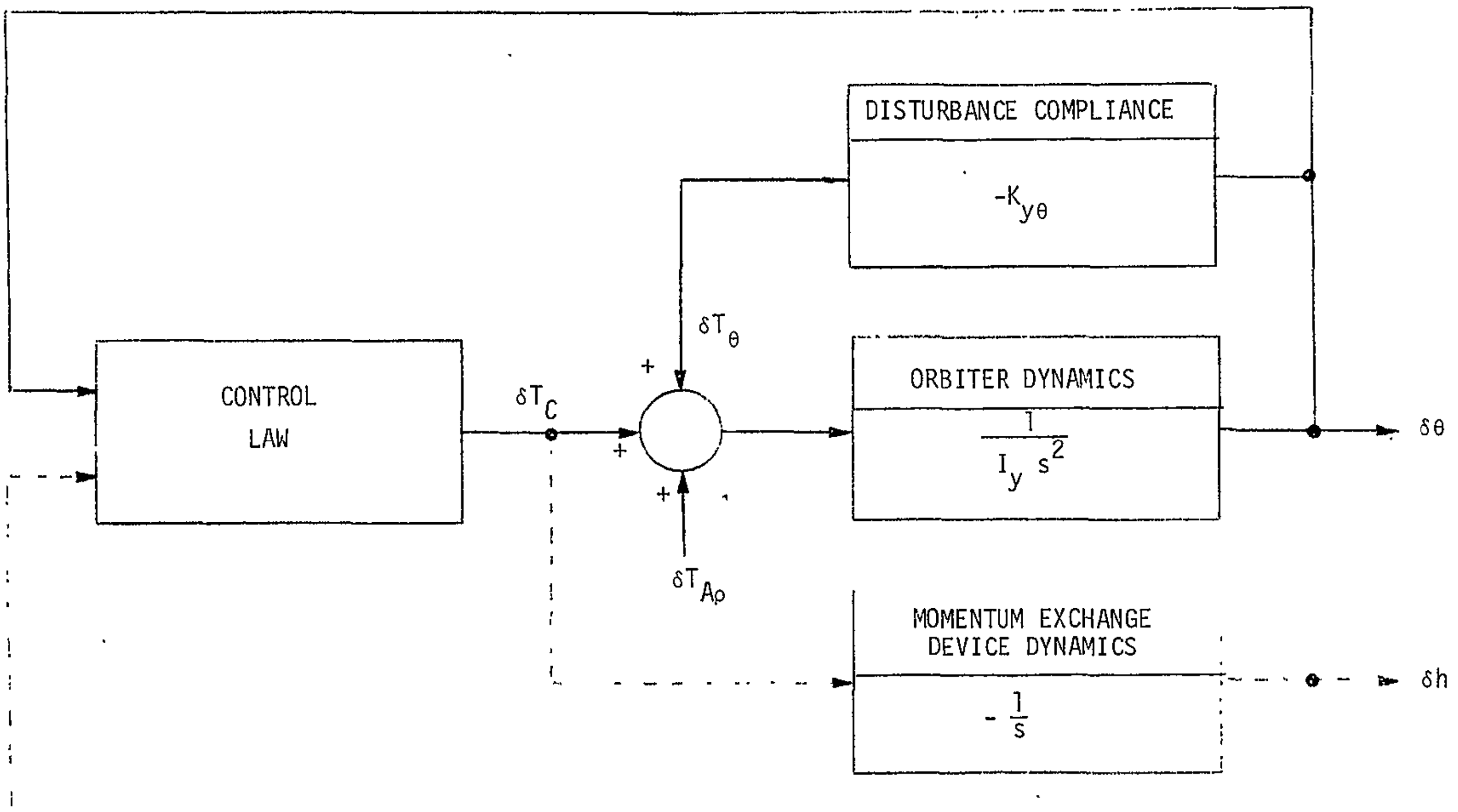

Figure 9-3. Incremental Pitch Model for Analysis of Response to Aerodynamic Disturbance Variations

With the first stragery, the total external disturbance torque perturbation vanishes, that is

$$\delta T_{\theta} + \delta T_{A\rho} = 0 \tag{9-38}$$

This implies

$$I_y \, \delta\ddot{\theta} = \delta T_c \tag{9-39}$$

and

$$\delta\theta = \frac{\delta T_{A\rho}(\omega)}{K_{y\theta}} \sin \omega T \tag{9-40}$$

Since $\delta\theta$ is given explicitly by Equation (9-40), derivatives can be taken to yield

$$\delta T_c = -\delta\dot{h} = -I_y \, \omega^2 \frac{\delta T_{A\rho}(\omega)}{K_{y\theta}} \sin \omega T \tag{9-41}$$

and

$$\delta h = -I_y \, \omega \frac{\delta T_{A\rho}(\omega)}{K_{y\theta}} \cos \omega t \tag{9-42}$$

Therefore the ratios of peak torque and momentum variation to aerodynamic disturbance variation are

$$G_1(\omega) = \left| \frac{\delta T_c}{\delta T_{A\rho}(\omega)} \right| = \frac{I_y \, \omega^2}{|K_{y\theta}|} \tag{9-43}$$

$$H_1(\omega) = \left| \frac{\delta h}{\delta T_{A\rho}(\omega)} \right| = \frac{I_y \, \omega}{|K_{y\theta}|} \tag{9-44}$$

With the second strategy, the attitude perturbation is zero

$$\delta\theta = 0 \tag{9-45}$$

resulting in

$$\delta T_c = - \delta T_{A\rho} \tag{9-46}$$

Therefore the ratios are in this case

$$G_2(\omega) = \left|\frac{\delta T_c}{\delta T_{A\rho}(\omega)}\right| = 1 \tag{9-47}$$

$$H_2(\omega) = \left|\frac{\delta h}{\delta T_{A\rho}(\omega)}\right| = \frac{1}{\omega} \tag{9-48}$$

Comparison of equations (9-43) and (9-44) with Equations (9-47) and (9-48) shows that the first strategy requires smaller actuators if $\omega < \sqrt{|K_{y\theta}|/I_y}$ while the second strategy requires the smaller actuators if $\omega > \sqrt{|K_{y\theta}|/I_y}$. For EVAL, the predominant component of $\delta T_{A\rho}$ is at $\omega = \omega_0 \simeq 1.1 \times 10^{-3}$ rad/sec and $I_y = 9.39 \times 10^6$ Kg-m^2. The value of $|K_{y\theta}|$ decreases with increasing offset angles but using the maximum value $|K_{y\theta}| = 33.92$ N-m/rad yields

$G_1(\omega_o)$ = 0.335 N-m/N-m

$H_1(\omega_o)$ = 304 N-m-sec/N-m

$G_2(\omega_o)$ = 1 N-m/N-m

$H_2(\omega_o)$ = 909 N-m-sec/N-m

Up to three times as much momentum and torque is thus required to hold a constant attitude compared to following the null torque attitude motion at orbit frequency.

Figure 9-4, based on Figure 8-16, is a plot of $\delta T_c = G_2(\omega_o)\ \delta T_{A\rho}$, or the pitch control torque required to hold the orbiter at the nominal null torque attitude in the face of a ±20% variation in atmospheric density at orbit frequency. The torque values are in all cases less than that required to capture from the nominal 0.01 deg/sec RCS limit cycle (6.23 N-m). However, in the nose down orientation below 235 km, the indicated control torques are greater than that required to capture from the reduced rate (0.001 deg/sec) RCS limit cycle (0.633 N-m).

Following the null torque attitude may lead to large orbiter motions at low altitude, and the linear analysis is not strictly valid for determining the control torque requirements. Under most conditions, however, the control torque requirement for following the null torque attitude is approximately one-third of that required to hold a constant attitude at the same altitude.

With the current nominal orbiter parameters, the largest torque requirement is for capture from the orbiter RCS limit cycle, rather than during normal steady state operation. The steady state torque requirement is sized largely by the variation and uncertainty in the location of the null torque attitude, as determined by the atmospheric denisty (the primary influence at low altitudes) and the orbiter mass properties. The dominant influence on the transient torque requirement for attitude capture from the RCS limit cycle is the nominal

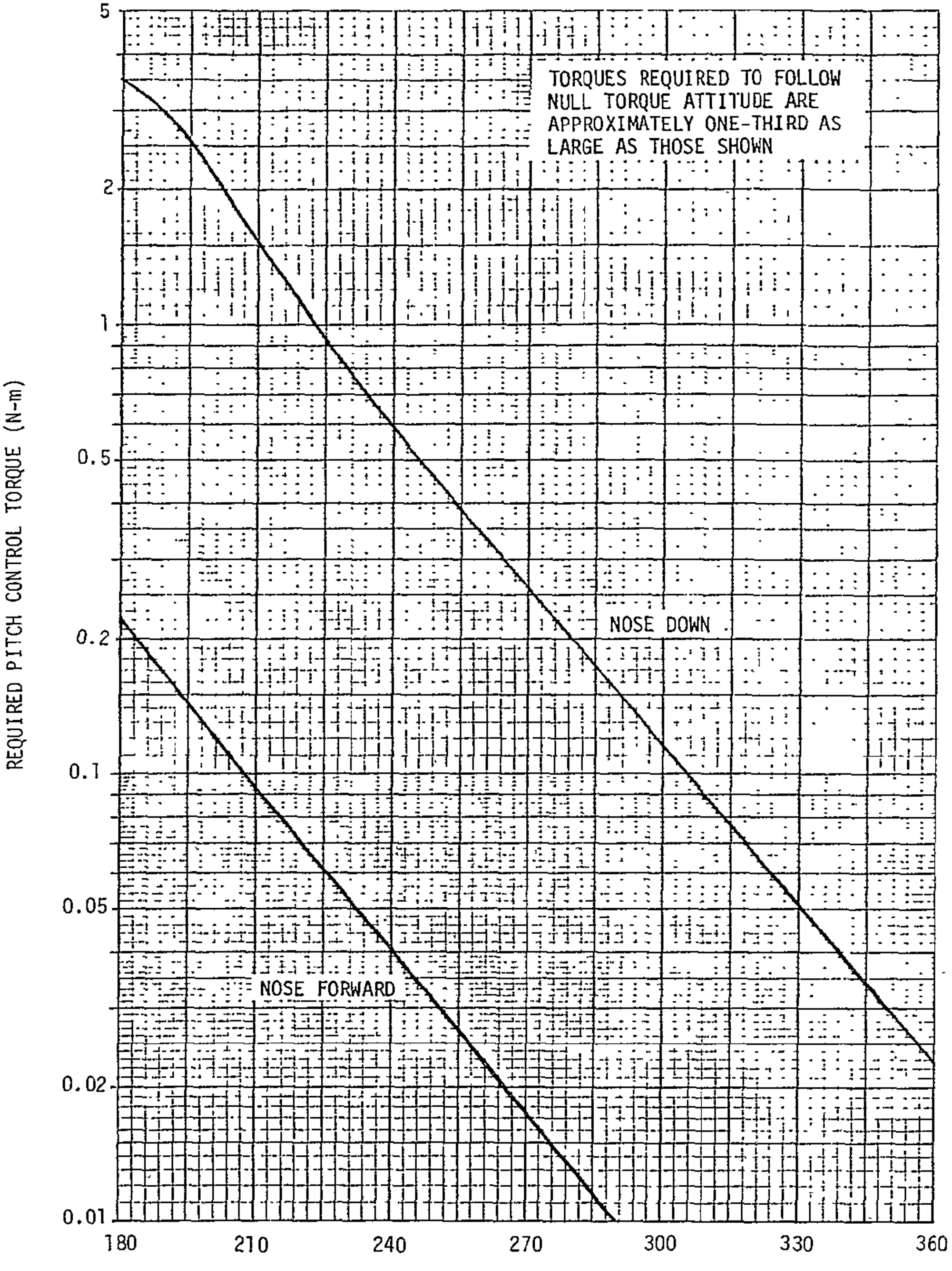

Figure 9-4. Pitch Control Torque Required to Hold at Nominal Null Torque Attitude With 20% Atmospheric Density Variation

limit cycle rate of 0.01 deg/sec rather than the nominal limit cycle deadzone of 0.1 deg. The size of the actuators required for the null torque attitude stabilization system can be reduced significantly if an additional "low rate" RCS mode is made available. It is recommended that such a mode be provided, with the limit cycle rates reduced by at least a factor of 10 from the current nominal. A proportional increase in the RCS deadzone, if required to achieve the reduced rates, would be acceptable.

It should be emphasized that idealized control has been assumed. Means of implementing practical approximations to these idealized control strategies are described in the following sections.

10.0 MAGNETIC CONTROL OF ORBITER

If electromagnets are used for control, the magnetic torque is related to the magnetic moment of the magnet bars $\overline{M}$ and the earth's magnetic field $\overline{B}$ by

$$\overline{T}_M = \overline{M} \times \overline{B} \tag{10-1}$$

From the properties of the cross product, it is clear that no torque can be generated in the direction of $\overline{B}$ and in general there will be a torque error $\overline{T}_e$ between $\overline{T}_M$ and the desired control torque $\overline{T}_C$. That is,

$$\overline{T}_M = \overline{T}_C + \overline{T}_e \tag{10-2}$$

It can be shown that the magnitude of the error torque, $(\overline{T}_e \cdot \overline{T}_e)^{1/2}$ is minimized if the magnetic moment is chosen to be

$$\overline{M} = \frac{\overline{B} \times \overline{T}_C}{\overline{B} \cdot \overline{B}} \tag{10-3}$$

The minimum magnitude error torque is along $\overline{B}$ and proportional to the component of $\overline{T}_C$ along $\overline{B}$, that is

$$(\overline{T}_e)_{min} = - \frac{(\overline{T}_C \cdot \overline{B})}{\overline{B} \cdot \overline{B}} \overline{B} \tag{10-4}$$

The relation between these vectors is illustrated in Figure 10-1.

In a practical implementation, two additional complication enter. The ambient magnetic field must be measured with a three-axis magnetometer to implement equation (10-3), leading to the magnetic moment command

$$\overline{M}_C = \frac{\hat{B} \times \overline{T}_C}{\hat{B} \cdot \hat{B}} \tag{10-5}$$

where $\hat{B}$ is the measured field. In addition, a given magnet can only produce a limited magnetic moment. A simple but realistic model for the magnets is therefore

$$\overline{M} = \text{SAT}\ (\overline{M}_C, \overline{m}) \tag{10-6}$$

where

$\overline{M}$ = actual magnetic moment

SAT(·, ·) = vector saturation function

m = saturation magnetic moment

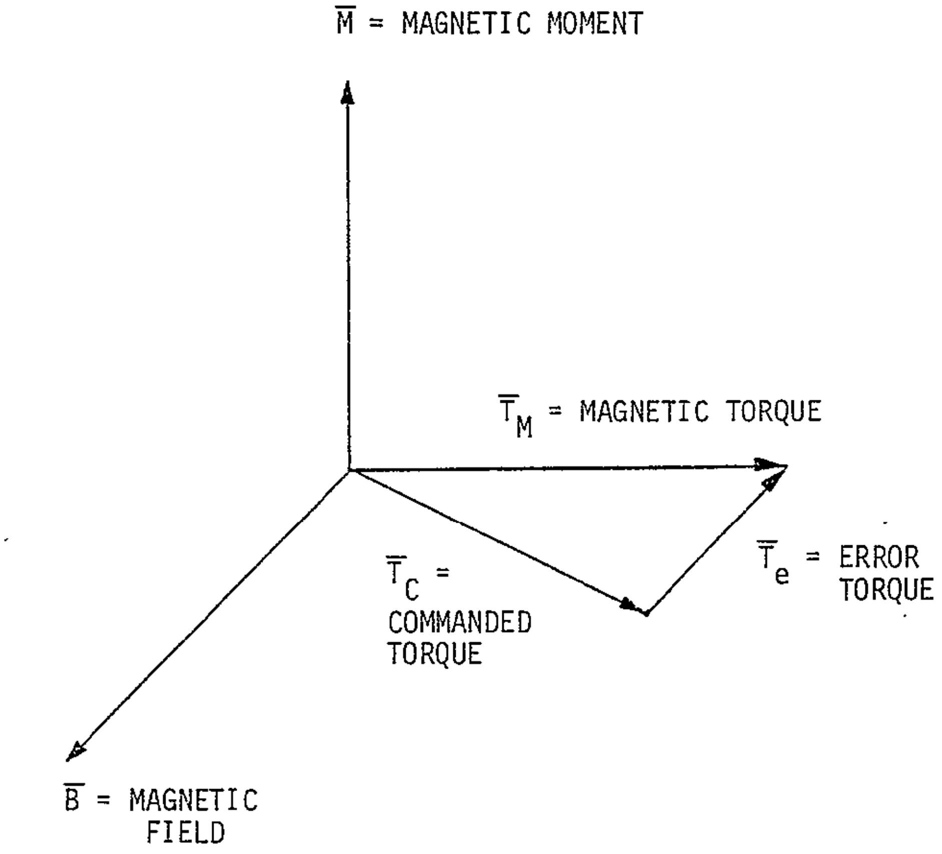

$$\overline{M} = \frac{\overline{B} \times \overline{T}_C}{\overline{B} \cdot \overline{B}}$$

$$\overline{T}_M = \overline{M} \times \overline{B} = \overline{T}_C + \overline{T}_e$$

$$\overline{T}_e = - \frac{(\overline{T}_C \cdot \overline{B})}{(\overline{B} \cdot \overline{B})} \overline{B}$$

Figure 10-1. VECTOR RELATIONSHIPS FOR MAGNETIC CONTROL SYSTEM

A magnet control system incorporating these features is illustrated in Figure 10-2.

10.1 CONTROL DESIGN

The error torques in Equation (10-4) introduce undesirable time-varying coupling between the control axes that may intefere with control performance. Since control torque is not available in the direction of $\overline{B}$, three-axis stability cannot be assured, especially if the open loop system is unstable. The "most unstable" axis for the null torque orientations under consideration is pitch in the nose forward orientation and therefore attention will be focused on pitch.

Figure 10-3 shows a pitch control system using magnets. The disturbance torque model explicitly includes the offset of the null torque attitude from the nominal attitude, θ_0, and the attitude error from the torque null θ. The total pitch angle from the nominal attitude (i.e., nose along orbit velocity in nose forward orientation, nose towards nadir in nose down orientation is

$$\theta_B = \theta_0 + \theta \tag{10-7}$$

while the rate variable is

$$\dot{\theta}_B = \omega_y - \omega_0 \tag{10-8}$$

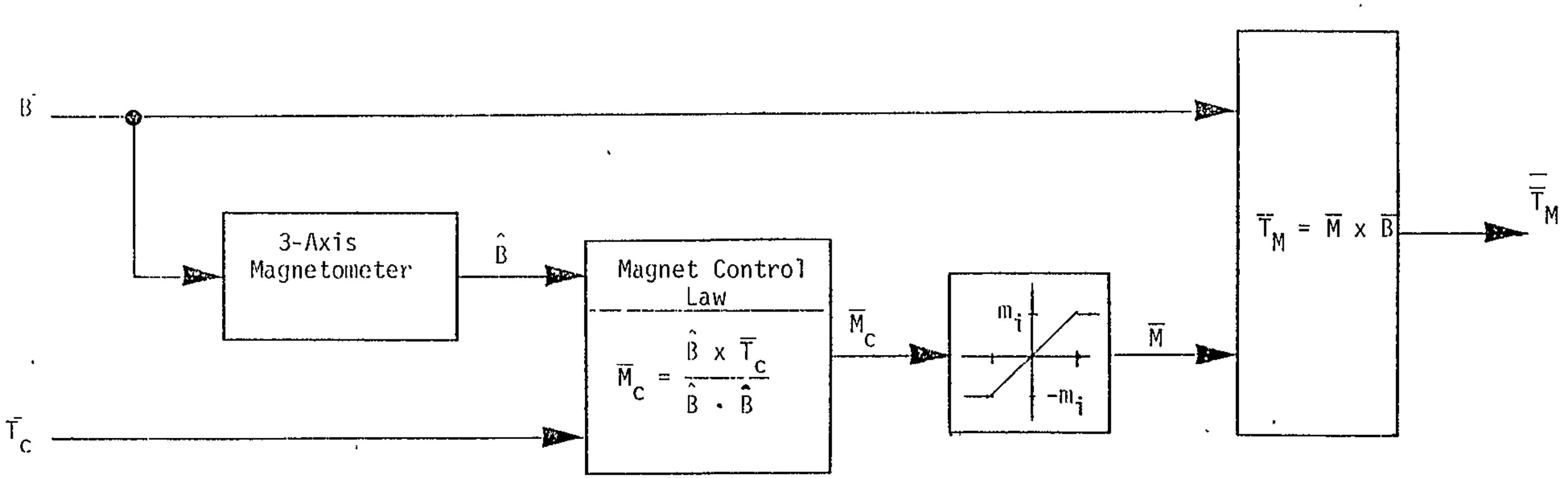

NOTATION:

$\bar{T}_c$ = Command Torque

$\bar{T}_M$ = Actual Magnetic Torque on Orbiter

$\bar{B}$ = Actual Magnetic Field

B = Measured Magnetic Field

$\bar{M}_c$ = Commanded Magnetic Moment

$\bar{M}$ = Actual Magnetic Moment

m_i = Saturation Magnetic Moment, i = x, y, z

Figure 10-2. Magnet Control System

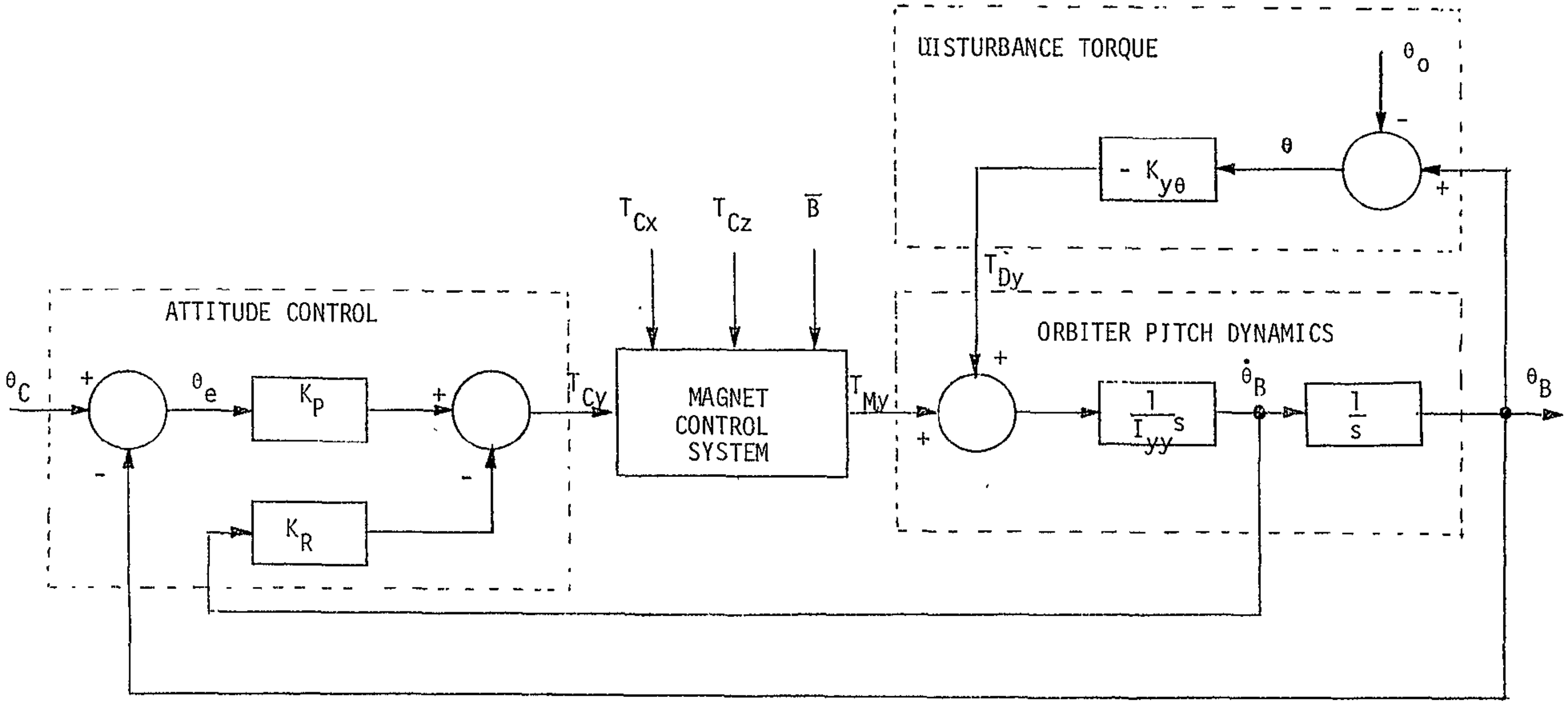

Figure 10-3. Pitch Control System Using Magnets

A command input θ_c is shown entering the attitude control block of Figure 10-3. For present purposes it is sufficient to assume that this input will be used to implement one of the idealized control strategies presented in Section 9.2.2. That is, θ_c is used as follows in each of the control strategies

(1) θ_c = actual null torque attitude at all times, to follow the null torque attitude

(2) θ_c = nominal null torque attitude at all times, to hold a fixed attitude

Practical means of approximating these strategies will be discussed in a later section.

10.2 IMPLICATIONS OF MAGNETIC CONTROL

In the previous section it was assumed that the required pitch control torque could be produced by the magnets. This assumption will now be examined, along with the inter-axis coupling effects introduced by the magnets.

10.2.1 Interaxis Coupling

Commanding a torque about one body axis with a magnetic control system will in general produce magnetic torques in all three axes. In particular, if the commanded torque is about pitch only

$$\overline{T}_C = \begin{bmatrix} T_{Cx} \\ T_{Cy} \\ T_{Cz} \end{bmatrix} = \begin{bmatrix} 0 \\ T_{Cy} \\ 0 \end{bmatrix} \tag{10-9}$$

Equations (10-2) and (10-4) give the magnetic torque as

$$\overline{T}_M = \overline{T}_C - \frac{(\overline{T}_C \cdot \overline{B})}{\overline{B} \cdot \overline{B}} \overline{B} \tag{10-10}$$

or in this case

$$\overline{T}_M = \begin{bmatrix} - b_x \; b_y/b^2 \\ (1 - b_y^2)/b^2 \\ - b_y \; b_z/b^2 \end{bmatrix} T_{Cy} \tag{10-11}$$

where

$$b^2 = b_x^2 + b_y^2 + b_z^2 \tag{10-12}$$

It is clear that $\overline{T}_M = \overline{T}_C$ in this case if and only if $b_y = 0$.

Using the tilted dipole magnetic field model described in Appendix E, Figures 10-4 to 10-6 contain plots of the normalized magnetic torques $\overline{T}_M/T_{Cy}$ for orbit inclinations of 30, 60 and 90 degrees. These plots are representative over the entire 150 to 1000 km EVAL altitude range.

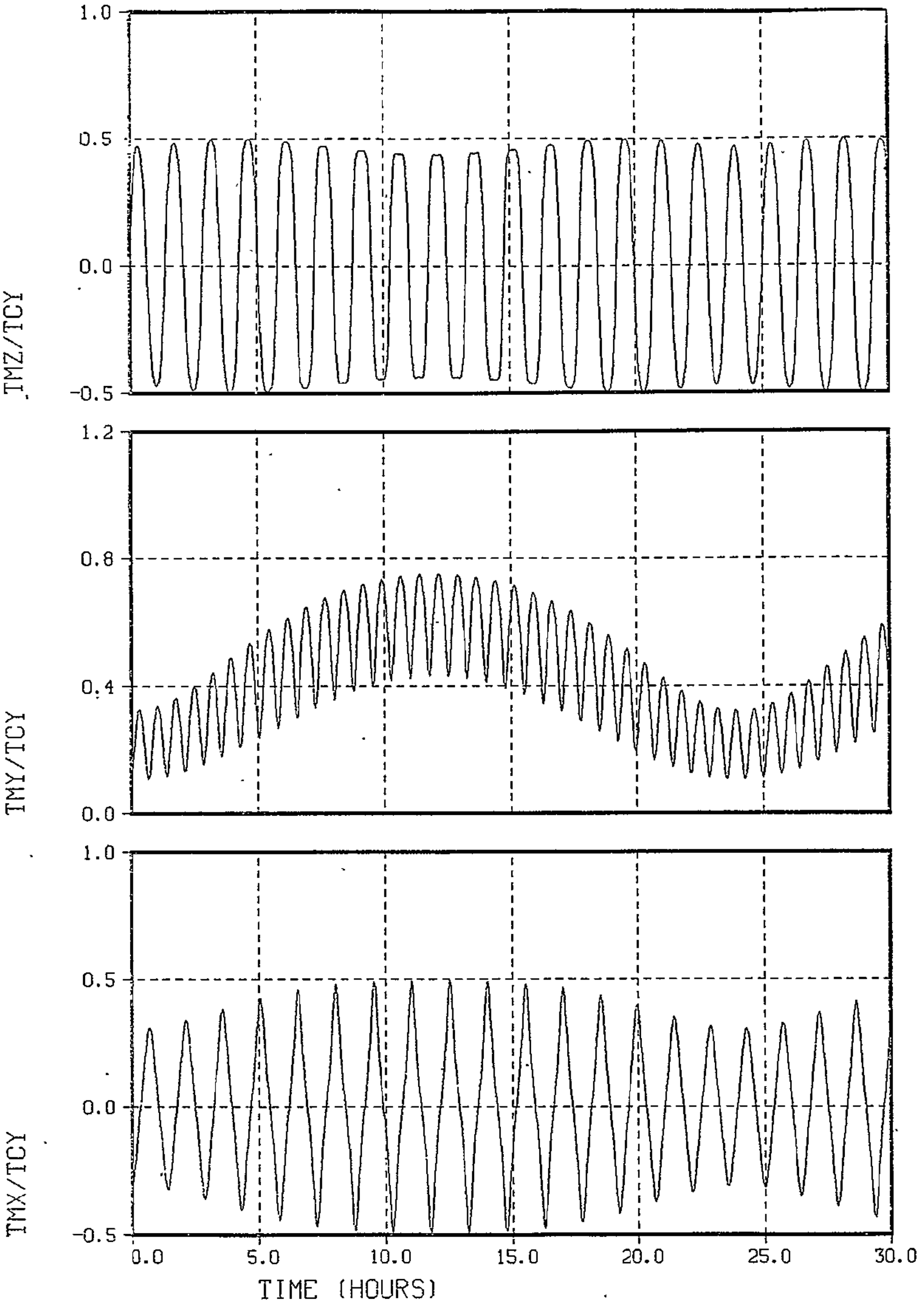

Figure 10-4. Normalized Magnetic Torque for Pitch Torque Command, h = 200 Km, i = 30 Deg

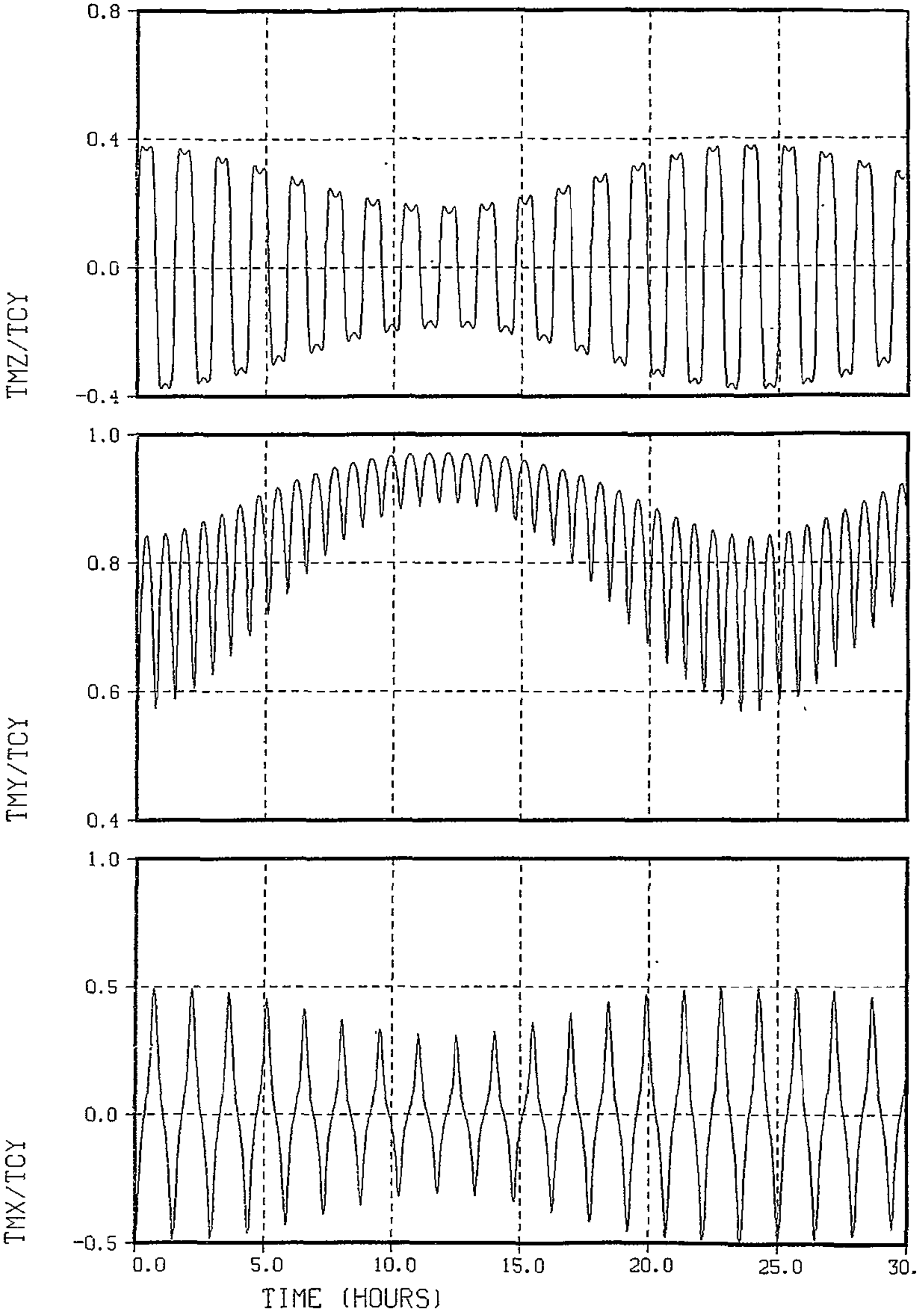

Figure 10-5. Normalized Magnetic Torque for Pitch Torque Command,
h = 200 Km, i = 60 Deg

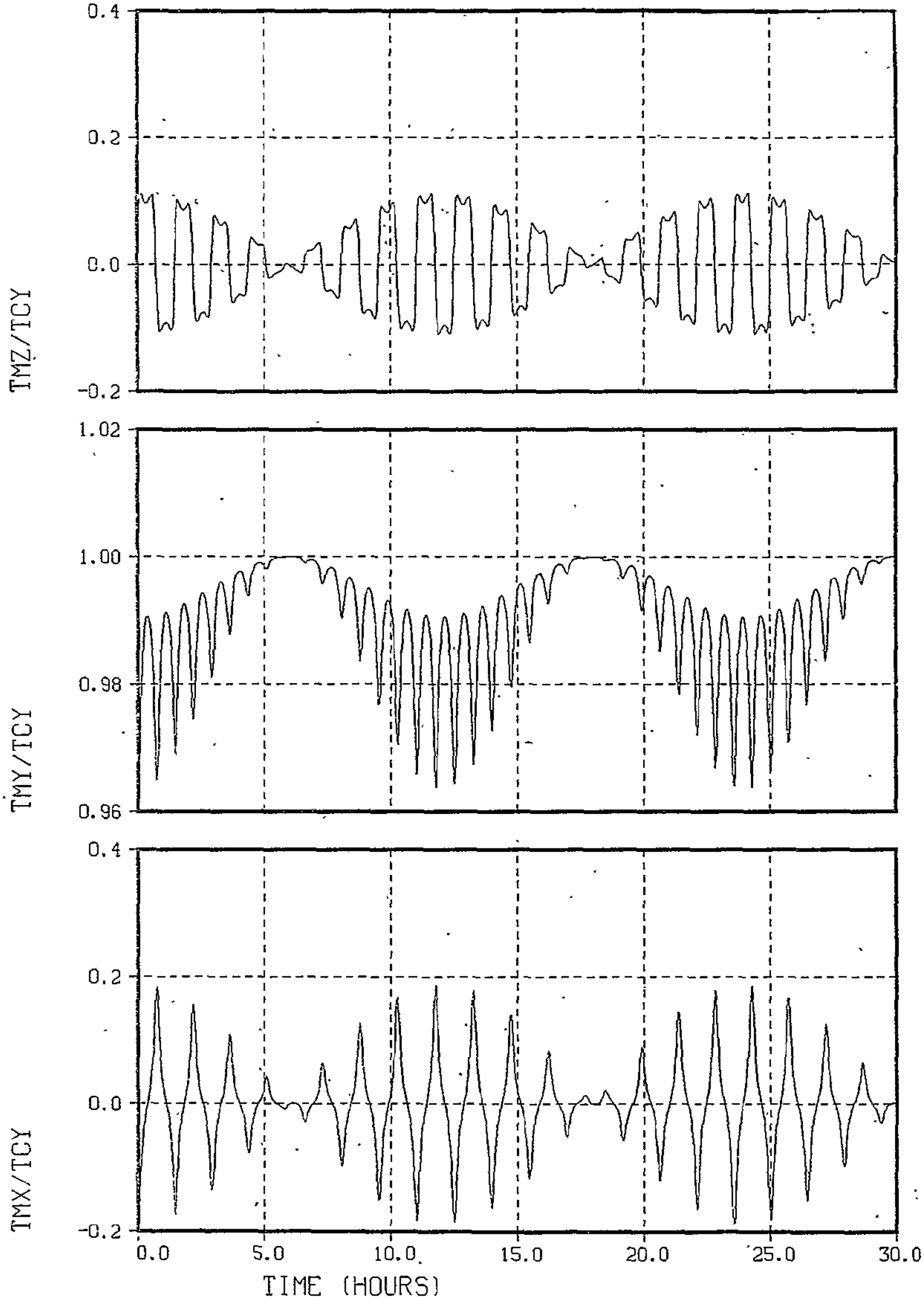

Figure 10-6. Normalized Magnetic Torque for Pitch Torque Command, h = 200 Km, i = 90 Deg

It is obvious from these figures that in low inclination orbits it is impossible to generate a magnetic torque solely, or even predominantly, along pitch. As has been previously stated, the control law embodied in Equation (10-10) is <u>optimal</u> with respect to minimizing the error between $\overline{T}_C$ and $\overline{T}_M$ and therefore no improvement is possible.

Figure 10-7 summarizes the ranges of the normalized magnetic torques as a function of orbit inclination. The maximum and minimum values are generally reached at least once each day. Therefore even at the "best" orbit inclination, i = 90 degrees, the coupling between the pitch torque command and roll magnetic torque will reach

$$T_{Mx}/T_{Cy} = 0.19$$

and the coupling between pitch torque command and yaw magnetic torque command and yaw magnetic torque will reach

$$T_{Mz}/T_{Cy} = 0.11$$

part of each day. Since pitch is unstable (at all altitudes) in the nose forward orientation, pitch control torque must be applied continuously and not just when the magnetic field conditions are favorable. Interference with roll and yaw control is therefore inevitable and, considering that roll is also open loop unstable, three-axis stability cannot be guaranteed.

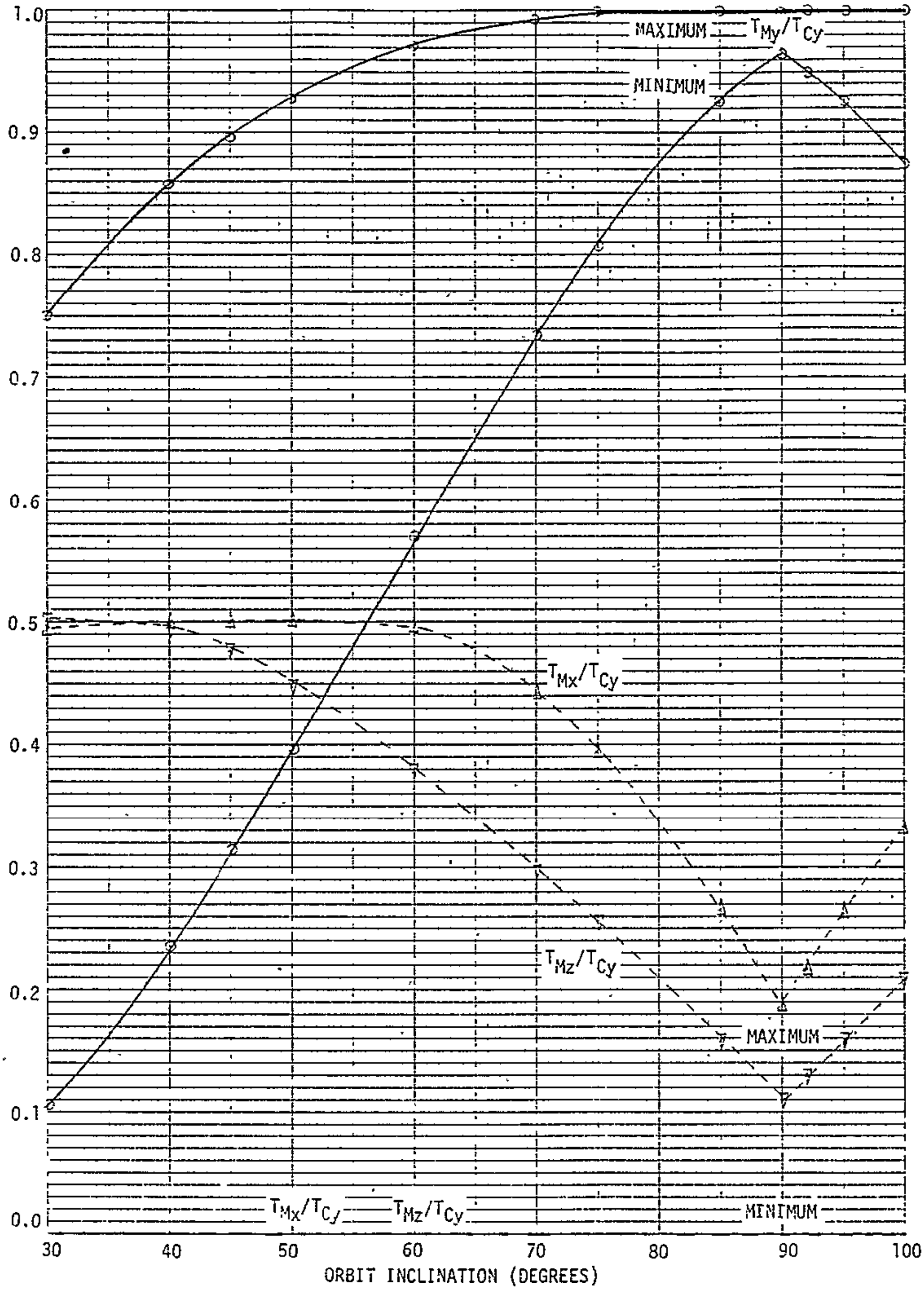

Figure 10-7. Normalized Magnetic Torque for Pitch Torque Command

10.2.2 Magnet Sizing

To successfully control an unstable axis, the magnets must be sized to produce sufficient control torque at all points of the orbit. From Equation (10-3), the magnetic moments implied by a pitch torque command T_{Cy} are

$$M_X = - (b_z/b^2)T_{Cy} \tag{10-13}$$

$$M_y = 0 \tag{10-14}$$

$$M_z = (b_x/b^2)T_{Cy} \tag{10-15}$$

The normalized magnetic moments M_x/T_{Cy} and M_z/T_{Cy} are plotted in Figures 10-8 to 10-10 for orbit inclinations of 30, 60 and 90 degrees at 200 km altitude. The peak values from these, and other similar plots, are summarized in Figure 10-11. It is apparent that the normalized magnetic moments range from about 2×10^7 to 5×10^7 pole-cm/N-m over the EVAL altitude range. Recall (Figure 10-7), however, that only near 90 degree inclination does the actual magnetic torque along y, T_{My}, come close to equalling the command torque T_{Cy}. When this fact is taken into consideration, the magnetic moment required to produce a given actual magnetic torque along pitch is minimized by assuming a 90 degree inclination orbit. This highly optimistic assumption is made in the following analysis.

Magnets with magnetic moments in the 10^4 pole-cm range have been used for momentum management on such spacecraft as TIROS, OSO, OAO,

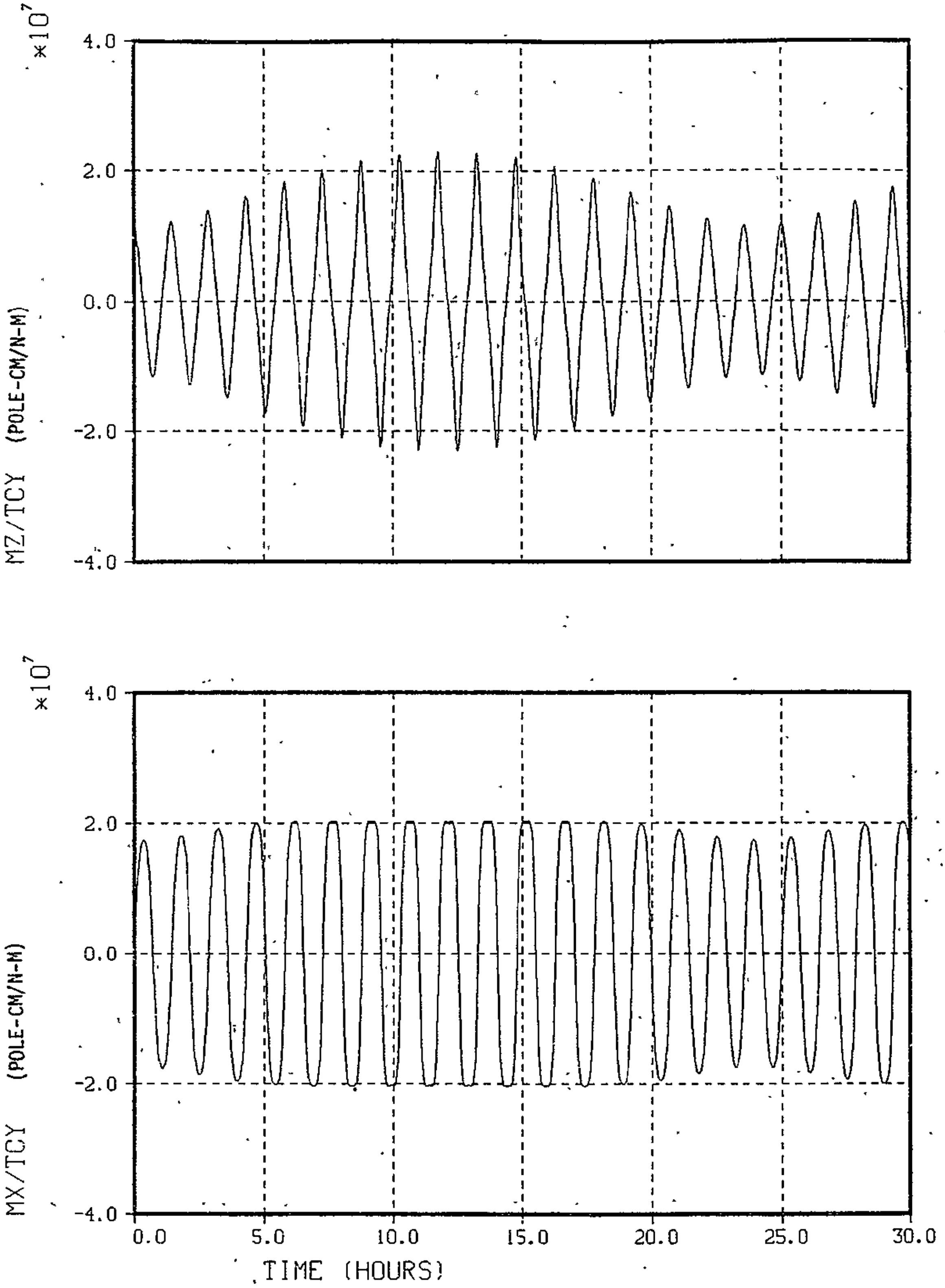

Figure 10-8. Normalized Magnetic Moments for Pitch Torque Command,
h = 200 km, i = 30 deg

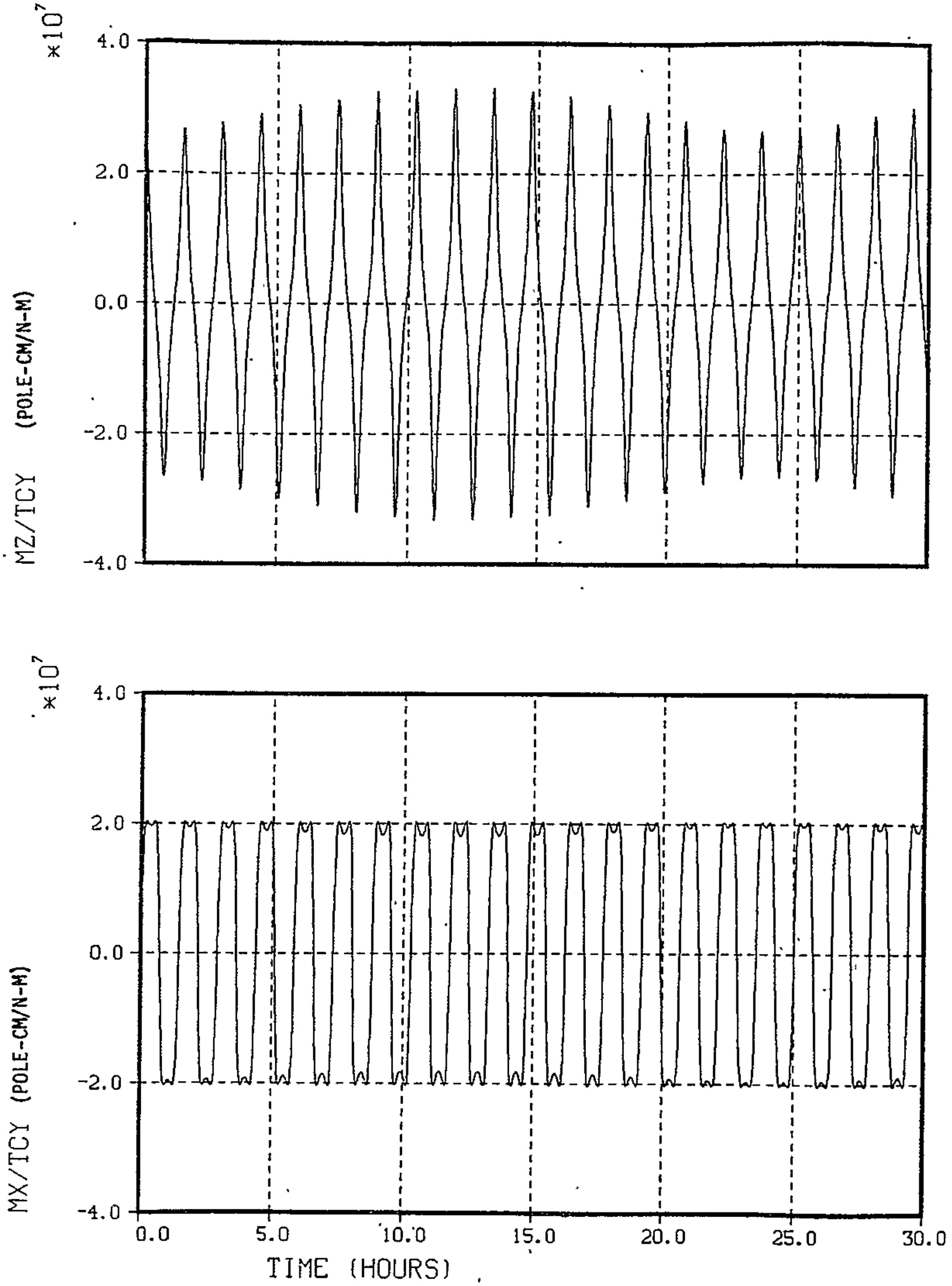

Figure 10-9. Normalized Magnetic Moments for Pitch Torque Command, h = 200 km, i = 60 deg

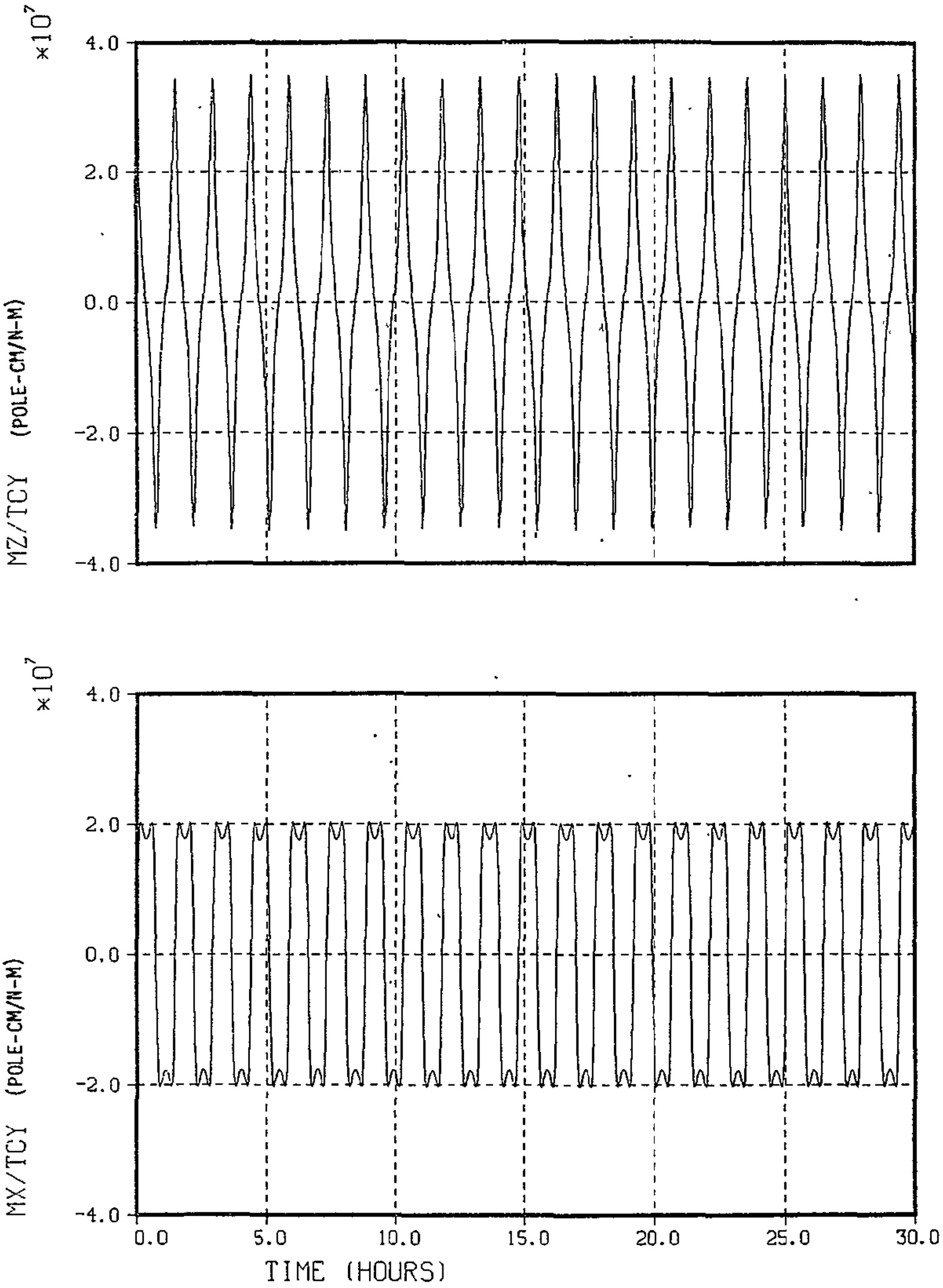

Figure 10-10. Normalized Magnetic Moments for Pitch Torque Command, h = 200 kn, i = 90 deg

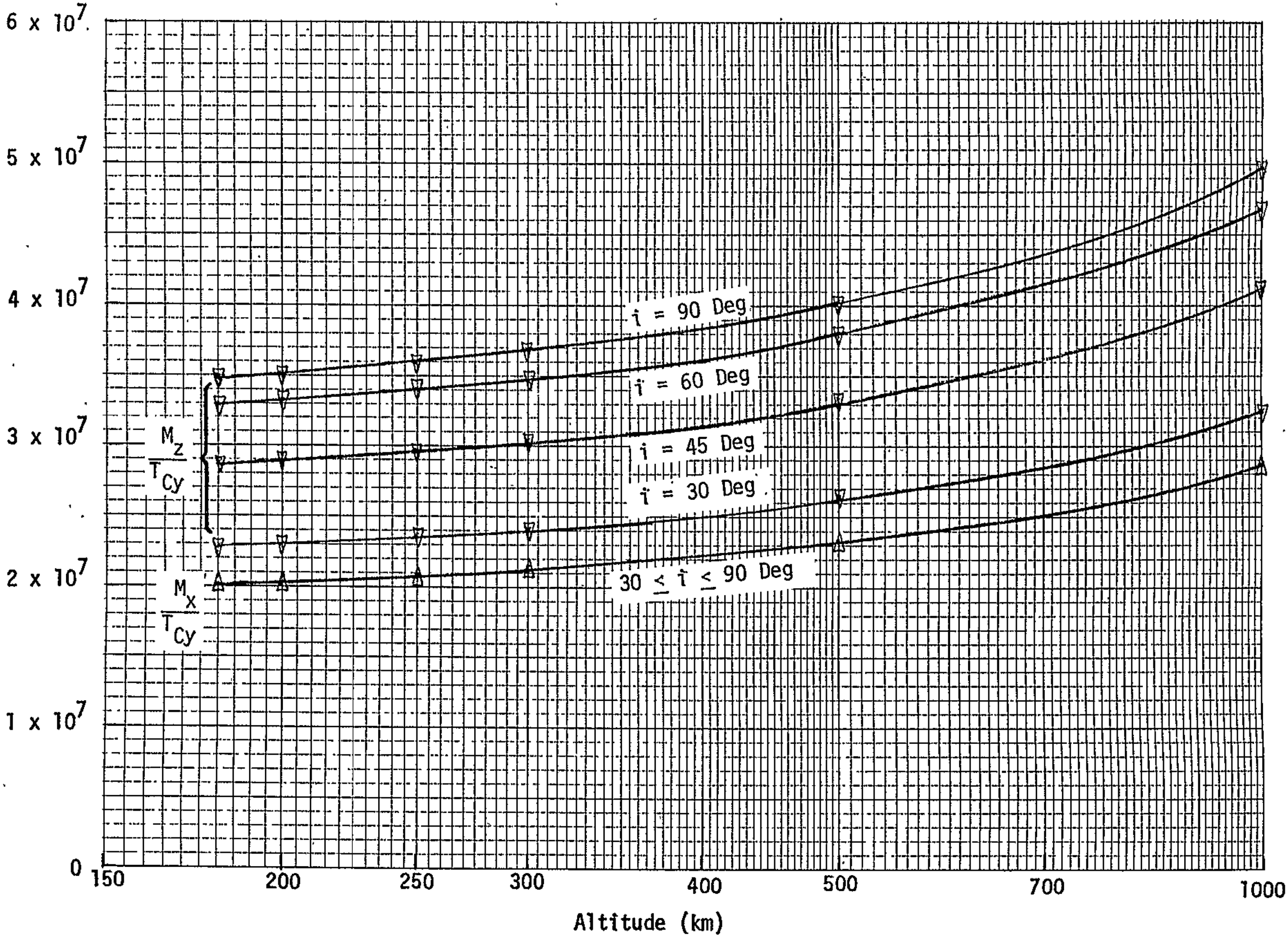

Figure 10-11. Peak Normalized Magnetic Moments

and SAS. Larger magnets, in the 10^6 pole-cm range, have been proposed for LST and other large spacecraft. It will be assumed here that the current practical limit is 10^7 pole-cm per axis. The estimated physical properties of such a set of magnets are listed in Table 10-1.

Another important consideration, that will not be addressed here, is the effect such large magnets will have on the operation of nearby payloads.

The maximum RCS limit cycle rates in pitch, from which attitude capture is possible with the 10^7 pole-cm magnets, are listed as a function of altitude in Table 10-2. The table is based on Figures 9-2 and 10-11 with a 90 degree inclination orbit. The table shows that capture from the nominal 0.01 deg/sec limit cycle is not possible, even with the optimistic assumptions made. In fact, the limit cycle rates must be reduced by a factor ranging from 23 at 200 km, to 40 at 1000 km. Even if a "low rate" RCS mode were provided, the variability and uncertainty inherent in the RCS would almost certainly preclude reliably achieving the rates required.

Assuming that the limit cycle rates can, somehow, be reduced to the required levels for attitude capture, there remains the need to supply continuous control torques to either follow the atmospheric density variation induced changes in the null torque attitude or to hold a constant atttitude. Figure 10-12 compares the pitch torque required to hold a constant attitude with the torque available using 10^7 pole-cm magnets. It is clear from the figure that even 10^7 pole-cm magnets are incapable of stabilizing the orbiter against short term atmospheric density variations in the nose down orientation below 265 km altitude.

10.3 CONCLUSIONS

Even if several optimistic assumptions are made, magnets are incapable of providing prolonged three axis stabilization for the orbiter. Among the points weighing against magnets are the following

Table 10-1. Estimated Physical Properties of 10^7 Pole-cm Per Axis Magnets

Parameter	Per Axis	Total 3-Axis
Magnetic Moment (Pole-cm)	10^7	-
Mass (kg)	146	438
Length (m)	7.70	-
Diameter (m)	0.065	-
Volume (m^2)	0.026	0.077
Power (Watts)	43.3	130

Table 10-2. Maximum RCS Limit Cycle Rate for Pitch Attitude Capture With 10^7 Pole-cm per Axis Magnets in 90 Degree Inclination Orbit

Altitude (Km)	Normalized Magnetic Moment (Pole-cm/N-m)		Pitch Torque With $m_x=m_z=10^7$ Pole-cm	Maximum RCS Limit Cycle Rate for Attitude Capture	Ratio of Nominal* to maximum RCS Limit Cycle Rate
	M_x/T_{Cy}	M_z/T_{Cy}	T_{Cy} (N-m)	$\dot{\theta}_{max}$ (deg/sec)	$\dot{\theta}_{Nom}/\dot{\theta}_{Max}$
180	2.01×10^7	3.49×10^7	0.287	4.3×10^{-4}	23
200	2.03×10^7	3.51×10^7	0.285	4.3×10^{-4}	23
250	2.08×10^7	3.60×10^7	0.278	4.0×10^{-4}	25
300	2.13×10^7	3.69×10^7	0.271	3.9×10^{-4}	26
500	2.32×10^7	4.02×10^7	0.249	3.5×10^{-4}	29
1000	2.87×10^7	4.97×10^7	0.201	2.5×10^{-4}	40

* $\dot{\theta}_{Nom} = 0.01$ deg/sec

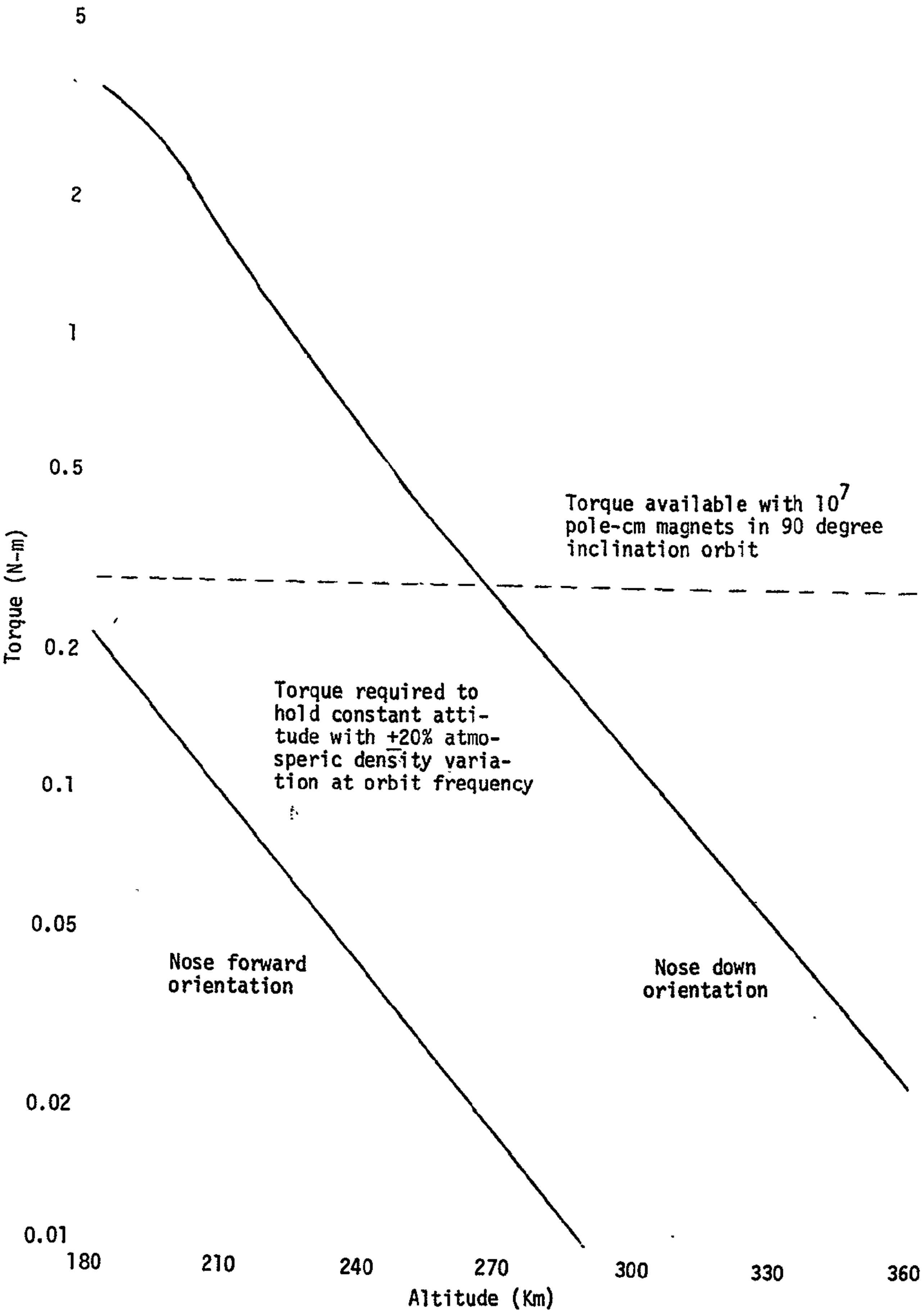

Figure 10-12. Comparison of Required Control Torque With Available Magnetic Torque

- Physical limitations of magnetic control due to the relative orbiter/magnetic field geometry introduce undesirable inter-axis coupling, with adverse effects on stability.

- very large magnets (10^7 pole-cm per axis) required for even marginal performance.

- RCS limit cycle rates must be reduced from current nominal values by a factor of 25 to 40 to permit attitude capture. The feasibility of doing this is highly doubtful.

- lack of reserve torque capability can result in loss of control due to variations in atmospheric density or orbiter mass properties.

- possible adverse effects of large magnetic field on nearby payloads

11.0 MOMENTUM EXCHANGE CONTROL OF ORBITER

Compared to magnets, momentum exchange devices offer the possibility of more accurate and sophisticated control, due to the higher magnitude and arbitrary direction of the available control torque. Potentially applicable momentum exchange devices include single gimbal and double gimbal CMG's (control moment gyros) and RW's (reaction wheels). For brevity, the discussion that follows is stated in terms of CMG's; the analysis applies to RW's as well, however.

11.1 SYSTEM EQUATIONS

Rather than assuming a particular CMG configuration, the discussion will be in terms of the orbiter body axis components of the CMG cluster momentum

$$\bar{h} = \begin{bmatrix} h_x \\ h_y \\ h_z \end{bmatrix}$$

The state vector $\bar{x}$ will be defined as the 12-vector

$$\bar{x} = \begin{bmatrix} \bar{\delta} \\ --- \\ \bar{\omega}_R \\ --- \\ \bar{h} \\ --- \\ \bar{n} \end{bmatrix}$$

where $\bar{h}$ was defined above and

$$\bar{\delta} = \begin{bmatrix} \phi \\ \theta \\ \psi \end{bmatrix} = \text{small angle perturbations from null torque attitude.} \qquad (11\text{-}3)$$

$$\bar{\omega}_R = \bar{\omega} - \omega_o \, \hat{y}_B = \begin{bmatrix} \omega_x \\ \omega_y - \omega_o \\ \omega_z \end{bmatrix} = \text{inertial rates of body relative to orbit reference frame.} \qquad (11\text{-}4)$$

$$\bar{\eta} = \begin{bmatrix} \eta_x \\ \eta_y \\ \eta_z \end{bmatrix} = \text{time integrals of wheel momenta} \qquad (11\text{-}5)$$

The reason for including $\bar{\eta}$ will become apparent later.

With these definitions, the small angle dynamic and kinematic equations become

$$\dot{\bar{\omega}}_R = \bar{\bar{I}}^{-1} \cdot [\bar{\omega} \times (\bar{\bar{I}} \cdot \bar{\omega} + \bar{h}) + K\bar{\delta} + \dot{\bar{h}} + \delta\bar{T}_{A_p}] \qquad (11\text{-}6)$$

$$\dot{\bar{\delta}} = \bar{\omega}_R + \tilde{\omega}\, \bar{\delta} \qquad (11\text{-}7)$$

where $\overline{\overline{I}}$ is the orbiter inertia dyadic, K is the disturbance torque compliance matrix, $\dot{\bar{h}}$ is the CMG torque vector, $\delta \bar{T}_{A\rho}$ is the aerodynamic disturbance perturbation due to atmospheric density variations and

$$\tilde{\omega} = \begin{bmatrix} 0 & 0 & -\omega_0 \\ 0 & 0 & 0 \\ \omega_0 & 0 & 0 \end{bmatrix} \tag{11-8}$$

The differential equation for $\bar{n}$ is, by assumption,

$$\dot{\bar{n}} = \bar{h} \tag{11-9}$$

There remains to determine the differential equation for $\bar{h}$, defining the CMG control law. The form of this equation can be selected to yield the desired control characteristics, and will be assumed here to be a combination of linear state variable feedback and a term to cancel the nonlinear coupling terms in the dynamics

$$\dot{\bar{h}} = G\,\bar{x} - \bar{\omega} \times (\overline{\overline{I}} \cdot \bar{\omega} + \bar{h}) \tag{11-10}$$

where G is in general a 3 x 12 gain matrix composed of four 3 x 3 submatrices

$$G = \left[G_\delta \;\vdots\; G_\omega \;\vdots\; G_h \;\vdots\; G_n \right] \quad (11\text{-}11)$$

Since the exact location of the null torque attitude is not known <u>a priori</u>, a more realistic form of the control law is

$$\dot{\bar{h}} = G\,\hat{x} - \bar{\omega} \times (\bar{\bar{I}} \cdot \bar{\omega} + \bar{h}) \quad (11\text{-}12)$$

where $\hat{x}$ is obtained from $\bar{x}$ by substituting for the actual $\bar{\delta}$ vector the estimated small angle perturbation from the null torque attitude

$$\hat{\delta} = \bar{\delta}_B - \hat{\delta}_o \quad (11\text{-}13)$$

where

$$\bar{\delta}_B = \begin{bmatrix} \phi_B \\ \theta_B \\ \psi_B \end{bmatrix} = \text{Actual euler angles in } A_{BN} \text{ matrix} \quad (11\text{-}14)$$

$$\hat{\delta}_o = \begin{bmatrix} \hat{\phi}_o \\ \hat{\theta}_o \\ \hat{\psi}_o \end{bmatrix} = \text{Estimated euler angles in } A_{ON} \text{ matrix} \quad (11\text{-}15)$$

and the A_{BN} and A_{ON} matrices are as defined in Section 8.1.1.

Similarly,

$$\bar{\delta} = \bar{\delta}_B - \bar{\delta}_o \tag{11-16}$$

where

$$\bar{\delta}_o = \begin{bmatrix} \phi_o \\ \theta_o \\ \psi_o \end{bmatrix} = \text{Actual euler angles in } A_{ON} \text{ matrix} \tag{11-17}$$

The implicit assumption is made in Equations (11-13) and (11-17) that at most one element of $\hat{\delta}_o$ or $\bar{\delta}_o$ is a large angle; this is true for the nose forward and nose down orientations under consideration, with $\phi_o \cong \psi_o \cong 0$.

With the assumed CMG control law the orbiter dynamics are described by

$$\dot{\bar{\omega}} = - \bar{\bar{I}}^{-1} \cdot [G\hat{x} + K\bar{\delta} + \delta\bar{T}_{A\rho}] \tag{11-18}$$

or in terms of the euler angles

$$\bar{\delta} = \tilde{\omega}\, \dot{\bar{\delta}} - \bar{\bar{I}}^{-1} [G\hat{x} + K\bar{\delta} + \delta\bar{T}_{A\rho}] \tag{11-19}$$

11.2 CONTROL DESIGN

As the pitch axis has the largest potential control problems (highly unstable in the nose forward orientation, large variation in null torque attitude in the nose down orientation, this axis will be treated here. Figure 11-1 contains a block diagram of a control system of the type discussed in the previous section, with the notation slightly changed to emphasize the physical structure. The nonlinear coupling compensation terms in Equation (11-12) do not appear in the single axis analysis and are in any case relatively small. The control system can be understood in terms of a conventional attitude loop and two ada

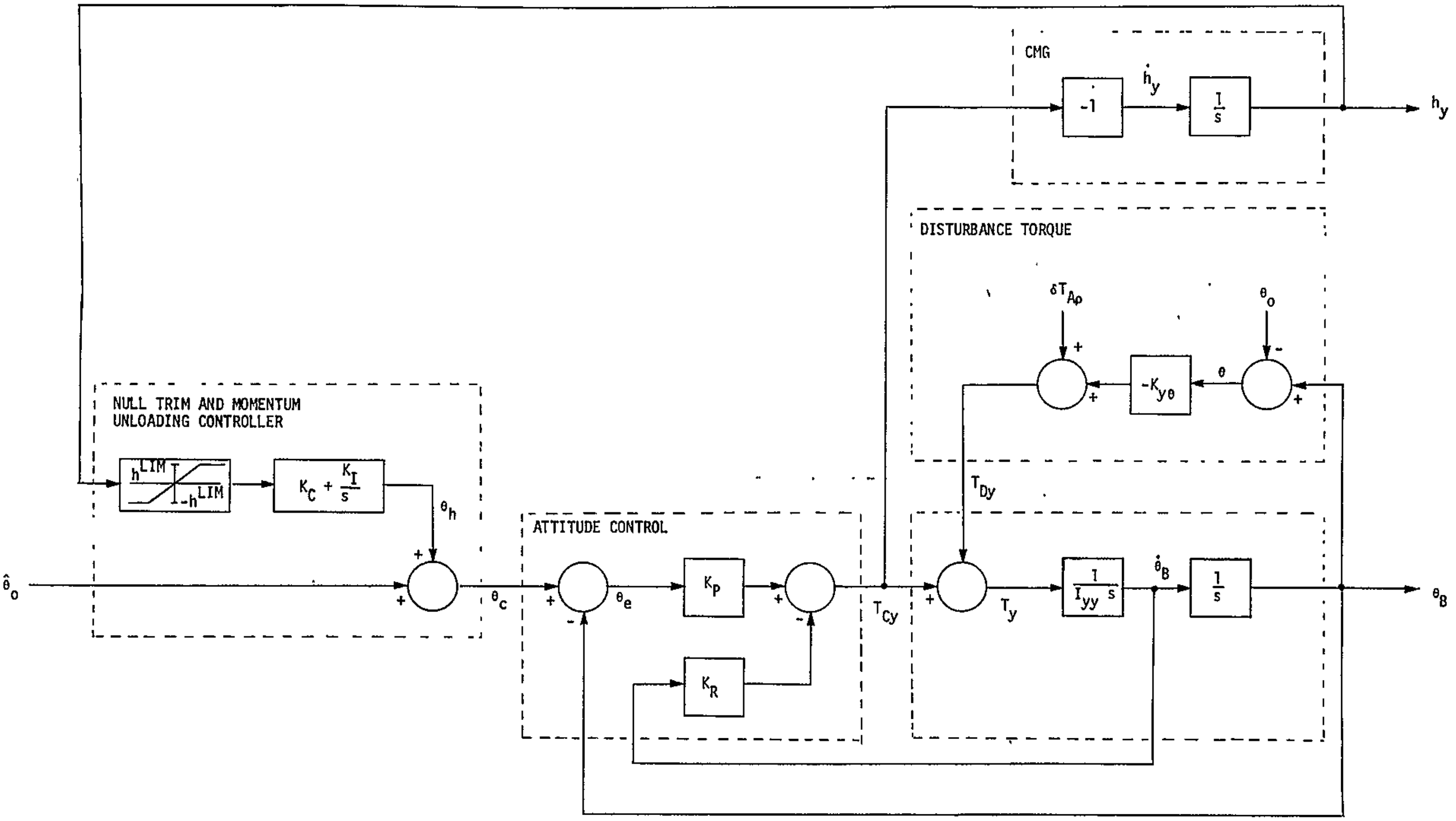

Figure 11-1. CMG Pitch Control System

- attitude loop (K_P and K_R) - tends to drive θ_B to $\theta_C = \hat{\theta}_0 + \theta_h$ and $\dot{\theta}_B$ to zero.

- null trim loop (K_C) - provides adaptive attitude command correction based on momentum stored in CMG to drive θ_B to the true null torque attitude θ_0 despite errors in the estimate of its location $\hat{\theta}_0$.

- momentum unloading loop (K_I) - provides offset, from adaptively determined null torque attitude, based on integral of wheel momentum, to utilize disturbance torque for unloading the CMG. (Most effective when $|K_{y\theta}|$ is large.)

When both adaptive loops are used, and the gains are selected to yield a stable system, the final steady state values will be $\theta_B = \theta_0$, $h_y = 0$ in a constant atmospheric density environment. If the K_I loop is omitted, the stored CMG momentum will reach a steady state value different from zero, unless $\hat{\theta}_0 = \theta_0$. In this case the RCS thrusters could be fired briefly for momentum unloading. The adaptive loop feedback limiter improves the large signal transient response during initial captive from the RCS limit cycle.

The gains required to yield a particular set of closed loop roots can be obtained by matching coefficients in the characteristic equation. In the case where two roots are complex conjugates and two are real, the characteristic equation is

$$d(s) = (s^2 + 2\omega\,\zeta\, s + \omega^2)(s + \lambda)(s + \eta) \tag{11-20}$$

and the required control gains are

$$K_P = \left[\omega^2 + 2\omega\,\varepsilon\,(\lambda + \eta) + \lambda\eta - \frac{\lambda\,\eta\,\omega^2\, I_{yy}}{K_{y\theta}}\right] I_{yy} - K_{y\theta} \tag{11-21}$$

$$K_R = \left\{ 2\omega\,\varepsilon + \lambda + \eta - \left[\frac{2\omega\,\varepsilon\,\lambda\,\eta + \omega^2(\lambda + \eta)}{K_{y\theta}}\right] I_{yy} \right\} I_{yy} \tag{11-22}$$

$$K_C = \frac{I_{yy}}{K_P}\left[\frac{2\omega\,\varepsilon\,\lambda\,\eta + \omega^2(\lambda + \eta)}{K_{y\theta}}\right] \tag{11-23}$$

$$K_I = \frac{1}{K_P}\left[\frac{\lambda\,\eta\,\omega^2\, I_{yy}}{K_{y\theta}}\right] \tag{11-24}$$

Different sets of gains will in general be required depending on whether the orbiter is in the nose forward or nose down orientation, and whether the operating mode is initial capture from the orbiter RCS limit cycle or normal long term stabilization. The considerations entering the design for each of these conditions and sample designs are presented in the following subsection.

11.3 INITIAL CAPTURE FROM RCS LIMIT CYCLE

In general, the largest torque and momentum requirements will be during the initial capture transient from the RCS limit cycle rather than during steady state operation. Because of the complexity of the system, accurate sizing can only be done by simulation. Analysis is useful, however, for obtaining a rough sizing estimate and establishing the relative importance of the various factors influencing the torque and momentum requirements. The analysis here assumes a constant atmospheric density over the capture interval; density variations are considered in the normal operation section.

11.3.1 Momentum Estimate

If no unloading takes place during the transient, the stored momentum consists of two terms

- the excess momentum initially stored in the orbiter due to its RCS limit cycle rate.
- the net momentum absorbed from the disturbance torque due to being off the null torque attitude.

The first term is, assuming the nominal RCS limit cycle rates of 0.01 deg/sec.

$$\bar{h}_R = \bar{\bar{I}} \cdot \omega_R \qquad (11\text{-}25)$$

$$= \begin{bmatrix} (1.24 \times 10^6 \text{ kg-m}^2)(1.75 \times 10^{-4} \text{ rad/sec}) \\ (9.39 \times 10^6 \text{ kg-m}^2)(1.75 \times 10^{-4} \text{ rad/sec}) \\ (9.72 \times 10^6 \text{ kg-m}^2)(1.75 \times 10^{-4} \text{ rad/sec}) \end{bmatrix} = \begin{bmatrix} 216 \text{ N-m-sec} \\ 1639 \text{ N-m-sec} \\ 1696 \text{ N-m-sec} \end{bmatrix}$$

The peak value of the second term depends on the details of the transient response and is therefore more difficult to determine. As a rough estimate, the steady state value for the control system describec in the previous section will be examined. If $K_I = 0$, the steady state momentum stored is, for pitch,

$$- \; h_{Dy}^{ss} = \frac{\theta_o - \hat{\theta}_o}{K_C} \tag{11-26}$$

or in terms of the closed loop roots

$$h_{Dy}^{ss} = \left(1 + \frac{2\,\zeta\,\lambda}{\omega} - \frac{K_{y\theta}}{\omega^2\, I_{yy}}\right) \frac{K_{y\theta}\,(\theta_o - \hat{\theta}_o)}{\lambda} \tag{11-27}$$

For example if

$\omega = 0.002$ rad/sec

$\zeta = 0.5$

$\lambda = 0.001$ rad/sec

$K_{y\theta} = -\,33.8$ N-m/rad

$I_{yy} = 9.39 \times 10^6$ kg-m^2

$\theta_o - \hat{\theta} = 0.2$ deg

the steady state momentum would be

$$h_{Dy}^{ss} = 283 \text{ N-m-sec}$$

The peak stored momentum due to the disturbance torque is actually several times as large, as will be shown by simulation. However, the momentum due to the limit cycle rate is still the largest term.

11.3.2 Torque Estimate

The largest control torque is required in pitch in the unstable nose forward orientation. Equation 11-12 shows that the pitch control torque $(T_{Cy} = -\dot{h}_y)$ consists of a feedback term

$$(T_{Cy})_{FB} = - G\hat{x} = K_P \left(\hat{\theta}_o - \theta_B + K_C h_y + K_I \int h_y \, dt\right) - K_R \dot{\theta}_B \qquad (11\text{-}28)$$

and a decoupling term.

$$(T_{Cy})_{DEC} = [\bar{\omega} \times (\bar{\bar{I}} \cdot \bar{\omega} + \bar{h})]_y = \omega_x \omega_z (I_{xx} - I_{zz}) + (h_x \omega_z - h_z \omega_x) \qquad (11\text{-}29$$

As with the momentum, the actual peak torque depends on details of the transient behavior and is best determined by simulation. If the damping ratio ζ is relatively high, however, the peak torque will occur near $t = 0$ and can be approximated by

$$(T_{Cy})_{PEAK} \approxeq K_P(\hat{\theta}_o - \theta_B(0)) - K_R \dot{\theta}_B(0) + \omega_x(0)\, \omega_z(0)(I_{xx} - I_{zz}) . \qquad (11\text{-}30)$$

For example, suppose the initial conditions are

$\hat{\theta}_o - \theta_B = 0.2$ deg

$\dot{\theta}_B(0) = \omega_x(0) = \omega_z(0) = 0.01$ deg/sec

and the closed loop roots are selected as

$\omega = 0.002$ rad/sec

$\zeta = 0.5$

$\lambda = \eta = 0.001$ rad/sec

with

$I_{xx} = 1.24\times10^6$ kg-m^2

$I_{yy} = 9.39\times10^6$ kg-m^2

$I_{zz} = 9.72\times10^6$ kg-m^2

$K_{y\theta} = - 33.8$ N-m/rad

The position gain is then

$$K_P = 129 \text{ N-m/rad}$$

and the rate gain is

$$K_R = 63600 \text{ N-m/(rad/sec)}$$

The feedback components of the control torque are in turn

$$K_P(\theta_0 - \theta_B(0)) = 0.45 \text{ N-m}$$

$$K_R \dot{\theta}_B(0) = 11.1 \text{ N-m}$$

while the decoupling term is

$$\omega_x(0)\ \omega_z(0)\ (I_{xx} - I_{zz}) = 0.26 \text{ N-m}$$

The total torque, 11.8 N-m, is clearly dominated by the rate feedback term, while the decoupling term gives the smallest contribution.

11.3.3 Simulation

To better understand the control system operation and verify the sizing estimates of the previous sections, a single-axis simulation of the pitch control system shown in Figure 11-1 was conducted. The parameter values used are listed in Table 11-1, the results are

Table 11-1. Initial Capture Transient Simulation Parameter Summary

Symbol	Parameter	Value	Units
ω	Bandwidth } Of dominant roots	0.002	rad/sec
ζ	Damping } Of dominant roots	0.5	-
λ	Null Trim Loop Root	0.001	rad/sec
η	Momentum Unloading Loop Root	0.001	rad/sec
K_P	Position Gain	129	N-m/rad
K_R	Rate Gain	6.36×10^4	N-m/(rad/sec)
K_C	Momentum Feedback Gain	-2.16×10^{-5}	rad/(N-m-sec)
K_I	Momentum Integral Feedback Gain	-8.63×10^{-9}	rad/(N-m)
I_{yy}	Pitch Inertia	9.39×10^6	kg-m^2
$K_{y\theta}$	Pitch Disturbance Compliance	-33.8	N-m/rad
h^{LIM}	Adaptive Loop Feedback Limit	1500	N-m-sec

summarized in Table 11-2, and time plots are presented in Figures 11-2 to 11-4. The two cases run represent the open loop unstable nose forward orientation, and differ only in the value of the initial rate. For added realism, the initial attitude $\theta_B(0) = 0.1$ degree differs from both the actual null torque attitude $\theta_0 = -0.2$ degree and the estimated null torque attitude $\hat{\theta}_0 = 0$. Both cases cover 6000 seconds, or slightly more than one orbit.

In case 1, the rate initial condition is the nominal RCS limit cycle rate of 0.01 deg/sec. As shown in Figure 11-2, the torque reaches a peak value of 11.3 N-m at t = 0. This is in reasonable agreement with the estimate of the feedback terms in the previous section. The stored momentum reaches a peak value of 2580 N-m-sec, of which approximately 1640 N-m-sec can be attributed to the transfer of the limit cycle motion momentum from the orbiter body to the CMG's. The stored momentum is almost completely unloaded at the end of the run, while the attitude is slowly converging to the true torque null. The nonlinear effect of the adaptive loop feedback limiter is apparent in the plots; use of this limiter reduces the peak momentum requirement by 410 N-m-sec.

In case 2, the initial rate was reduced by a factor of 10 compared to case 1, to 0.001 deg/sec. As shown in Figures 11-3 and 11-4, the convergence to the true torque null is considerably more rapid, the momentum is unloaded sooner, and the peak torque is reduced to 1.34 N-m, while the peak momentum is reduced to 429 N-m-sec.

11.4 NORMAL OPERATION

In normal operation following the initial capture transient, the major influence on the orbiter null torque attitude stabilization system performance at low altitudes is variations in atmospheric density. The design example presented in the previous subsection provides adequate performance during the capture transient, but is excessively sensitive to disturbance torque variations with frequency components near orbit frequency. Designs with lower sensitivities will now be described.

Table 11-2. Initial Capture Transient Simulation Result Summary

Case	Figures	Initial Conditions					Peak Values	
		θ_B (deg)	$\dot{\theta}_B$ (deg/sec)	θ_o (deg)	$\hat{\theta}_o$ (deg)	h_y (N-m-sec)	$\dot{h}_y$ (N-m)	h_y (N-m-sec)
1	11-2	0.1	0.01	-0.2	0	0	11.3	2580
2	11-3, 11-4	0.1	0.001	-0.2	0	0	1.34	429

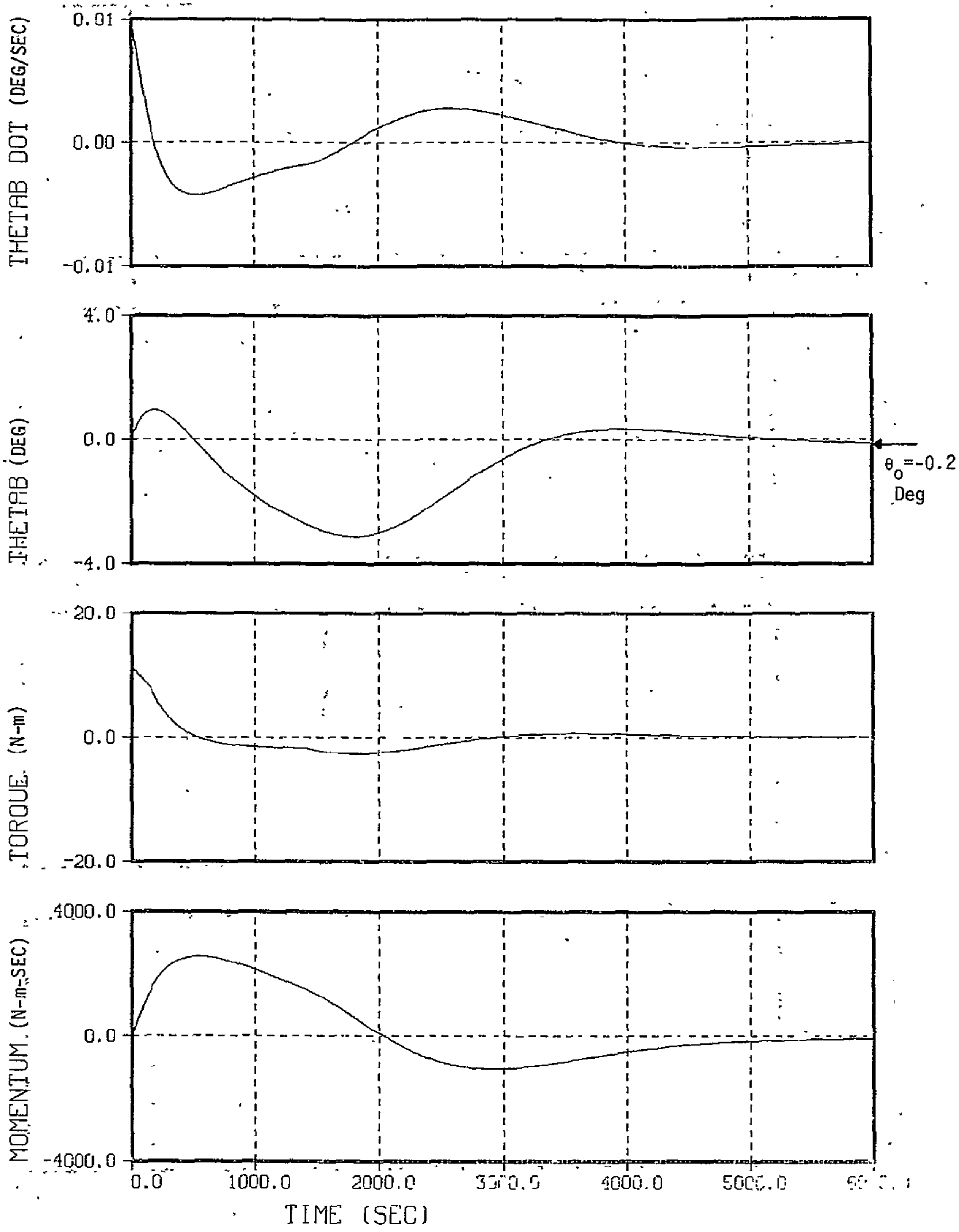

Figure 11-2. Case 1: Pitch Convergence From Nominal RCS Limit Cycle in the Nose Forward Orientation

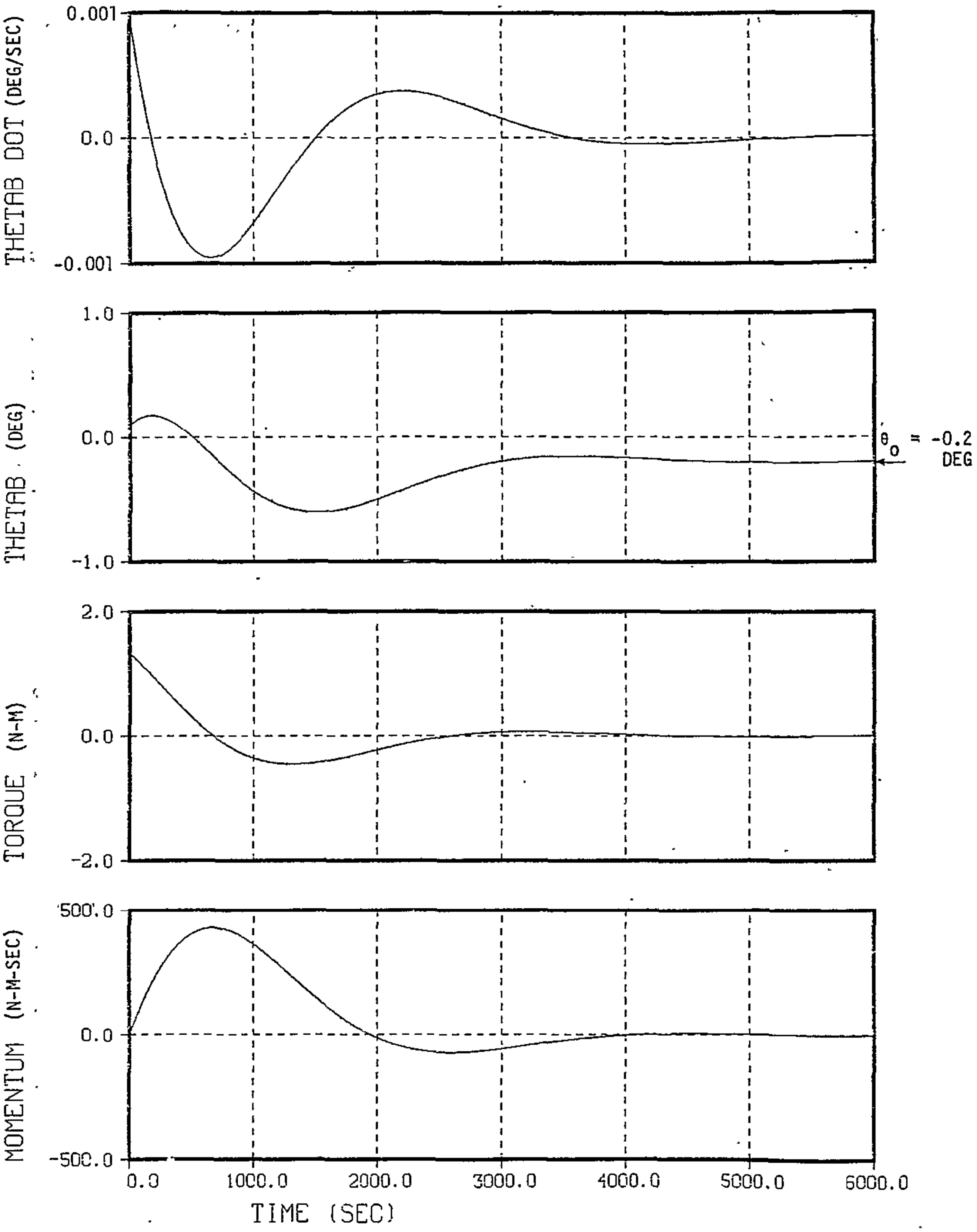

Figure 11-3. Case 2: Pitch Convergence From 0.1 x Nominal Rate RCS Limit Cycle in Nose Forward Orientation

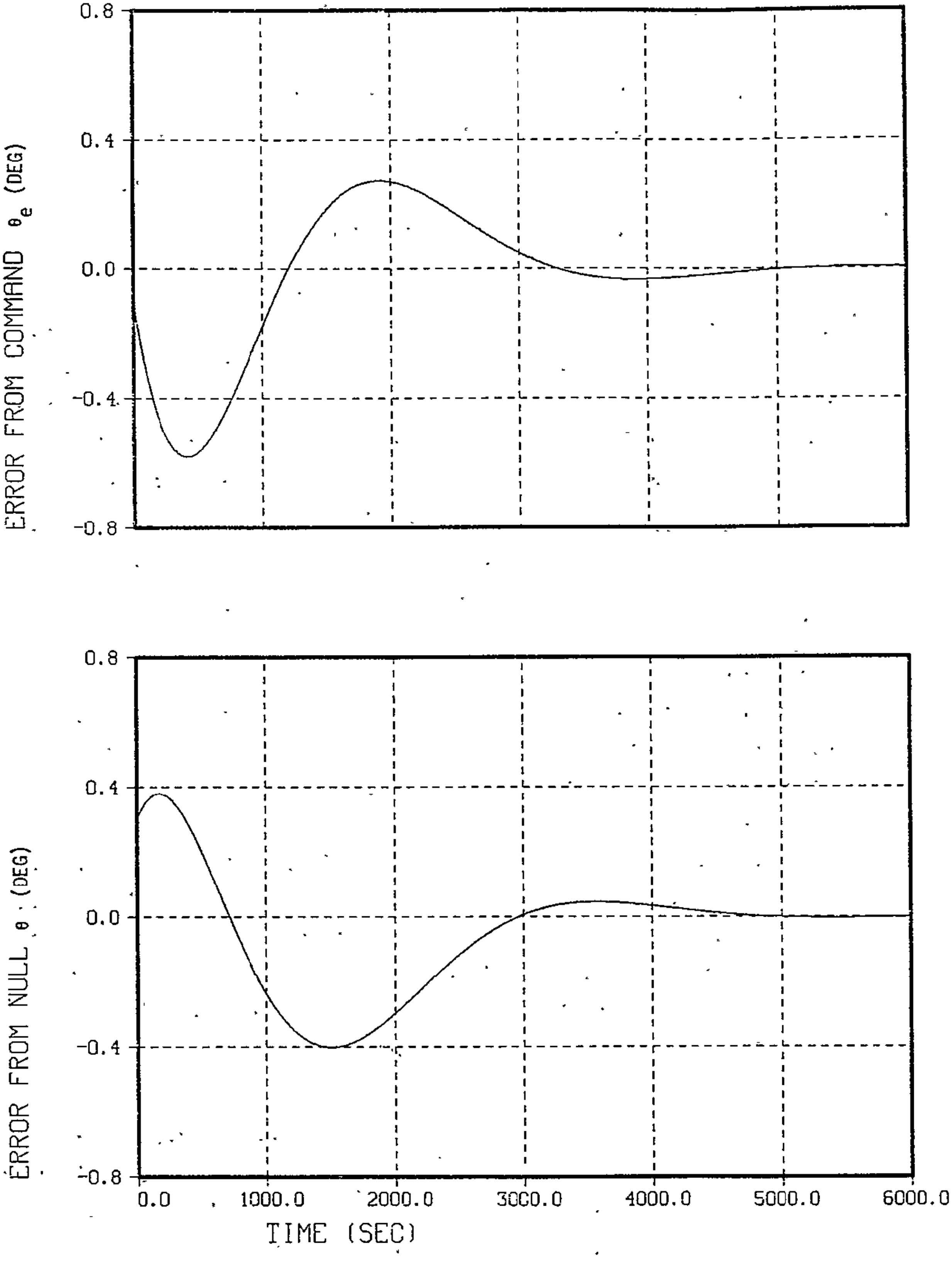

Figure 11-4. Case 2: Pitch Convergence From 0.1 x Nominal Rate RCS Limit Cycle in Nose Forward Orientation

11.4.1 Selection of Control Law

Two idealized control strategies for dealing with periodic disturbance torque variations were described in Section 9.2.2. These were:

(1) Follow the null torque attitude exactly at all time

(2) Hold the nominal null torque attitude exactly at all times

The first strategy requires a precise knowledge of the location of the instantaneous orbiter null torque attitude, a condition that is all but impossible to meet in practice. The second strategy only requires the mean or nominal null torque attitude, but any error in its estimate results in a secular momentum buildup in the CMG's. To achieve a practical control design, a compromise must be made between holding the orbiter attitude steady and minimizing the required CMG momentum storage capability.

The nature of the design depends strongly on the orbiter orientation. In the nose forward orientation, even a ±50% variation in atmospheric density at h = 180 Km results ideally in a momentum perturbation δh of only ±167 N-m-sec and an attitude perturbation $\delta\theta_B$ of ±1.2 deg if the null torque is followed, or a momentum perturbation of ±500 N-m-sec and no attitude perturbation if the attitude is held. In either case, the momentum change is less than that required to capture from a 0.001 deg/sec limit cycle. On the other hand, in the nose down orientation very large attitude and momentum perturbations are possible at altitudes below 250 Km. Figure 11-5 shows the peak-to-peak momentum and attitude perturbations resulting from ±20% variations in atmospheric density using either of the control strategies previously described. For all altitudes above 185 Km less momentum is required to follow the null torque attitude variations at orbit frequency than to hold a constant attitude. However, this approach results in large attitude excursions at low altitudes.

It was demonstrated in Section 9.2.2 that the momentum storage requirement is minimized by following variations in the null torque attitude with frequencies less that $\sqrt{|K_{y\theta}|/I_y}$ and resisting attitude perturbations caused by null torque attitude variations with frequencies greater than $\sqrt{|K_{y\theta}|/I_y}$.

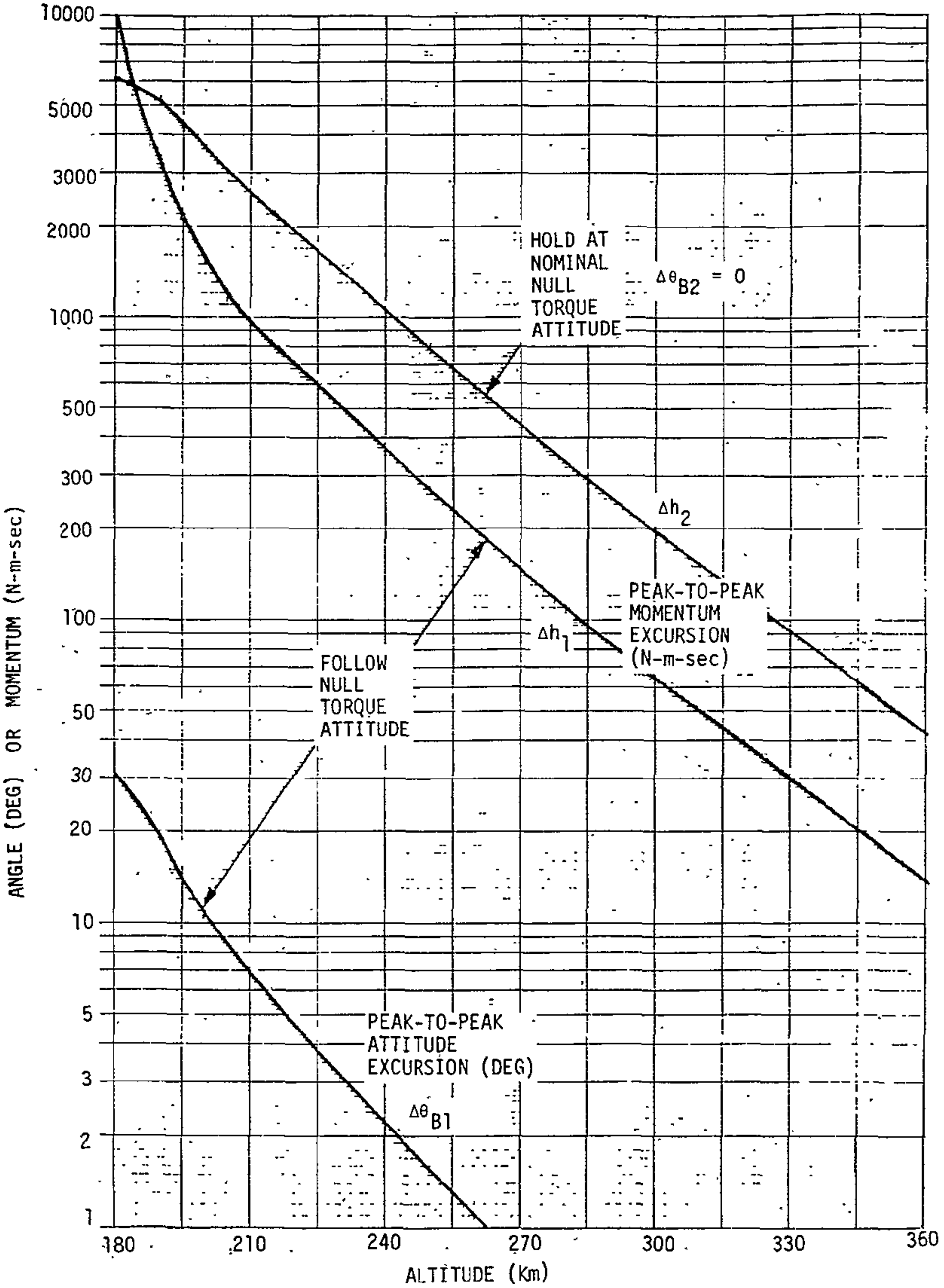

Figure 11-5. Attitude and Momentum Excursions Due to ±20% Atmospheric Density Variation at Orbit Frequency in Nose Down Orientation With Idealized Control

This control strategy, which approximates each of the two idealized control strategies over different frequency bands, is adopted for normal pitch control.

The assumed structure of the pitch control law is shown schematically in Figure 11-6. The compensation is more general than in Figure 11-1, with a lag (T_L) added to the momentum feedback shaping and integral compensation (K_F) added to the attitude loop. Since the null torque attitude is not known a priori, the momentun feedback shaping is used to attempt to adaptively seek the true null torque attitude and also unload excess momentum. Each of the two orbiter orientations is treated separetely, due to the open loop stability differences.

11.4.2 Nose Forward Orientation

In this orientation the disturbance compliance $K_{y\theta}$ is dominated by the gravity gradient slope of 33.92 N-m/rad for small offset angles, and pitch is open loop unstable. A large number of cases were analyzed with various combinations of non-zero gains. Five of the better cases are summarized in Table 11-3 and the ratios $H(\omega) = \delta h/\delta T_{A\rho}$ are plotted in Figure 11-7. In case 1, $K_c = K_I = 0$ and there is no adaptive action to seek the null torque attitude. The attitude therefore remains nearly constant and the momentum grows without bound, indicated by the fact that $H(0) = \infty$. In case 2, $K_c \neq 0$, and a step change in $T_{A\rho}$ results in a finite net change in h because H(0) is finite. Making $K_I \neq 0$ in case 3 causes $H(0) = 0$, resulting in no net momentum change for a step change in $T_{A\rho}$. The response now parallels the desired function at low frequencies, but is much larger at high frequencies. In case 4, the lag in the momentum feedback shaping is made non-zero. This "rolls off" the adaptive loop resulting in lowered momentum perturbation from high frequency disturbance variations, compared to case 3. The low frequency response is significantly degraded however. In case 5, $T_L = 0$ again, but the integral gain in the attitude loop, K_F, is non zero. Only a small improvement in high frequency response results.

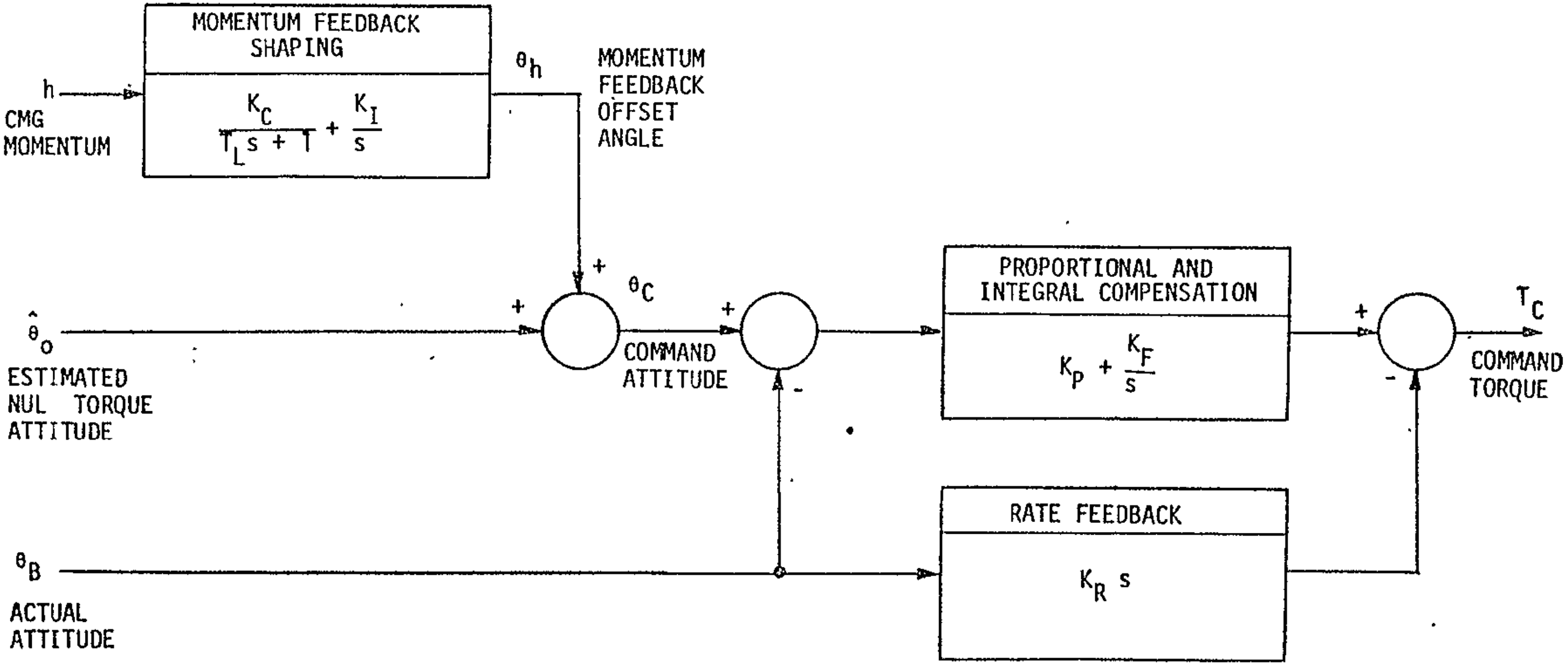

Figure 11-6. Pitch Control Law Structure

Table 11-3. Compensation Parameter Summary - Nose Forward Orientation

Case	K_P N-m/rad	K_R N-m/(rad/sec)	K_C rad/(N-m-sec)	K_I (rad/sec)/(N-m-sec)	T_L sec	K_F N-m/(rad-sec)	$H(\omega_o)$ db	$H(2\omega_o)$ db
Desired Response	-	-	-	-	-	-	49.9	53.0
1	9.73×10^{2}	9.39×10^{4}	0	0	0	0	59.8	53.8
2	1.07×10^{3}	3.63×10^{5}	-2.59×10^{-5}	0	0	0	58.3	55.0
3	2.56×10^{4}	1.31×10^{7}	-5.30×10^{-5}	-3.90×10^{-8}	0	0	55.8	58.2
4	4.84×10^{4}	3.30×10^{5}	-2.74×10^{-5}	-3.25×10^{-8}	526	0	58.5	61.0
5	2.59×10^{4}	8.47×10^{6}	-3.31×10^{-5}	-4.02×10^{-8}	0	18.6	55.8	58.2

ALL CASES:

$I_y = 9.39\times10^{6}$ Kg-m^2

$K_G = 33.92$ N-m/rad

$\omega_o = 1.1 \times 10^{-3}$ rad/sec

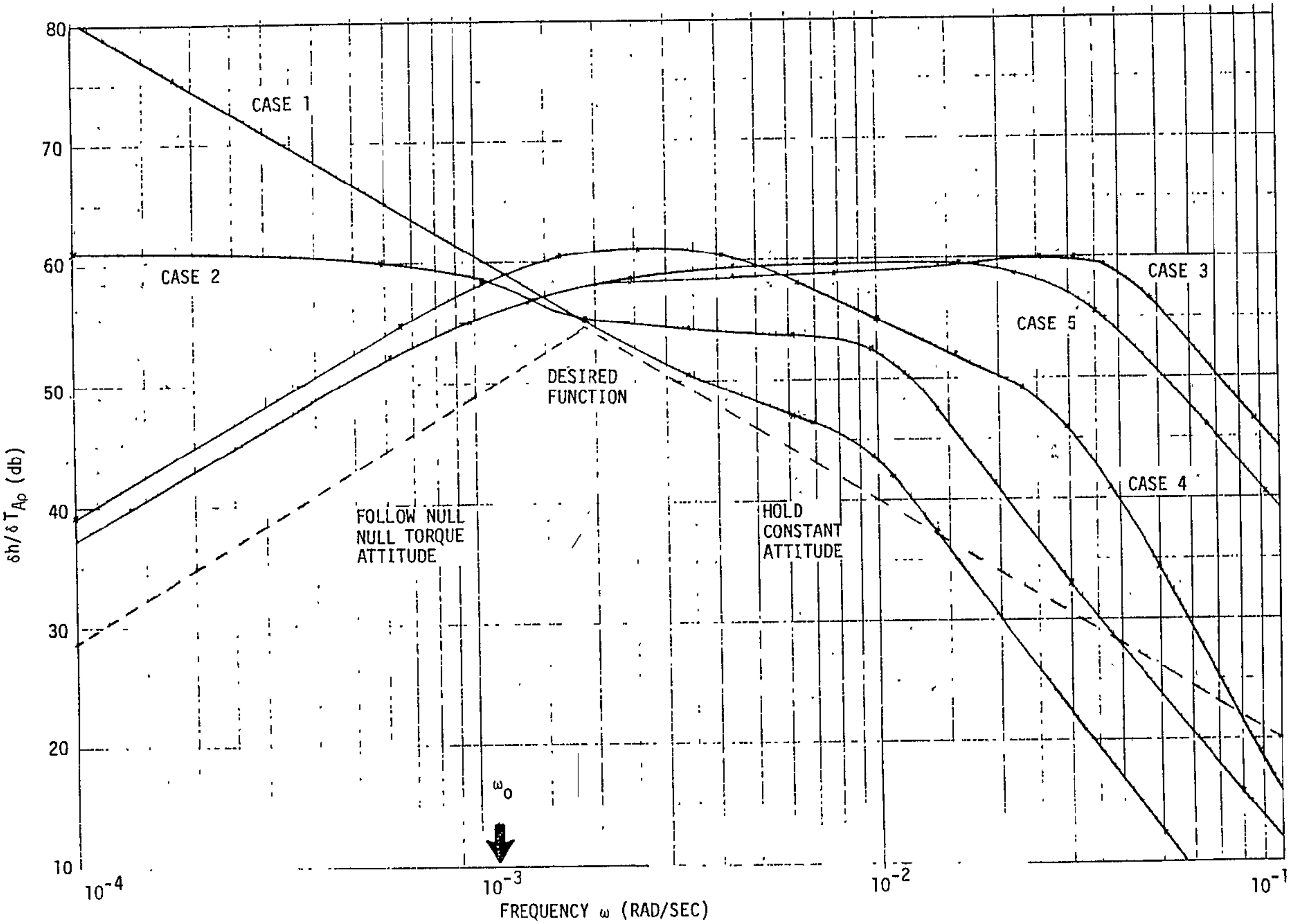

Figure 11-7. Momentum Response to Disturbance Variations in Nose Forward Orientation

It is obvious that no one case matches the desired function closely over the entire frequency range. Since the disturbance variation is basically at $\omega = \omega_0$, the momentum response should be minimized at ω_0. Case 3 is therefore selected as the nominal gain set, for having the smallest $H(\omega)$ at ω_0 and for all $\omega < 10\ \omega_0$. $H(\omega_0)$ is, however, 55.8 db = 615 N-m-sec/N-m or about twice the ideal value.

Figure 11-8 contains a plot of the attitude response ratio $\delta\theta_B/\delta T_{A\rho}$ for gain set 3. At low frequencies the ratio closely approximates the value $1/K_{y\theta}$ that would result from exactly following the null torque attitude. The response begins to roll off at the desired break frequency, initially with a slope of -1 and then with a slope of -2. The attitude response at ω_0 is 1.4 db or a factor of 1.18 greater than in the ideal case. As the attitude variations are small in the nose forward orientation, the linear analysis is valid over the entire EVAL altitude range.

11.4.3 Nose Down Orientation

In this orientation the gravity gradient slope is $K_G = -33.92$ for small offset angles ($h > 250$ Km), and pitch is open loop stable. A suitable set of gain is

$$K_P = 74.7 \text{ N-m-rad}$$
$$K_R = 2400 \text{ N-m/(rad/sec)}$$
$$K_c = 6.94 \times 10^{-5} \text{ rad/(N-m-sec)}$$
$$K_I = 3.5 \times 10^{-8} \text{ (rad/sec)/(N-m-sec)}$$

These gains are much lower than in the nose forward orientation because of the open loop stability, but $H(\omega_0) \simeq 55.8$ db again, as shown in Figure 11-9. At high frequencies, the response is actually better than that which would result from holding a constant attitude.

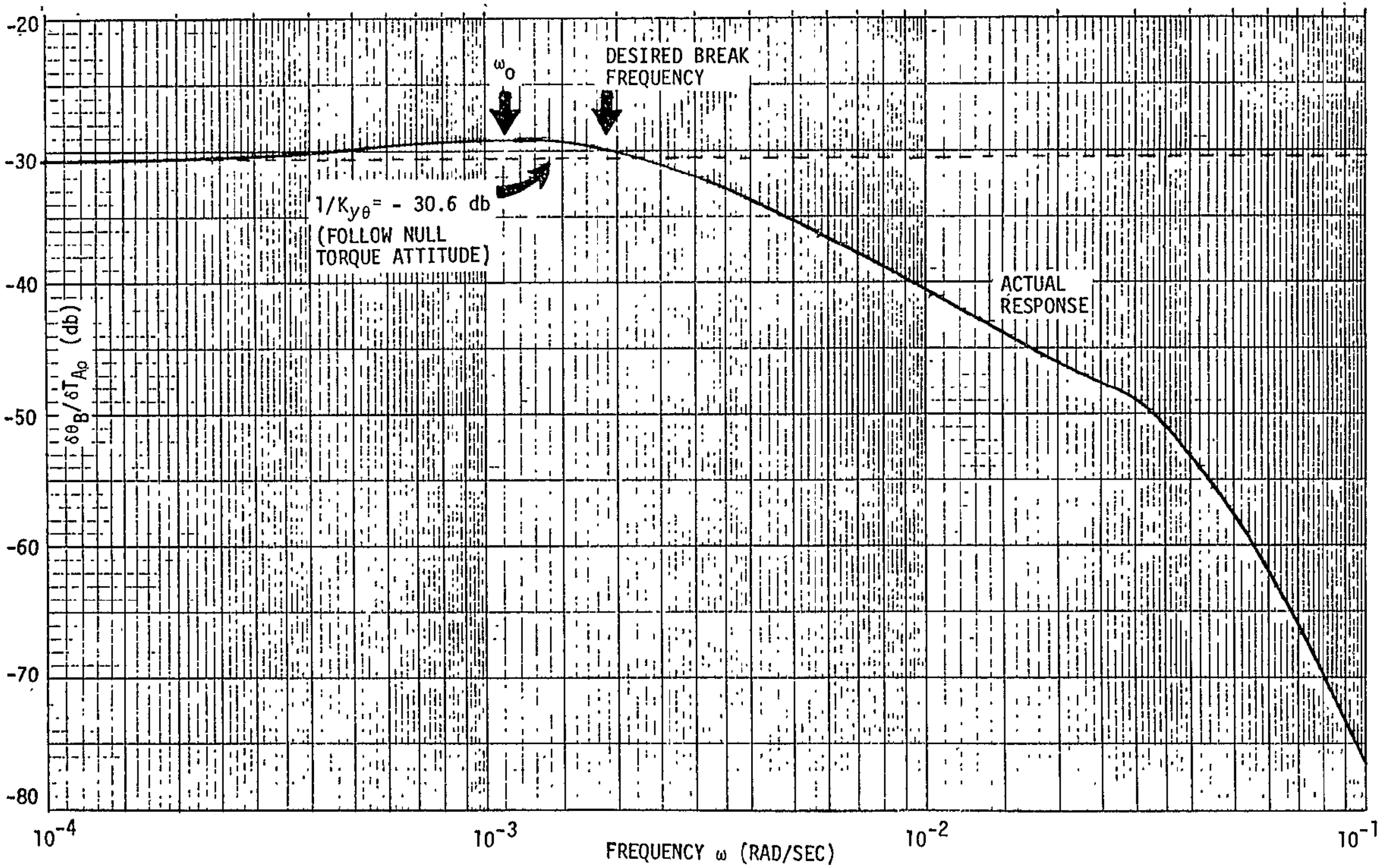

Figure 11-8. Attitude Response to Disturbance Variation in "Nose Forward" Orientation (Gain Case 3)

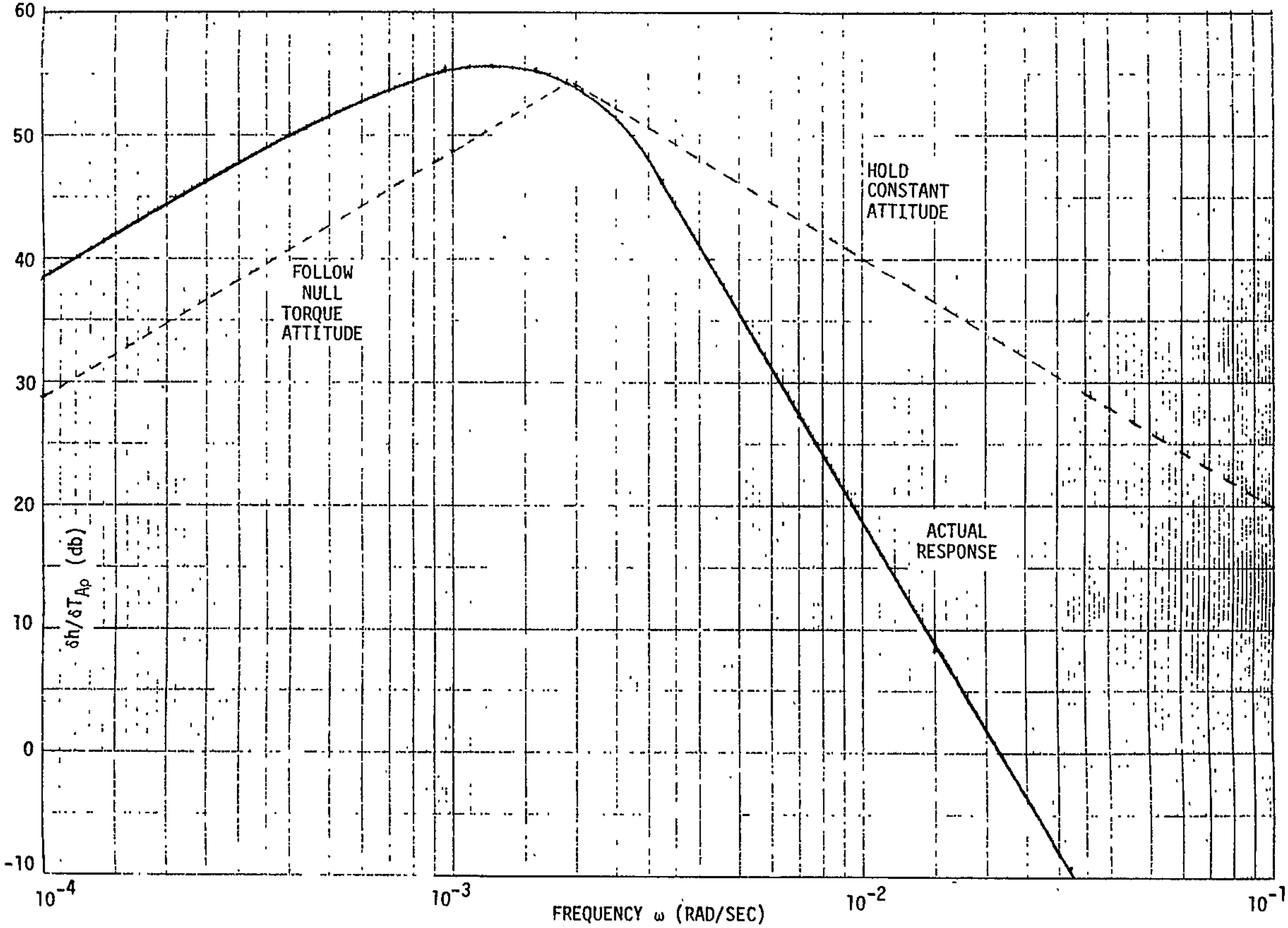

Figure 11-9. Momentum Response to Disturbance Variations in "Nose Down" Orientation

The attitude response ratio $\delta\theta_B/T_{A_p}$ is plotted in Figure 11-10. At low frequencies, the ratio again approximates $1/K_{y\theta}$, but the initial slope after the break is now -2, resulting in improved rejection of high frequency disturbance variations. The attitude response at ω_0 is 3.2 db or a factor of 1.45 greater than in the idealized case.

At low altitudes, large momentum and attitude variations may occur, and due to the nonlinear nature of the disturbance torques the linear analysis is not strictly valid. To verify performance at low altitudes, several simulation cases were run with a large angle single axis simulation. The results of these simulations are summarized in Figure 11-11. Above 250 Km, the simulation results agree closely with the linear analysis. Below 250 Km, deviations from the linear analysis appear, as expected. The combination of large attitude variations and momentum storage requirements may make operation in the nose down orientation unfeasible at the low end of the altitude range.

11.5 MOMENTUM EXCHANGE DEVICE SELECTION

A tradeoff analysis of momentum exchange devices capable of meeting the control requirements developed in the previous subsection is contained in Appendix F. Or the basis of size, weight, power, cost and feasibility, double gimbal control moment gyros rate as the most suitable control actuators for the orbiter null torque attitude stabilization system.

Table 11-4 summarizes the characteristics of the required CMG's under two sets of assumptions on allowable operational restrictions. The first CMG set allows capture from the nominal RCS limit cycle rates and can stabilize the orbiter in the nose forward orientation at all altitudes above 180 Km and in the nose down orientation above 200 Km. The second CMG set can only be used if the RCS limit cycle rates are reduced by a factor of 10 and if operation in the nose down orientation is not required below 230 Km.

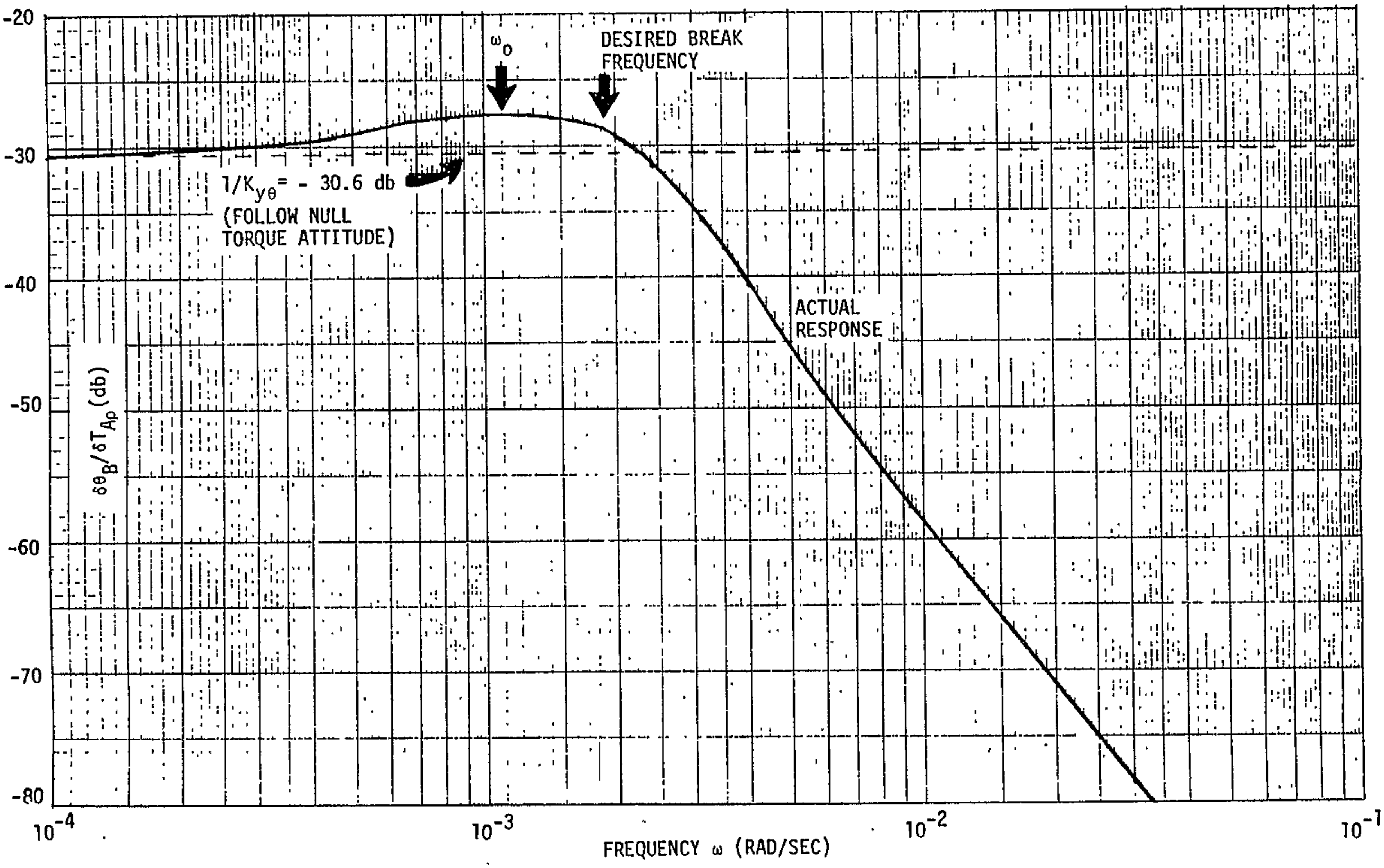

Figure 11-10. Attitude Response to Disturbance Variation In "Nose Down" Orientation

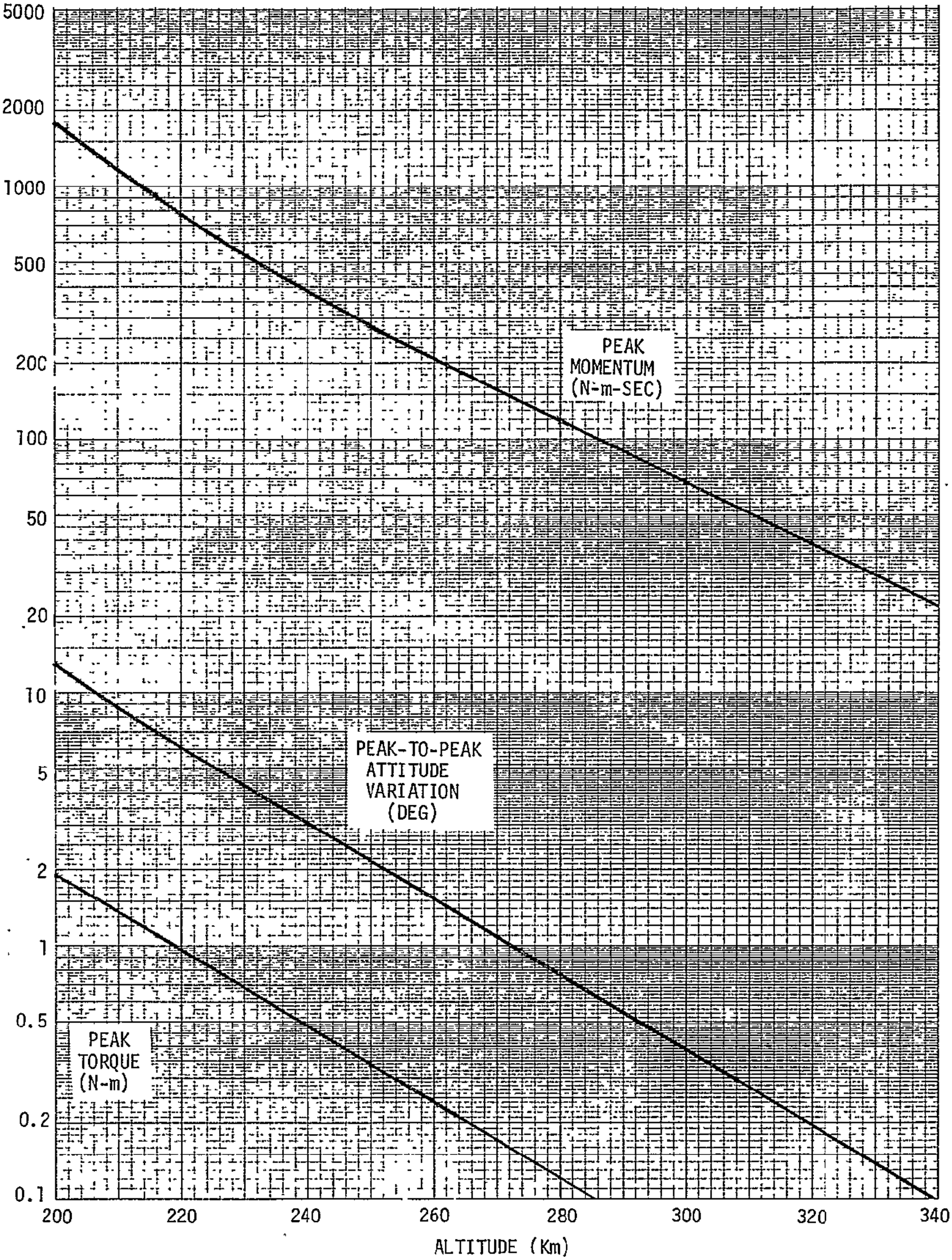

Figure 11-11. Control Performance With Practical Control Law in Nose Down Orientation With ±20% Atmospheric Density Variation at Orbit Frequency

Table 11-4. Summary of Double Gimbal CMG Characteristics

CMG Set	CMG Characteristics					Operational Restrictions		
	Per Unit		Total for Cluster of 3 Units			Maximum RCS Limit Cycle Rate (Deg/Sec)	Minimum Altitude (Km) for Orientation **	
	Torque (N-m)	Momentum (N-m-Sec)	Weight (Kg)	Power* (Watts)	Volume (m^3)		Nose Forward	Nose Down
1	13.6 (10 ft-lb)	2710 (2000 ft-lb-sec)	281	93	2.70	0.01 (Nominal)	180	200
2	1.36 (1 ft-lb)	678 (500 ft-lb-sec)	136	45	0.97	0.001 (0.1 Nominal)	180	230

* Peak power at maximum torque output.

** ±20% Atmospheric Density Variation at Orbit Frequency Assumed.

12.0 ORBITER NULL TORQUE ATTITUDE STABILIZATION SYSTEM DEFINITION

An overall design of the orbiter null torque atttitude stabilization system is presented in this section. The system concept stresses autonomous operation, with nearly all control function performed by dedicated programmable digital electronics (PDE).

The orbiter null torque attitude stabilization system maintains the orbiter attitude near the null torque attitude, that is, the attitude at which the total external torque on the orbiter vanishes. The system attempts to hold the orbiter roll and yaw attitudes at the estimated null torque attitude, while adaptively seeking the true null torque attitude in pitch. The orbiter RCS is disabled during operation of the null torque attitude stabilization system, except for occasional brief firings of the vernier RCS thrusters to unload CMG momentum when the CMG cluster is near saturation.

A functional block diagram, showing the major blocks and data flow of the orbiter null torque attitutde stabilization system, is presented in Figure 12-1. Descriptions and more detailed data flow diagrams of the major blocks are contained in the following subsections.

12.1 COMMAND AND ERROR PROCESSING

Figure 12-2 shows a block diagram of the command and error processing performed by the orbiter stabilization system PDE. The only inputs required from the spacelab computer are orbiter attitude and ephemeris data, an indication of the orbiter orientation number, and a vector of estimated null torque offset angles. The orbiter attitude and ephemeris data originates in the orbiter GN&C computer, but is relayed through the spacelab to maintain a uniform interface. The orbiter orientation number indicates whether the "nose forward" or "nose down" nominal orientation is desired. The A_{NR} matrix is fixed for each orientation and contains only three nonzero (± 1) elements. The estimated null torque offset

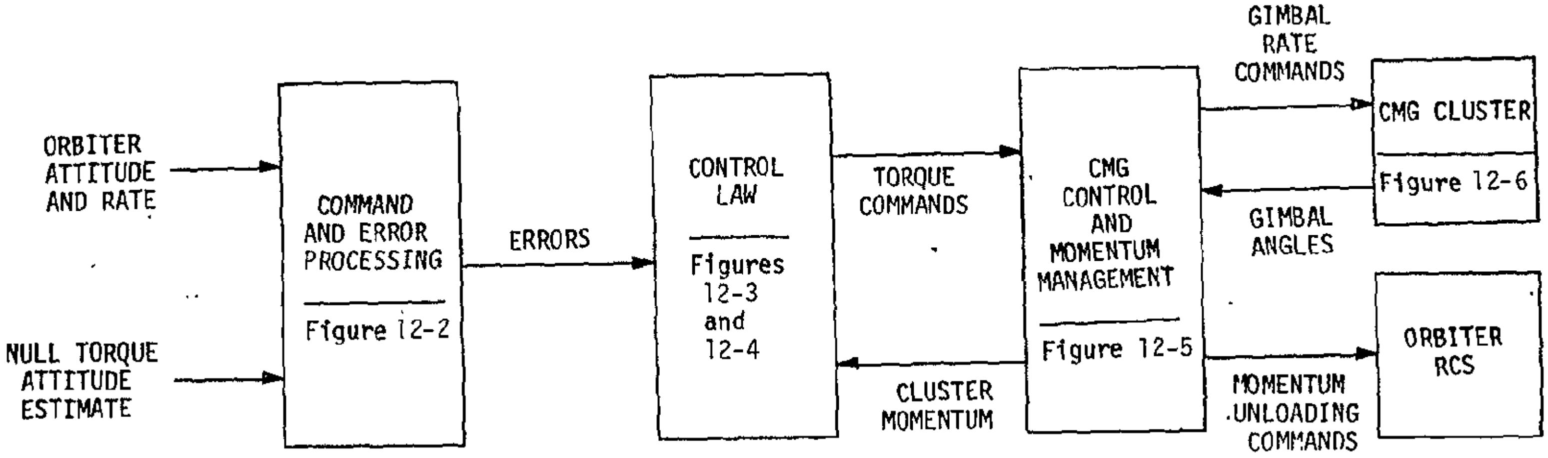

Figure 12-1. Orbiter Null Torque Attitude Stabilization System Functional Block Diagram

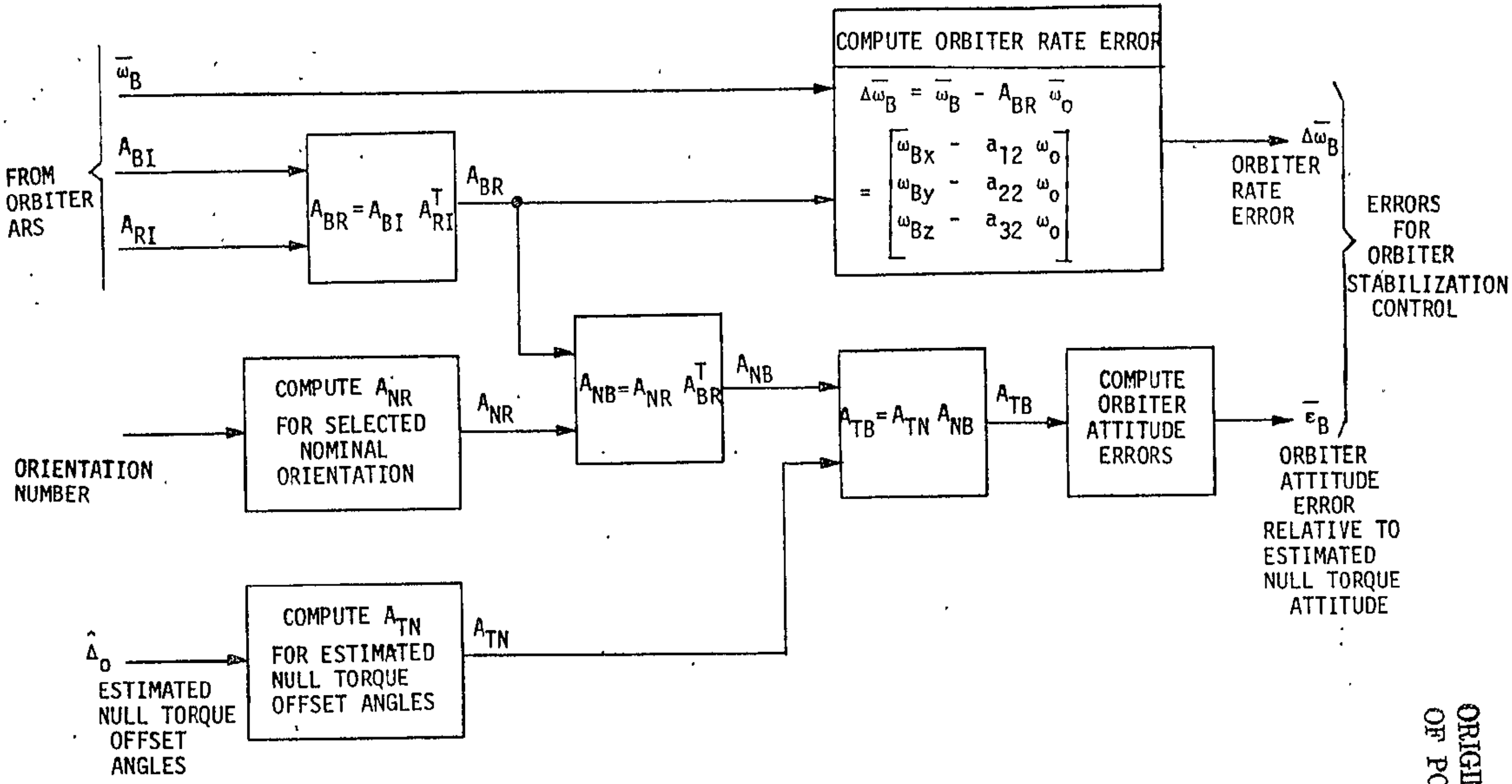

NOTATION:

A_{ij} = a 3 x 3 DIRECTION COSINE MATRIX INDICATING THE ATTITUDE OF COORDINATE FRAME "i" RELATIVE TO FRAME "j"

SUBSCRIPTS:

I = INERTIAL (ECI)
B = ORBITER BODY (GN&C BASE)
R = ORBIT REFERENCE
N = NOMINAL ORBITER ORIENTATION
T = ESTIMATED NULL TORQUE ORIENTATION

Figure 12-2. Orbiter Stabilization System Command and Error Processing angles are precomputed for each of the two nominal orbiter orientations, based on the estimated atmospheric density and orbiter mass properties for the particular EVAL mission being conducted.

The command and error processing outputs are the orbiter rate and attitude errors. The rate error output serves to cause the orbiter to rotate about the orbit normal, with respect to the inertial (I) frame, at orbit rate. This aids in keeping the orbiter locked to the earth pointing orbit reference (R) frame. The attitude error output consists of the small angle errors between the actual orbiter attitude and the estimated null torque attitude.

12.2 CONTROL LAW

A block diagram of the orbiter stabilization system control law data flow is shown in Figure 12-3. The control law, derived in Section 11.1 contains two branches. The primary attitude stabilization task falls upon the feedback control law. The momentum coupling compensation path assists in attitude control by attempting to cancel undesirable inter-axis coupling torques that result from the interaction of the orbiter inertial rate and system momentum vector. The output of the control law is a CMG torque command vector.

Figure 12-4 shows the data flow structure of the feedback control law. The upper two paths in the Figure implement a conventional proportional plus rate attitude control law and operate on all three (roll, pitch, yaw) control channels. The lower two paths use proportional plus integral feedback of the CMG cluster momentum to implement loops that adaptively seek the null torque attitude and use the gravity gradient torque to unload excess CMG momentum. These adaptive loops are used only on the pitch channel. The numerical values of the gain matrices (G_ε, G_ω, G_h, G_η) are different in the "nose forward" and "nose down" orientations.

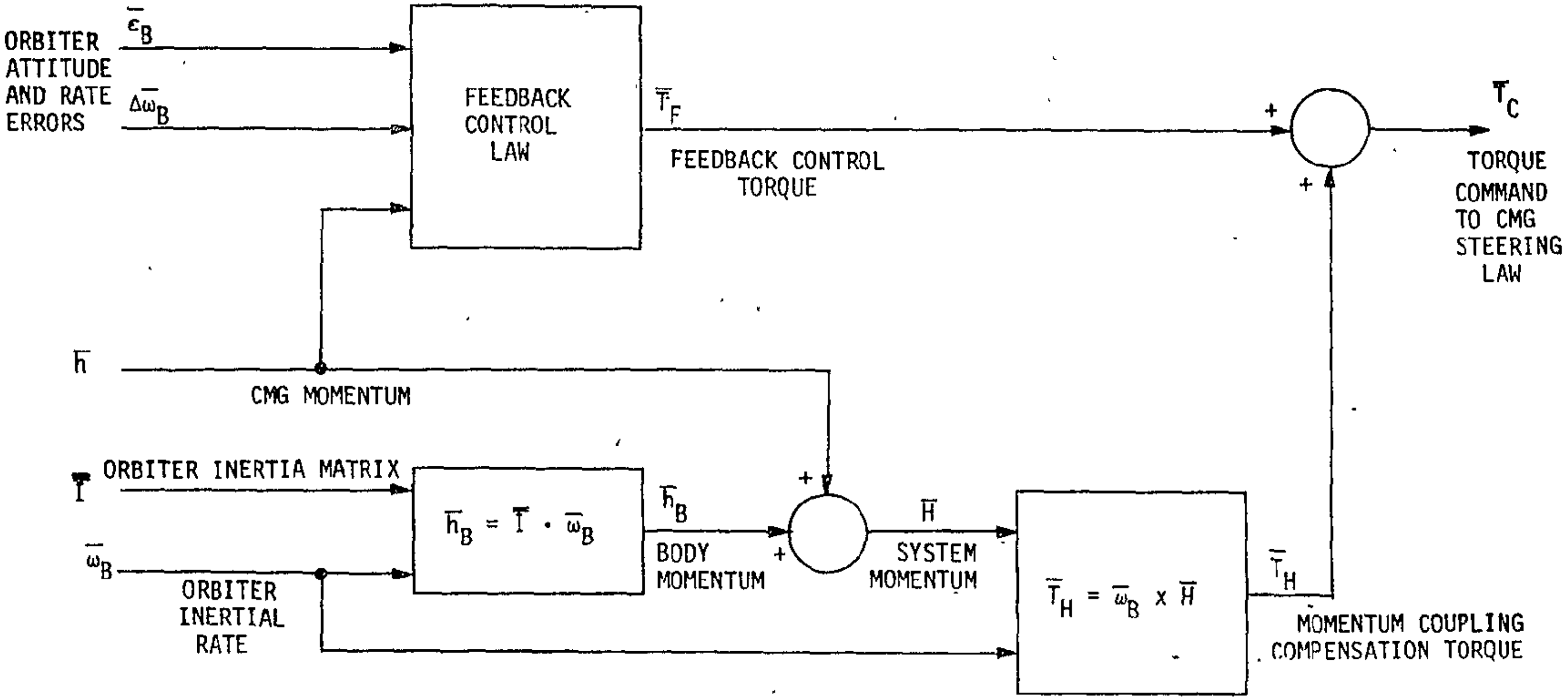

Figure 12-3. Orbiter Stabilization System Control Law

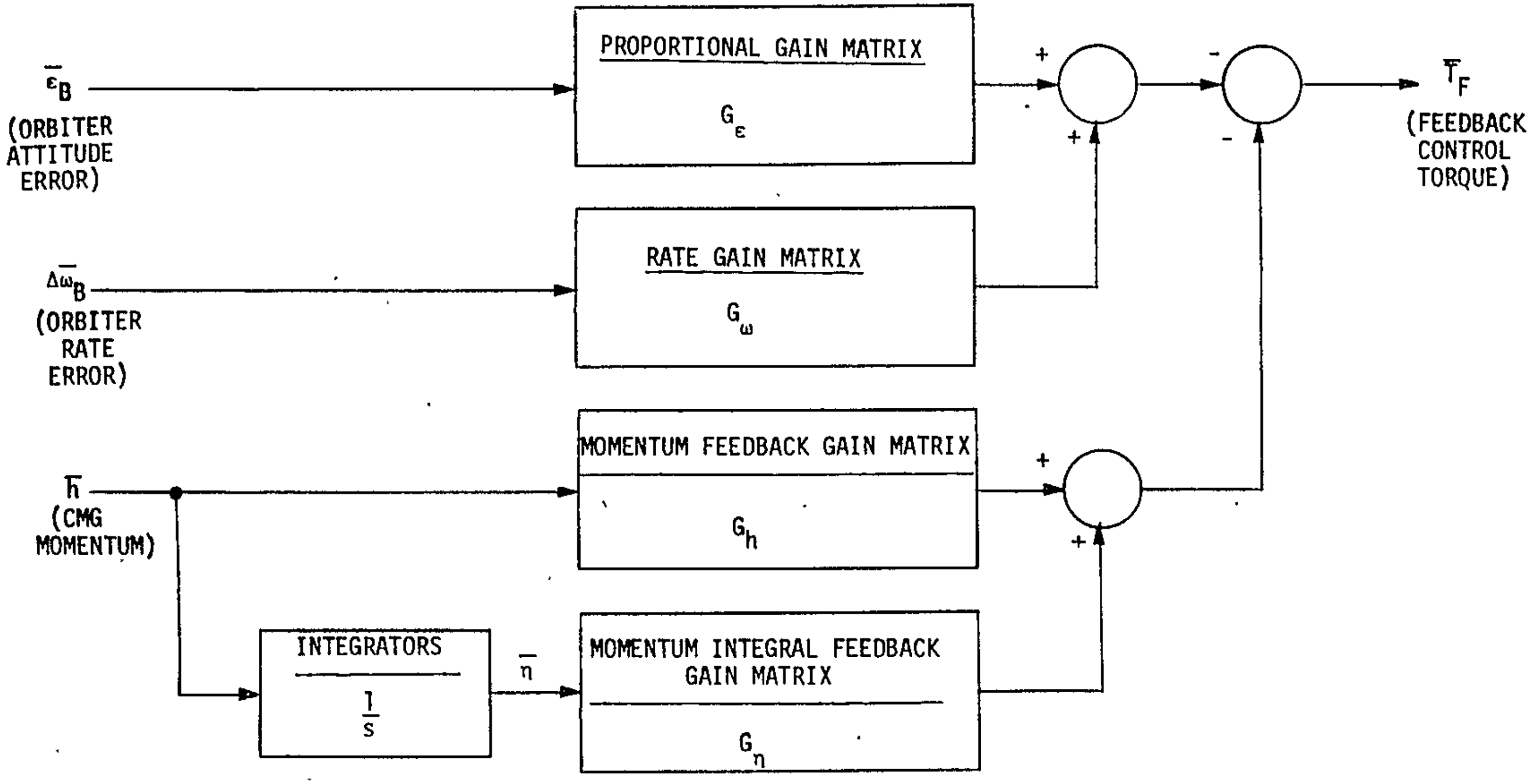

Figure 12-4. Orbiter Stabilization System Feedback Control Law

12.3 CMG CONTROL AND MOMENTUM MANAGEMENT

The data flow for CMG control and momentum management is shown in Figure 12-5. The CMG cluster consists of three double gimballed CMG's. As illustrated in Figure 12-6, the CMG's are mounted to have, with zero gimbal deflections, mutually orthogonal momentum vectors. Control torques on the orbiter are generated by commanding gimbal rates, while momentum is stored as gimbal deflections.

With all three CMG's operating, there are six degrees of freedom in the CMG cluster, and the CMG steering law performs three functions. The primary function, using three degrees of freedom, is to command combinations of gimbal rates such that the actual torque on the orbiter equals the commanded control torque. The remaining three degrees of freedom are used to distribute the individual CMG momentum vectors to avoid undesirable momentum configurations and to stay away from gimbal mechanical stops. These secondary functions are programmed in such a manner that no net torque on the orbiter results.

With one CMG failed, there are four degrees of freedom in the CMG cluster. Three of these degrees of freedom are used to generate control torques, while the remaining degree of freedom is used to reduce the gimbal angle of the gimbal axis that is nearest to a gimbal stop. Momentum storage and control torque capability is reduced with one CMG failed, but continued operation, with some performance degradation, is possible.

The CMG cluster momentum is computed from the CMG gimbal angles, as measured by the CMG gimbal angle resolvers. Logic is provided to indicate when the CMG cluster momentum is approaching a saturated condition. To maintain control, the cluster must be desaturated with torques provided by the orbiter RCS. To minimize the impact of the momentum unloading on experiment pointing, minimum on-time ($\sim$ 40 msec) vernier RCS thruster firings will be used, and transmission of thruster commands to the RCS can be inhibited, on a priority basis, by the spacelab computer.

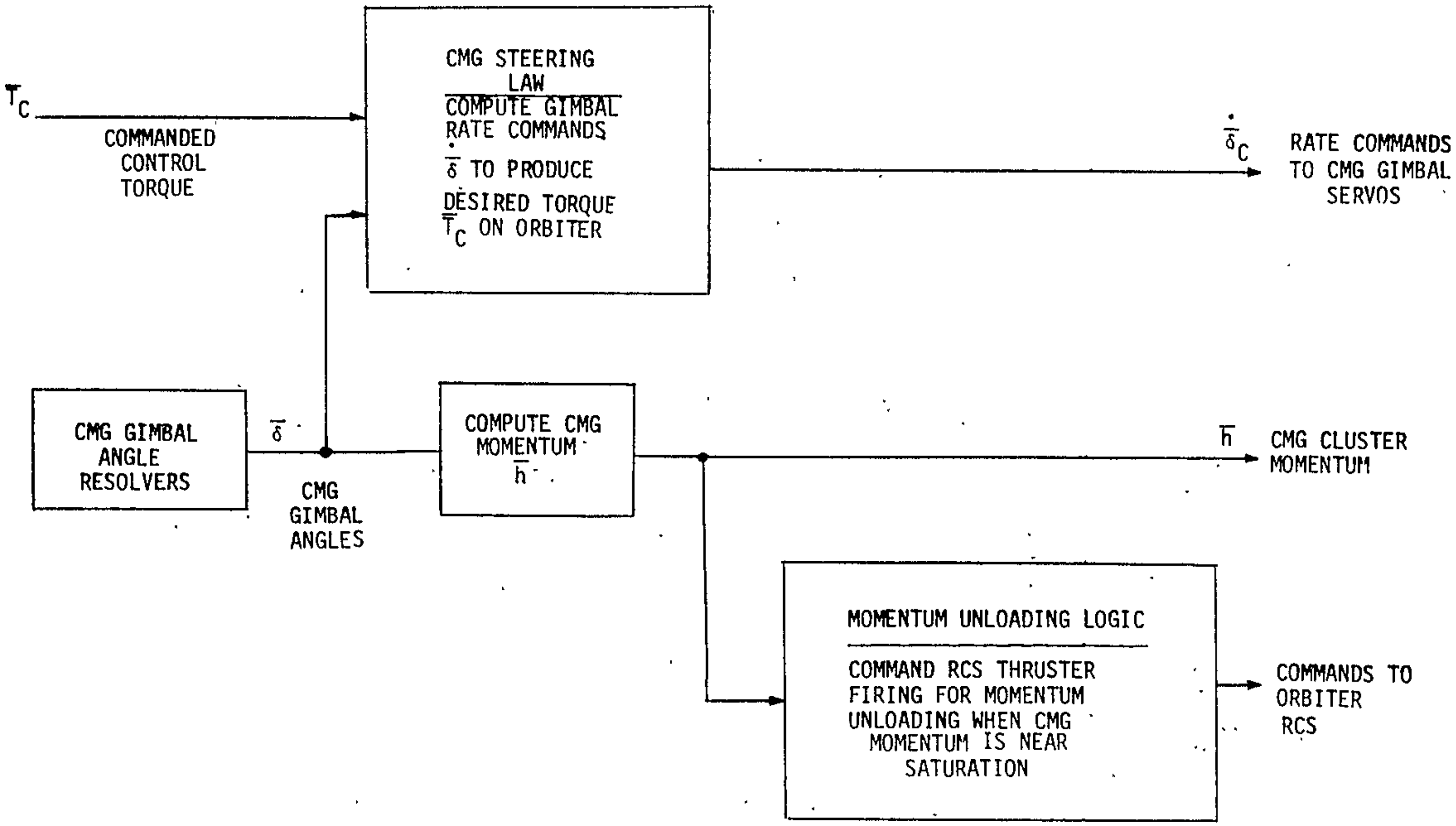

Figure 12-5. Orbiter Stabilization System CMG Control and Momentum Management

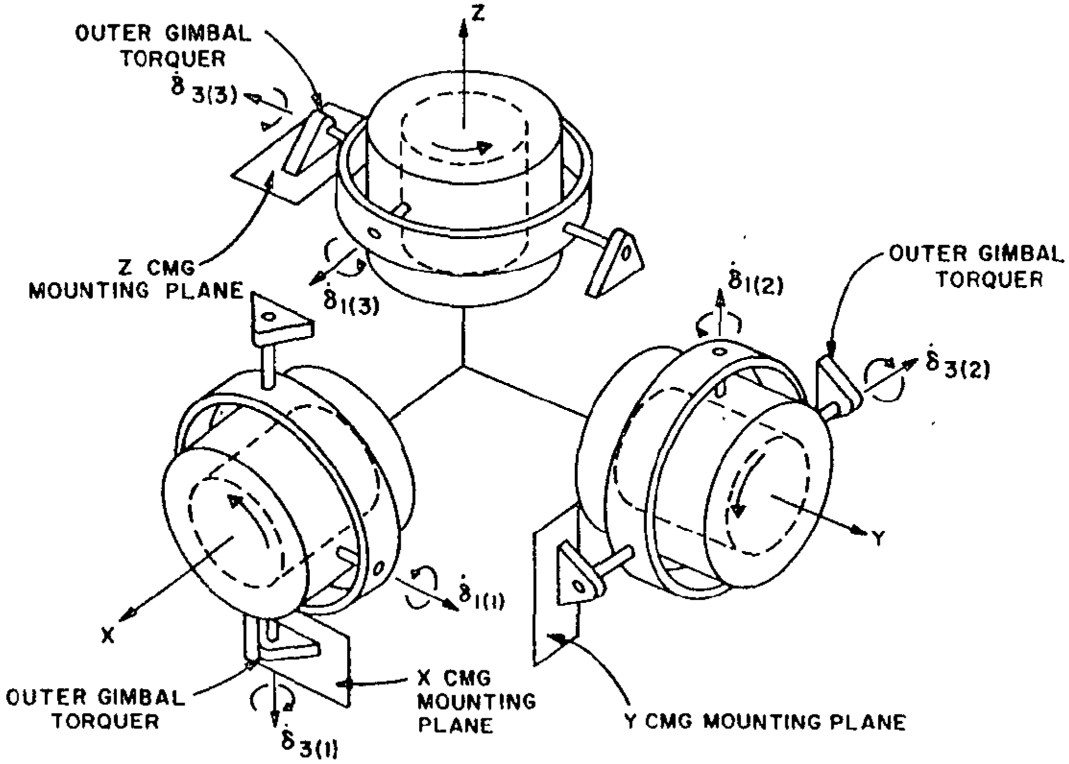

Figure 12-6. Orthogonal Double Gimballed CMG Cluster

REFERENCES

(1) ESTEC SLP/2104, "Spacelab Payload Accommodation Handbook", Review Issue, PDR-B, European Space Agency, 1976.

(2) William W. Hooker, "A Set of r Dynamical Attitude Equations for an Arbitrary n-Body Satellite Having r Rotational Degrees of Freedom," AIAA Journal, Volume 8, Number 7, July 1970, pages 1205-1207.

(3) S.S.L. Chang, "Minimum Time Control With Multiple Saturation Limits," IEEE Transactions on Automatic Control, Volume AC-8, pages 35-42, 1963.

(4) 13900-6012-RO-01, "PPCS System Design and Analysis," A. M. Frew et at., TRW DSSG, 1 July 1972.

(5) NASA TM X-73079, "A Computer-Aided Telescope Pointing System Utilizing a Video Star Tracker," December 1975.

(6) T. B. Garber, "Influence of Constant Disturbing Torques on the Motion of Gravity Gradient Stabilized Satellites," AIAA Journal, Volume 1, No.4, April 1963, pages 968-969.

APPENDIX A
SPACE SHUTTLE ORBITER DATA

A.0 INTRODUCTION

This appendix briefly summarizes basic space shuttle orbiter data that will be required for the Earth Viewing Applications Laboratory (EVAL) study. The areas covered include coordinate systems, payload bay characterization, internal disturbance sources, and mass properties. The MKS system has been adopted for the EVAL study and therefore units are converted to MKS where necessary.

A.1 COORDINATE SYSTEMS

Most shuttle orbiter source data is specified in the "orbiter coordinate system", (x_0, y_0, z_0), illustrated and described in Figure A-1. The "station numbers" appearing on dimensional drawings are the (x_0, y_0, z_0) coordinates, in inches. This frame is convenient for specifying locations on the orbiter because the (x_0, y_0, z_0) coordinates are always fixed in the orbiter.

A more useful frame for dynamics is the orbiter body coordinate system (x_B, y_B, z_B) illustrated in Figure A-2. This frame has its origin at the orbiter CG and body-fixed axes oriented in the standard "airplane" arrangement. The orbiter body coordinates are related to the orbiter coordinates by

$$\begin{bmatrix} x_B \\ y_B \\ z_B \end{bmatrix} = \begin{bmatrix} -1 & 0 & 0 \\ 0 & 1 & 0 \\ 0 & 0 & -1 \end{bmatrix} \begin{bmatrix} x_0 - x_0^{CG} \\ y_0 - y_0^{CG} \\ z_0 - z_0^{CG} \end{bmatrix}$$

where $(x_0, y_0, z_0)^{CG}$ is the CG location in orbiter coordinates.

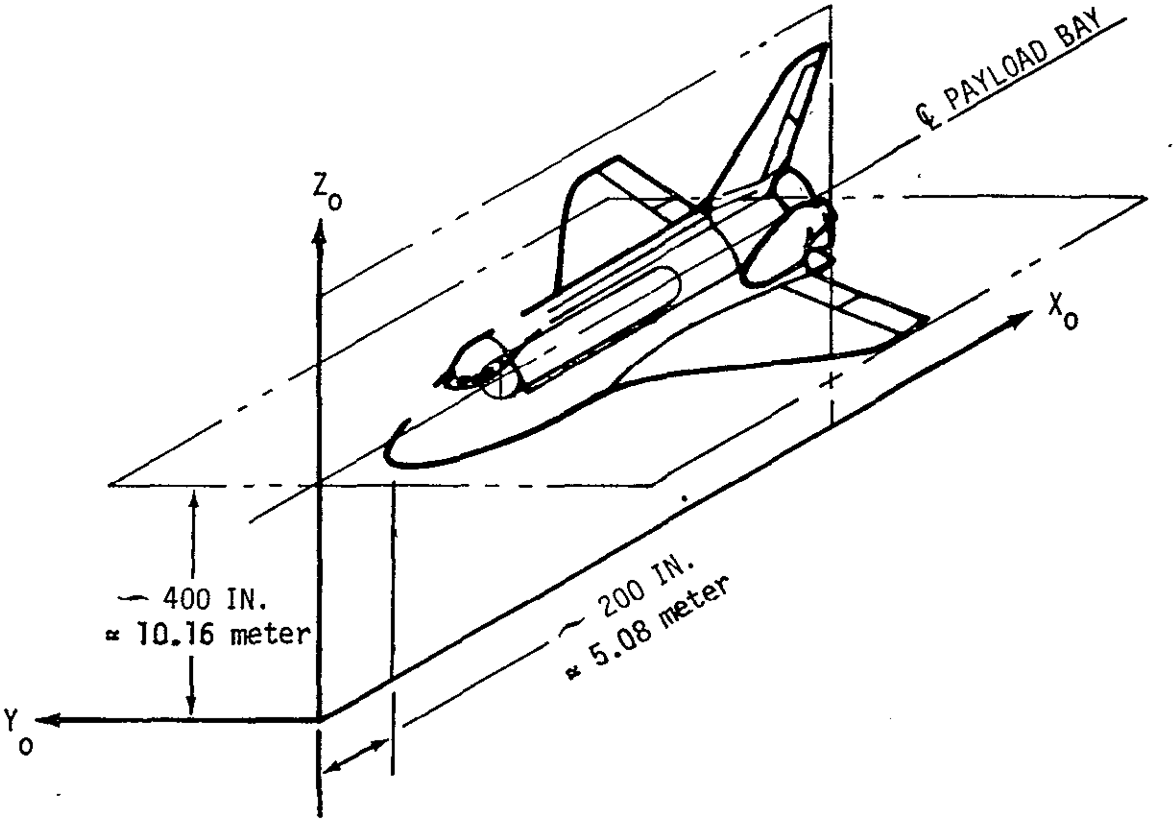

TYPE: ROTATING, ORBITER REFERENCED

ORIGIN: APPROXIMATELY 200 INCHES AHEAD OF THE NOSE AND APPROXIMATELY 400 INCHES BELOW THE CENTERLINE OF THE PAYLOAD BAY

ORIENTATION AND LABELING:

THE X AXIS IS PARALLEL TO THE CENTERLINE OF THE PAYLOAD BAY, NEGATIVE IN THE DIRECTION OF LAUNCH

THE Z AXIS IS POSITIVE UPWARD IN LANDING ATTITUDE

THE Y COMPLETES THE RIGHT-HANDED SYSTEM

THE STANDARD SUBSCRIPT IS 0

Figure A-1. ORBITER COORDINATE SYSTEM

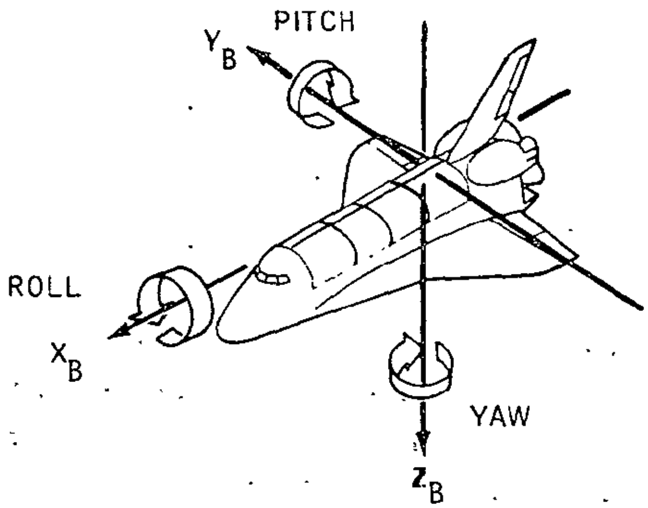

NAME:	ORBITER BODY COORDINATE SYSTEM
ORIGIN:	ORBITER CG
ORIENTATION:	THE X_B AXIS IS PARALLEL TO THE CENTERLINE OF THE PAYLOAD BAY, POSITIVE IN THE DIRECTION OF THE NOSE OF THE ORBITER THE Z_B AXIS LIES IN A PLANE PARALLEL TO THE PLANE OF SYMMETRY AND IS PERPENDICULAR TO THE X_B AXIS AND IS POSITIVE DOWN IN THE LANDING ATTITUDE THE Y_B AXIS COMPLETES THE RIGHT-HANDED SYSTEM
CHARACTERISTICS:	ROTATING RIGHT-HANDED SYSTEM

Figure A-2. ORBITER BODY COORDINATE SYSTEM

A.2 PAYLOAD BAY

The instrument pointing system (IPS) will be located in the payload bay, illustrated in Figure A-3. The payload envelope is restricted to a cylinder centered at

$$x_0 = 942 \text{ in} \simeq 23.9268 \text{ meters}$$

$$z_0 = 400 \text{ in} \simeq 10.16 \text{ meters}$$

with overall length 720 in = 18.288 meters and radius 90 in = 2.288 meters. A 180 degree lateral field of view is available at $z_0 = 427$ in = 10.8458 meters. The longitudinal fields of view at the payload bay center point are illustrated at the top of Figure A-3.

A.3 INTERNAL DISTURBANCE SOURCES

The two largest disturbance sources originating within the orbiter during attitude hold operation are crew motion and vernier reaction control system (RCS) thruster firings. External disturbances are mission dependent and are discussed in Appendix D.

A.3.1 Crew Motion

The worst case crew motion force profile is illustrated in Figure A-4. In general, this force profile can be applied at any point within the orbiter that the crew has access to.

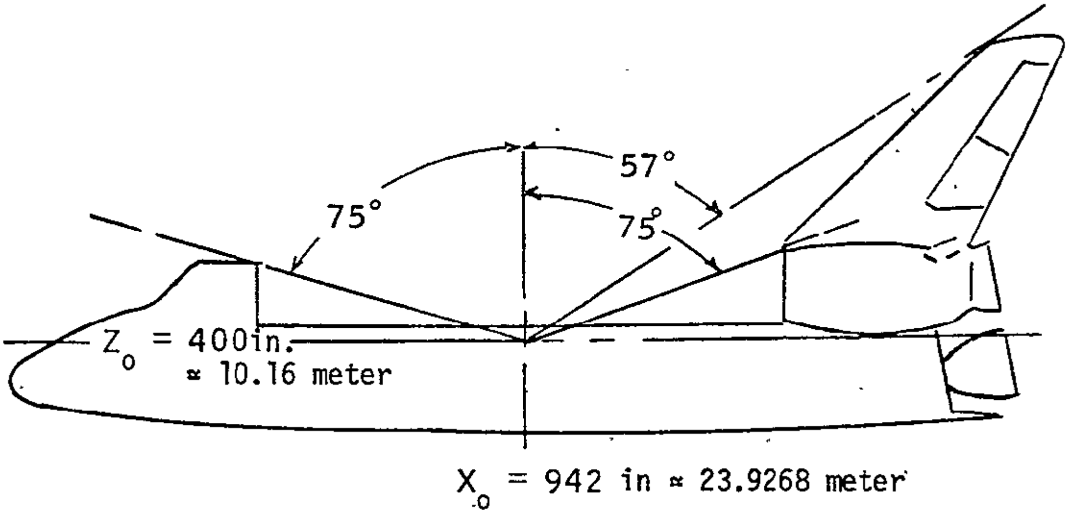

CLEARANCE ANGLES

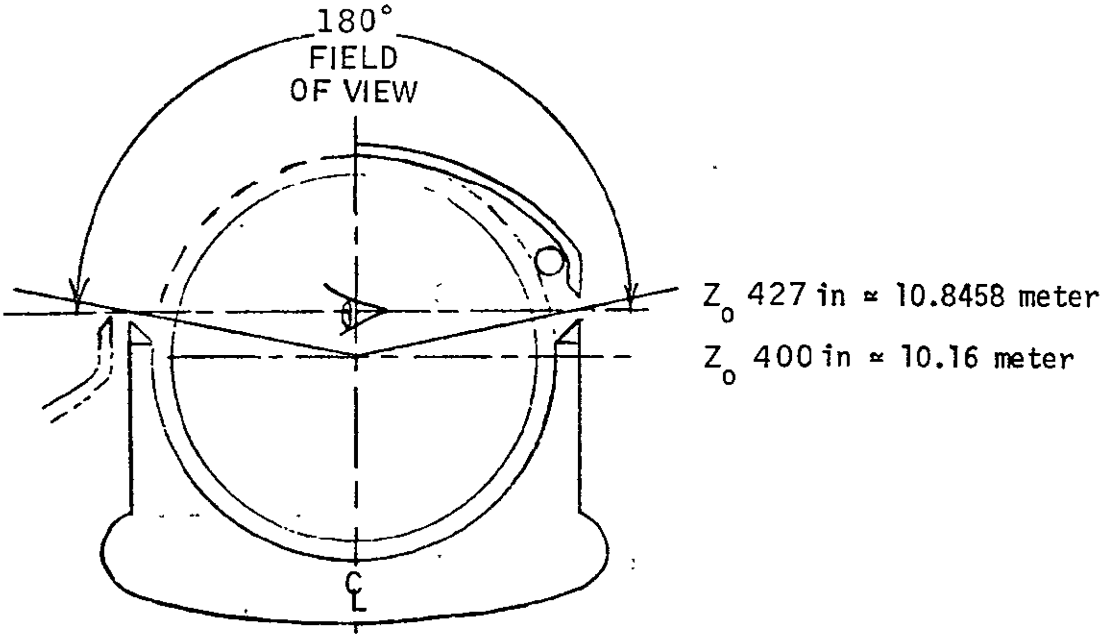

LATERAL FIELD OF VIEW

Figure A-3. Payload bay clearance and view angles

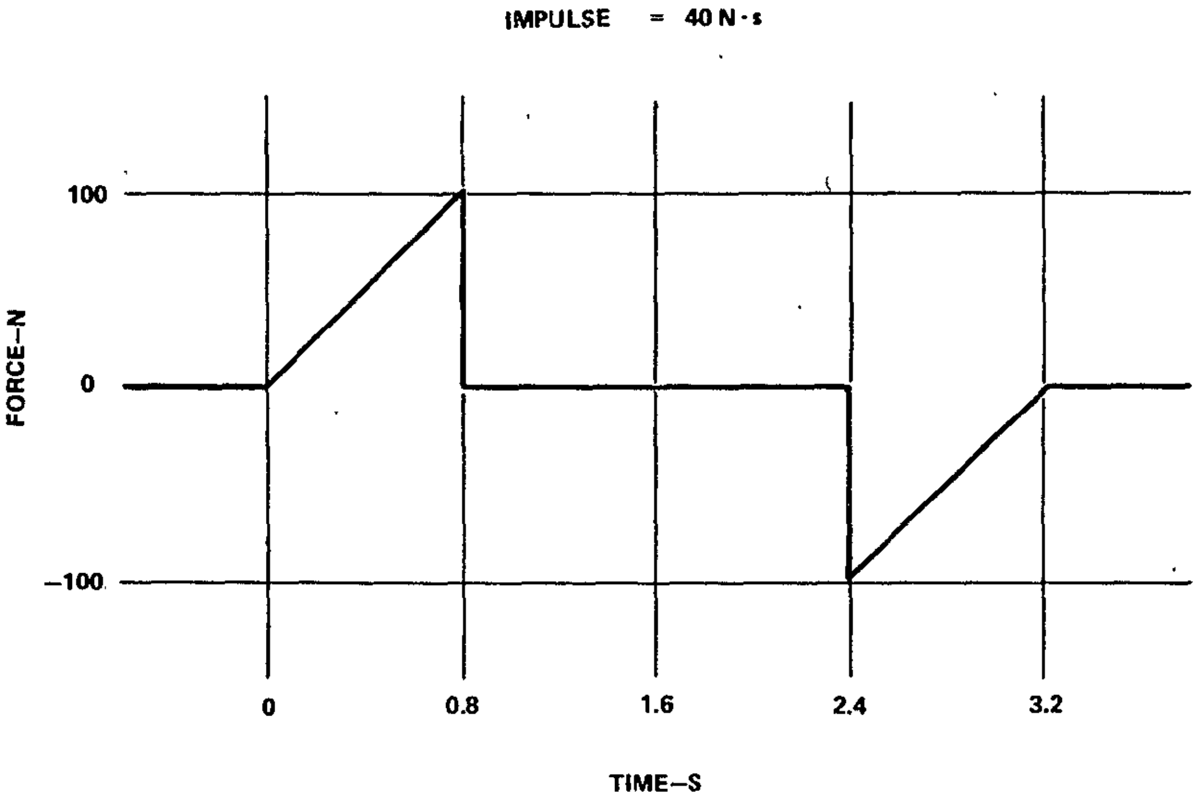

Figure A-4. Crew motion design profile.

A.3.2 Vernier RCS Thrusters

Fine orbiter attitude control is achieved with six vernier thrusters with thrust 25 LB_f = 111.2 N, specific impulse I_{sp} = 228 sec, and a minimum on-time of 0.04 sec. The thruster locations and force components are listed in Table A-1. Thruster torques depend on the overall orbiter/payload CG location and are therefore somewhat configuration dependent. The orbiter motion about each axis is a limit cycle with a selectable deadband of either ± 0.1, ± 0.5 or ± 1.0 degrees.

A.4 MASS PROPERTIES

Orbiter mass properties are highly configuration dependent. Table A-2 lists typical weights, less the payload. Definitive inertia values are not readily available. A typical set of principal axes inertias, including the payload, are

$$I_{xx} = 1.24 \times 10^6 \text{ kg-m}^2$$
$$I_{yy} = 9.39 \times 10^6 \text{ kg-m}^2$$
$$I_{zz} = 9.72 \times 10^6 \text{ kg-m}^2$$

The corresponding mass is

$$m = 97000 \text{ kg}$$

A.5 REFERENCES

A-1. NASA TM X-64978, "Experiment Pointing Subsystems (EPS) Requirements for Spacelab Missions," Marshall Space Flight Center, December 1975.

A-2. JSC 07700, Volume XIV, Revision D, Change 13, "Space Shuttle System Payload Accommodations", Johnson Space Center, 26 November 1975.

Table A-1. Vernier RCS Thruster Locations and Force Components

Thruster #	Coordinates * (M)			FORCE COMPONENTS (N)		
	x_o	y_o	z_o	F_x	F_y	F_z
1	8.260	- 1.228	9.166	0	72.95	- 84.96
2	8.260	1.228	9.166	0	- 72.95	- 84.96
3	39.751	- 3.641	11.659	0	111.2	0
4	39.751	3.641	11.659	0	-111.2	0
5	39.751	- 2.870	11.568	0	0	- 111.2
6	39.751	2.870	11.568	0	0	- 111.2

* In Orbiter Coordinate System, CG is approximately

$(x_o, y_o, z_o)^{CG} = (27.4, 0, 9.5)$ meters

Table A-2. **Typical Orbiter Weight Summary**

	Wt., lbs.	Wt., kg
Inert	150,000	68,039
Non-Propulsive Fluid	4,700	2,132
Personnel Group	2,411	1,094
RCS Peopellant (Fully loaded)	7,391	3,353
OMS Propellant (Fully loaded)	25,104	11,377
Orbiter Wt./Less Cargo	189,608	86,004
OMS Payload Bay Kits (1)	14,255	6,466
(2)	27,631	12,533
(3)	41,009	18,601
Cryogenic Wt. Per Kit	1,800	861

APPENDIX B
IPS DATA

B.0 INTRODUCTION

This appendix briefly summarizes the currently available Instrument Pointing System (IPS) data that is relevant to the Earth Viewing Applications Laboratory (EVAL) study. IPS, under development by ESA for the Spacelab program, is a precision, softmounted, three-axis gimballed platform primarily intended for pointing experiments at inertially fixed (stellar or solar) targets. The EVAL study assesses the suitability of the IPS for earth viewing applications.

Data on the following IPS characteristics is included:

- mechanical structure
- coordinate systems
- mass properties
- payload characteristics
- drive characteristics
- softmount characteristics
- gyro characteristics
- star tracker characteristics

B.1 MECHANICAL STRUCTURE

The overall IPS mechanical configuration, including the pallet and payload, is shown in Figure B-1. Much of the equipment illustrated (payload/gimbal separation mechanism, payload clamp, jettison device, softmount clamp) is used only during shuttle ascent/descent or emergency operation, and is not directly related to payload pointing. The star tracker assembly is not shown because its location and orientation for earth viewing applications has not been determined.

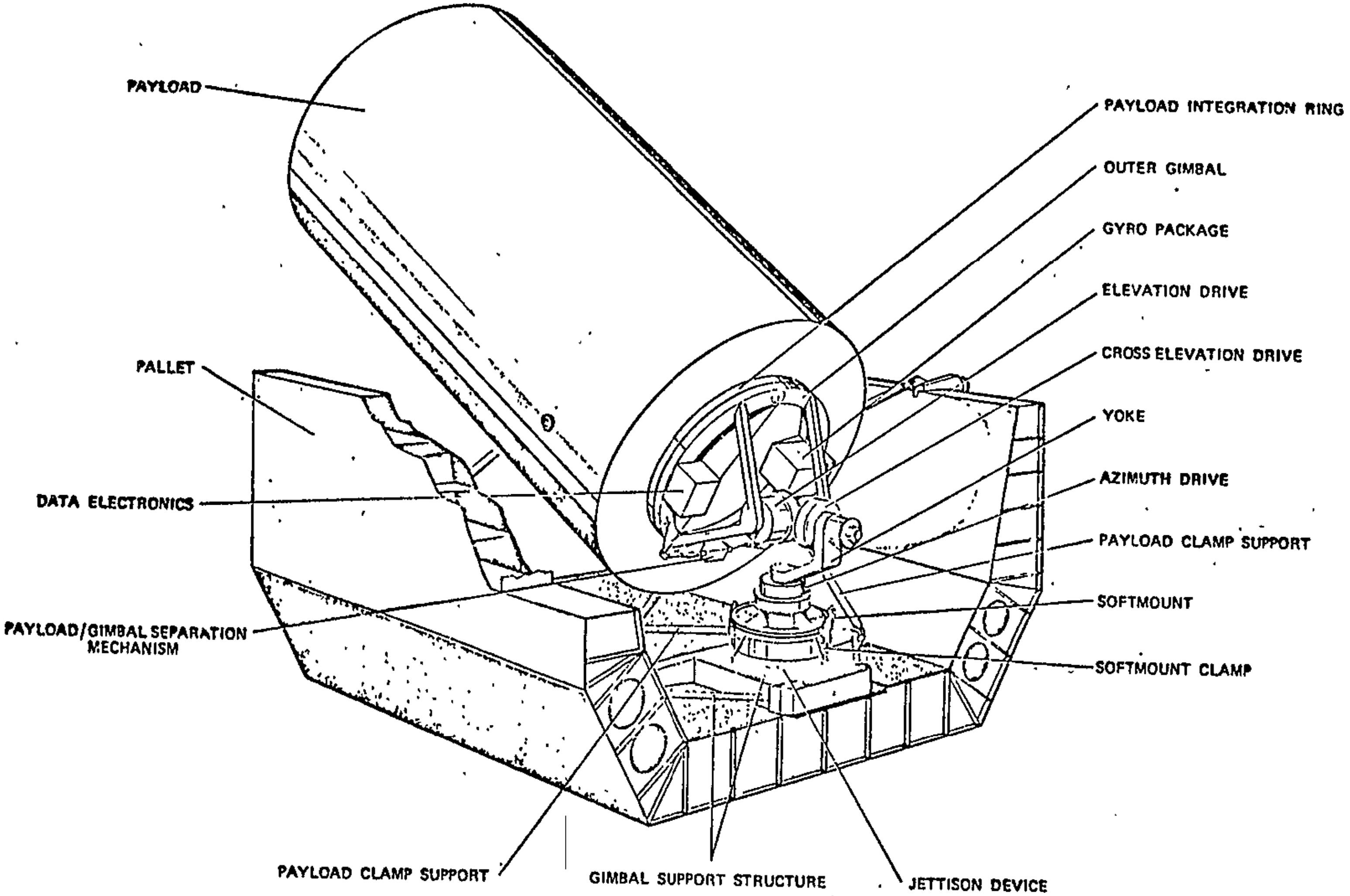

Figure B-1. IPS Mechanical Configuration

Figure B-2 is a more detailed illustration of the gimbal and softmount configuration. The gimbal is shown in the stowed position, with the payload integration ring normal to the pallet floor. For pointing operation, the nominal gimbal orientation is rotated 90 degrees about the elevation axis (payload integration ring parallel to pallet floor). During shuttle ascent and descent, the softmount is locked closed with the softmount clamp and the payload is locked to the pallet with a payload clamp. In order to center various size payloads properly in the payload clamp, the softmount/gimbal assembly position must be adjusted for each payload by sliding along a rail on the gimbal bottom structure and using a replaceable column for height adjustment.

B.2 COORDINATE SYSTEMS

Figure B-3 contains a simplified, exploded view of the IPS gimbal/softmount in the null pointing orientation. A coordinate system is defined in each of the seven bodies shown. The payload attitude relative to the orbiter is described by the three gimbal angles

α = azimuth angle (rotation about $\hat{z}_A$)

β = cross-elevation angle (rotation about $\hat{x}_C$)

γ = elevation angle (rotation about $\hat{y}_E$)

and the three (small) softmount angles

θ_x = x softmount angle

θ_y = y softmount angle

θ_z = z softmount angle.

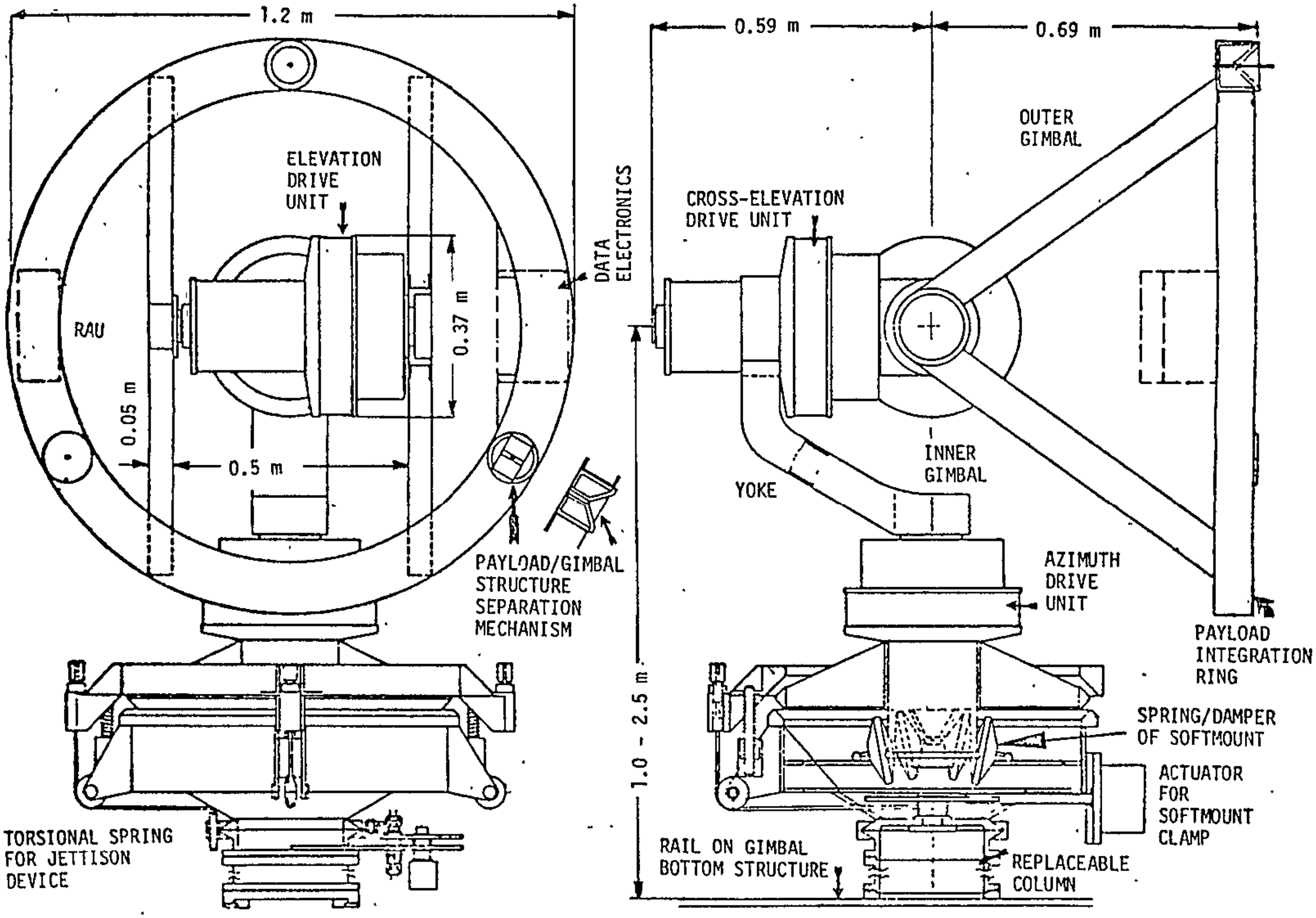

Figure B-2. IPS Gimbal Configuration

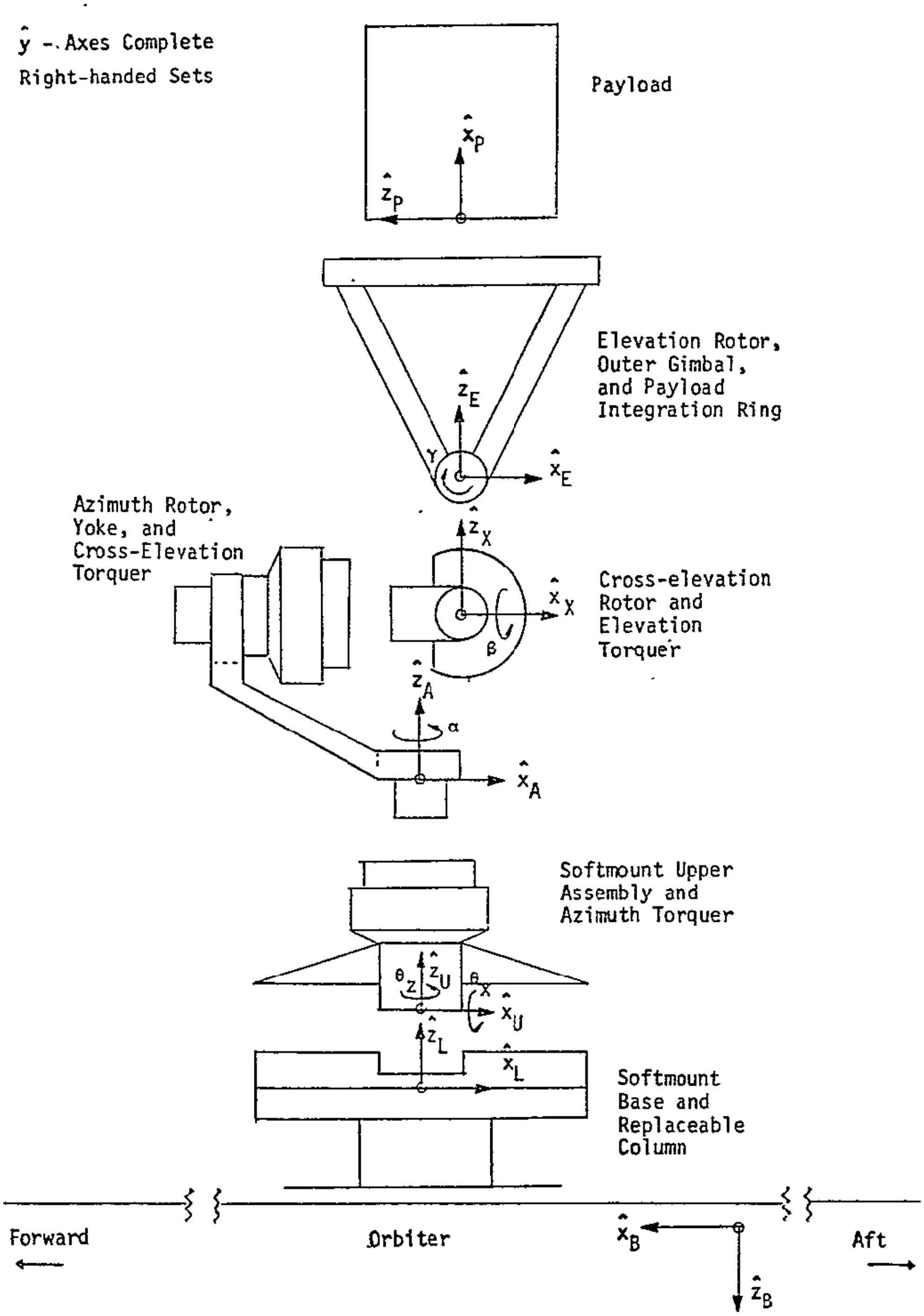

Figure B-3. Definition of Coordinate Systems

The payload unit vectors are related to the orbiter body unit vectors by the transformation

$$\hat{r}_P = A_{PB}\,\hat{r}_B$$

where the transformation A_{PB} can be factored into the product of transformations

$$A_{PB} = A_{PE}\,A_{EX}\,A_{XA}\,A_{AU}\,A_{UL}\,A_{LB}$$

Assuming zero IPS/orbiter mounting misalignments, the orbiter body (Appendix A) to softmount base transformation is

$$A_{LB} = \begin{bmatrix} -1 & 0 & 0 \\ 0 & 1 & 0 \\ 0 & 0 & -1 \end{bmatrix}$$

The softmount base to softmount upper assembly rotational transformation is the small angle transformation

$$A_{UL} = \begin{bmatrix} 1 & \theta_z & -\theta_y \\ -\theta_z & 1 & \theta_x \\ \theta_y & -\theta_x & 1 \end{bmatrix}$$

The softmount also allows three-axis translation between the L and U frames.

The gimbal angle transformations are, for azimuth

$$A_{AU} = \begin{bmatrix} \cos\alpha & \sin\alpha & 0 \\ -\sin\alpha & \cos\alpha & 0 \\ 0 & 0 & 1 \end{bmatrix}$$

for cross-elevation

$$A_{XA} = \begin{bmatrix} 1 & 0 & 0 \\ 0 & \cos\beta & \sin\beta \\ 0 & -\sin\beta & \cos\beta \end{bmatrix}$$

and for elevation

$$A_{EX} = \begin{bmatrix} \cos\gamma & 0 & -\sin\gamma \\ 0 & 1 & 0 \\ \sin\gamma & 0 & \cos\gamma \end{bmatrix}$$

Assuming zero payload mounting misalignment, the final transformation is

$$A_{PE} = \begin{bmatrix} 0 & 0 & 1 \\ 0 & 1 & 0 \\ -1 & 0 & 0 \end{bmatrix}$$

This transformation is for agreement with the IPS documentation (References B-1 B-2) convention of defining $\hat{x}_p$ as the payload LOS.

The gimbal angles have the ranges (Reference B-2)

azimuth: $-180 \leq \alpha \leq 180$ degrees

cross elevation: $-70 \leq \beta \leq 70$ degrees

elevation: $-70 \leq \gamma \leq 90$ degrees

The gimbal axes are specified to intersect within a 1.0 cm radius sphere, and are required to be aligned orthogonally to within 20 arc min with an uncertainty of less than 1 arc min. The softmount displacement limits are presented in Section B.7.

B.3 MASS PROPERTIES

A preliminary mass summary, from Reference B-1, is contained in Table B-1 with further details in Tables B-2 and B-3. Reliable inertia data is not available. Preliminary inertia estimates for some of the structural sections illustrated in Figure B-3 are contained in Reference B-3.

B.4 PAYLOAD CHARACTERISTICS

Figure B-4 illustrates the payload size/mass envelope derived from Reference B-2. The limits given for payload radius, length, and CG location are largely based on the requirement to center the payload CG

Table B-1. Mass Summary

Assembly	Subassembly/Unit	No.	Mass (Kg)	Comments
Gimbal Structure		1	256	See Table B-2 for breakdown
	Payload/Gimbal Separation	1		
	Jettison Device	1		
	Softmound Clamp	1		
Drive		3	126	See Table B-3 for breakdown
	Torque Motor	2		
	Load By-Pass Drive	1		
	Resolver	2		
Thermal Control			10	Distributed throughout gimbal system
Payload Clamp		1	144	Mounted on pallet
Attitude Measurement		1	57	
	Star Sensor	3	27	May not apply for earth viewing missions
	Solar Sensor	(1)	2	
	Optical Sensor Housings	1	18	
	Gyro Package	1	12	Mounted on payload integration ring
Power Electronics		1	27	
	PE Unit	2	21	Mounted on pallet
	Control Panel	2	6	External to pallet

Table B-1. Mass Summary (Cont'd)

Assembly	Subassembly/Unit	No.	Mass (Kg)	Comments
Data Electronics		1	24	
	Data Distribution Unit	1	5	Mounted on inner gimbal
	Harness	1	19	Distributed throughout gimbal system
MARGIN			106	
TOTAL			750	

Table B-2. Gimbal Structure Estimated Mass Breakdown

Integration Ring	20 kg
Outer Gimbal	35 Kg
Payload/Gimbal Structure Separation Mechanism	12 kg
Inner Gimbal	10 kg
Yoke	15 kg
Softmount Clamp	50 kg
Softmount Dampers (6)	7 kg
Jettison Device with Harness-Separator	35 kg
Plate	25 kg
Gimbal Bottom Structure Including Rails	40 kg
Miscellaneous	7 kg
	256 kg

Table B-3. Drive Assembly Estimated Mass Breakdown

Item	Mass/Assembly
2 Torquers	6 kg
2 Resolvers	4 kg
2 Angular contact bearings	1.5 kg
1 Radial contact bearing	
1 Motor for load by-pass mechanism	4.5 kg
1 Case with part of by-pass	12 kg
1 Shaft with part of by-pass	9 kg
Miscellaneous	5 kg
Total per assembly	42 kg
Total for 3 Drive Assemblies	126 kg

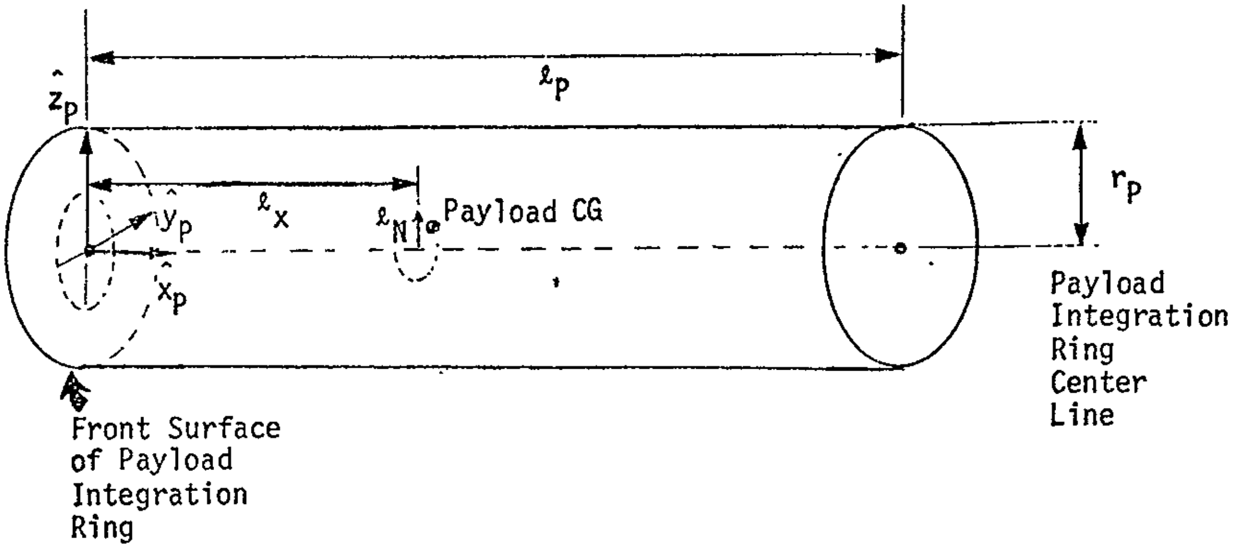

Quantity	Definition	Range	Units
m_p	Payload Mass	0 → 3000	Kg
ℓ_p	Payload length	1 → 6	m.
γ	Payload radius	0.25 → 1.5	m
ℓ_x	Payload cg location along payload integration ring center line	0.5 → 3	m
ℓ_N	Payload cg location normal to payload integration ring center line = $(\ell_y^2 + \ell_z^2)^{1/2}$	(0 → 0.3)*	m

* Reference B-2 is inconsistent on this point. Value given is from Table 3.2-1 of Reference, while Section 3.3.4-1 implies maximum is 0.05 m.

Figure B-4. Payload Envelope

in the payload clamp assembly during orbiter ascent/descent. This requirement imposes minimum as well as maximum payload dimensions.

Table B-4 contains physical data on the two reference payloads defined in Reference B-2, along with the computed payload inertias about the gimbal center of rotation (CR) expressed in $\bar{r}_E$ coordinates. The large CG/CR offsets greatly increase the inertias about the CR.

B.5 DRIVE CHARACTERISTICS

Each of the three gimbal drives is identical with the following characteristics (Reference B-2).

- 2 Torque motors for fine pointing and slewing

- type	brushless DC
- stall torque	10 N-m
- weight	3 kg
- ripple	< 7% of mean torque

- 2 Resolvers

- type	single speed/multispeed
- accuracy	3 arc min

- 3 Ball Bearings

- maximum friction torque	0.03 N-m per axis

- Cable follow-up

- flex lead spring torque	0.5 N-m for 90 deg rotation
- hysteresis	~0.005 N-m for 1 deg limit cycle

The two torque motors can be operated in parallel to yield up to 20 Nm torque. The drives can be locked with a self-contained load by-pass mechanism.

Table B-4. Definition of Reference Payload Physical Data

	Large Payload	Small Payload
Mass	2000 kg	200 kg
Dimensions:		
Length	4 m	1.5 m
Diameter	2 m	1.0 m
Moment of inertia about payload CG:		
about LOS axis	1000 kgm^2	25 kgm^2
about axes perp. to LOS	1200 kgm^2	20 kgm^2
CG offset from CR of gimbal axes:		
along LOS	2.50 m	1.50 m
perp. to LOS	0.30 m	0.10 m
Moment of inertia about CR in $\hat{r}_E$ - coordinates*		
I_{xx}	13880	472
I_{xy}	0	0
I_{xz}	0	0
I_{yy}	13700	470
I_{yz}	-1500	-30
I_{zz}	1180	27

* Assumes payload CR/CG offset perpendicular to LOS is along $\hat{y}_E$.

Figure B-5 contains a block diagram of the torquer drive system (Reference B-1). The primary input is the torque command from the DDU (Data Distribution Unit), and the motor torque nominally equals the command torque. The single speed resolver is used to derive gimbal angle and rate (with an accuracy of ± 2 deg and ± 0.15 deg/sec) for use in the angle and speed limit circuits. The speed limit is linearly decreased as the gimbal angle reaches its motion limits. The multi-speed resolver is used to commutate the brushless DC motor.

B.6. SOFTMOUNT CHARACTERISTICS

The softmount consists of six spring/dampers. Its purpose is to support and isolate the IPS gimbal system from high frequency shuttle disturbances, such as thruster firings and crew motion. Figure B-2 shows the location of the softmount in the IPS base, while Figure B-6 shows the arrangement of the individual spring/dampers. The softmount attachments use spherical bearings. Figure B-7 shows the details of a single spring/damper.

The rotational limits of the spring damper assembly are (Reference B-2)

- ± 5 mm translation (3-axis)
- ± 3 deg rotation (3-axis)

The translational spring constants for the assembly are (Reference B-3)

K_{Tx} = 2000 N/m

K_{Ty} = 2000 N/m

K_{Tz} = 800 N/m

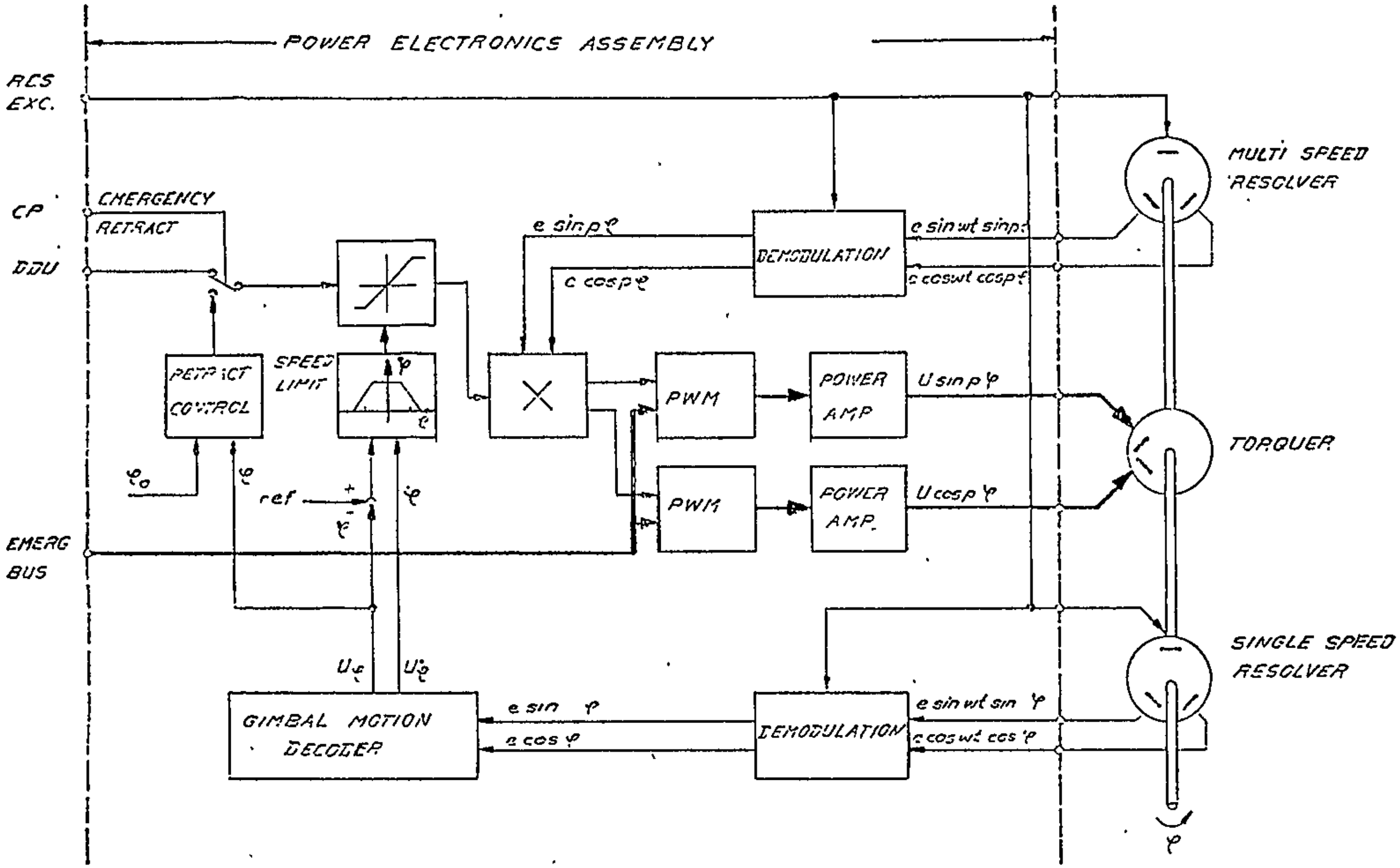

Figure B-5. Torquer Drive Block Diagram

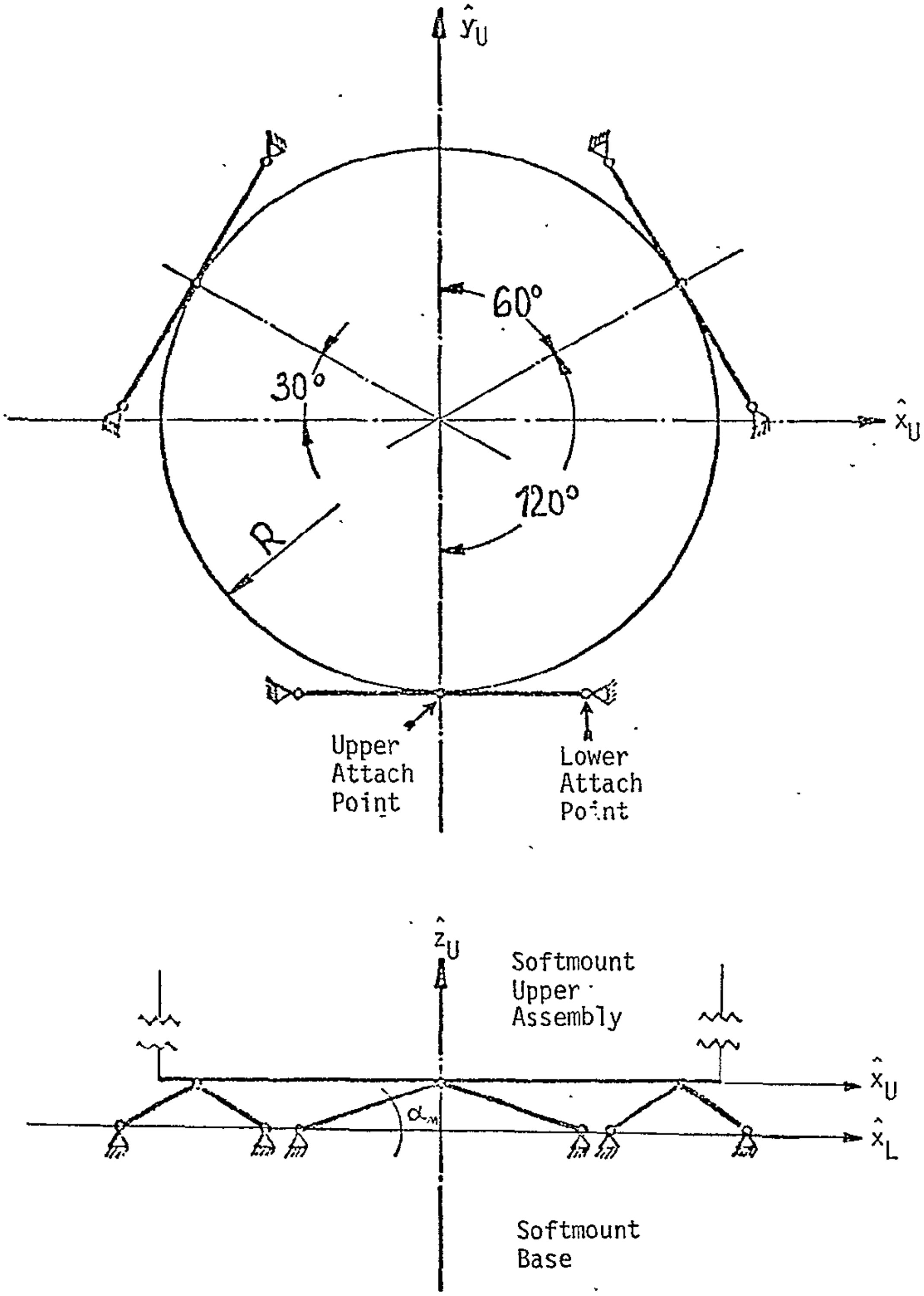

Figure B-6. Gimbal Structure/Softmount Suspension Arrangement

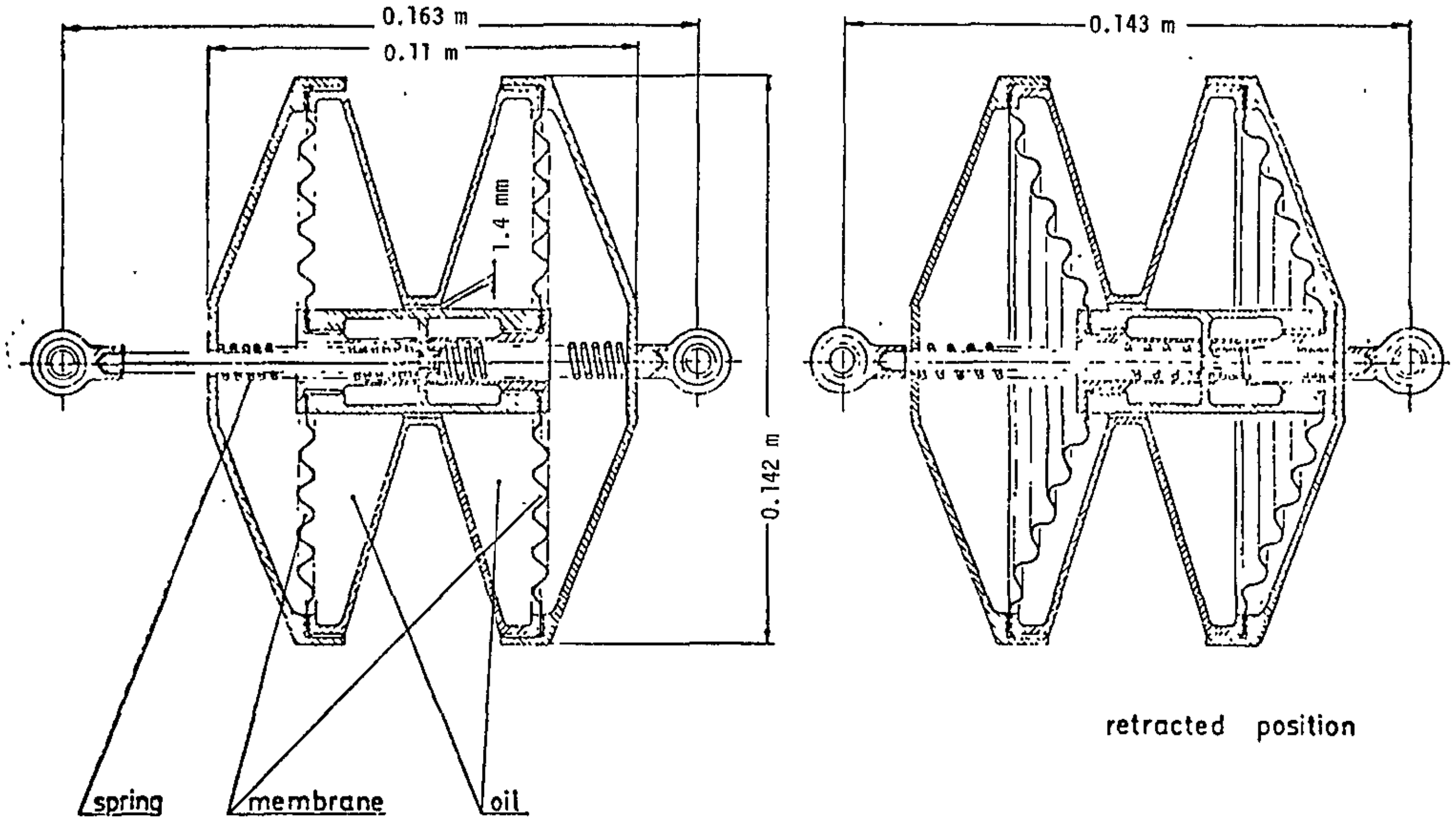

retracted position

normal position

Figure B-7. Softmount Spring/Damper

The translational damping constants are

B_{Tx} = 600 N/(m/sec)
B_{Ty} = 600 N/(m/sec)
B_{Tz} = 240 N/(m/sec)

The rotational spring constants are

$K_{\theta x}$ = 25 N-m/rad

$K_{\theta y}$ = 25 N-m/rad

$K_{\theta z}$ =250 N-m/rad

The rotational damping constants are

$B_{\theta x}$ = 7.5 N-m/(rad/sec)

$B_{\theta y}$ = 7.5 N-m (rad/sec)

$B_{\theta z}$ = 75 N-m (rad/sec)

The z-axis spring/damping constants depend on the skew angle α_M shown in Figure B-6. The value of α_M used for the above figures is not available.

B.7 GYRO CHARACTERISTICS

The inertial attitude and rate of the IPS payload is measured with a rate integrating gyro (RIG) package mounted on the payload integration ring. The gyro package has the following characteristics:

Type of gyros	Four strap-down pulse rebalanced, single DOF RIG Hamilton Standard RI-1139
Bandwidth	30 Hz
Gyro Output Noise	

Frequency Band (Hz)	RMS Noise (arc sec/sec)	
0.5 to 3	0.09	found by graphical
0.5 to 10	0.43	integration of PSD
0.5 to 50	2.99	

Short Term Random Drift (10 min):	0.005 deg/hr
Max Input Rate (operational)	2.5 deg/sec
Pulse weight (low mode)	0.0088 arc sec/pulse
Pulse weight (high mode)	0.07 arc sec/pulse
Configuration of input axes	3 orthogonal 1 equiangular skewed
Reliability	0.9999 (7 days) 0.9330 (1 year)

Rate is calculated from the incremental change of attitude (number of pulses) per 0.01 second sampling period. Rate is integrated to obtain attitude data. Attitude is updated periodically using star tracker data.

B.8 STAR TRACKER CHARACTERISTICS

Reference B-1 (Section 3.4.2.2.1) states that attitude information for gyro updates for earth missions will be provided by the payload. For completeness, however, data on the star tracker proposed for stellar missions is presented below.

Proposed FHST supplier:		Honeywell Inc.
Type of Sensor		HEAO-B with additional clock network
FOV		2° x 2°
IFOV		2 arc min x 2 arc min
Lens aperture		11.68 cm
Acquisition Probability		98.7% } for 8 Mv star with
False Acquisition		2.7% } + 10 Mv background
Bias Calibrated Accuracy		0.75 arc sec
Uncalibrated Accuracy		0.5 arc min
Noise equivalent angle		0.76 arc sec for 8 Mv star with + 10 Mv background averaged over 0.64 sec
7 threshold levels from +2.5 Mv to 9.3		
Maximum tracking rate		3 arc min/sec
Mass per Set (1 FHST, 1 BOD, 1 FEB, 1 IC)		9 kg
Power per Set		4 W
Size	FHST	60 x 21 x 21 cm
	BOD	17.5 x 10 x 10 cm

(FHST = fixed head star tracker)
(BOD = bright object detector)

B.9 REFERENCES

B-1. "Volume 2 - Technical Proposal, Part 1: Implementation", Dornier System.

B-2. IPS-SP-045-001, Issue 2, "Volume 2 - Technical Proposal, Part 2: Instrument Pointing Subsystem Specification", Dornier System, 19 December 1975.

B-3. Unpublished Notes from Marshall Space Flight Center, 18 June 1976.

APPENDIX C
DERIVATION OF EARTH POINTING RELATIONS

C.0 INTRODUCTION

This appendix contains a derivation of the gimbal angles, rates and accelerations required to point an orbiting payload at an earth-fixed aim point. The derivation is divided into two independent parts: orbit relations and gimbal relations. The orbit relations yield the aim vector in attitude reference coordinates, and do not involve the gimbal angles. The gimbal relations depend only on the orientation and order of rotation of the gimbal axes with respect to the attitude reference frame. For the IPS, it is assumed that the elevation and cross-elevation axes will be used for earth pointing. The derivation therefore assumes zero azimuth angle. The softmount angles are also assumed to be zero. Even with these simplifying assumptions, the resulting equations are sufficiently complex to preclude hand calculationof numerical results. A computer program for performing these calculations is described in Section C.3.

C.1 ORBIT RELATIONS

The position of the earth-fixed aim point, with respect to the spacecraft, is in vector notation

$$\bar{\rho} = \bar{r}_A - \bar{r}_S$$

where

$\bar{\rho}$ = vector from spacecraft to aim point

$\overline{r}_A$ = vector from geocenter to aim point
$\overline{r}_S$ = vector from geocenter to spacecraft

It is required here to find the attitude reference frame components of $\overline{P}$, and their first and second time derivatives, as explicit time functions. As a preliminary step, five coordinate frames are defined in Table C-1 and Figures C-1 and C-2.

The vector $\overline{r}_S$ in attitude reference coordinates is simply

$$\overline{r}_S = -r_S\,\hat{z}_R = -(r_o + h)\,\hat{z}_R$$

where

r_S = radius of S/C orbit
r_o = radius of earth
h = s/c altitude

The vector $\overline{r}_A$ is, for a given aim point, fixed in the geographic frame

$$\overline{r}_A = r_o \cos\phi_A \cos\lambda_A\,\hat{x}_g + r_o \cos\phi_A \sin\lambda_A\,\hat{y}_g + r_o \sin\phi_A\,\hat{z}_g$$

To express this vector in attitude reference coordinate components, the following series of transformations is required

Table C-1. Definition of Coordinate frames

Frame	Subscript	Origin	Type	Orientation*
Geographic	g	geocenter	rotating (fixed in earth)	$\hat{x}_g$ in equatorial plane along prime meridian $\hat{z}_g$ along earth rotation axis
Earth Centered Inertial	i	geocenter	inertial	$\hat{x}_i$ in equatorial plane in direction of vernal equinox $\hat{z}_i$ along earth rotation axis
Nodal	n	geocenter	inertial	$\hat{x}_n$ in equatorial plane along line of ascending node of S/C orbit $\hat{z}_n$ normal to orbit plane
Orbital	o	geocenter	rotating	$\hat{x}_o$ in orbit plane pointing towards S/C $\hat{z}_o$ normal to orbit plane
Attitude Reference	R	S/C	rotating	$\hat{x}_R$ in orbit plane along velocity vector $\hat{z}_R$ pointed at geocenter

* $\hat{y}$ completes right handed set

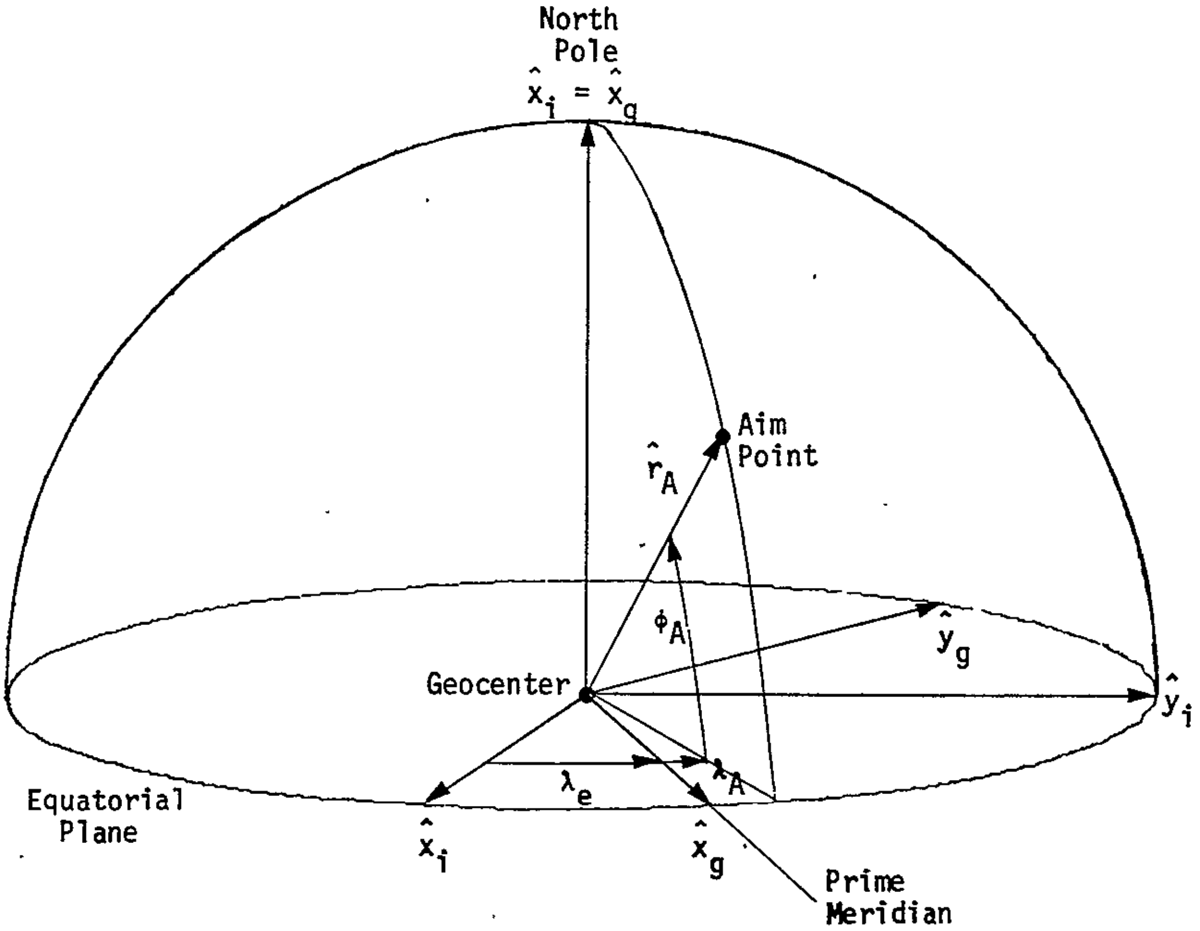

Symbol	Definition
i (subscript) g (subscript)	ECI frame Geographic frame
λ_A ϕ_A	Geographical longitude of aim point Geographical latitude of aim point
λ_e λ_o ω_e	$= \lambda_o + \omega_e t$ Angle between $\hat{x}_i$ and $\hat{x}_g$ at $t = 0$ Earth rotation rate

Figure C-1. Definition of Aim Point Unit Vector

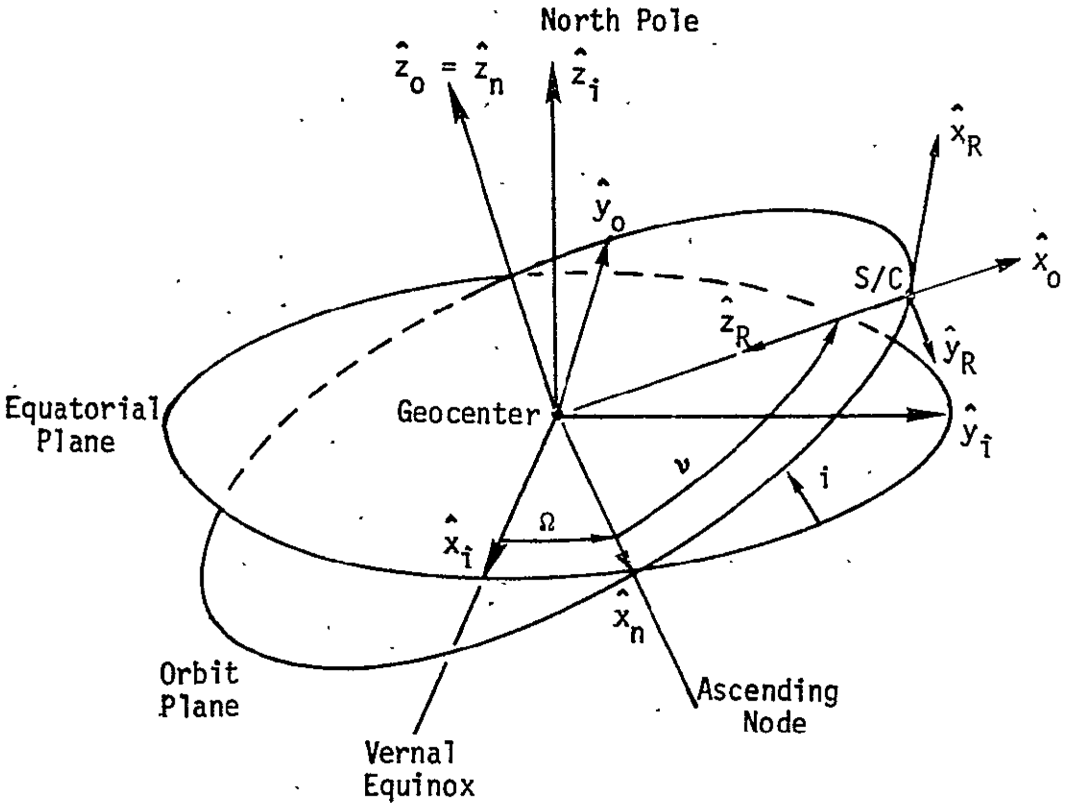

Symbol	Definition
i (subscript)	ECI frame
n (subscript)	Nodal frame
o (subscript)	Orbital frame
R (subscript)	Attitude Reference frame
Ω	Longitude of ascending node
i	Orbit inclination
ν	$= \nu_0 + \omega_0 t$
ν_0	orbit angle at $t = 0$
ω_0	orbit rate

Figure C-2. Definition of Orbit Parameters

$$T_{Rg} = T_{Ro}\ T_{on}\ T_{ne}\ T_{eg}$$

In matrix form, these transformations are

$$T_{eg} = \begin{bmatrix} \cos\lambda_e & -\sin\lambda_e & 0 \\ \sin\lambda_e & \cos\lambda_e & 0 \\ 0 & 0 & 1 \end{bmatrix}$$

$$T_{ne} = \begin{bmatrix} \cos\Omega & \sin\Omega & 0 \\ -\sin\Omega\cos i & \cos\Omega\cos i & \sin i \\ \sin\Omega\sin i & -\cos\Omega\sin i & \cos i \end{bmatrix}$$

$$T_{on} = \begin{bmatrix} \cos\nu & \sin\nu & 0 \\ -\sin\nu & \cos\nu & 0 \\ 0 & 0 & 1 \end{bmatrix}$$

$$T_{Ro} \begin{bmatrix} 0 & 1 & 0 \\ 0 & 0 & -1 \\ -1 & 0 & 0 \end{bmatrix}$$

The vector $\bar{\rho}$ can now be expressed in attitude reference coordinate components as

$$(\bar{\rho})_R = T_{Rg}\,(\bar{r}_A)_g - (\bar{r}_S)_R$$

Performing the indicated operations, yields the result

$$\rho_x = r_o\Big[-\cos\phi_A \sin\nu \cos(\Omega - \lambda_e - \lambda_A) - \cos\phi_A \cos i \cos\nu \sin(\Omega - \lambda_e - \lambda_A) + \sin\phi_A \sin i \cos\nu\Big] \qquad (C-1)$$

$$\rho_y = r_o\Big[-\cos\phi_A \sin i \sin(\Omega - \lambda_e - \lambda_A) - \sin\phi_A \cos i\Big] \qquad (C-2)$$

$$\rho_z = r_o\Big[-\cos\phi_A \cos\nu \cos(\Omega - \lambda_e - \lambda_A) + \cos\phi_A \cos i \sin\nu \sin(\Omega - \lambda_e - \lambda_A) - \sin\phi_A \sin i \sin\nu\Big] + r_S \qquad (C-3)$$

where

$$\nu = \nu_o + \omega_o t \qquad (C-4)$$

$$\lambda_e = \lambda_o + \omega_e t \qquad (C-5)$$

and

$$\omega_o = [GM/r_S^3]^{1/2} \tag{C-6}$$

$$GM = 0.3986 \times 10^6 \text{ Km}^3/\text{sec}^2 = \text{gravitational constant} \tag{C-7}$$

$$r_S = r_o + h \tag{C-8}$$

$$r_o = 6371 \text{ Km} = \text{mean earth radius} \tag{C-9}$$

$$\omega_e = 7.27 \times 10^{-5} \text{ rad/sec} = \text{earth rate} \tag{C-10}$$

Substituting for ν and λ_e and taking derivatives yields the first derivatives of the aim vector components

$$\begin{aligned}\dot{\rho}_X = r_o\,[&-(\omega_e - \omega_o \cos i) \cos \phi_A \sin \nu \sin (\Omega - \lambda_e - \lambda_A)\\ &+(\omega_e \cos i - \omega_o) \cos \phi_A \cos \nu \cos (\Omega - \lambda_e - \lambda_A)\\ &- \omega_o \sin \phi_A \sin i \sin \nu]\end{aligned} \tag{C-11}$$

$$\dot{\rho}_y = r_o\,[\omega_e \cos \phi_A \sin i \cos (\Omega - \lambda_e - \lambda_A)] \tag{C-12}$$

$$\begin{aligned}\dot{\rho}_Z = r_o\,[&-(\omega_e - \omega_o \cos i) \cos \phi_A \cos \nu \sin (\Omega - \lambda_e - \lambda_A)\\ &-(\omega_e \cos i - \omega_o) \cos \phi_A \sin \nu \cos (\Omega - \lambda_e - \lambda_A)\\ &- \omega_o \sin \phi_A \sin i \cos \nu]\end{aligned} \tag{C-13}$$

and the second derivatives of the aim vector components

$$\begin{aligned}\ddot{\rho}_x = r_o \Big\{ & [(\omega_o^2 + \omega_e^2) - 2\,\omega_o\,\omega_e \cos i] \cos \phi_A \sin \nu \cos (\Omega - \lambda_e - \lambda_A) \\ & + [(\omega_o^2 + \omega_e^2) \cos i - 2\,\omega_o\,\omega_e) \cos \phi_A \cos \nu \sin (\Omega - \lambda_e - \lambda_A) \\ & - \omega_o^2 \sin \phi_A \sin i \cos \nu \Big\}\end{aligned} \qquad \text{(C-14}$$

$$\ddot{\rho}_y = r_o\,[\omega_e^2 \cos \phi_A \sin i \sin (\Omega - \lambda_e - \lambda_A)] \qquad \text{(C-15}$$

$$\begin{aligned}\ddot{\rho}_z = r_o \Big\{ & [(\omega_o^2 + \omega_e^2) - 2\,\omega_o\,\omega_e \cos i] \cos \phi_A \cos \nu \cos (\Omega - \lambda_e - \lambda_A) \\ & - [(\omega_o^2 + \omega_e^2) \cos i - 2\,\omega_o\,\omega_e] \cos \phi_A \sin \nu \sin (\Omega - \lambda_e - \lambda_A) \\ & + \omega_o^2 \sin \phi_A \sin i \sin \nu \Big\}\end{aligned} \qquad \text{(C-16)}$$

The distance between the S/C and the aim point and its derivatives, are

$$\rho = |\bar{\rho}| = [r_o^2 - r_S^2 + 2\,r_S\,\rho_z]^{1/2} \qquad \text{(C-17}$$

$$\dot{\rho} = r_S\,\dot{\rho}_z/\rho \qquad \text{(C-18)}$$

$$\ddot{\rho} = r_S\,[\rho\,\ddot{\rho}_z - \dot{\rho}_z\,\dot{\rho}]/\rho^2 \qquad \text{(C-19)}$$

C.2 GIMBAL RELATIONS

With the shuttle orbiter flying in an inverted attitude, the attitude reference and orbiter body frames are related by (Appendix A)

$$A_{RB} = \begin{bmatrix} 1 & 0 & 0 \\ 0 & -1 & 0 \\ 0 & 0 & -1 \end{bmatrix}$$

With zero softmount and azimuth gimbal angles, the payload LOS unit vector $\hat{x}_P$ has the attitude reference coordinate components (Appendix B)

$$\begin{aligned} n_x &= (\hat{x}_P \cdot \hat{x}_R) = -\sin\gamma \\ n_y &= (\hat{x}_P \cdot \hat{y}_R) = -\sin\beta\cos\gamma \\ n_z &= (\hat{x}_P \cdot \hat{z}_R) = \cos\beta\cos\gamma \end{aligned}$$

The condition for alignment of the payload LOS along the aim vector is

$$\hat{\rho} = \overline{\rho}/\rho = \hat{x}_P$$

Resolved into attitude reference components, this vector equation is equivalent to the three scalar equations

$$\rho_x/\rho = \eta_x = -\sin\gamma$$

$$\rho_y/\rho = \eta_y = -\sin\beta\cos\gamma$$

$$\rho_z/\rho = \eta_z = \cos\beta\cos\gamma$$

The required gimbal angles are therefore

$$\gamma = \sin^{-1}[-\rho_x/\rho] \tag{C-20}$$

$$\beta = \tan^{-1}[-\rho_y/\rho_z] \tag{C-21}$$

The first derivatives of the gimbal angles are

$$\dot{\gamma} = \frac{\dot{\rho}\,\rho_x - \rho\,\dot{\rho}_x}{\rho^2\cos\gamma} \tag{C-22}$$

$$\dot{\beta} = \cos^2\beta\left[\frac{\rho_y\,\dot{\rho}_z - \dot{\rho}_y\,\rho_z}{\rho_z^2}\right] \tag{C-23}$$

while the second derivatives are

$$\ddot{\gamma} = \frac{\rho^2 \cos \gamma [\ddot{\rho}\, \rho_X - \rho\, \ddot{\rho}_X] - [\dot{\rho}\, \rho_X - \rho\, \dot{\rho}_X]\, [2\, \rho\, \dot{\rho} \cos \gamma + \rho\, \rho_X\, \dot{\gamma}]}{\rho^4 \cos^2 \gamma} \tag{C-24}$$

$$\begin{aligned} \ddot{\beta} = &- 2\, \dot{\beta} \sin \beta \cos \beta \left(\frac{\rho_y\, \dot{\rho}_z - \dot{\rho}_y\, \rho_z}{\rho_z^2} \right) \\ &+ \cos^2 \beta \left[\left(\frac{\rho_y\, \ddot{\rho}_z - \ddot{\rho}_y\, \rho_z}{\rho_z^2} \right) - \frac{2\, \dot{\rho}_z\, (\rho_y\, \dot{\rho}_z - \dot{\rho}_y\, \rho_z)}{\rho_z^3} \right] \end{aligned} \tag{C-25}$$

C.3 PROGRAM AIM

Program AIM, written in FORTRAN for timeshare use, performs the calculations represented by Equations (C-1) to (C-25). The program listing, contained in Section C.3.2, is intended to be largely self-explanatory. An option exists to limit printout and computation of peak values to the time period in which the aim point is within a cone of half angle CONE around the local vertical. It should be noted that the assumption $\lambda_o = 0$ does not really restrict the generality of the program, as λ_o always appears together with λ_A and Ω in the grouping $\Omega - \lambda_e - \lambda_A = \Omega - \omega_e t - \lambda_o - \lambda_A$.

C.3.1 Example

To illustrate the use of the program and the type of results obtained, an example case is presented. The example uses the following parameter values

```
1$LIST
  ALT       =  2.0E+02,
  RLAMDA    =  -1.5,
  PHI       =  0.,
  ALPHA0    =  0.,
  OMEGA0    =  0.,
  RINC      =  6.0E+01,
  CONE      =  6.0E+01,
  ISTEP     =  1,
  $END
```

Physically, the S/C is in a 200 Km orbit with 60 deg inclination, at its ascending node at t = 0. The aim point is on the equator, separated 1.5 deg in longitude from the S/C ascending node at t = 0.

Figures C-3 and C-4 contain time history plots of the elevation and cross-elevation angles, rates, and accelerations (units are deg, deg/sec, and deg/sec^2) obtained from the data on TAPE13 with ICONE = 60 deg, points are only plotted for times when

$$\hat{x}_P \cdot \hat{z}_R = \cos\gamma \cos\beta \geq \cos(60 \text{ deg})$$

that is, for

$$-55 \leq t \leq 35 \text{ sec}$$

Action must be taken before the aim point enters the 60 degree half-angle cone to ensure the proper combination of angles, rates, and accelerations at t = - 55.

The peak value output on TAPE6, with explanatory annotation, is presented below.

MINIMUM	MAXIMUM	
-55.00000000	35.00000000	t
-49.94639430	53.69544861	γ
.57495583	1.67338781	$\dot{\gamma}$
-.03288377	.03277787	$\ddot{\gamma}$
31.76995201	36.30556084	β
-.12547415	-.01716867	$\dot{\beta}$
-.00129794	-.00091252	$\ddot{\beta}$
250.67326736	420.03802473	ρ

Note that the peak values of $\dot{\beta}$ and $\ddot{\beta}$ are more than an order of magnitude less than the peak values of $\dot{\gamma}$ and $\ddot{\gamma}$

C.3.2 Listing of Program AIM

A listing of program AIM follows.

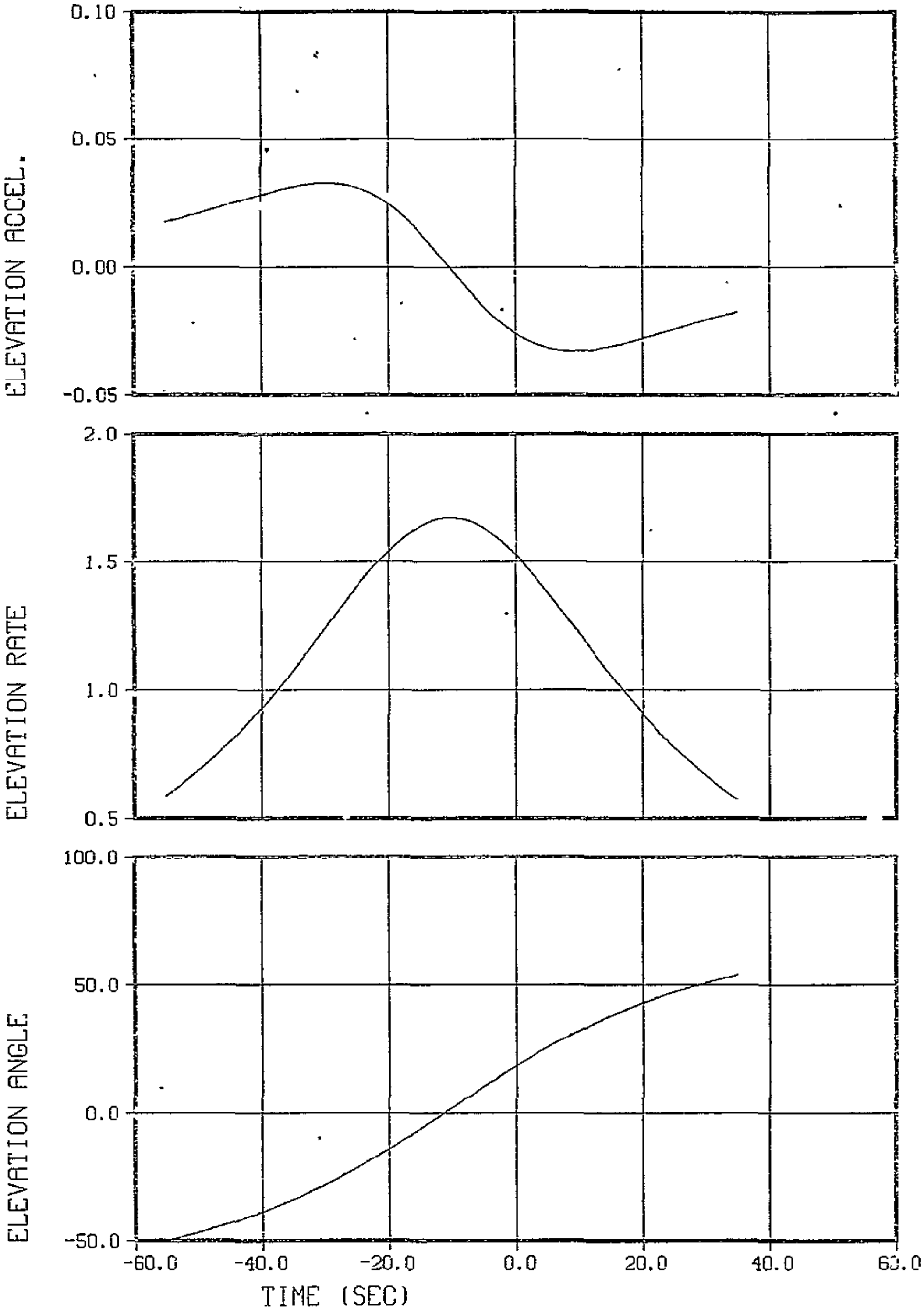

Figure C-3. Elevation Angle Time History

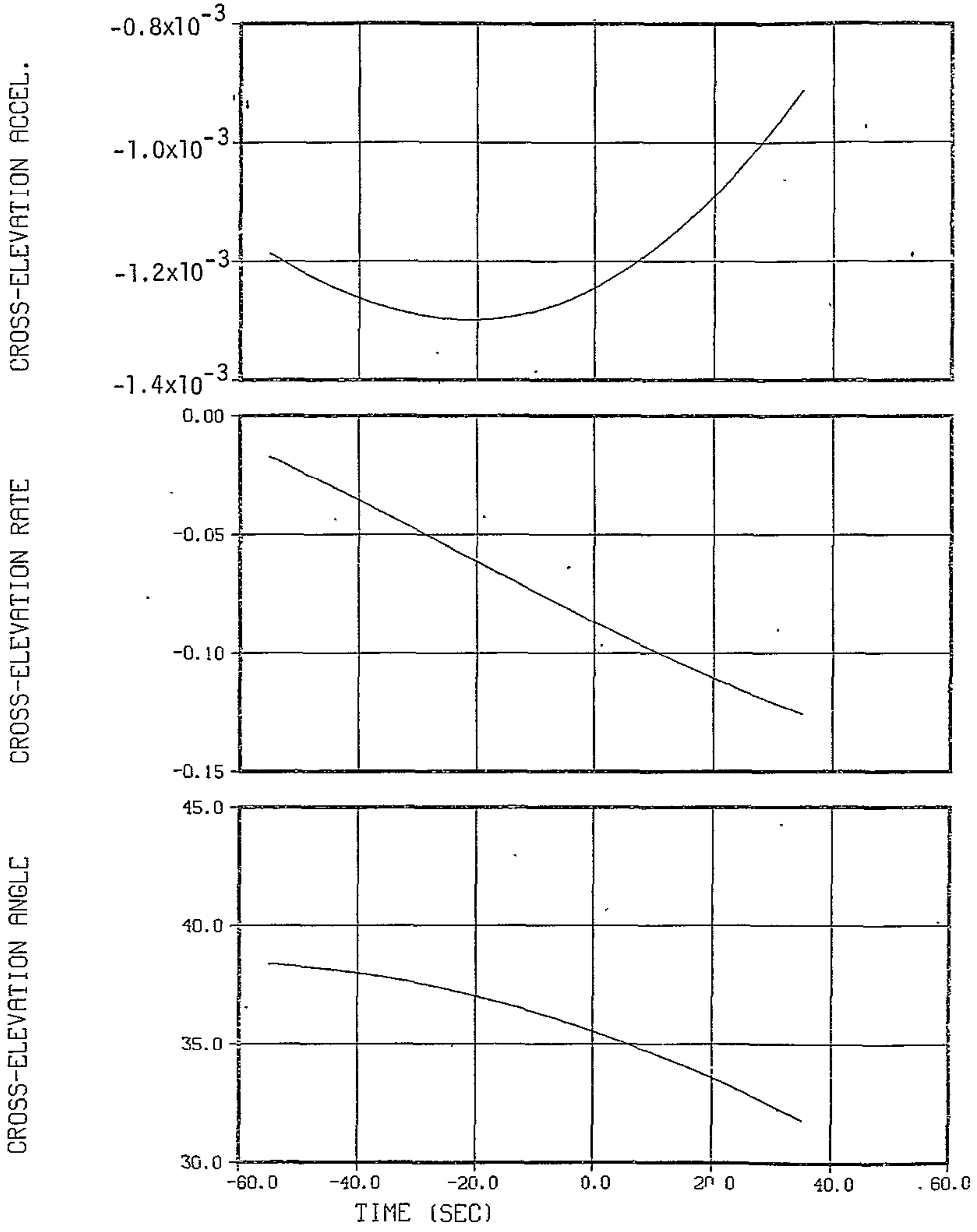

Figure C-4. Cross Elevation Time History

```
      PROGRAM AIM(INPUT,TAPE5=INPUT,TAPE6,TAPE13)
      COMMON/FIOBUFR/BUF(241)
C
C    **** PROGRAM TO COMPUTE GIMBAL ANGLES, RATES, AND ACCELERATIONS
C         REQUIRED TO POINT IPS PLATFORM AT EARTH-FIXED AIM POINT
C
C    **** COMPUTES TIME HISTORY (ON TAPE13) FOR PLOTTING
C         AND PEAK MAXIMUM AND MINIMUM VALUES (ON TAPE6)
C
C    **** REQUIRED INPUT DATA:          (ANGLES IN DEGREES)
C             ALT    = ORBIT ALTITUDE (KM)
C             RLAMDA = LONGITUDE OF AIM POINT (IN GEOGRAPHIC COORDINATES)
C             PHI    = LATITUDE OF AIM POINT (IN GEOGRAPHIC COORDINATES)
C             ALPHAO = ORBIT ANGLE FROM ASCENDING NODE AT T=0
C             OMEGAO = LONGITUDE OF ASCENDING NODE (ECI COORDINATES)
C             RINC   = ORBIT INCLINATION
C             CONE   = HALF CONE ANGLE AROUND LOCAL VERTICAL FOR WHICH
C                      DATA IS TO BE CALCULATED
C             ISTEP  = COMPUTATION TIME STEP (SEC)
C
C    **** FOLLOWING DATA IS PRESET FOR EARTH ORBIT
C           RO     = EARTH RADIUS (KM)
C           WE     = EARTH ROTATION RATE (RAD/SEC)
C           GM     = GRAVITATIONAL CONSTANT (KM**3/SEC**2)
C
C    **** THESE ASSUMPTIONS HAVE BEEN MADE:
C              - CIRCULAR ORBIT
C              - SPHERICAL EARTH
C              - LAMDAO=0 (I.E. PRIME MERIDIAN ALONG VERNAL EQUINOX
C                AT T=0)
C              - ZERO AZIMUTH AND SOFTMOUNT ANGLES
C
      CALL LINESIZ(240)
      NAMELIST/LIST/ALT,RLAMDA,PHI,ALPHAO,OMEGAO,RINC,CONE,ISTEP
      DATA RO,WE,GM/6371., 7.2722052E-5, 0.3986E6/
      DATA GMIN,GDMIN,GDDMIN,BMIN,BDMIN,BDDMIN/6*1.E50/
      DATA GMAX,GDMAX,GDDMAX,BMAX,BDMAX,BDDMAX/6*-1.E50/
      DATA RMIN,TMIN,RMAX,TMAX/2*1.E50,2* -1.E50/
      DATA PI/3.141592653589793/
      DATA CONE,ISTEP/60.,1/
      REWIND 13
      RADDEG=180./PI
```

ORIGINAL PAGE IS
OF POOR QUALITY

```
      DEGRAD=1./RADDEG
      READ(5,LIST)
      WRITE(6,LIST)
      WRITE(13,101) ALT,RLAMDA,PHI,ALPHAO,OMEGAO,RINC
  101 FORMAT(5X,6E12.4)
C
C   **** COMPUTE CONSTANTS
C
      RS=RO+ALT
      ROS=RO*RO-RS*RS
      WO=SQRT(GM/RS**3)
      WOE=WO*WE
      WO2=WO*WO
      WE2=WE*WE
      W2=WO2+WE2
      RL=DEGRAD*RLAMDA
      PH=DEGRAD*PHI
      ALO=DEGRAD*ALPHAO
      OMO=DEGRAD*OMEGAO
      RI=DEGRAD*RINC
      CI=COS(RI)
      SI=SIN(RI)
      CP=COS(PH)
      SP=SIN(PH)
      X11=CP*(WE-WO*CI)
      X12=CP*(WE*CI-WO)
      X13=WO*SP*SI
      X21=(W2-2.*WOE*CI)*CP
      X22=(W2*CI-2.*WOE)*CP
      X23=WO2*SP*SI
      Y11=WE*CP*SI
      Y21=WE*Y11
      CCONE=COS(DEGRAD*CONE)
      NSTEP=1+600/ISTEP
      KSTEP=1+(NSTEP-1)/2
      JJ=0
C
C   **** START OF COMPUTATIONAL LOOP
C
      DO 10 I=1,NSTEP
      T=ISTEP*(I-KSTEP)
      AL=ALO+WO*T
```

```
      CAL=COS(AL)
      SAL=SIN(AL)
      OMEG=OMO-WE*T
      GAM=OMEG-RL
      CGAM=COS(GAM)
      SGAM=SIN(GAM)
C
C  **** S/C-AIM POINT VECTOR IN ATTITUDE REFERENCE COORDINATES
C
      RX=RO*(-CP*SAL*CGAM-CP*CI*CAL*SGAM+SP*SI*CAL)
      RY=RO*(-CP*SI*SGAM-SP*CI)
      RZ=RO*(-CP*CAL*CGAM+CP*CI*SAL*SGAM-SP*SI*SAL)+RS
C
C  **** FIRST DERIVATIVE OF S/C AIM POINT VECTOR
C
      RXD=RO*(-X11*SAL*SGAM+X12*CAL*CGAM-X13*SAL)
      RYD=RO*Y11*CGAM
      RZD=RO*(-X11*CAL*SGAM-X12*SAL*CGAM-X13*CAL)
C
C  **** SECOND DERIVATIVE OF S/C-AIM POINT VECTOR
C
      RXDD=RO*(X21*SAL*CGAM+X22*CAL*SGAM-X23*CAL)
      RYDD=RO*Y21*SGAM
      RZDD=RO*(X21*CAL*CGAM-X22*SAL*SGAM+X23*SAL)
C
C  **** S/C AIM POINT DISTANCE AND DERIVATIVES
C
      R=SQRT(ROS+2.*RS*RZ)
      RR=R*R
      RD=RS*RZD/R
      RDD=RS*(R*RZDD-RZD*RD)/RR
C
C  **** ELEVATION ANGLE AND DERIVATIVES
C
      G=ASIN(-RX/R)
      CG=COS(G)
      CD=(RD*RX-R*RXD)/(RR*CG)
      GDD=RR*CG*(RDD*RX-R*RXDD)-(RD*RX-R*RXD)*(2.*R*RD*CG+R*RX*GD)
      GDD=GDD/(RR*RR*CG*CG)
C
C  **** CROSS-ELEVATION ANGLE AND DERIVATIVES
C
```

ORIGINAL PAGE IS
OF POOR QUALITY

```
      B=0.
      IF(RY.NE.0. .OR. RZ.NE.0.) B=ATAN2(-RY,RZ)
      CB=COS(B)
      SB=SIN(B)
      RZ2=RZ*RZ
      BD=CB*CB*(RY*RZD-RYD*RZ)/RZ2
      BDD=-2.*BD*CB*SB*(RY*RZD-RYD*RZ)/RZ2
     X +CB*CB*((RY*RZDD-RYDD*RZ)/RZ2-2.*RZD*(RY*RZD-RYD*RZ)/(RZ*RZ2))
C
C   **** CHECK IF AIM POINT IS WITHIN GIMBAL CONSTRAINTS
C
      ACONE=CG*CB
      IF(ACONE.LT.CCONE .AND. JJ.EQ.0) GO TO 10
      IF(ACONE.LT.CCONE .AND. JJ.EQ.1) GO TO 20
      JJ=1
C
C   **** CONVERT ANGLES TO DEGREES
C
      DG=RADDEG*G
      DGD=RADDEG*GD
      DGDD=RADDEG*GDD
      DB=RADDEG*B
      DBD=RADDEG*BD
      DBDD=RADDEG*BDD
C
C  ****  FIND PEAK VALUES
C
      GMIN=AMIN1(GMIN,DG)
      GDMIN=AMIN1(GDMIN,DGD)
      GDDMIN=AMIN1(GDDMIN,DGDD)
      GMAX=AMAX1(GMAX,DG)
      GDMAX=AMAX1(GDMAX,DGD)
      GDDMAX=AMAX1(GDDMAX,DGDD)
      BMIN=AMIN1(BMIN,DB)
      BDMIN=AMIN1(BDMIN,DBD)
      BDDMIN=AMIN1(BDDMIN,DBDD)
      BMAX=AMAX1(BMAX,DB)
      BDMAX=AMAX1(BDMAX,DBD)
      BDDMAX=AMAX1(BDDMAX,DBDD)
      RMIN=AMIN1(RMIN,R)
      RMAX=AMAX1(RMAX,R)
      TMIN=AMIN1(TMIN,T)
```

```
      TMAX=AMAX1(TMAX,T)
C
C  **** WRITE ON TAPE13 IF AIM POINT IS WITHIN GIMBAL CONSTRAINTS
C          WRITE PEAK VALUES ON TAPE6 LAST TIME THROUGH
C
      WRITE(13,100) T,RX,RY,RZ,RXD,RYD,RZD,RXDD,RYDD,RZDD,R,RD,RDD
     X ,DG,DGD,DGDD,DB,DBD,DBDD
  100 FORMAT(F6.0,18E13.5)
   10 CONTINUE
   20 WRITE(6,102) TMIN,TMAX,GMIN,GMAX,GDMIN,GDMAX,GDDMIN,GDDMAX,
     X BMIN,BMAX,BDMIN,BDMAX,BDDMIN,BDDMAX,RMIN,RMAX
  102 FORMAT(/5X,2F15.8,//,3(5X,2F15.8/)/,3(5X,2F15.8/)/,5X,2F15.8,/)
      ENDFILE 13
      END
```

APPENDIX D
ORBITER DISTURBANCE MODEL

D.0 INTRODUCTION

Four types of external disturbance torques act on the shutt orbitor

- aerodynamics ($\overline{T}_A$)
- gravity gradient ($\overline{T}_G$)
- solar ($\overline{T}_S$)
- residual magnetism ($\overline{T}_M$)

A null torque attitude is, by definition, one at which the total external disturbance torque is zero

$$\overline{T} = \overline{T}_A + \overline{T}_G + \overline{T}_S + \overline{T}_M = \overline{0} \tag{D-1}$$

At the expected range of orbiter altitudes for EVAL (150 to 1000 km) the gravity gradient and aerodynamic torques predominate. Therefore the total torque will be approximated by the aerodynamic and gravity gradient torques alone

$$\overline{T} \simeq \overline{T}_A + \overline{T}_G \tag{D-2}$$

In general, the mission-to-mission and time-to-time variability of the orbiter and environmental properties exceeds the neglected disturbance sources. For example, the orbiter is estimated to have a residual magnetic moment density of from 2 to 5 pole-cm (0.002 to 0.005 Amp-m^2) per kilogram mass. With a typical orbiter mass of 97000 kg the total residual moment would be in the range

194 to 485 Amp-m^2. The worst case condition occurs with the residual magnetic moment normal to the earths $\overline{B}$ field with the orbiter 150 km over the magnetic pole. The magnitude of the resulting torque on the orbiter is

$$T_M = \frac{2 M_e M_r}{r_s^3} \tag{D-3}$$

where $M_e/r_s^3 = 2.9 \times 10^{-5}$ weber/m^2 at 150 km. The residual magnetism torque is thus no more than 0.0113 to 0.0281 N-m, under worst case conditions. This is at least an order of magnitude less than the nominal gravity gradient and aerodynamic torques.

The aerodynamic and gravity gradient disturbance models used in this study are discussed in the following sections.

D.1 AERODYNAMIC TORQUES

The aerodynamic torque model is based on Reference D-1, with the torque in body coordinates expressed as

$$\overline{T}_A = \begin{bmatrix} qSb\ C_\ell(\alpha, \beta) \\ qS\overline{c}\ C_m(\alpha, \beta) \\ qSb\ C_n(\alpha, \beta) \end{bmatrix} \tag{D-4}$$

The factors entering into Equation (D-4) can be conveniently divided into three groupings. The influence of the external environment on the aerodynamic torque is summarized by the single factor

q = dynamic pressure.

Orbiter dimensions enter through the quantities

S = reference area = 2690 ft^2 = 249.9 m^2
b = wing span = 936.68 in = 23.792 m
$\bar{c}$ = mean aerodynamic chord = 474.81 in = 12.060 m

Finally, the influence of the orbiter attitude on the aerodynamic torque is summarized by the moment coefficients

C_l = rolling-moment coefficient
C_m = pitching-moment coefficient
C_n = yawing-moment coefficient

and the associated attitude angles with respect to the air stream

α = angle of attack
β = angle of side slip

Each of these groupings is discussed, in turn, in the subsections that follow.

D.1.1 Environmental Factors

The dynamic pressure q is dependent on the spacecraft environment through the relation

$$q = \frac{1}{2} \rho v_r^2 \tag{D-5}$$

where

ρ = atmospheric density
v_r = relative velocity between orbiter and atmosphere

Although dynamic pressure is nominally a function of altitude, many other factors can produce significant long and short term variations.

Atmospheric Density Model

This section contains a brief discussion of an atmospheric density model and an example case of density variations over an orbit. Details can be found in References D-1 to D-6.

Recognizing that the atmospheric density at a given altitude can undergo large (factor of 5 or more) variations, it is necessary to adopt a density model that is both realistic and tractible. The purposes of the study are served by adopting the density model in Reference D-1 as the nominal altitude/density model. This model, converted to metric units and extrapolated for altitude above 240 Km, is plotted in Figure D-1. Data on density variations is provided by the MSFC Modified Jacchia Atmospheric Density Model (References D-5 and D-6).

Measurements made with density gauges, mass spectrometers, and derived from satellite drag data, have revealed a number of effects other than altitude that result in variations in upper atmospheric density. All, except the last, of the following effects are included in the MSFC Modified Jacchia Model Atmosphere:

- Variations with solar activity
- diurnal variation
- variations with geomagnetic activity
- semi annual variation
- seasonal-latitudinal variations
- rapid density variations (probably associated with tidal and gravity waves)

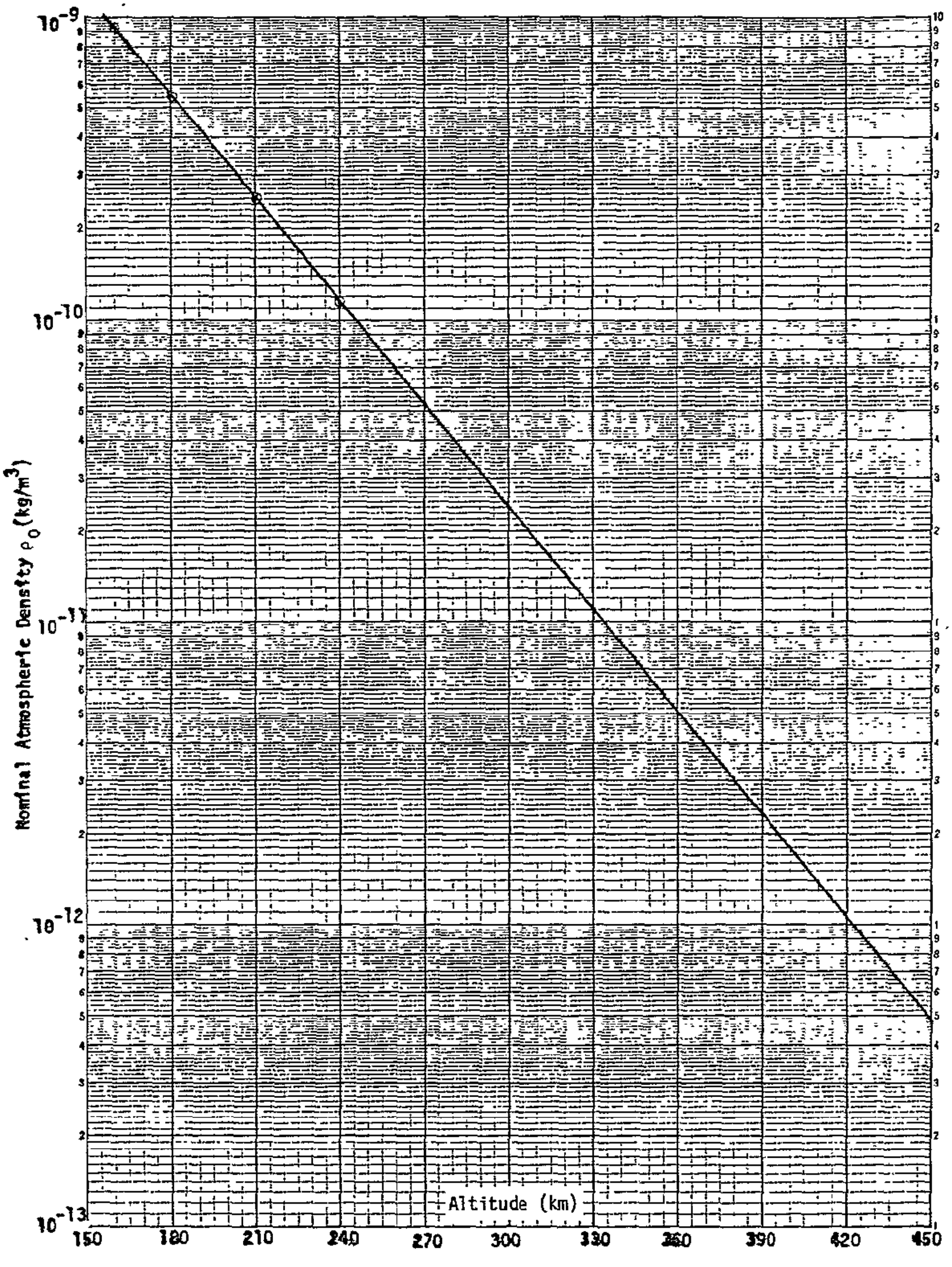

Figure D-1. Nominal Atmospheric Density

The primary physical mechanism affecting upper atmospheric density is the heating and dissociation of the atmosphere caused by solar ultraviolet radiation. The intensity and spectral content of the radiation varies with solar activity with periods ranging from less than a day to the 11 year solar cycle. Diurnal variations are caused by the rotation of the earth, resulting in a density bulge around 1400 solar time at a latitude approximately equal to that of the sub solar point, and an anti-bulge centered around 0300 hours at about the same latitude in the opposite hemisphere. The ratio of day over night density increases with altitude, and is largest at lower latitudes. Geomagnetic activity, caused by solar flares, can be correlated with large short term density increases. There is an average delay of 6.7 hours from the start of the geomagnetic storm to the time of the density perturbation. Semi-annual variations are not well understood, but observations indicate the density shows a high maximum in October, a secondary minimum in January, a secondary maximum in April, and a primary minimum in July. Seasonal-Latitudinal variations are small over the EVAL altitude range.

The "Quick-Look Density Model" in Reference D-6 incorporates all the effects in the MSFC Modified Jacchia Model in the form of equations and tables. The complexity of the model precludes determining the "worst case" variation over an orbit for EVAL. Instead, a "typical" low altitude (200 Km) case was worked to obtain an estimate of the short term density variation that can be expected on a day with low geomagnetic activity. The results are plotted in Figure D-2, which also contains a listing of the parameters used.

The density varies from approximately 1.8×10^{-10} to 2.8×10^{-10} Kg/m^3, or a variation about the mean of ± 20%. The variation is also almost sinusoidal at orbit frequency.

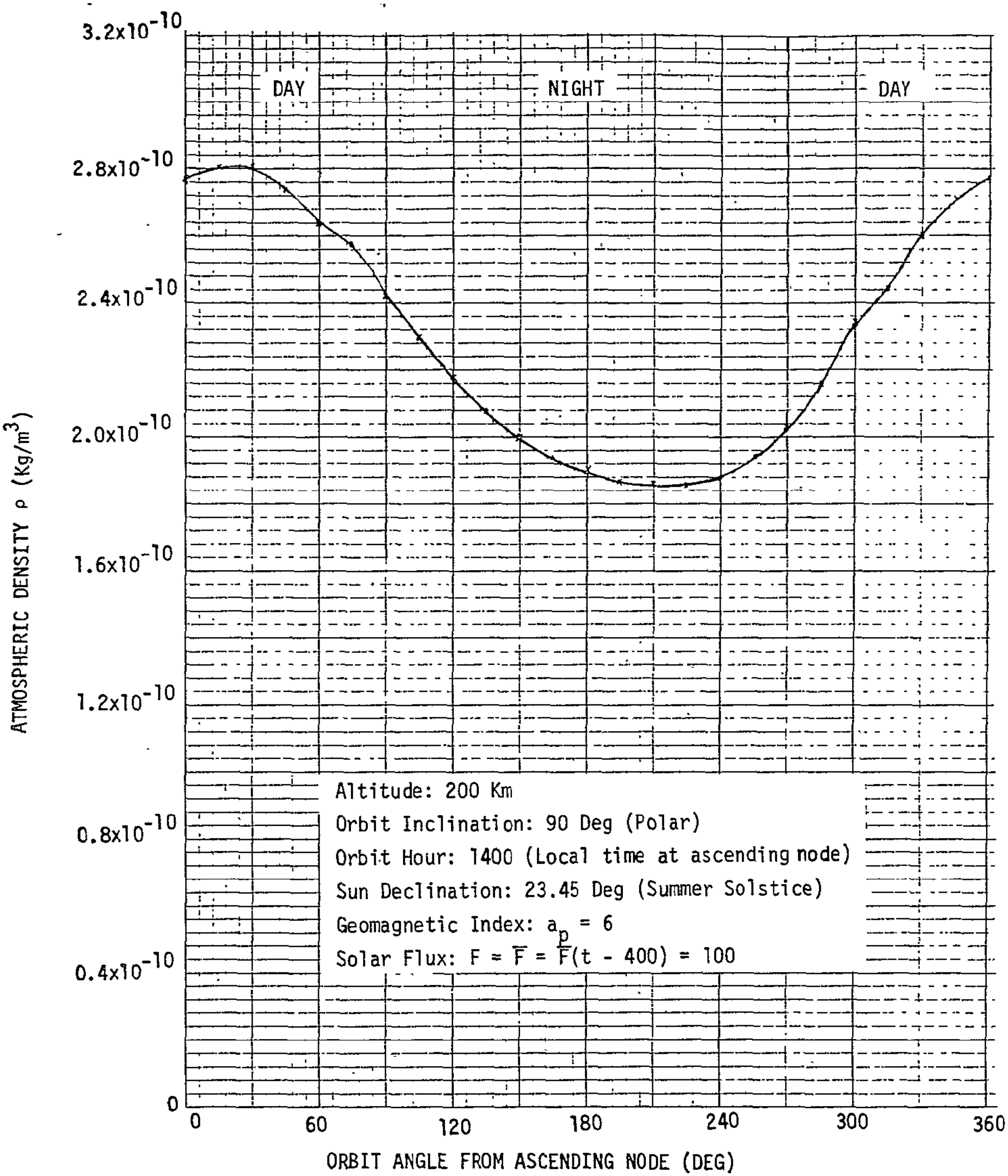

Altitude: 200 Km

Orbit Inclination: 90 Deg (Polar)

Orbit Hour: 1400 (Local time at ascending node)

Sun Declination: 23.45 Deg (Summer Solstice)

Geomagnetic Index: $a_p = 6$

Solar Flux: $F = \overline{F} = \overline{F}(t - 400) = 100$

Figure D-2. Variation In Atmospheric Density Over One Orbit

Note that the mean density under the conditions in Figure D-2, about $2.3\text{x}10^{-10}$ Kg/m^3, is somewhat less than the $3.3\text{x}10^{-10}$ K_g/m^3 density at 200 Km implied by Figure D-1. Rather than being an error, this discrepancy illustrates the wide range of values possible under varying environmental conditions. For purposes of consistency, the analysis in the main body of this report always assumes the short term density variations occur about the nominal density values shown in Figure D-1. That is, the assumed atmospheric density model has the form

$$\rho = \rho_0 + \Delta\rho \tag{D-6}$$

where

ρ_0 = nominal density (Figure D-1)

$\Delta\rho$ = density variation

Relative Velocity

The relative velocity between the orbiter and atmosphere is in vector form

$$\bar{v}_r = \bar{v}_0 - \omega_e \times \bar{r}_s \tag{D-7}$$

where

$\bar{v}_0$ = orbiter inertial velocity vector

$\bar{\omega}_e$ = earth rotation rate vector

$\bar{r}_s$ = orbiter position vector

The magnitude and direction of $\bar{v}_r$ thus depends on the orbiter altitude, orbit inclination, and orbit position. As an approximation, the rotation of the atmosphere with the earth will be neglected, resulting in

$$\bar{v}_r \simeq \bar{v}_0 = \omega_0 \, r_s \, \hat{x}_R \tag{D-8}$$

where

$$\omega_o = \left(\frac{GM}{r_S^3}\right)^{1/2} = \text{orbit rate}$$

GM = earth gravitational constant = 3.986×10^5 km^3/sec^2

$r_s = r_o + h$

h = orbiter altitude

r_o = earth radius = 6371 km

$\hat{x}_R$ = unit vector in direction of orbit velocity (Appendix C)

The maximum error in the direction of $\bar{v}_r$ introduced by this approximation is

$$\tan^{-1}\left[\frac{\omega_e}{\omega_o}\right] \simeq \tan^{-1}\left[\frac{7.27 \times 10^{-5}}{1.1 \times 10^{-3}}\right] = 3.8 \text{ degrees}$$

The maximum relative error in the magnitude of $\bar{v}_r$, over the altitude range where aerodynamic torques are significant, is $\omega_e/\omega_o \cong 0.066 = 6.6\%$.

Dynamic Pressure Model

The nominal dynamic pressure, with the above approximations, is plotted as a function of altitude in Figure D-3. As a consequence of the atmospheric density model and Equation (D-5), the dynamic pressure model has the form

$$q = q_o + \Delta q \qquad \text{(D-9)}$$

where

q_o = nominal dynamic pressure (Figure D-3)

Δq = dynamic pressure variation

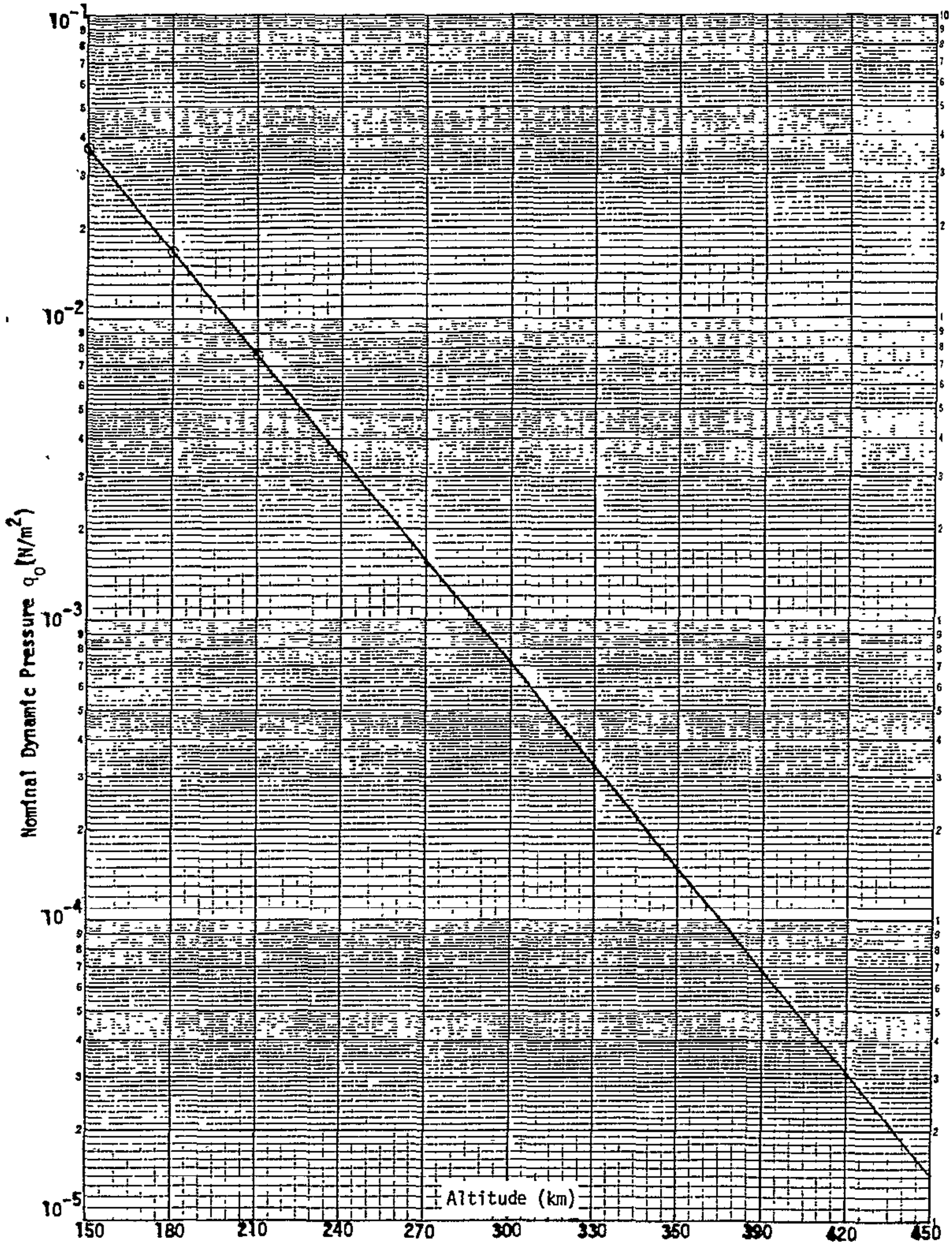

Figure D-3. Nominal Dynamic Pressure

D.1.2 Dimensional Factors

The orbiter dimensional factors, obtained from Reference D-1 are

S = reference area = 2690 ft^2 = 249.9 m^2
b = wing span = 936.68 in = 23.792 m
$\bar{c}$ = mean aerodynamic chord = 474.81 in = 12.060 m

Combining the dynamic pressure with the appropriate orbiter dimensions yields the nominal lateral (roll/yaw) aerodynamic torque constant qSb and the longitudinal (pitch) constant $qS\bar{c}$. These are plotted as a function of altitude in Figure D-4.

D.1.3 Attitude Factors

The attitude dependence of the aerodynamic torques appears through the moment coefficients $C_\ell(\alpha,\beta)$, $C_m(\alpha,\beta)$ and $C_n(\alpha,\beta)$. The correspondence of these coefficients to the orbiter body axes and the direction of the relative wind is illustrated in Figure D-5. With the approximation of Equation (D-7), the relative wind is along $\hat{x}_R$ and the angle of attack is

$$\alpha = \tan^{-1}\left[\frac{\hat{x}_R \cdot \hat{z}_B}{\hat{x}_R \cdot \hat{x}_B}\right] = \tan^{-1}\left[\frac{a_{31}}{a_{11}}\right] \qquad \text{(D-10)}$$

while the angle of side slip is

$$\beta = \sin^{-1}\left[\hat{x}_R \cdot \hat{y}_B\right] = \sin^{-1}\left[a_{21}\right] \qquad \text{(D-11)}$$

where a_{11}, a_{21}, and a_{31} are elements of the A_{BR} matrix. Table D-1

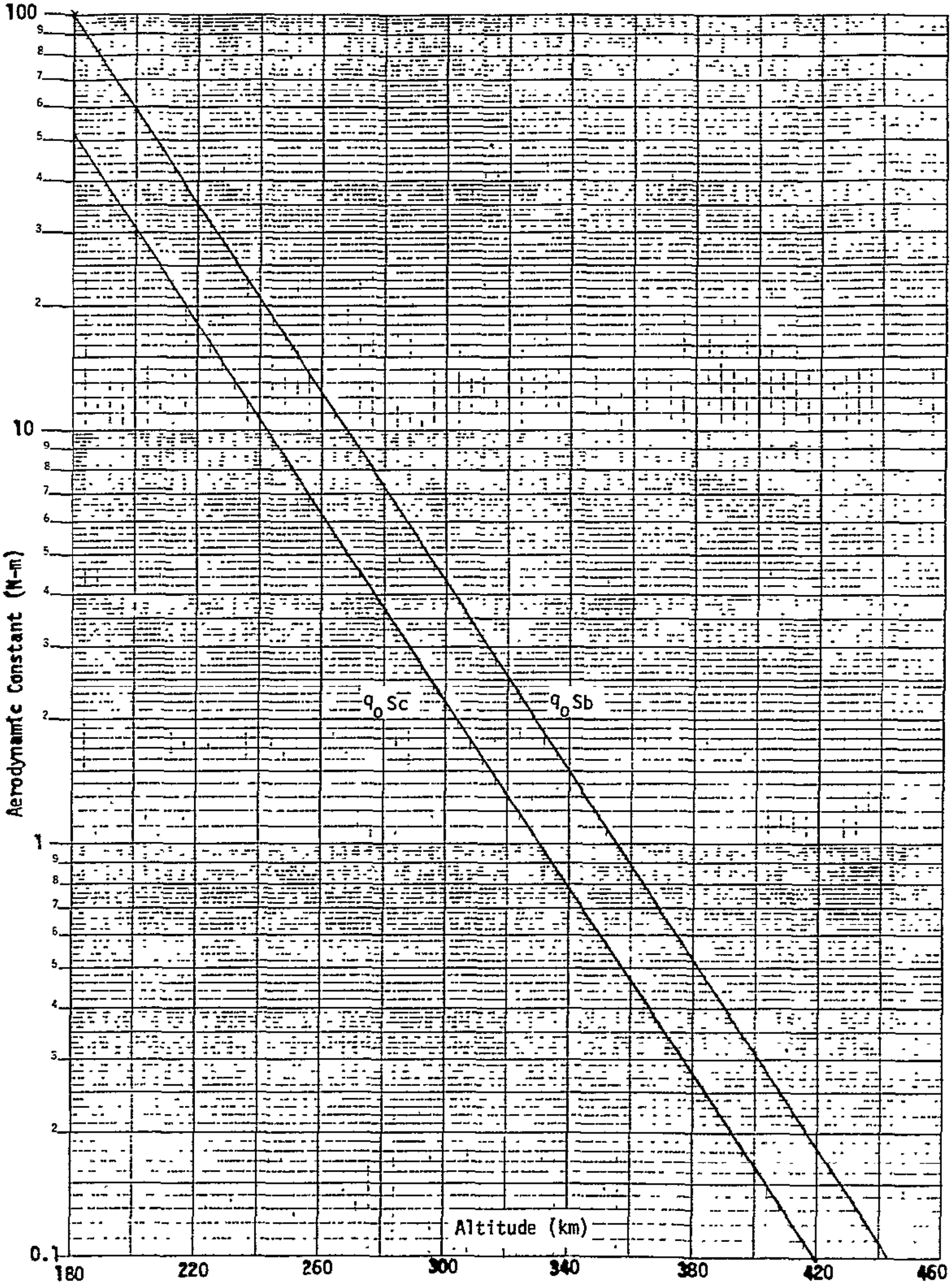

Figure D-4. Nominal Orbiter Aerodynamic Constants

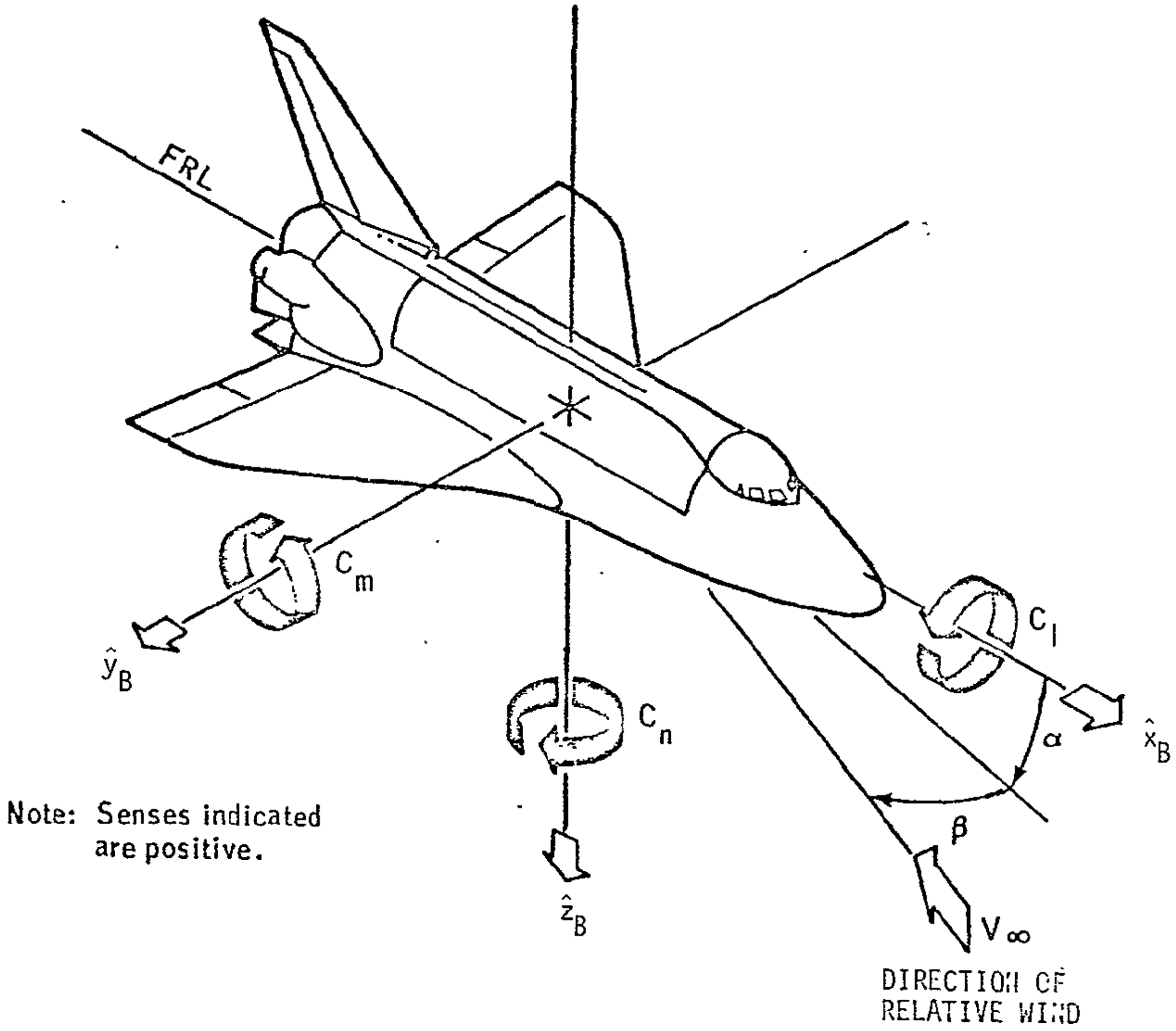

Figure D-5. Definition of Aerodynamic Moment Coefficients

Table D-1. Angles of Attack and Sideslip for Small Perturbations from Nominal Orientations

Orientation	Direction Cosines From A_{BR} Matrix			Angle of Attack	Angle of Sideslip
	a_{11}	a_{21}	a_{31}	α	β
1A	θ	$-\phi$	-1	$\theta - \frac{\pi}{2}$	$-\phi$
1B	$-\theta$	ϕ	1	$\theta + \frac{\pi}{2}$	ϕ
2*	$\pm\psi$	± 1	$\mp\phi$	$\tan^{-1}\left[\frac{\mp\phi}{\pm\psi}\right]$	$\pm\pi/2$
3C	1	$-\psi$	θ	θ	$-\psi$
3D	-1	ψ	$-\theta$	$\theta + \pi$	ψ
4A	θ	$-\phi$	-1	$\theta - \frac{\pi}{2}$	$-\phi$
4B	$-\theta$	ϕ	1	$\theta + \frac{\pi}{2}$	ϕ
5*	$\pm\psi$	± 1	$\mp\phi$	$\tan^{-1}\left[\frac{\mp\phi}{\pm\psi}\right]$	$\pm\pi/2$
6C	1	$-\psi$	θ	θ	$-\psi$
6D	-1	ψ	$-\theta$	$\theta + \pi$	ψ

Angles in radians

* Signs depend on which wing is forward

lists the correspondence between α and β and the small perturbation angles ϕ, θ, ψ with zero offset angles ϕ_0, θ_0, ψ_0 for the nominal orientations outlined in Section 8.

The values of the moment coefficients are plotted and tabulated in Reference D-1 for $0 \leq \alpha \leq 350$ degrees in 10 degree increments and for $0 \leq \beta \leq 180$ degrees in 15 degree increments. The plots are reproduced here as Figures D-6 to D-8. Because the orbiter is symmetrical with respect to the $\hat{x}_B$ - $\hat{z}_B$ plane, the moment coefficients for $-180 \leq \beta \leq 0$ are given by

$$C_\ell(\alpha, -\beta) = -C_\ell(\alpha, \beta) \tag{D-12}$$

$$C_m(\alpha, -\beta) = C_m(\alpha, \beta) \tag{D-13}$$

$$C_n(\alpha, -\beta) = -C_n(\alpha, \beta) \tag{D-14}$$

It should be noted that the moment coefficients in Reference D-1 were computed with the X_{CG} located 65% of the orbiter length back from the nose and with the payload bay doors closed. Data with the doors open is not available at this time. As shown in Figure D-9 the payload bay doors fold down over the wings with little protrusion. The main effect of opening the doors is therefore to replace the smooth upper shell of the orbiter with the contents of the payload bay. The mission dependence and complex shape of the payload bay contents makes a general evaluation of the impact on the moment coefficients a difficult task.

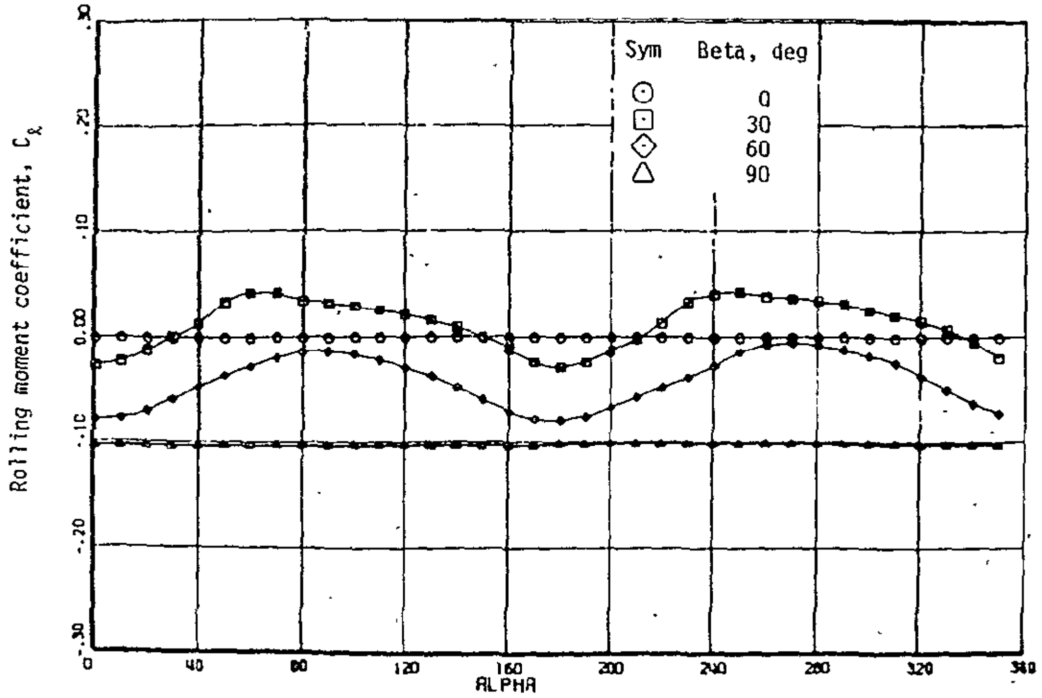

(a) β = 0° to 90°

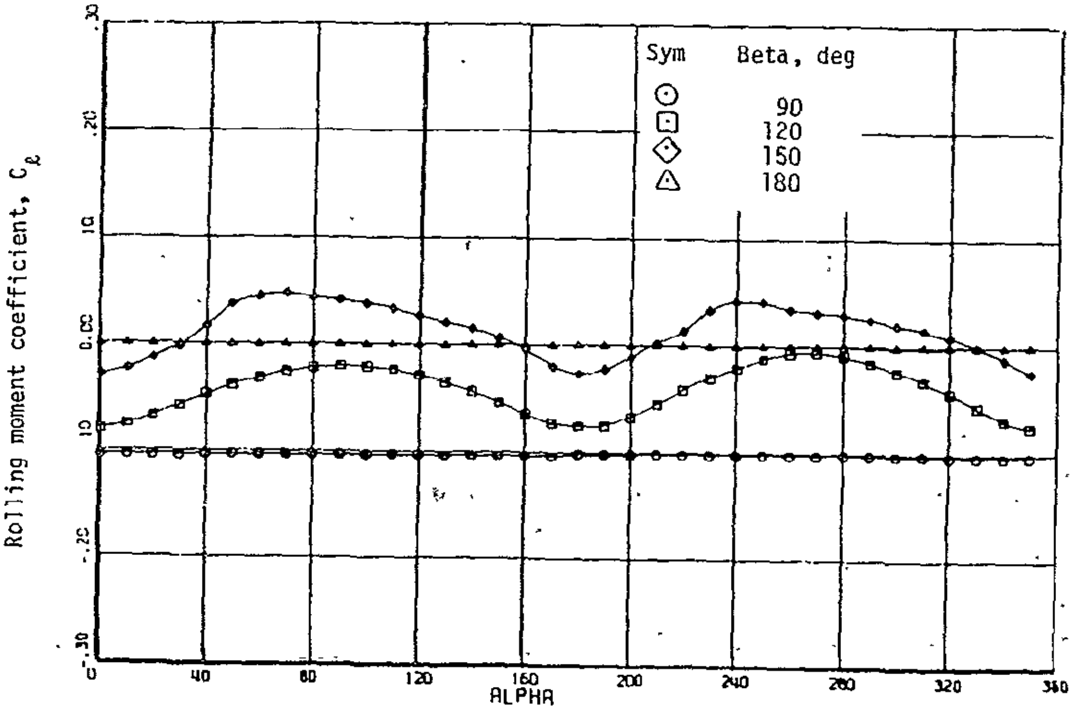

(b) β = 90° to 180°

Figure D-6. Variation of Rolling Moment Coefficient With Angle of Attack

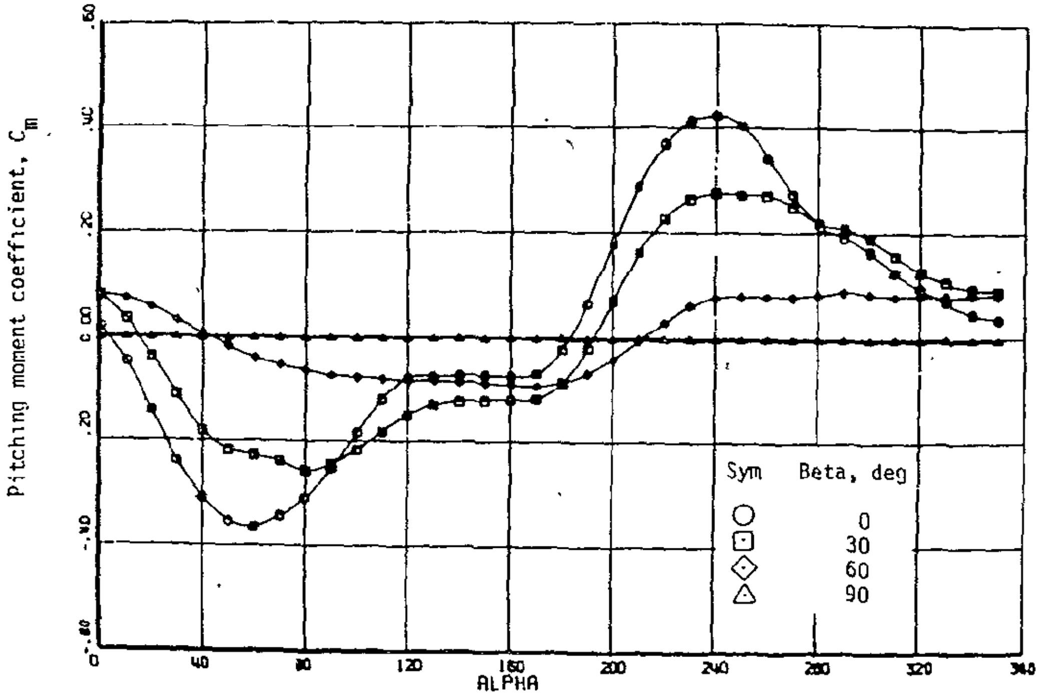

(a) β = 0° to 90°

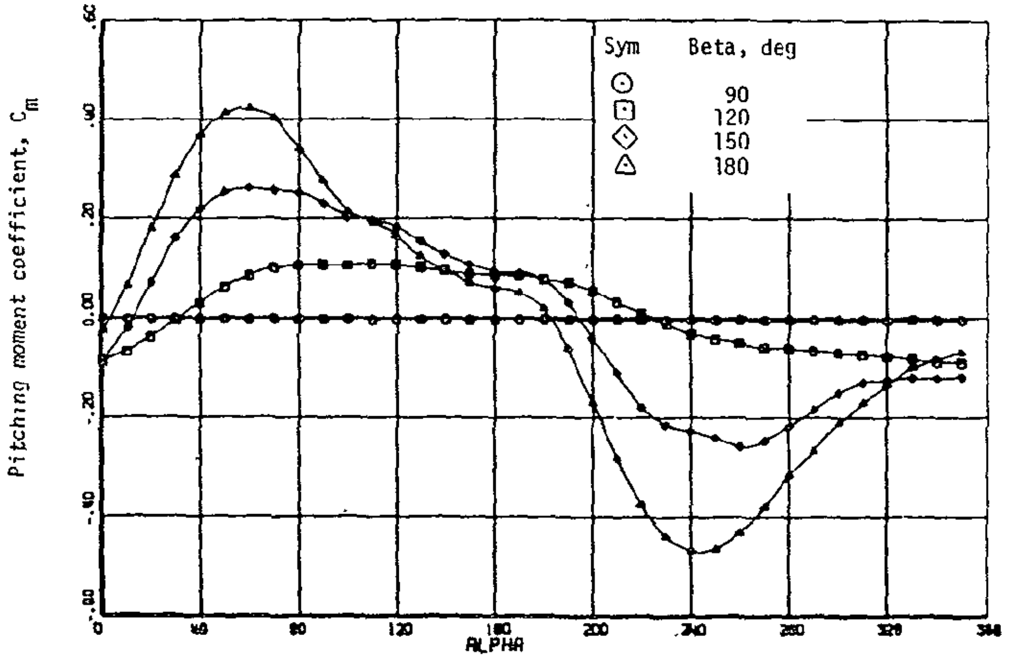

(b) β = 90° to 180°

Figure D-7. Variation of Pitching Moment Coefficient With Angle of Attack

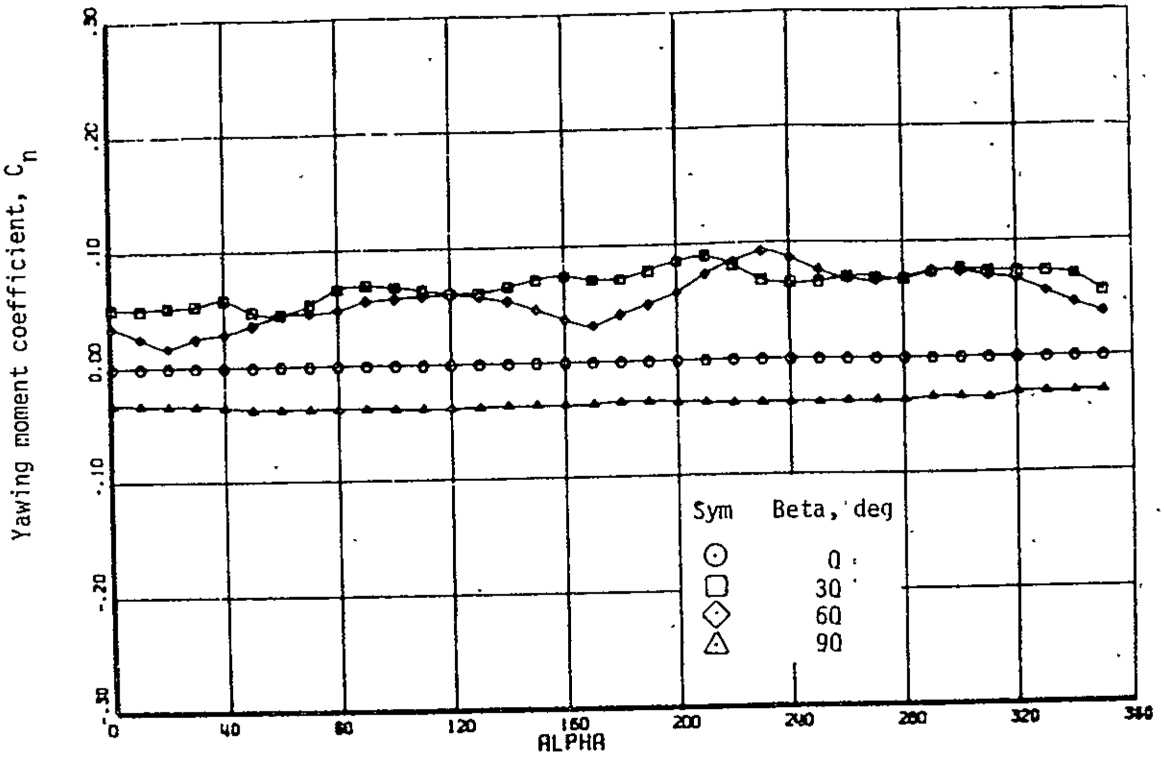

(a) β = 0° to 90°

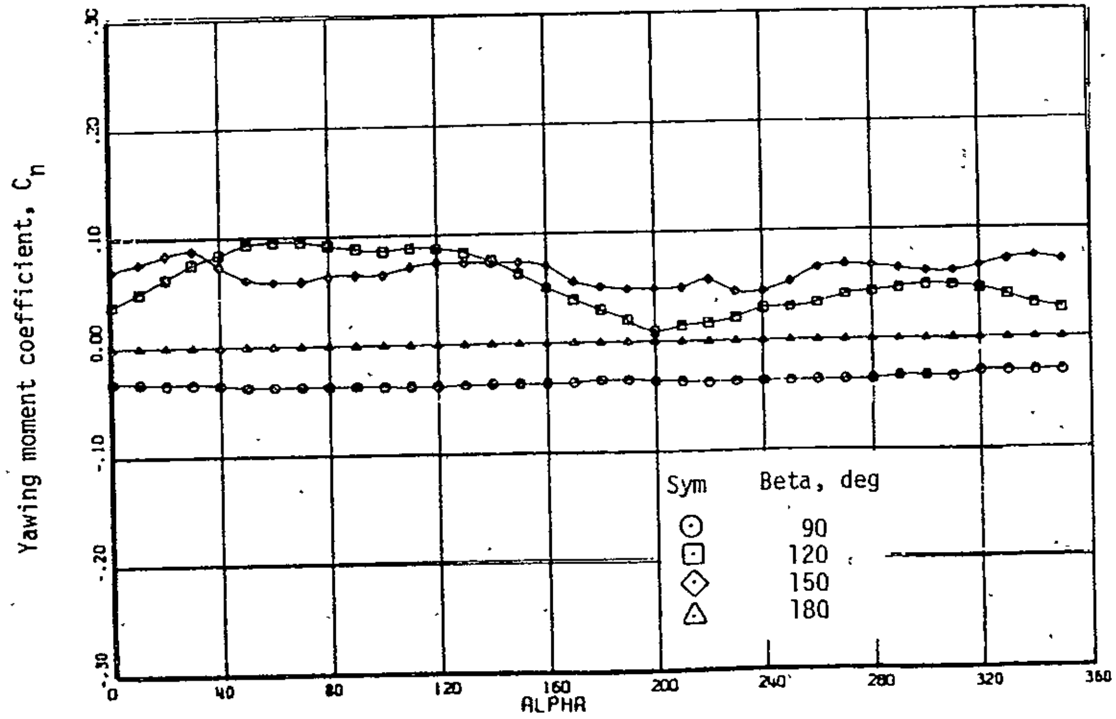

(b) β = 90° to 180°

Figure D-8. Variation of Yawing Moment Coefficient With Angle of Attack

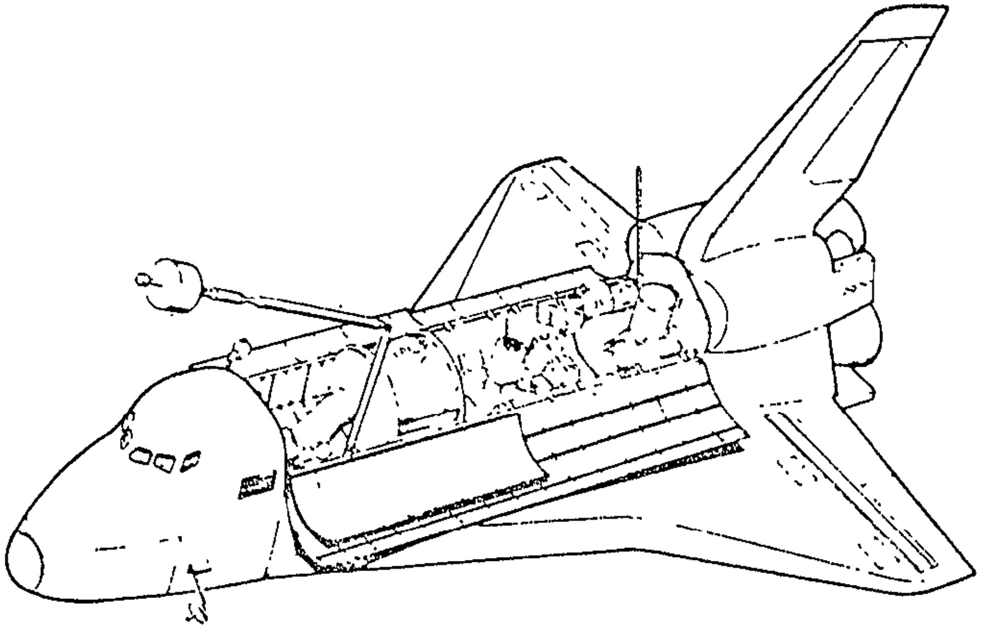

Figure D-9. Shuttle Orbiter with Payload Bay Doors Open

D.2 GRAVITY GRADIENT TORQUES

The gravity gradient disturbance torque model is

$$\overline{T}_G = 3\,\omega_o^2\,\hat{r} \times \overline{\overline{I}} \cdot \hat{r} \tag{D-15}$$

where

ω_o = orbit rate

$\hat{r}$ = unit vector from orbiter to geocenter

$\overline{\overline{I}}$ = orbiter inertia dyadic

In terms of the body axis inertias and elements of the A_{BR} matrix the torque is

$$\overline{T}_G = 3\omega_o^2 \begin{bmatrix} (I_{zz} - I_{yy})a_{23}\,a_{33} + I_{xy}\,a_{13}\,a_{33} - I_{xz}\,a_{13}\,a_{23} + I_{yz}\,(a_{33}^2 - a_{23}^2) \\ (I_{xx} - I_{zz})a_{13}\,a_{33} + I_{yz}\,a_{13}\,a_{23} - I_{xy}\,a_{23}\,a_{33} + I_{xz}\,(a_{13}^2 - a_{33}^2) \\ (I_{yy} - I_{xx})a_{13}\,a_{23} + I_{xz}\,a_{23}\,a_{33} - I_{yz}\,a_{13}\,a_{33} + I_{xy}\,(a_{23}^2 - a_{13}^2) \end{bmatrix} \tag{D-16}$$

The orbiter mass properties, in particular the products of inertia, are mission dependent. For this study the typical values from Appendix A will be assumed.

$$I_{xx} = 1.24 \times 10^6 \text{ Kg-m}^2$$

$$I_{yy} = 9.39 \times 10^6 \text{ Kg-m}^2$$

$$I_{zz} = 9.72 \times 10^6 \text{ Kg-m}^2$$

$$I_{xy} = I_{xz} = I_{yz} = 0$$

The gravity gradient torque therefore reduces to

$$\overline{T}_G = 3\omega_o^2 \begin{bmatrix} (I_{zz} - I_{yy})\, a_{23}\, a_{33} \\ (I_{xx} - I_{zz})\, a_{13}\, a_{33} \\ (I_{yy} - I_{xx})\, a_{13}\, a_{23} \end{bmatrix} \tag{D-17}$$

The factor $3\omega_o^2$ is related to the altitude h in km by

$$3\omega_o^2 = \frac{3\ GM}{(r_o + h)^3} = \frac{1.1958 \times 10^6}{(6371 + h)^3} \qquad \left[\frac{\text{rad}}{\text{sec}^2}\right] \tag{D-18}$$

This relation is plotted in Figure D-10. Whereas doubling the altitude from 180 km to 360 km reduces the nominal aerodynamic constants by more than two orders of magnitude (Figure D-4) the gravity gradient constant

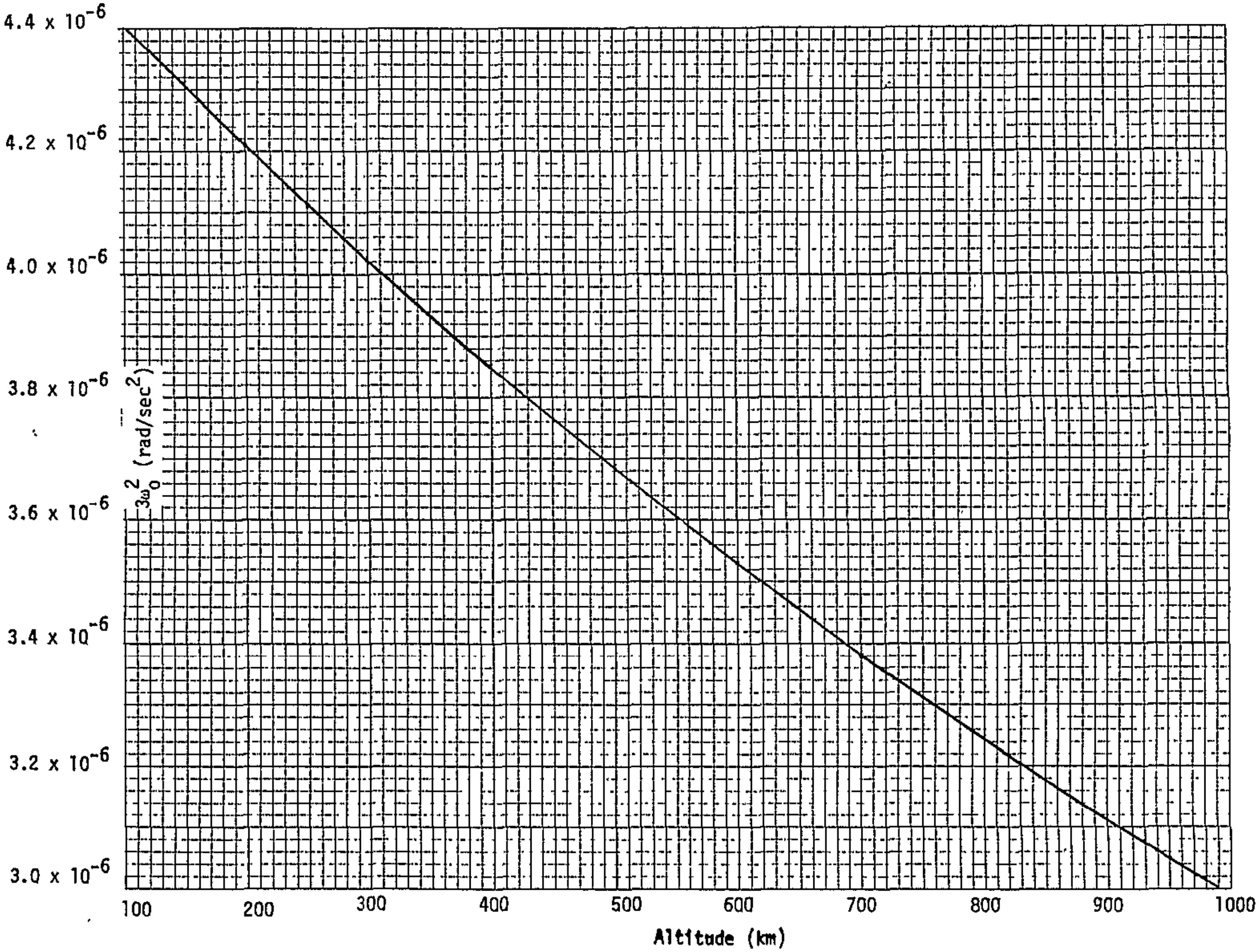

Figure D-10. $3\omega_o^2$ vs Altitude

$3\omega_0^2$ is reduced by only 7.8%. In view of this, and the fact that the aerodynamic constants are subject to wide variations from environmental factors, the altitude dependence of the gravity gradient torque can be safely neglected at low altitudes. The value $3\omega_0^2 = 4 \times 10^{-6}$ rad/sec^2, corresponding to $h \approx 300$ km is therefore assumed in deriving the gravity gradient torques for small perturbations from the nominal orientations listed in Table D-2.

D.3 REFERENCES

D-1. EX 33/7605-97, "Orbital Aerodynamic Characteristics of the SSV Orbiter," J. Underwood, JSC, 25 May 1976.

D-2. Weidner, D. K. (Editor), "Natural Environment Criteria for the NASA Space Station Program", NASA TM X-53865, 31 October 1969.

D-3. Smith, R. E., "Solar Activity Indices," NASA MSFC, S&E-AERO-YS (131-71), 8 April 1971.

D-4. Weidner, D. K. (Editor), "Space Environment Guidelines for Use in Space Vehicle Development (1969 Revision)," NASA TM X-53957, October 1969.

D-5. NASA TM X-53815, "Variations in Orbital Altitude Atmospheric Density for MSFC 1971-1976 Space Station Programs," 13 February 1969.

D-6. NASA SP-8021, "Models of Earth's Atmosphere (90 to 2500 Km)," March 1973.

Table D-2. Gravity Gradient Torques for Small Perturbations from Nominal Orientations

Orientation	Direction Cosines From A_{BR} Matrix			Gravity Gradient Torque (N-m)		
	a_{13}	a_{23}	a_{33}	T_{gx}	T_{gy}	T_{gz}
1A 1B	$-\psi$ ψ	-1 1	ϕ $-\phi$	$-1.32\ \phi$	$33.92\ \phi\ \psi$	$32.60\ \psi$
2	θ	$-\phi$	-1	$1.32\ \phi$	$33.92\ \theta$	$-32.60\ \phi\ \theta$
3C, 3D	θ	$-\phi$	-1	$1.32\ \phi$	$33.92\ \theta$	$-32.60\ \phi\ \theta$
4A, 4B	1	$-\psi$	θ	$-1.32\ \phi\ \psi$	$-33.92\ \theta$	$-32.60\ \psi$
5	1	$-\psi$	θ	$-1.32\ \theta\ \psi$	$-33.92\ \theta$	$-32.60\ \phi$
6C 6D	ψ $-\psi$	1 -1	$-\phi$ ϕ	$-1.32\ \phi$	$33.92\ \phi\ \psi$	$32.60\ \psi$

Angles in radians

Torque values given hold within ± 10% for altitudes in the range $150 \leq h \leq 550$ km

APPENDIX E

TILTED DIPOLE MAGNETIC FIELD MODEL

For present purposes, an adequate description of the earth's magnetic field is the tilted dipole model. In attitude reference coordinates, the field is

$$\overline{B}_R = -\frac{M_e}{(r_o + h)^3}\begin{bmatrix} -\cos\varepsilon \sin i \cos\alpha + \sin\varepsilon\,(\sin\alpha \sin u + \cos i \cos\alpha \cos u) \\ \cos\varepsilon \cos i + \sin\varepsilon \sin i \cos u \\ -2\cos\varepsilon \sin i \sin\alpha - 2\sin\varepsilon\,(\cos\alpha \sin u - \cos i \sin\alpha \cos u) \end{bmatrix} \quad \text{(E-}$$

where

$M_e = 8.056 \times 10^{10}$ gauss - km^3

$r_o = 6371$ km

h = orbiter altitude

ε = dipole tilt $\simeq 11$ deg

i = orbit inclination

$\alpha = \omega_o t$

$u = \omega_e t$

$\omega = [GM/(r_o+h)^3]^{\frac{1}{2}}$

$GM = 3.986 \times 10^5$ km^3/sec^2

$\omega_e = 7.27 \times 10^{-5}$ rad/sec

The field in body coordinates is found by transforming through the A_{BR} matrix

$$\overline{B}_B = A_{BR}\,\overline{B}_R \tag{E-2}$$

The "most unstable" axis for control purposes is the y-body axis in Orientation 3C, and this will be adopted for sizing purposes. The A_{BR} matrix for orientation 3C is approximately

$$A_{BR}^{3C} = \begin{bmatrix} 1 & 0 & 0 \\ 0 & -1 & 0 \\ 0 & 0 & -1 \end{bmatrix}$$

Using this transformation, the body components of $\overline{B}$ are plotted in Figures E-1 and E-2 for h = 200 km and i = 30 and i = 90 degrees. The corresponding plots of b_x vs b_z are in Figures E-3 and E-4. The field components are plotted in the common units of Gauss. The more proper MKS units of weber/m^2 can be obtained by multiplying the field strength in Gauss by 10^{-4}.

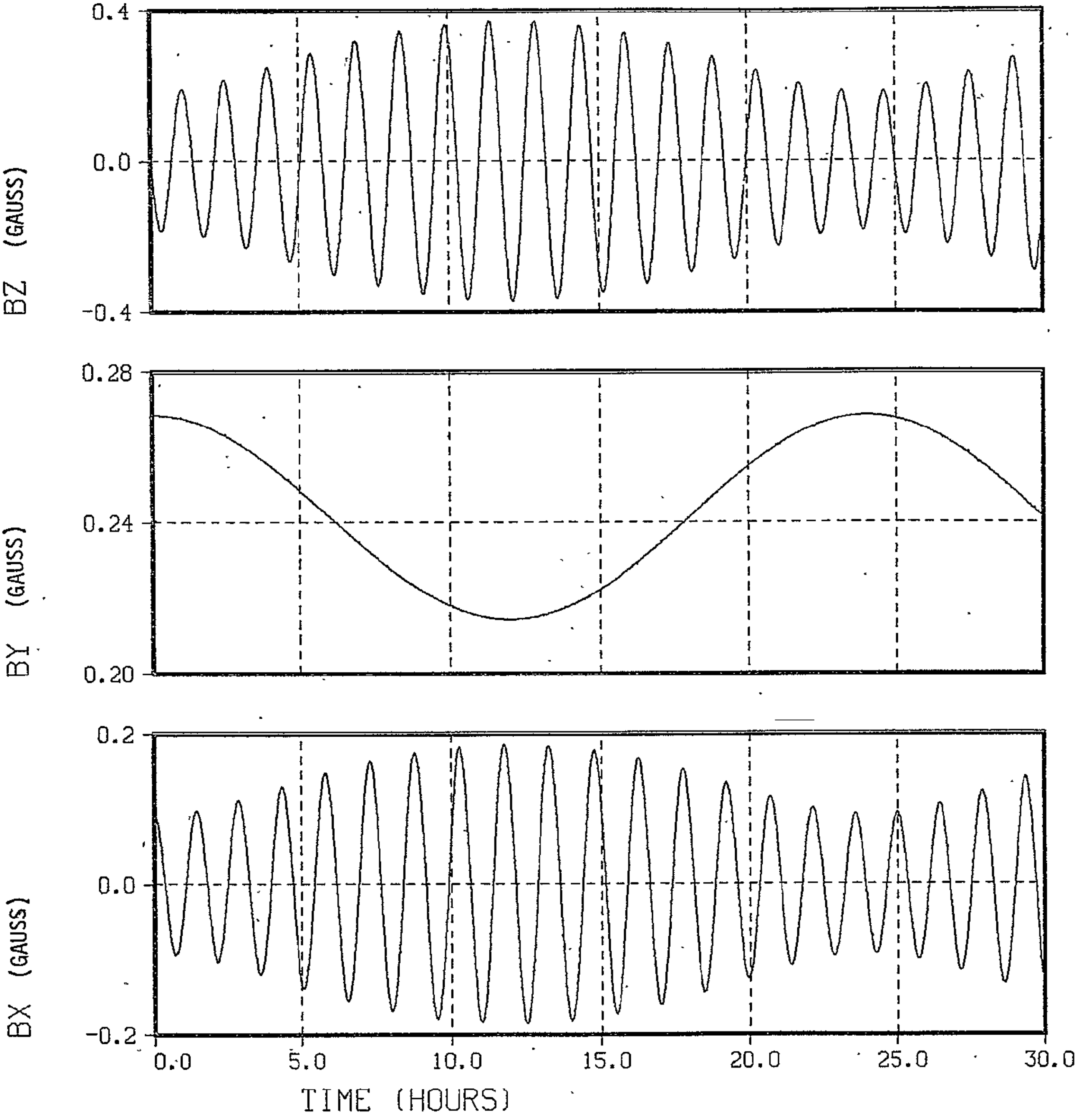

Figure E-1. Body Components of $\bar{B}$ in Orientation 3C at 200 km With 30 Degree Orbit Inclination

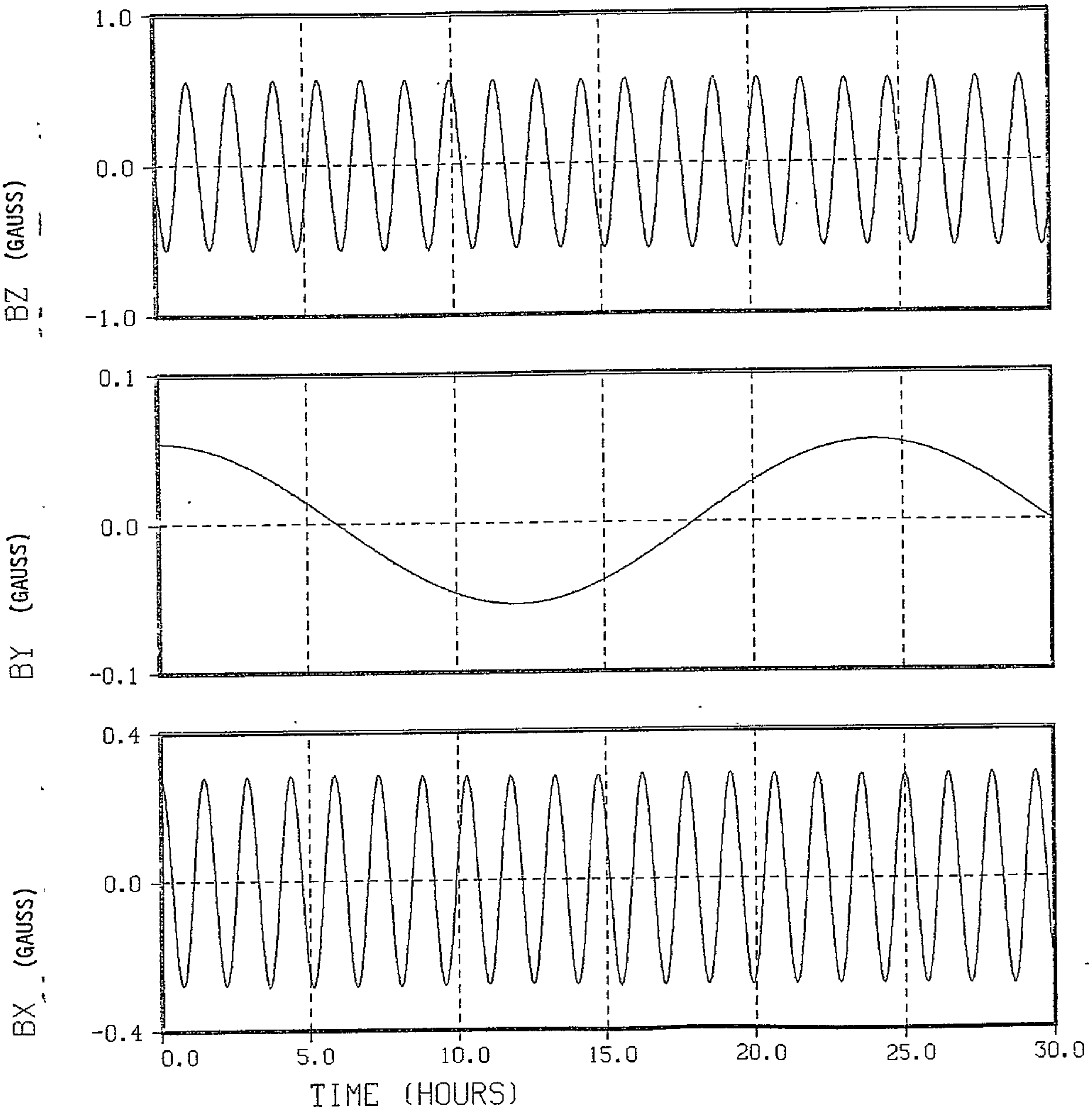

Figure E-2. Body Components of $\bar{B}$ in Orientation 3C at 200 km With 90 Degree Orbit Inclination

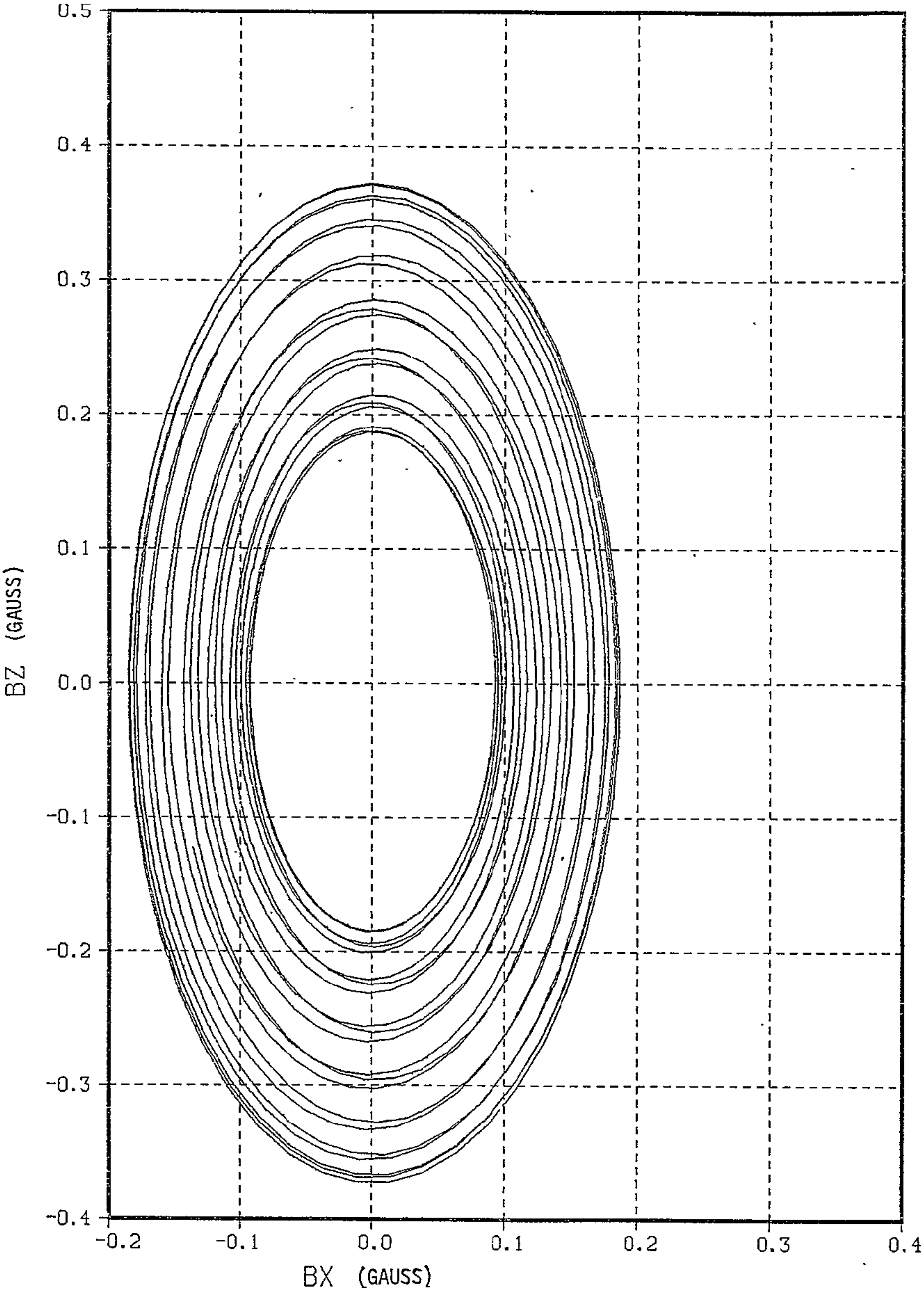

Figure E-3. X- and Z- Body Components of $\bar{B}$ for Orientation 3C at 200 km With 30 Degree Orbit Inclination

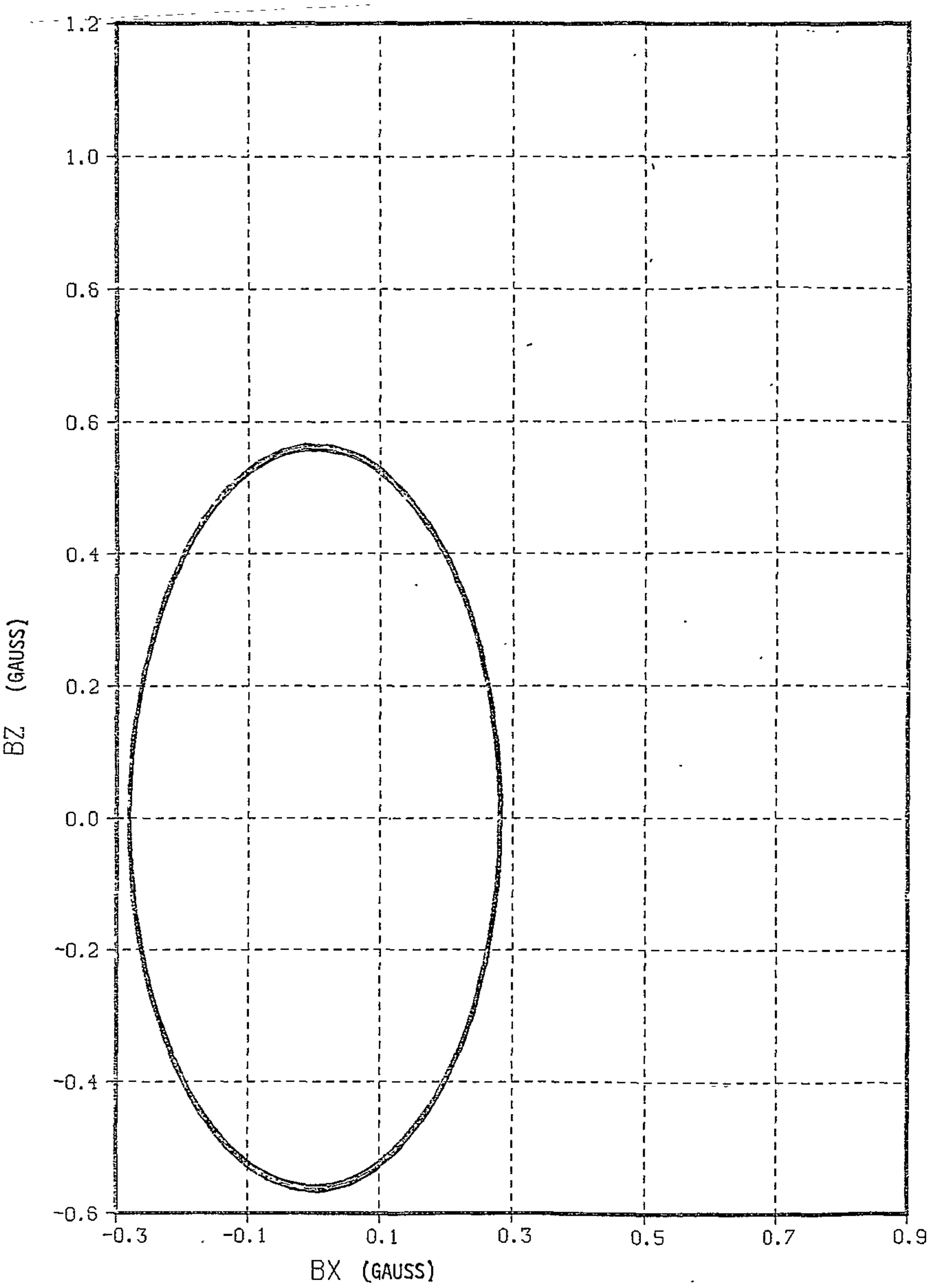

Figure E-4. X- and Z- Body Components of $\bar{B}$ for Orientation 3C at 200 km With 90 Degree Orbit Inclination

APPENDIX F

MOMENTUM EXCHANGE DEVICE TRADEOFF

F.0 INTRODUCTION

This appendix documents the tradeoff study of momentum exchange actuators for the orbiter null torque attitude stabilization system for EVAL. The candidate actuator types are the reaction wheel (RW), single gimbal control moment gyro (SG CMG) and double gimbal control moment gyro (DG CMG).

F.1 ACTUATOR REQUIREMENTS

The actuator requirements fall into two main categories, namely, control requirements and accommodation requirements. Each of these groups will be discussed below.

F.1.1 Control Requirements

The primary control requirements on the momentum exchange actuators are adequate control torque and momentum storage capability for capture from the orbiter RCS limit cycle and during extended operation in a variable disturbance environment. Table F-1, based on the analysis and simulation in the main body of this report, summarizes the estimated control torque and momentum requirements under a variety of conditions. The largest requirements, by far, occur for capture from the nominal orbiter RCS limit cycle rates. Note that the capture requirements imply an essentially spherical momentum envelope.

An additional important control requirement is continued, although possibily degraded, three-axis control capability with one unit failed. This implies that a minimum of four RW's or SG CMG's, or three DG CMG's are required. Further desirable control features are simple actuator control (steering) laws and freedom from control singularities.

Table F-1.. Estimated Control Torque and Momentum Requirements

Case				Control Requirements			
Mode	Orientation	Altitude (Km)	Conditions	Torque (N-m)		Momentum (N-m-sec)	
				Pitch	Roll/Yaw	Pitch	Roll/Yaw
Capture from RCS Limit Cycle	Nose Forward (worst case)	180 to 1000	Nominal Rate Limit Cycle (0.01 deg/sec)	12	8	2700	2700
			0.1 x Nominal Rate Limit Cycle (0.001 deg/sec)	1.3	1	500	500
Follow Null Torque Attitude (practical control law)	Nose Forward	200	± 20% Atmospheric Density Variation at Orbit Frequency	0.12	*	105	*
	Nose Down	200		1.9	*	1740	*
		250		0.34	*	288	*

*Nominally zero; depends on unloading policy, products of inertia, pitch motion, etc.

F.1.2 Accommodation Requirements

The orbiter payload size, weight, and power accommodations are subject to the limitations outlined in Reference F-2. Since the size/weight/power used by the momentum exchange actuators must be deducted from the experiment allowance, it is essential that these be minimized.

Size

Depending on the spacelab configuration used on a particular mission, the volume available for payload, outside the spacelab module, ranges from about 32 meter^3 (1 pallet segment) to 184 meter^3 (5 pallet segments with overhang). As a goal, the actuator volume should be limited to about 10% of a pallet segment or 3 meter^3.

Weight

Again depending on the spacelab configuration, the mission dependent payload weight allowance ranges from about 5800 to 9350 kg (12,760 to 20,570 pounds). As a goal, the actuator weight should be limited to about 10% of the minimum weight allowance or 580 kg (1276 pounds).

Power

Electrical power for the orbiter is provided by hydrogen/oxygen fuel cells. The orbiter baseline provides only 50 KWh of electrical energy for spacelab; however, an additional 840 KWh "energy kit" is included in the spacelab weight, providing a total of 890 KWh for the spacelab and its payloads. The heat rejection capability of the orbiter limits the total spacelab/payload electrical power dissipation to 7 KW continuous, and 12 KW peak (15 minutes out of 3 hours). Of this total, the power available to the payloads and mission dependent equipment ranges from 2.57 to 5.37 KW continuous and 7.00 to 10.2 KW peak. As a goal, the actuator power, at peak torque, should be limited to about 10% of the minimum continuous available payload power, or about 250 watts.

F.2 SIZING ANALYSIS

Estimates of the weight, size, and power of each type of actuator (RW, SG CMG, DG CMG) are derived in this section, using data in Reference F-1. Three combinations of torque and momentum are included in the analysis to span the requirement range implied by various sets of operational conditions, as summarized in Table F-2.

The sizing analysis is in terms of individual actuator units of each type capable of producing equal magnitudes of peak torque and momentum. The actual control capabilities of a set of actuators depends not only on the individual unit characteristics but also on the number of units used and the mounting configuration (orthogonal, skewed, pyramid, etc.).

The reaction wheel is fundamentally a servo motor with a large inertia rotor. On command, motor torque accelerates or decelerates the rotor, changing its angular momentum. The reaction to this torque is transmitted through the unit mounting pads to the vehicle structure. The wheel motor can continue to apply torque to the vehicle until a maximum speed somewhat below the motor no-load speed is reached. At this speed, the maximum amount of angular momentum is stored in the reaction wheel. Because the motor torque and rotor rate vectors are parallel in a reaction wheel, the electrical power input required to produce a given torque is relatively large. The electrical power P_E (watts) required to produce a torque T (N-m) with the rotor spinning at an angular rate ω (rad/second) with a motor power efficiency η can be expressed as $P_E = T\,\omega/\eta$. This relation restricts reaction wheels to low torque applications.

The SG CMG operates with a fixed momentum magnitude with one gimbal rotational degree of freedom and the output torque $\overline{T} = \overline{\omega}_g \times \overline{H}_W$ is thus constrained to lie along the line normal to both the gimbal axis and the wheel momentum vector $\overline{H}_W$. This is the SG CMG output torque axis, and since it lies normal to the gimbal axis there is no component of output torque about

Table F-2. Actuator Torque/Momentum Combinations for Sizing Analysis

Actuator Characteristics		Operational Condition Restrictions		
Torque N-m (ft-lb)	Momentum N-m-sec (ft-lb-sec)	Maximum RCS Limit Cycle Rate deg/sec	Minimum Altitude (km) for Orbiter Orientation	
			Nose Forward	Nose Down
1.36 (1)	678 (500)	0.001 (0.1 x Nominal)	180	230
13.6 (10)	1360 (1000)	0.001 (0.1 x Nominal)	180	210
13.6 (10)	2710 (2000)	0.01 (Nominal)	180	200

the gimbal torquer axis. The SG CMG output torque is thus limited only by the radial load carrying capacity of the gimbal and momentum wheel bearings. The gimbal torquer must only accelerate the gimbal and since there are no large reaction torques about the gimbal axis, relatively large gimbal rates are possible. The SG CMG is thus a torque multiplier, i.e., small torques applied about the gimbal axis to establish rate $\bar{\omega}_g$ can produce large torques about the output axis. In broad terms the single gimbal CMG is well suited to high torque applications, but has a constrained momentum storage capability.

The momentum envelope of one SG CMG is the plane normal to the gimbal axis and the envelope of an actuator cluster is dependent on the mounting configuration of the individual actuators. While the basic cluster can be arranged to give a more or less regular momentum envelope, a single CMG failure strongly distorts the envelope and causes quite complex software problems in the steering laws. Another severe problem with a SG CMG cluster is the existence of singularity surfaces within the momentum envelope occurring when the torque output vectors of the individual actuators are coplanar, i.e., no control torque is possible about the axis normal to the plane. A total analytic solution for the location of these surfaces and general software for singularity avoidance does not exist, and the normal strategy is local avoidance of the surfaces along with varying amounts of excess momentum storage capability over the basic requirements.

The DG CMG has two rotational degrees of freedom, one about each of the two perpendicular gimbal axes. Motion of the two gimbals can produce an effective gimbal rate $\bar{\omega}_g$ anywhere in the plane normal to the wheel momentum $\bar{H}_w$ thus the output torque $\bar{T} = \bar{\omega}_g \times \bar{H}_w$ can lie anywhere in this plane which can then be called the DG CMG output torque plane. However, the output torque always has a component along one of the gimbal axes, therefore, it is limited by torque capability of the gimbal torquers. Again in broad terms, the double gimbal CMG is more suited to applications with moderate torque requirements, but has a more flexible (i.e., optimum) momentum storage capability.

The DG CMG momentum envelope is spherical in the absence of gimbal stops and even with limited gimbal rotation the envelope of a single actuator is a portion of a sphere. The envelope of a DG CMG cluster of any number of actuators is thus also spherical and the failure of a single actuator while decreasing the envelope size does not change its spherical character. Desaturation strategies can thus be devised to decrease or control the stored momentum with the guarantee that the momentum vector is always moving away from the envelope in both normal and failure modes of operation. DG CMG singularity occurs only when the individual actuator momentum vectors are colinear and this situation can be avoided through relatively simple logic involving redistribution of the individual momenta through the use of the excess degrees of freedom provided when more than a single actuator is in use.

F.2.1 RW Sizing

For given saturation momentum and peak output torque requirements, optimization of a RW design involves basically the selection of the rotor saturation speed that minimizes a weighted combination of weight, size and power. The total weight is the sum of three components

- The rotor and housing
- The motor
- The power supply and drive electronics

The first two of these components are presented in graphical form in Reference F-1, along with size and power relations. The weight of the power supply and drive electronics is largely related to the peak motor power requirements, but is subject to wide variations (based on cooling constraints) with respect to the required torque time history and duty cycle. A reasonable value for the power supply and drive electronics weight is 1.0 pounds/watt of peak power.

Figure F-1 summarizes the weight/power tradeoff for H = 500 foot-pound-seconds, T = 1 foot-pounds. The straight solid line represents the peak power, while the upper solid curve represents the total RW + electronics weight with a 1.0 pound/watt power supply/drive electronics weight penalty. The minimum weight of 400 pounds occurs at $\omega \cong 400$ RPM, with a power input at peak torque $p \cong 125$ watts. For the required four units, the total weight is 1600 pounds (727 kg) and the total power is 500 watts. Both these figures exceed the previously stated goals: maximum weight = 1276 pounds (580 kg), maximum power = 250 watts.

The tradeoff was reworked with an optimistic power supply/drive electronics weight penalty of 0.1 pound/watt and the result is plotted as the lower solid curve in Figure F-1. The minimum weight per unit is reduced to less than 200 pounds for $1300 < \omega < 2400$ RPM, but the power to run at these speeds ranges from 400 to 720 watts. The power can be reduced to 102 watts by reducing the wheel speed to 340 RPM and increasing the weight per unit to one-quarter of the total weight goal or 319 pounds (145 kg). The power for four units is 408 watts, exceeding the power goal. It is thus apparent that simultaneous satisfaction of the weight and power goals is not feasible with reaction wheels. The design coming closest to meeting the weight/power goals is indicated by the small circles in Figure F-1. The diameter of each of these RW's is 44 inches. If it is assumed that the volume occupied by the RW plus electronics corresponds to a cube with the RW diameter as a side, the volume is 85,184 inch^3 per unit or 340,736 inch^3 = 5.58 meter^3 per cluster of four. This is almost twice the volume goal of 3 meter^3.

Figure F-2 shows the tradeoff curves for the H = 1000 foot-pound-seconds, T = 10 foot-pounds reaction wheel units. It is clear that regardless of wheel speed, the size/weight/power goals will be far exceeded, and no satisfactory RW design exists. The H = 2000 foot-pound-seconds, T = 10 foot-pounds units are even more futile and no curves are provided for these.

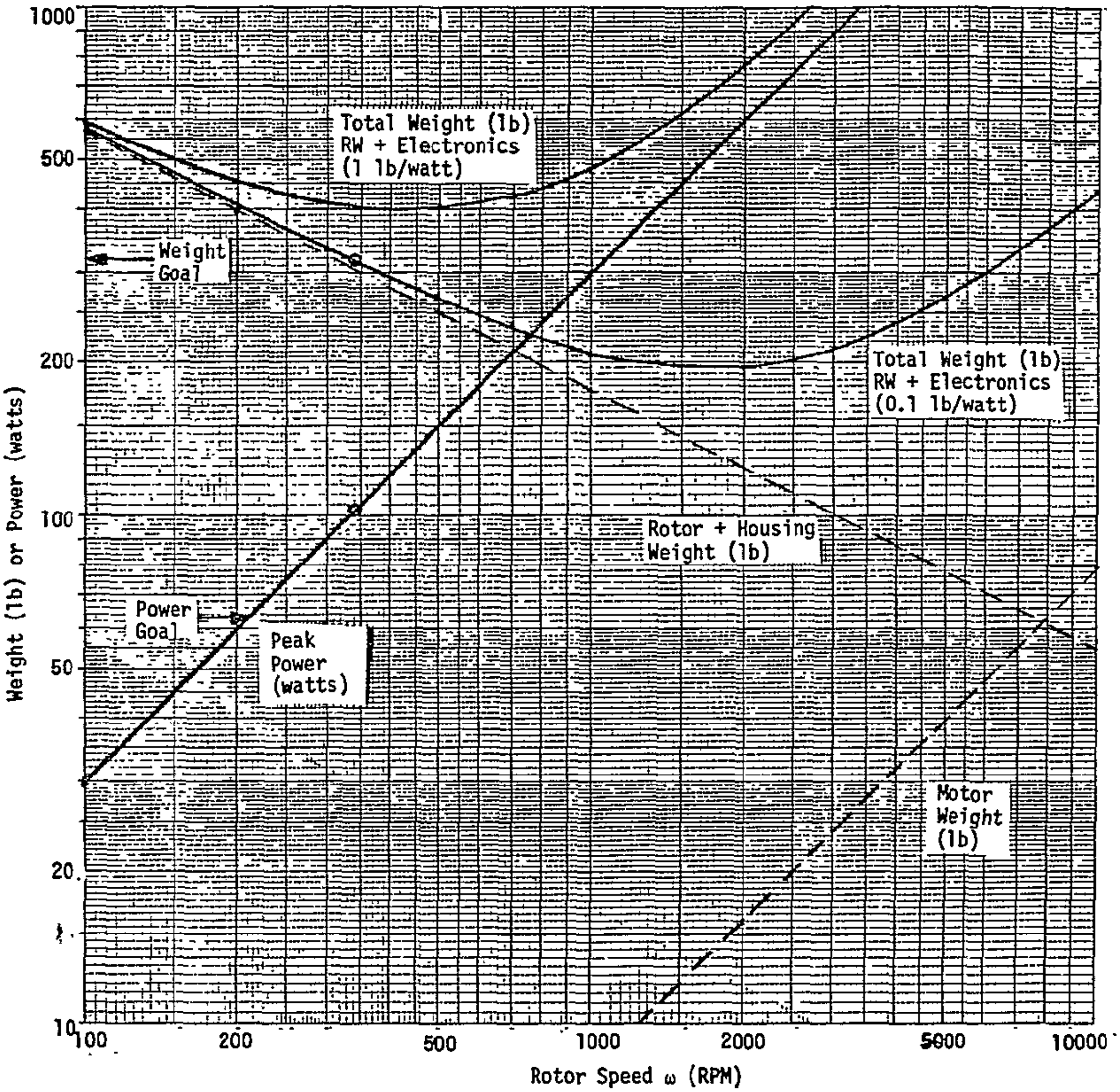

Figure F-1. Reaction Wheel Weight/Power Tradeoff
H = 500 ft-lb-sec, T = 1 ft-lb

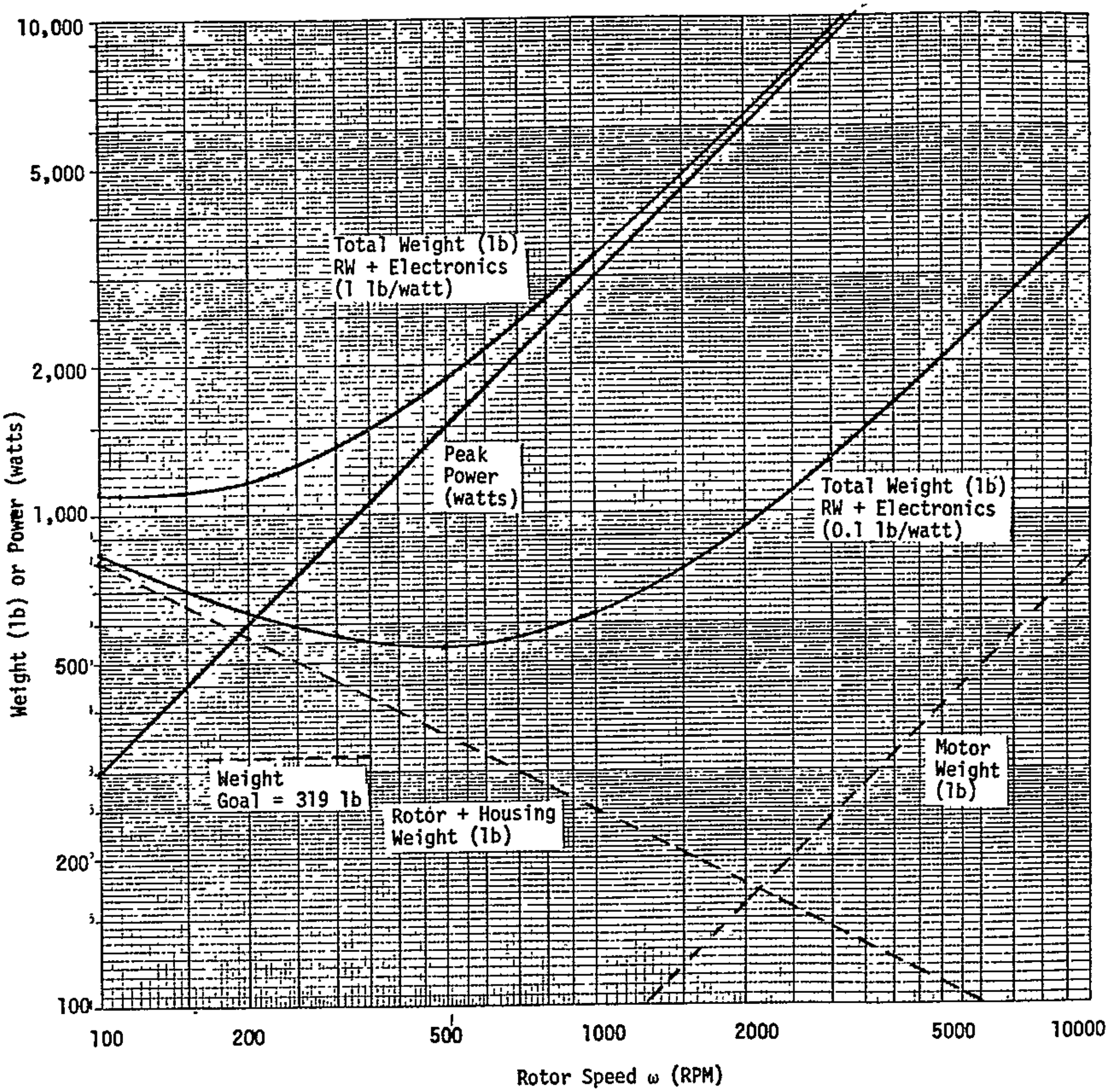

Figure F-2. Reaction Wheel Weight/Power Tradeoff
H = 1000 ft-lb-sec, T = 10 ft-lb

F.2.2 SG CMG Sizing

With the exception of the initial run-up period, the CMG rotor operates at fixed speed and the input power to the spin motor only has to make up for losses. It is, therefore, practical to run the CMG rotor at a higher speed than with a RW, and all the CMG design data in Reference F-1 is based on an optimum rotor speed of 11,700 RPM. The total weight and power is relatively insensitive to rotor speed over the range from 8,000 to 14,000 RPM, however.

The SG CMG power requirement, after run-up, consists of the rotor running power and the gimbal torque power. The rotor running power is 14 watts for the 500 foot-pound-seconds units, 20 watts for the 1000 foot-pound-seconds case, and 26 watts for the 2000 foot-pound-seconds CMG's. The torquer power is in all cases negligible for the required output torque levels. The SG CMG total weight consists of the CMG rotor/housing/gimbal weight plus the power supply/drive electronics weight. The power/weight/size values for the three momentum/torque combinations are summarized in Table F-3.

F.2.3 DG CMG Sizing

The sizing analysis of the DG CMG is very similar to that of the SG CMG, with the basic difference of the addition of an extra gimbal and its associated drive electronics. This increases the weight and size of each unit, compared to a SG CMG with the same torque and momentum capability. However, fewer units are required in the cluster. The larger reaction torques on the gimbals in the DG CMG increases the required gimbal drive torques so that the gimbal drive power is no longer negligible. The DG CMG sizing results, derived from Reference F-1, are summarized in Table F-4.

Table F-3. SG CMG Summary*

Torque (ft-lb)	Momentum (ft-lb-sec)	Power (watts)			Weight (lb)			Size	
		Spin Motor	Gimbal Drive	Total	CMG	Electronics**	Total	Diameter (in)	Volume (in^3)
1	500	14	< 0.1	14	70	14	84	24	13,824
10	1000	20	< 0.1	20	95	20	115	26	17,576
10	2000	26	< 0.1	26	130	26	156	30	27,000

*Per unit, four required
**1 lb/watt

Table F-4. DG CMG Summary*

Torque (ft-lb)	Momentum (ft-lb-sec)	Power (watts)			Weight (lb)			Size	
		Spin Motor	Gimbal Drive	Total	CMG	Electronics**	Total	Diameter (in)	Volume (in^3)
1	500	14	0.5 x 2 = 1	15	85	15	100	27	19,683
10	1000	20	2.5 x 2 = 5	25	140	25	165	32	32,768
10	2000	26	2.5 x 2 = 5	31	175	31	206	38	54,872

*Per unit, three required
**1 lb/watt

F.3 CONCLUSIONS

The results of the momentum exchange actuator sizing analysis are summarized in Table F-5 using metric units. Reaction wheels clearly fail to meet the requirements in all three size categories, and can, therefore, be eliminated from further consideration. Both single gimbal and double gimbal CMG's, on the other hand, are consistent with the assumed torque/momentum requirements and size/weight/power limitations. The size/weight/power figures, on a total system basis (four single gimbal or three double gimbal CMG's) are sufficiently close that additional criteria must be considered to make a final decision on the actuator type.

For a given momentum, the cost of an individual double gimbal CMG is higher than a single gimbal CMG. However, because fewer double gimballed units are required, the total system costs are likely to be comparable. Likewise, it is technically feasible to build either single or double gimballed CMG's in the momentum range required.

On performance grounds, the double gimballed CMG has several advantages:

- Better match to the required nearly spherical momentum envelope, especially with one unit failed.
- Relatively simple steering law.
- Less problem with singularities.

The double gimballed CMG, therefore, appears to have the best combination of properties for the EVAL mission.

Table F-5. Momentum Exchange Actuator Sizing Summary

Capability per Actuator Unit		Type	Number in Cluster	Total Requirement for Cluster		
Torque (N-m)	Momentum (N-m-sec)			Weight (kg) Goal = 580 kg	Power (watts) Goal = 250 watts	Volume (m^3) Goal = 3 m^3
1.36	678	RW	4	580	408*	5.58*
		SG CMG	4	153	56	0.91
		DG CMG	3	136	45	0.97
13.6	1360	RW	4	> 964*	> 1200*	> 7.25*
		SG CMG	4	209	80	1.15
		DG CMG	3	225	75	1.61
13.6	2710	RW	4	*	*	*
		SG CMG	4	284	104	1.77
		DG CMG	3	281	93	2.70

*Does not meet goal

RW = reaction wheel
SG CMG = single gimbal control moment gyro
DG CMG = double gimbal control moment gyro

F.4 REFERENCES

F-1. Dohogne, J. R., "Momentum Exchange Actuator Size, Weight and Power Analysis", Sperry Phoenix Copany, March 1965.

F-2. ESTEC SLP/2104, "Spacelab Payload Accommodation Handbook", Review Issue, PDR-B, European Space Agency, 1976.